REACTIVE CHEMICAL DYNAMICS: BORN-OPPENHEIMER AND BEYOND

A Thesis submitted for the degree of

DOCTOR OF PHILOSOPHY

By

T. RAJAGOPALA RAO

SCHOOL OF CHEMISTRY
UNIVERSITY OF HYDERABAD
HYDERABAD 500046
INDIA

NOVEMBER 2012

School of Chemistry
University of Hyderabad
Central University P. O.
Hyderabad 500 046
India

STATEMENT

I hereby declare that the matter embodied in this thesis is the result of investigations carried out by me in the School of Chemistry, University of Hyderabad, Hyderabad, under the supervision of **Prof. Susanta Mahapatra**.

In keeping with the general practice of reporting scientific observations, due acknowledgement has been made wherever the work described is based on the findings of other investigators.

(T. Rajagopala Rao)

School of Chemistry
University of Hyderabad
Central University P. O.
Hyderabad - 500 046
India

CERTIFICATE

Certified that the work embodied in this thesis entitled "**REACTIVE CHEMICAL DYNAMICS: BORN-OPPENHEIMER AND BEYOND"** has been carried out by Mr. **Tammineni Rajagopala Rao** under my supervision and the same has not been submitted elsewhere for a Degree.

(Prof. Susanta Mahapatra)

Thesis Supervisor

Dean
School of Chemistry

List of Abbreviations

BF	-	Body-fixed
BO	-	Born-Oppenheimer
BW	-	Bian-Werner
CC	-	Coriolis coupling
CP	-	Chebyshev polynomial
CRP	-	Cumulative reaction probability
CS	-	Centrifugal sudden
CW	-	Capecchi Werner
DVR	-	Discrete variable representation
FBR	-	Finite basis representation
FC	-	Franck-Condon
FFT	-	Fast Fourier transform
FT	-	Fourier transform
FT^{-1}	-	Inverse Fourier transform
FWHM	-	Full-width at half-maximum
GWP	-	Gaussian wave packet
JT	-	Jahn-Teller
MCTDH	-	Multi-configuration time-dependent Hatree
MP4	-	Fourth order Móller-Plesset perturbation theory
MRCI	-	Multireference configuration interaction
IC-MRCI	-	Internaly-cintracted Multireference configuration interaction
NAC	-	Nonadiabatic coupling
NIP	-	Negative imaginary potential
PES(s)	-	Potential energy surface(s)
PJT	-	pseudo-Jahn-Teller
QCT	-	Quasiclassical trajectory
RT	-	Renner-Teller
SF	-	Space-fixed
SI	-	Symplectic integrator
SIL	-	Short-iterative Lancozs
SO	-	Spin-orbit
SOD	-	Second-order differencing
SQM	-	Spectral quantization method
TDSE	-	Time-dependent Schrödinger equation
TISE	-	Time-independent Schrödinger equation
TDWP	-	Time-dependent wave packet
TS	-	Transition state
VTST	-	Variational-transition-state-theory
WP	-	Wave packet

Synopsis of the thesis entitled

Reactive Chemical Dynamics: Born-Oppenheimer And Beyond

to be submitted to the
University of Hyderabad
for the degree of

Doctor of Philosophy

by

T. Rajagopala Rao

Supervisor
Prof. Susanta Mahapatra

School of Chemistry
University of Hyderabad
Hyderabad 500 046, INDIA

November 2012

SYNOPSIS

The present thesis entitled "**Reactive Chemical Dynamics: Born-Oppenheimer And Beyond**" deals with treatment of nuclear dynamics on a single adiabatic potential energy surface (PES) and on coupled (nonadiabatic) electronic states and consists of six chapters. First, the effect of nonadiabatic interactions on dynamical observables *viz.*, the initial state-selected reaction probabilities, integral reaction cross sections and thermal rate constants of H + D_2 (HD) and D + H_2 (HD) reactions is investigated. Later, the effect of geometric phase (GP), Born-Haung (BH) corrections to the adiabatic Born-Oppenheimer (BO) Hamiltonian and of explicit surface coupling on the nuclear dynamics in the degenerate electronic ground state of D_3 is studied. In addition, the electronic and spin-orbit (SO) coupling effects on the photodetachment spectroscopy of ClH_2^- and ClD_2^- are studied. Finally, the initial state-selected and state-to-state dynamical attributes of $C(^3P)$ + $OH(X^2\Pi) \rightarrow CO(a^3\Pi)$ + H (^2S) reaction on its first excited adiabatic electronic PES ($1^2A''$) are examined. To this effort, a time-dependent wave packet (TDWP) method is employed throughout and the obtained theoretical results are compared with the available experimental and other theoretical results from the literature.

Chapter 1 starts with a discussion on the well celebrated BO approximation and explains the situations where it breaks down completely. In the latter situation, the singular or diverging nature of the nonadiabatic coupling (NAC) elements, and the occurrence of topological effects limit the use of adiabatic electronic representation. To circumvent it, a nonunique electronic representation, so called, diabatic was invented. In the latter representation the total molecular wavefunction is expanded in the diabatic electronic basis which is obtained *via* a unitary transformation of the adiabatic ones. The resulting nuclear Schrödinger equation in the diabatic representation is diagonal in nuclear kinetic energy terms. The nonadiabatic coupling here is introduced by the off-diagonal elements of the diabatic electronic potentials. A proper choice of the diabatic electronic basis ensures the removal of the singular NAC elements and also corrects for the geometric phase change.

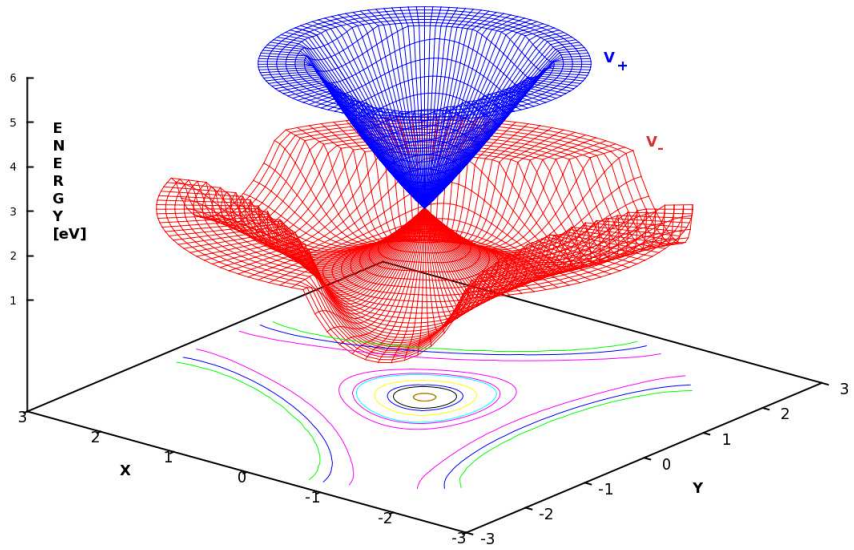

FIG. 1: DMBE PESs of H_3. Lower and upper adiabatic sheets are, respectively, shown in red and blue colors. These represent the equatorial view of the PESs in hyperspherical coordinates at a fixed $\rho = 2.5\ a_0$.

Chapter 1 also describes few important features of the PESs obtained for H_3, ClH_2 and COH molecules. For example, a cross-section of the global three dimensional PES, well known in the literature as the double many body expansion (DMBE) PES for H_3 is plotted in Fig. 1 using hyperspherical coordinates ρ, θ, and ϕ [ρ determines the size and (θ, ϕ) determine the shape of the molecular triangle]. For a better portrayal of the two adiabatic sheets and their CIs, equatorial views of these surfaces are shown here. In an equatorial view, the central region corresponds to the D_{3h} configurations where hyperangle $\theta = 0^o$. As one moves from the center towards the periphery θ increases and H_3 approaches to the linear geometries. At the periphery $\theta = 180°$, which defines the collinear geometry of H_3 and various dissociation channels (reactive and nonreactive) appear in this geometry. It can be seen from Fig. 1 that the lower (red color) and upper (blue color) adiabatic sheets are degenerate at D_{3h} configurations. But this degeneracy is split along other geometries, leading to CIs of these PESs. The hydrogen exchange reaction takes place on the repulsive lower adiabatic PES. There exists a saddle point ($\sim$ 0.418

eV above the reactant asymptote) at symmetric collinear conformation with H-H distance = 1.757 a_0 on this repulsive surface [Varandas *et al.* , Chem. Phys. 86 (1987) 6258] . This discussion on PESs is followed by an overview of the theoretical and experimental advances and the aims of various works presented in the thesis.

In chapter 2, the theoretical framework to treat the nuclear dynamics by a TDWP approach is discussed. The body-fixed Jacobi or hyperspherical coordinates are utilized to numerically solve the time-dependent Schrödinger equation (TDSE) and to calculate the dynamical observables. The nuclear dynamics is treated with a n-state diabatic Hamiltonian considering the electronic nonadiabatic coupling effects. The quantum flux operator is represented both in the adiabatic as well as in a diabatic electronic representation. Preparation of the initial WP, its propagation and the final analysis - each of these topics are discussed at length in this chapter. The fast Fourier transformation and the discrete variable representation method have been used for the spatial propagation and the chebyshev polynomial expansion, split operator and chebyshev real wavepacket methods are used for the time propagation of the WP. The reaction probabilities depending on the total angular momentum J are calculated within the coupled-states (CS) approximation. These J-dependent reaction probabilities are utilized to calculate the integral reaction cross sections and thermal rate constants. For obtaining the state-to-selected reaction attributes, the initial WP pertinent to the reagent asymptote is prepared in the reagent Jacobi coordinates and immediately transformed to the product Jacobi coordinates . Only the real part of this initial wave packet is evolved in space and time using chebyshev real wavepacket method. At the end of each time step, the time-dependent expansion coefficients are obtained. Using these coefficients the state-to-state reaction attributes like differential and integral cross sections are calculated.

In chapter 3, the initial state-selected and energy resolved reaction probabilities, integral reaction cross sections and thermal rate constants obtained for the H + D_2 (HD) and D + H_2 (HD) reactions using the formalism outlined in chapter 2 are presented and discussed. The H + D_2 ($v = 0$, $j = 0$) $\rightarrow$ HD ($\sum v'$, $\sum j'$) + D

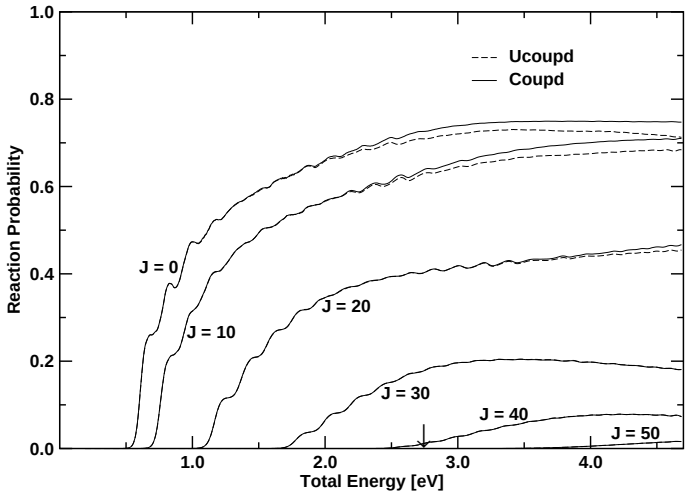

FIG. 2: Total reaction probabilities as a function of the total energy E for the H + D_2 (v = 0, j = 0) $\rightarrow$ HD ($\sum v'$, $\sum j'$) + D reaction for the total angular momentum, J = 0, 10, 20, 30, 40 and 50 (indicated in the panel) and Ω = 0. The coupled and uncoupled surface results are shown by the solid and dashed lines, respectively.

reaction probability values as a function of the total energy E are plotted in Fig. 2 for a few selected values of the total angular momentum, J = 0, 10, 20, 30, 40 and 50 (indicated in the panel) and for Ω = 0. The coupled and uncoupled surface results are shown by the solid and dashed lines, respectively. It can be seen from Fig. 2 that the threshold for the reaction shifts to the higher energy with increasing J value. The difference between the coupled and uncoupled surface results disappears below the energetic minimum ($\sim$ 2.74 eV) of CIs. But above this minimum, the difference becomes noticeable. As J increases the difference between the coupled and uncoupled surface results becomes negligible. It can be seen that above J = 20, the coupled and uncoupled surface results merge together. Oscillations in the probability curves reveal that at low energies the reaction proceeds via resonance formation which becomes more direct at higher energies. The reaction probabilities obtained for the D + H_2, H + HD and D + HD reactions also showed similar behavior.

The thermal rate constants obtained by statistically averaging over the rotational states, j = 0 - 3, of the D_2 molecule are shown in Fig. 3 for the H + D_2 (v = 0) re-

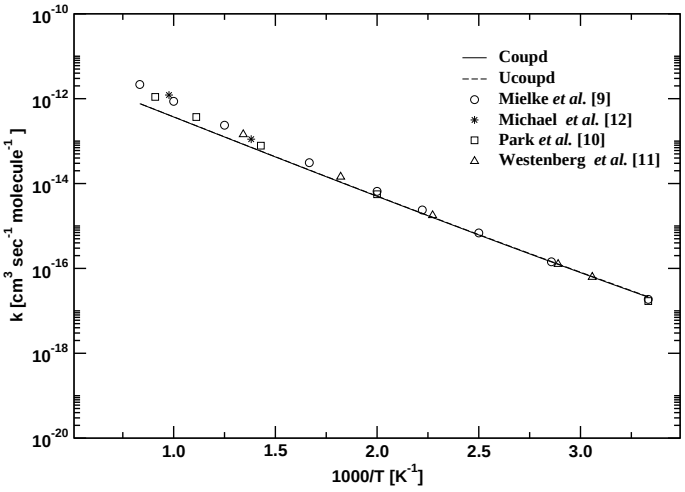

FIG. 3: Arrhenius plot of the Boltzmann averaged (over j = 0 - 3 of the reagent diatom) thermal rate constants for the H + D_2 ($v = 0$) reaction. The coupled and uncoupled surface results are shown by the solid and dashed lines, respectively.

action. The coupled and uncoupled surface results are shown by the full and dashed lines, respectively. The rate constant values available in the literature are shown by the circles [Mielke *et al.* , Phys. Rev. Lett. 91 (2003) 63201], squares [Park *et al.* , J. Chem. Phys. 96 (1992) 8853], triangles [Westenberg *et al.* , J. Chem. Phys. 47 (1967) 1393] and asterisks [Michael *et al.* , J. Phys. Chem. 94 (1990) 3318] on the diagram. The present rate constants reveal the expected Arrhenius behavior in agreement with the experimental and other theoretical data. The observed discrepancy with the literature data mainly arises from insufficient number of j values used in the Boltzmann averaging in the present case. Furthermore, other contributing factors to this discrepancy are, use of CS approximation (although it is a very good approximation for the hydrogen exchange reaction) and possible inaccuracies of the underlying PESs. Fig. 3 reveals that the difference between the coupled and uncoupled surface results is insignificant (within the drawing accuracy) in the reported temperature range of 300 - 1200 K. Rates obtained for the D + H_2, H + HD and D + HD reactions also showed similar trends.

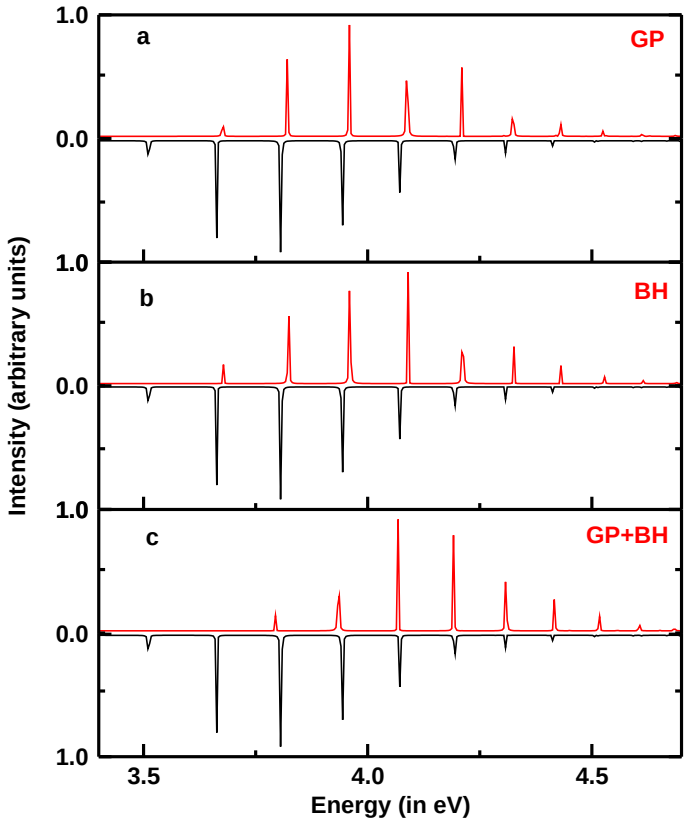

FIG. 4: The emission profile of D_3 from the n=3 Rydberg electronic state to its upper adiabatic electronic states of the $2pE'$ ground electronic manifold. Here, emission profiles calculated without the inclusion of GP and BH corrections are plotted in the inverted Y-axis and in black color whereas, the profiles with inclusion of GP or BH or both GP and BH corrections are plotted in the normal Y-axis and shown in red color.

In chapter 4, the nuclear dynamics of D_3, when prepared in the immediate neighborhood of the seam of CIs of its degenerate electronic ground state, is presented and discussed. The emission profile of Rydberg-excited D_3 for a transition to the upper adiabatic sheet of its $2pE'$ ground electronic manifold is shown in Figs. 4(a-c). The spectrum calculated without the GP and BH corrections is shown in the inverted Y- axis (in black color), whereas, the spectrum obtained with these corrections is shown in red color in the normal Y- axis. The upper adiabatic cone of D_3 is bound in nature in the absence of explicit coupling with its lower repulsive sheet. The emission spectrum in Fig. 4 therefore portrays the discrete vibrational

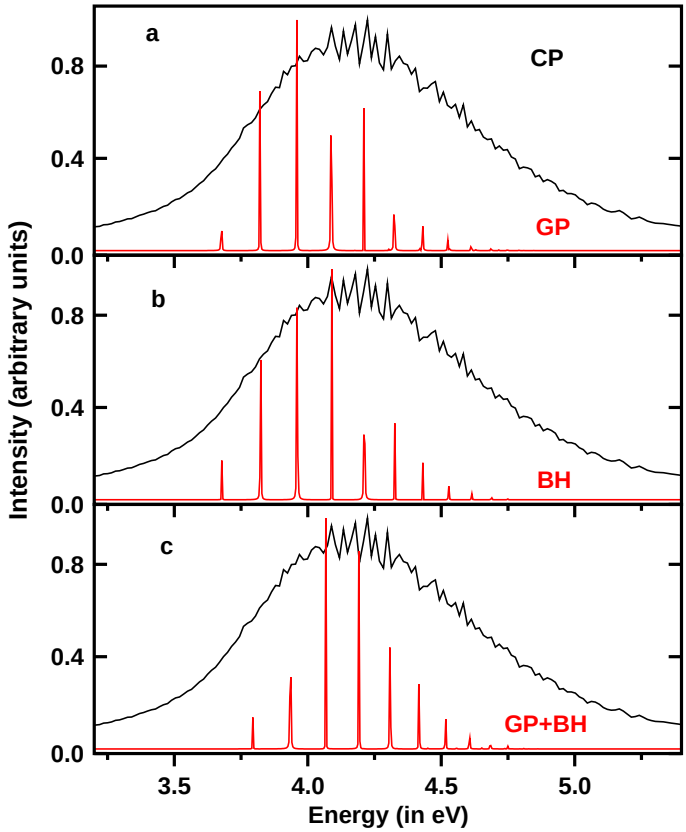

FIG. 5: Same as in FIG. 4, but including the complete surface coupling in the dynamics.

level structure in this case. It can be seen from these figures that the sharp vibrational structures remain unaltered when the GP and BH corrections are included. The maximum of each peak, however, shifts significantly to the higher energy. The inclusion of the GP correction introduces an additional angular momentum term in the effective Hamiltonian. Contribution of this term causes a shift of the energy eigenvalue. The BH term, on the other hand, is like any other centrifugal term and causes an effective decrease of the depth of the well of the upper adiabatic sheet by ∼0.32 eV. This results into a shift of the vibrational energy eigenvalues. Similar emission profile of Rydberg-excited D_3 for a transition to the lower adiabatic sheet of its $2pE'$ ground electronic manifold is also discussed in this chapter.

In Figs. 5(a-c) it is shown how the spectral features change upon inclusion of

the surface coupling, when the WP is launched on the upper adiabatic sheet of the ground electronic manifold of D_3. In these figures the broad envelope represents the vibronic energy level structure of the upper adiabatic sheet when its coupling to the lower sheet is explicitly included in the dynamics. The sharp line structures on the other hand represent uncoupled surface results including the GP and BH corrections as given in Figs. 4(a-c). It can be immediately seen that neither the GP nor the BH correction contributes to the huge broadening of the spectrum of this adiabatic sheet! Therefore, it is clear that this broadening solely originates from the off-diagonal derivative coupling terms of the nonadiabatic coupling operator. Furthermore, it is important to note that neither the GP nor the BH correction alone could place the maximum (center-of-gravity) of the exact spectral envelope at the right energy eigenvalue. It can be seen from panel c that a combined contribution from the GP plus BH correction is required to obtain this maximum at the right place. The observation supports to conclude that, with inclusion of both the GP and BH corrections, the shape of the spectral peaks remains unaffected however, their energy eigenvalue is altered.

In chapter 5, the electron detachment spectroscopy of ClH_2^- and ClD_2^- is examined and the results are presented, compared with recent high-resolution measurement and discussed. The partial spectra corresponding to the transition from ClH_2^- anion to V_Σ , $V_{\Pi-A}$ and $V_{\Pi+A}$ spin states of neutral ClH_2 are calculated and combined to obtain the full composite spectrum. This is plotted in the upper part of Fig. 6 (panel a) showing the results in the energy range of V_Σ and $V_{\Pi+A}$ separately. The results obtained from the uncoupled and coupled states spectra are shown by dotted lines and as shaded area in Fig. 6(a), respectively. In order to compare, the experimental and theoretical results of Garand *et al.* [Science 319 (2008) 72] are reproduced in the lower part of Figs. 3 (panel b). It is noted that the present theoretical spectra of panel a are shifted slightly to correct for the zero point energy contribution in order to obtain the experimental adiabatic ionization position at ~ 29521 cm^{-1}. It can be seen that the present theoretical results are in excellent agreement with the experimental and theoretical results of Garand *et al.* .

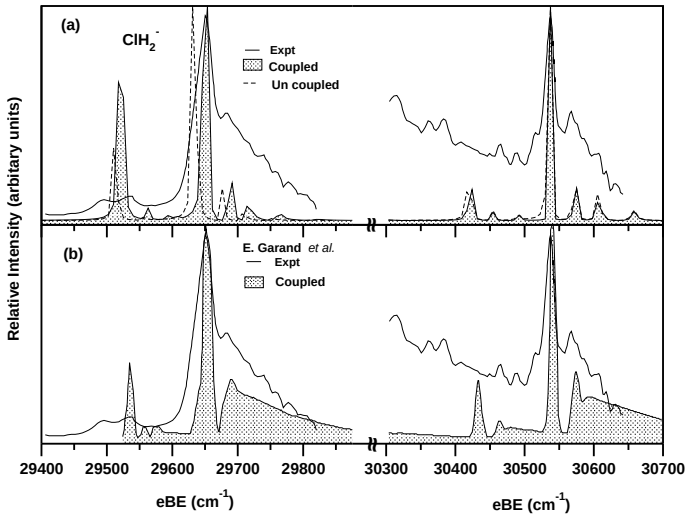

FIG. 6: Composite theoretical photodetachment spectrum of ClH_2^- in the energy range of V_Σ and $V_{\Pi+A}$ SO states of ClH_2 . The present theoretical and experimental results are shown in panel a and the results of Garand *et al.* [Science 319 (2008) 72] are shown in panel b. Relative intensity in arbitrary units is plotted as a function of the electron binding energy in cm^{-1}.

The peaks in the spectrum are assigned to the bend-stretch states of the Cl...H_2 van der Waals complex. The separation between the two intense peaks of panel a is $\sim$ 885 cm^{-1}, compares well with its experimental value of 887 cm^{-1}. This separation corresponds to the SO splitting of the V_Σ and $V_{\Pi+A}$ states of ClH_2 . This separation is slightly larger (by $\sim$ 20 cm^{-1}) in the uncoupled state results. The nonadiabatic coupling of the electronic states causes a reduction of this value. A similar discussion on the electron detachment spectroscopy of ClD_2^- is also presented in this chapter.

In chapter 6, the initial state-selected and state-to-state dynamical attributes for the $C(^3P)$ + $OH(X^2\Pi)$ $\rightarrow$ $CO(a^3\Pi)$ + H (^2S) reaction on the first excited PES ($1^2A''$) are presented and discussed. The initial state-selected and energy resolved integral reaction cross sections for this reaction on the first excited PES ($1^2A''$) are plotted in Fig. 7. The cross sections obtained for rotationally ground OH(v=0, j=0) and excited reagent OH(v=0, j=1) are shown in black and red colors, respectively, in panel a. Similarly, the cross sections obtained for vibrationally ground OH(v=0, j=0), first excited OH(v=1, j=0) and second excited reagent OH(v=2, j=0) are

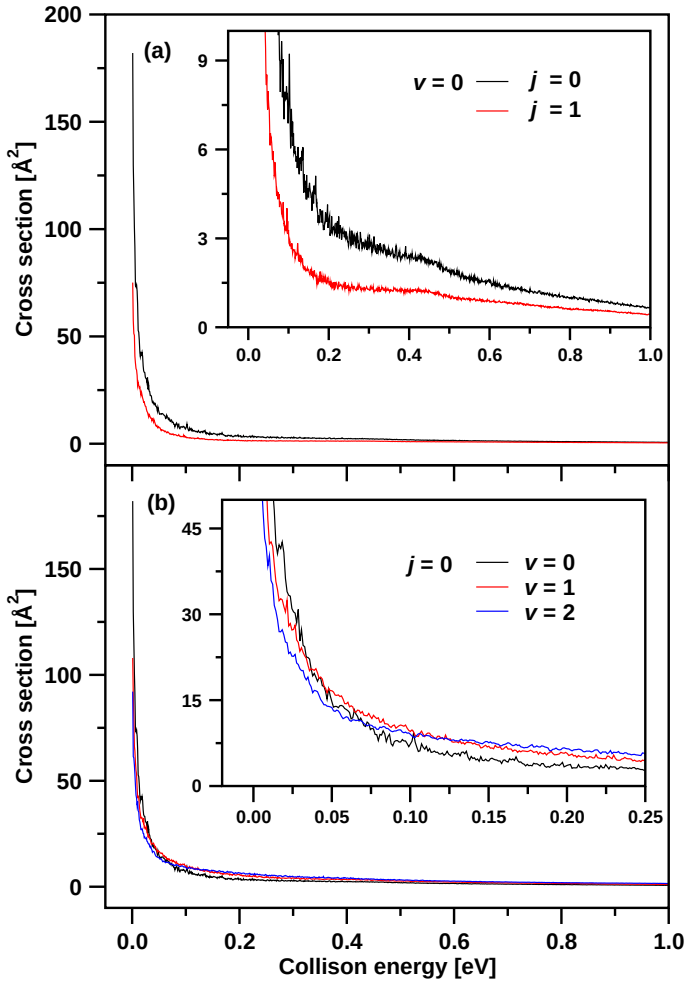

FIG. 7: Initial state-selected integral reaction cross sections as a function of the collision energy for the C(^{3}P) + OH(ε=X$^2\Pi$, v=0-2, j=0-1) $\rightarrow$ CO(a$^3\Pi$) + H (^{2}S) reaction on the first excited PES (1^2A$''$). Panel a shows cross sections for the reagent in its ground (black) and first excited (red) rotational states. Similarly, panel b shows cross sections for the reagent in ground (black), first (red) and second (blue) excited vibrational states.

shown in black, red and blue colors, respectively, in panel b. Within CS approximation, all the partial wave contributions of the total angular momentum up to J = 95 [and 120 for OH(v=1, j=0) and OH(v=2, j=0) reagents] are included to obtain the converged cross sections up to 1.0 eV collision energy. In case of rotationally excited reagent ($j = 1$), the partial wave contributions from $\Omega > 0$ are also included. It can be seen from panel a of Fig. 7 that, for a given value of j, the magnitude of

reaction cross sections is maximum at the onset ($\sim$ 181 Å^2 for j=0; $\sim$ 75 Å^2 for j = 1) and then falls steeply at low collision energies ($<$ 0.2 eV) to reach a value of $\sim$ 4 Å^2 ($\sim$ 1.5 Å^2 for j =1) and thereafter it decreases slowly with the increase in collision energy. This behavior of reaction cross sections is typical for a barrierless reaction. In regard to the effect of rotational excitation, It can be seen from panel a that the reaction cross sections obtained for rotationally excited reagent [OH(v=0, j=1)] are relatively lower in magnitude when compared with the same obtained for OH(v=0, j=0). It is to be noted that the signature of the resonances due to the two deep wells present in the (1^2A$''$) PES is observed in the reaction cross sections as clearly shown in the inset of panel a. Vibrational excitation of the reagent also shows similar effects on the observed reaction cross sections. But in this case, two different trends are observed. At low collision energies ($<$ 0.05 eV), the reaction cross sections decrease with the increasing vibrational quantum number of the reagent (see inset of panel b). In contrast, at collision energies greater than $\sim$ 0.1 eV, the reaction cross sections increase with increasing excitation of the reagent vibrational state. But in either case, the raise or fall in the magnitude of the cross sections with the vibrational excitations is not as prominent as observed during rotational excitation (cf. panel a and panel b).

The initial state-selected and temperature dependent rate constants for the C(^{3}P) + OH(ε=X$^2\Pi$, v=0-2, j=0-1) $\rightarrow$ CO(a$^3\Pi$) + H (^{2}S) reaction on the first excited PES (1^2A$''$) are plotted in Fig. 8(a). Here the rate constants obtained for the reagent in ground [OH ($j = 0$, $v = 0$)] and first rotational excited state [OH ($j = 1$, $v = 0$)] are shown by the solid line and dashed line, respectively, in panel a. It can be seen from Fig. 8(a) that for a given value of j, the magnitude of rate constant increases sharply at the onset and reaches a maximum value ($\sim 4.65 \times 10^{-11}$ cm^3 sec^{-1} molecule^{-1} at $\sim$ 34 K for $j = 0$; $\sim 2.14 \times 10^{-11}$ cm^3 sec^{-1} molecule^{-1} at $\sim$ 38 K for $j = 1$) and then slowly decreases with increasing temperature. Analogous to the cross section results of Fig. 7(a), the reaction rates also decrease (by about a factor of two) with rotational excitation of the reagent OH molecule. The effects of vibrational excitation of the reagent on reaction rates are also presented in panel b. Here the rate

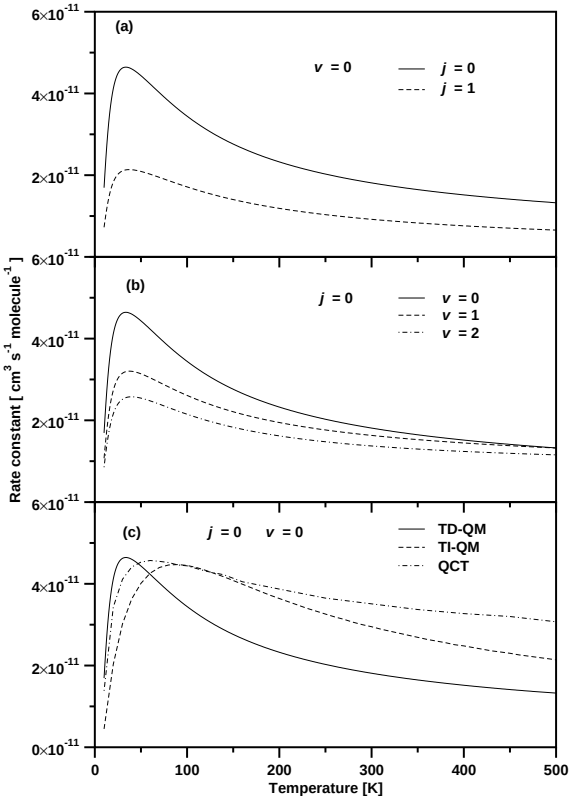

FIG. 8: Initial state-selected rate constants as a function of temperature for the C(^{3}P) + OH(ε=X$^2\Pi$, v=0, j=0-1) $\rightarrow$ CO(a$^3\Pi$) + H (^{2}S) reaction on the first excited PES ($1^2A''$). Panel a shows rate constants obtained in the present time-dependent quantum mechanical calculations and for the reagent $j = 0$ (solid line) and $j = 1$ (dashed line) rotational states. Similarly panel b shows rate constants obtained for vibrationally ground (solid line), first (dashed line) and second (dot-dashed line) excited reagent. Panel c compares the rate constants obtained in the present work (solid line) with those obtained by Jorfi and Honvault [J. Phys. Chem. A 114 (2010) 4742] by a time-independent quantum mechanical method (dashed line) and the quasi classical trajectory method (dot-dashed line) and for the reagent in the $j = 0$ rotational state.

constants obtained for the reagent in its ground, first and second excited vibrational states are, respectively, shown by the solid, dashed and dot-dashed lines. It can be seen from panel b that the rates decrease with the vibrational excitation. But the decrement observed in this case is not as large as obtained with the rotational excitation of the reagent (cf. panel a and b). As stated above the cross sections also showed similar behavior at collision energies less than $\sim$ 0.05 eV (where the

magnitude of the cross sections is dominant). Now it is clear from panels a and b that both rotational and vibrational excitations demotes the reaction with former showing more dominant effect. As many factors govern the reactivity of the system, it is hard to find the precise cause for this demotion. One possible factor could be the degree of alignment and orientation of the reagent species. For this reaction going via a complex formation mechanism, these might play a vital role. In general, the rotationally excited reagent has less degree of alignment or orientation which could interrupt the formation of the intermediate complex (COH or HCO). As a result, a lower reactivity is observed for the reagent in rotationally excited state. On the other hand, vibrational excitation does not lower the degree of orientation as much as obtained for the rotational excitation. Hence in this case the decrement in the rates is less prominent.

In order to compare, the results obtained by Jorfi and Honvault [J. Phys. Chem. A 114 (2010) 4742] using the time-independent quantum mechanical method (dashed line) and quasi classical trajectory method (dot-dashed line) are reproduced in panel c of Fig. 8 along with the same obtained in present study (solid line). It can be seen from panel c that the rates obtained here using the time-dependent quantum mechanical methods are of the same order of magnitude when compared to the rates obtained using time-independent quantum mechanical and quasi classical trajectory methods. The rates obtained by latter methods are overestimated in the broad temperature range 60-500 K but in the low temperature range (0-60 K) they are underestimated. It is to be noted that Jorfi and Honvault used the J-shifting approximation in their time-independent quantum mechanical study to calculate the reaction probabilities for non-zero total angular momentum J. The J-shifting approximation obviously is not a good approximation here and thus leading to the observed discrepancies.

Contents

Chapter 1

Introduction

It is worthwhile to start the thesis with a famous quote of Paul Dirac: "***The underlying physical laws necessary for the mathematical treatment of a large part of physics and whole of chemistry are thus completely known, and the difficulty is only that the exact application of these laws leads to equations much too complicated to be soluble. It therefore becomes desirable that approximate practical methods of applying quantum mechanics should be developed, which can lead to an explanation of the main features of complex atomic systems without too much computation*** [1]." Even after a century this quote still looks fresh and capable of motivating many young aspirants of this field of quantum dynamics.

Most of the theoretical investigations in molecular physics and chemistry start with the invocation of Born-Oppenheimer (BO) adiabatic approximation [2, 3]. The latter simplifies the theoretical treatment by decoupling the electronic motion from the nuclear and thus allowing to treat them separately. Hence to study the

nuclear dynamics of a molecule, the first step involves clamping of the atomic nuclei at fixed positions in space and then solving the electronic eigenvalue equation to obtain the electronic energies (which are also referred as adiabatic potential energy surface (PES)) and the electronic eigenfunctions. It is to be noted that the latter can only be determined up to a phase factor which may be an arbitrary function of the nuclear coordinates. In 1928, Fock [4] showed that such a phase can be set to unity. However in 1963, Herzberg and Longuet-Higgins [5] showed that this usual phase convention leads to geometric phase (GP) effect (more about this is discussed later in the text below).

Using the calculated electronic eigenfunctions (which parametrically depend on nuclear coordinates), the total wavefunction of the molecule is expressed as a linear combination of these electronic eigenfunctions (also referred as adiabatic electronic basis). The coefficients of this expansion parametrically depend on the nuclear coordinates and represent the nuclear wavefunctions. Substitution of the total wavefunction in the molecular Schrödinger equation and integration over the electronic coordinates gives rise to the coupled channel eigenvalue equation for the nuclear wavefunction in the adiabatic representation (related equations are presented in section 2.2). In the latter representation, the coupling between different electronic states is caused by the derivatives of the electronic wavefunction with respect to the nuclear coordinates and are called nonadiabatic coupling (NAC) elements. In a strict BO picture all of these NAC elements are neglected [2] whereas some of the diagonal NAC elements are retained in the Born-Huang (BH) approximation [3]. In either case, the coupled states nuclear eigenvalue equation reduces to a single state nuclear eigenvalue equation and thus confines the motion of the nuclei on a single adiabatic state. This approximation is justified on the

basis of the fact that the kinetic energy of the nuclei is in general much smaller than that of the electrons as the latter are $\sim$ 1800 times lighter. However, after studying more and more molecular systems it is realize that this approximation is valid only in a small regions of entire configurations space.

Now the question is when does the BO approximation break? When the potential energy of two electronic states is close (i.e. within one quantum of energy of nuclear vibration) then the magnitude of NAC elements becomes too large to be neglected. And in the worst case, i.e, when there exists a degeneracy, these NAC elements become singular. Hence in these situations BO approximation breaks down and the nuclear motion is no longer confined to a single adiabatic PES. Earlier it was thought that such situations are rare. For example, in diatomic molecule, the non-crossing rule [6] prohibits the crossing of electronic states of same symmetry. But this does not apply to polyatomic molecules which have more degrees of freedom for the internal atomic motion. Indeed it is now realized that the crossing of the PESs is very common. For example, consider the simple case of triatomic molecule H_3. It has an equilateral triangular geometry (D_{3h} symmetry) in its degenerate ground electronic state ($2pE'$). But this degeneracy is split along the degenerate e asymmetric stretching normal mode of vibration resulting in to two adiabatic sheets meeting at the D_{3h} symmetric configurations. This splitting of electronic degeneracy due to the vibronic (vibrational + electronic) interactions is well known as $E \otimes e$ Jahn-Teller (JT) splitting [7]. The topography of such type of intersections resemble a double cone (cf. Fig. 1.1) and are commonly called conical intersections (CIs). Apart from the singular behavior of NAC elements at CIs, the usual phase convention for the adiabatic electronic wavefunction causes the topological effects. As discussed above, Herzberg and

Longuet-Higgins [5] showed that when nuclei move along a closed path encircling the CIs, the electronic wavefunction changes its sign and therefore the the total molecular wavefunction becomes multivalued! This effect is purely topological and well known in the literature as GP effect (more discussion on this is given in sections 1.2.1 and 4.2). Similar to the JT splitting, an analogous situation arises in the linear molecules where the PESs do not cross but coincide and result in a glancing topography leading to Renner-Teller (RT) coupling [8]. Apart from these couplings, for open shell systems like ClH_2, the spin of the unpaired electrons often leads to the spin-orbit (SO) coupling [9]. The latter is due to the magnetic interaction of the electronic spin with its orbital motion and resulting in the splitting of the spin-degenerate states. Near degenerate electronic states also show the coupling similar to the JT couplings and are called pseudo-Jahn-Teller (PJT) couplings [10]. The latter involves coupling of a JT state with a nondegenerate or another JT state. To sum up, the existence of near degenerate states (resulting in avoided crossings) and degenerate states (resulting in CIs) in molecules causes a break down of the BO approximation and results in nonadiabatic transitions between the coupled adiabatic electronic states.

When BO breaks down, the singular or diverging nature of the NAC elements, and the occurrence of topological effects limits the use of adiabatic electronic representation. To circumvent it, a nonunique electronic representation called diabatic was invented [11]. In the latter representation the total molecular wavefunction is expanded in the diabatic electronic basis which is obtained *via* a unitary transformation of the adiabatic ones. The resulting nuclear Schrödinger equation in the diabatic representation is diagonal in nuclear kinetic energy terms (related equations are presented in section 2.2). The NAC here is introduced by

the off diagonal elements of the diabatic electronic potentials. A proper choice of the diabatic electronic basis ensures the removal of the singular NAC elements and also corrects for the GP change.

Finally, the nuclear Schrödinger equation (either in adiabatic or diabatic representations) is numerically solved to study a desired molecular process. This can be done either by a time-independent or a time-dependent quantum mechanical (TDQM) approach. Both methods have various advantages and disadvantages. Time-independent methods are best suited for the calculations at low energies such as energies needed to study cold and ultra cold systems. Because, a low translation energy results in a large de Broglie wave lengths. Consequently, the wave packet (WP) in the time-dependent calculations needs a large absorption region. In contrast, time-independent methods have boundary conditions replacing these absorbing functions. The other class that suits well for the time-independent methods is the dynamics involving long-lived resonances. In this case the WP has to be propagated for a very long time in a time-dependent calculations which often becomes unfeasible. On the other hand time-dependent methods have the advantage that they scale better than the time-independent methods and also one can capture the physical picture of the dynamics by recording the snapshots of the time-evolved WPs. In the current thesis, the time-dependent methods are used to investigate the nuclear dynamics. The full theoretical and computational details of this method is presented in chapter 2. .

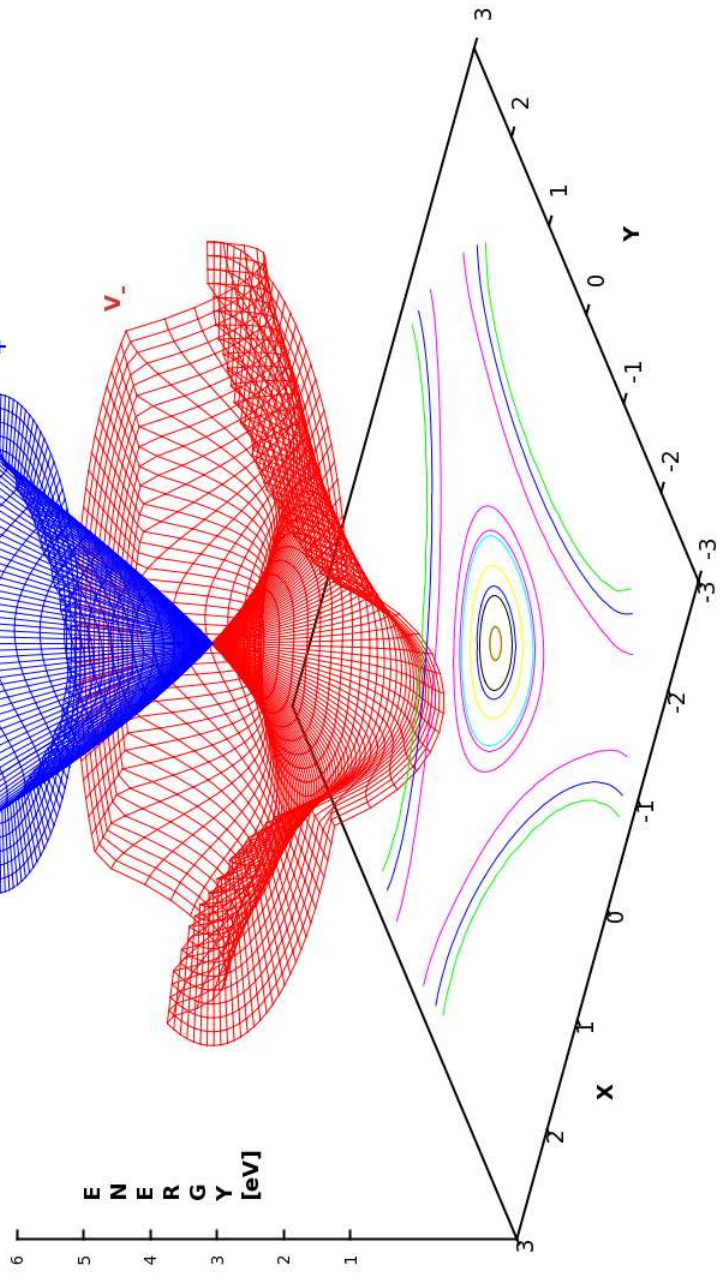

Figure 1.1: DMBE PESs of H_3. Lower and upper adiabatic sheets are respectively shown in red and blue colors. These represent the equatorial view (see section 4.4 for details) of the PESs in hyperspherical coordinates at a fixed $\rho = 2.5\ a_0$.

1.1 Potential energy surfaces

1.1.1 DMBE PES for H_3

Varandas *et al.* reported a global PES for the two lowest electronic states of H_3 [12] which exhibits CIs at its D_{3h} equilibrium geometries. These authors have applied double many body expansion (DMBE) method to obtain a functional form which represents the correct analytical properties for a PES at the D_{3h} equilibrium configurations. The advantage of this method is that the upper surface can be obtained from the functional form of the lower surface except for a sign change. They have considered 316 *ab initio* points (299 points they used from Refs. [13–15] and remaining they have calculated) to fit their chosen functional form. For *ab initio* calculations, they employed [4s3p1d] contracted basis set for complete active space self consistent field (CASSCF) calculations [16] with three active orbitals, which yields eight configurations alltogether. Then with all single and double excitations out of this eight configurations reference space, they performed a multireference configuration interaction (MRCI) calculation. A cross-section of this global three dimensional PES, well known in the literature as the DMBE PES is plotted in Fig. 1.1 using hyperspherical coordinates ρ, θ, and ϕ [ρ determines the size and (θ, ϕ) determine the shape of the molecular triangle]. For a better portrayal of the two adiabatic sheets and their CIs, equatorial views (see section 4.4 for more details) of these surfaces are shown here. In an equatorial view, the central region corresponds to the D_{3h} configurations where the hyperangle, $\theta = 0^o$. As one moves from the center towards the periphery θ increases and H_3 approaches to the linear geometries. At the periphery $\theta = 180°$, which defines the collinear geometry of H_3 and various dissociation channels (reactive and nonreactive) appear in this geometry. It can be seen from Fig. 1.1

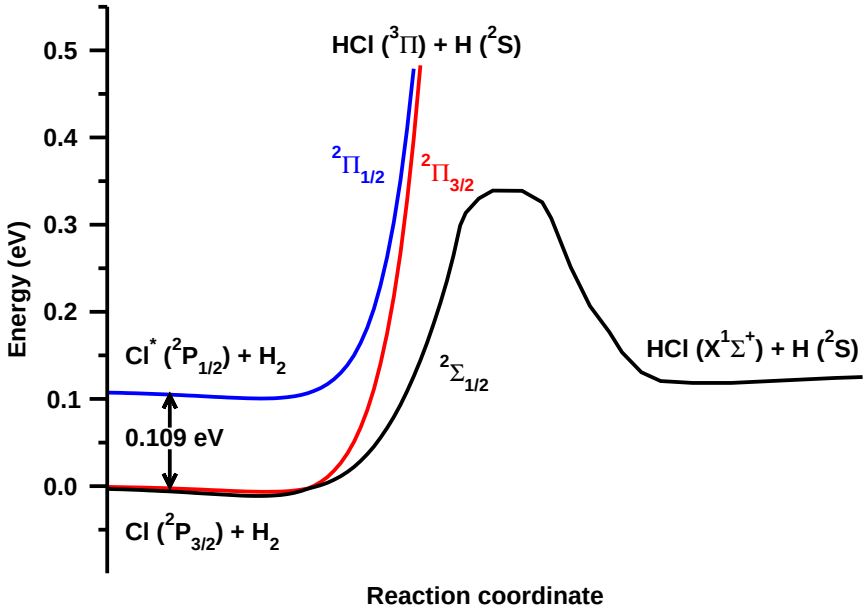

Figure 1.2: Schematic potential energy profiles for the Cl + H_2 reaction (see text for the details).

that the lower (red color) and upper (blue color) adiabatic sheets are degenerate at the D_{3h} configurations. But this degeneracy is split along other geometries, leading to CIs of these PESs. The hydrogen exchange reaction takes place on the repulsive lower adiabatic PES. On the latter, there exists a saddle point ($\sim$ 0.418 eV above the reactant asymptote) at a symmetric collinear conformation with H-H distance = 1.757 a_0 [12].

1.1.2 CW PES for ClH_2

The coupling of orbital and spin angular momenta of Cl atom yields two SO states viz., $^2P_{\frac{3}{2}}$ and $^2P_{\frac{1}{2}}$, energetically separated by about 0.109 eV. Moreover, the approach of the closed shell H_2 molecule to the Cl atom split the three-fold degeneracy of the ^{2}P state and yields three adiabatic electronic states of $^2\Sigma_{\frac{1}{2}}$, $^2\Pi_{\frac{3}{2}}$

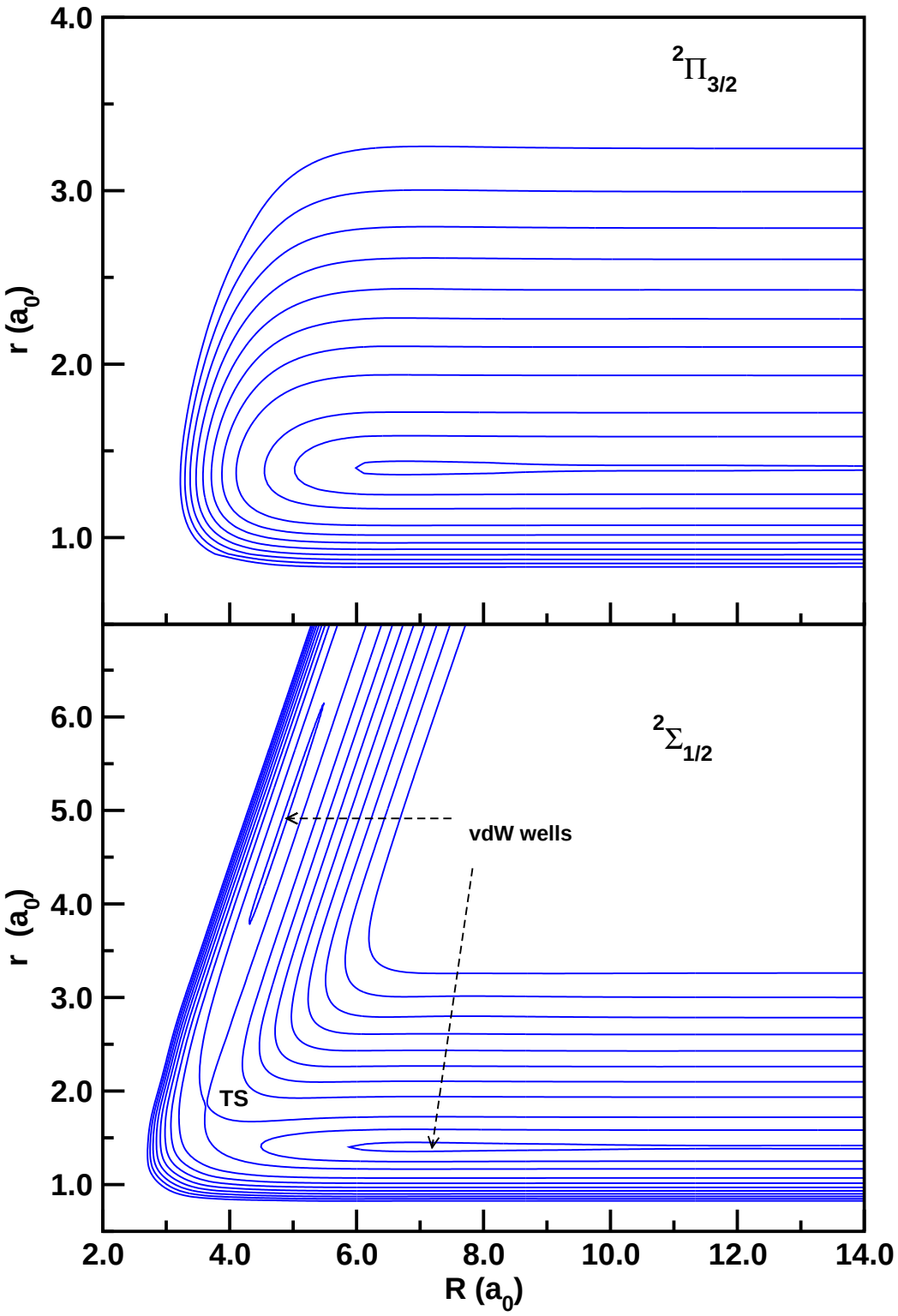

Figure 1.3: Contour plots of $^2\Sigma_{\frac{1}{2}}$ (lower panel) and $^2\Pi_{\frac{3}{2}}$ (upper panel) adiabatic PESs as a function of Jacobi coordinates R and r ($\gamma = 180^0$). Contours are obtained at some selected values of energy (-0.01, 0.1, 0.33, 0.8, 1.2, 1.6, 2.0, 2.4, 2.8, 3.2, 3.6 eV).

and $^2\Pi_{\frac{1}{2}}$ symmetry in collinear geometries of Cl...H_2 [17, 18]. In non collinear arrangements these states transform as 1 ^{2}A′, 1 ^{2}A″ and 2 ^{2}A′ symmetry species, respectively. In the reagent (Cl + H_2) arrangement, the first two states ($^2\Sigma_{\frac{1}{2}}$ and $^2\Pi_{\frac{3}{2}}$) asymptotically correlate to the ground $^2P_{\frac{3}{2}}$ SO state while the third state ($^2\Pi_{\frac{1}{2}}$) correlates to the excited $^2P_{\frac{1}{2}}$ SO state of the Cl atom [19] (see the schematic representation in Fig. 1.2). In the product arrangement (HCl + H), the $^2\Sigma_{\frac{1}{2}}$ electronic state adiabatically correlates to the electronic ground state of the products, HCl ($X^1\Sigma^+$) + H (^{2}S), whereas the other two states ($^2\Pi_{\frac{3}{2}}$ and $^2\Pi_{\frac{1}{2}}$) correlate to the energetically higher excited electronic states of products [19]. The latter states are inaccessible at low and moderate collision energies and the reaction mainly proceeds on the energetically lowest $^2\Sigma_{\frac{1}{2}}$ electronic state. Furthermore, at low and moderate collision energy the SO excited $^2P_{\frac{1}{2}}$ can form products in their electronic ground state only via nonadiabatic transition to the ground $^2P_{\frac{3}{2}}$ SO state. Considerable efforts have therefore been made in recent years to develop PESs and the coupling surfaces of the mentioned SO states of ClH_2 at various levels of sophistication [17, 18, 20]. In the year 2004, Capecchi and Werner (CW) [18] reported three adiabatic PESs (1 ^{2}A′, 1 ^{2}A″ and 2 ^{2}A′), their diabatic counter parts (V_Σ , $V_{\Pi-A}$ and $V_{\Pi+A}$), electronic and SO coupling surfaces. For *ab initio* calculations, these authors have used a large basis set (aug-cc-pV5Z[8s7p5d4f3g] for chlorine and aug-cc-pVQZ[5s4p3d2f] for hydrogen) and internally-contracted multireference configuration-interaction (IC-MRCI) level of theory to obtain the energies at about 1000 geometries. Then they fit all the six diabatic PESs to analytical functions. To describe some topological features of these surfaces, the contour plots obtained for $^2\Sigma_{\frac{1}{2}}$ (lower panel) and $^2\Pi_{\frac{3}{2}}$ (upper panel) adiabatic PESs are shown in Fig. 1.3 as a function of Jacobi coordinates (R = distance of Cl atom from center of mass of reagent H_2; r = H_2 internuclear

distance; γ = angle between $\vec{R}$ and $\vec{r}$ = 180^0 for these plots). As described above, the Cl + H_2 $\rightarrow$ HCl ($X^1\Sigma^+$) + H reaction takes place on $^2\Sigma_{\frac{1}{2}}$ (1 ^{2}A$'$ for non collinear configurations) adiabatic PES. The latter supports two shallow potential wells, one at the entrance channel (depth= $\sim$ 0.022 eV relative to the reagent asymptote; R=5.78 a_0 , r=1.403 a_0 , γ = 90^0) and the other at the exit channel (depth= $\sim$ 0.019 eV relative to the product asymptote; R=4.80 a_0 , r=4.77 a_0 , γ = 180^0). Location of these wells are indicated in the lower panel of Fig. 1.3 along with the location of the transition state ($\sim$ 0.33 eV relative to the reagent asymptote; R=3.63 a_0 , r=1.85 a_0 , γ = 180^0). The $^2\Pi_{\frac{3}{2}}$ (1 ^{2}A$''$) and $^2\Pi_{\frac{1}{2}}$ (2 ^{2}A$'$) adiabatic PESs also support shallow wells in the collinear configurations (cf. upper panel of Fig. 1.3). Contour plots for the $^2\Pi_{\frac{1}{2}}$ PES is not shown here as it looks similar to that of $^2\Pi_{\frac{3}{2}}$ PES except that the energy value of the contours are shifted to higher energies.

1.1.3 PESs of excited electronic states of COH

The interaction of ground state reactants, OH($X^2\Pi$) and C(^{3}P), leads to $^{2,4}\Sigma^+$, $^{2,4}\Sigma^-$, $^{2,4}\Pi$ and $^{2,4}\Delta$ states in linear configurations. Among these, $^2\Sigma^+$ (=X^2A' in C_s symmetry) and $^{2,4}\Pi$ (=$^2A'$,$^2A''$,$^4A'$ and $^4A''$ in C_s symmetry) correlates, respectively, with the ground state products CO($X^1\Sigma^+$) + H (^{2}S) (energetically lying $\sim$ 6.49 eV below the ground state reactants) and higher energy products, CO($a^3\Pi$) + H (^{2}S) (energetically lying $\sim$ 0.41 eV below the ground state reactants). This is schematically shown in the left panel of Fig. 1.4. Recently, Zanchet *et al.* have reported the global PESs of the ground X^2A' states [24] and $^2A''$ and $^4A''$ excited states [25]. For *ab initio* calculations, these authors have used Dunning aug-cc-pVQZ basis set [26] and multireference (MR) internally contracted single and double configuration interaction (SDCI) method [27] plus

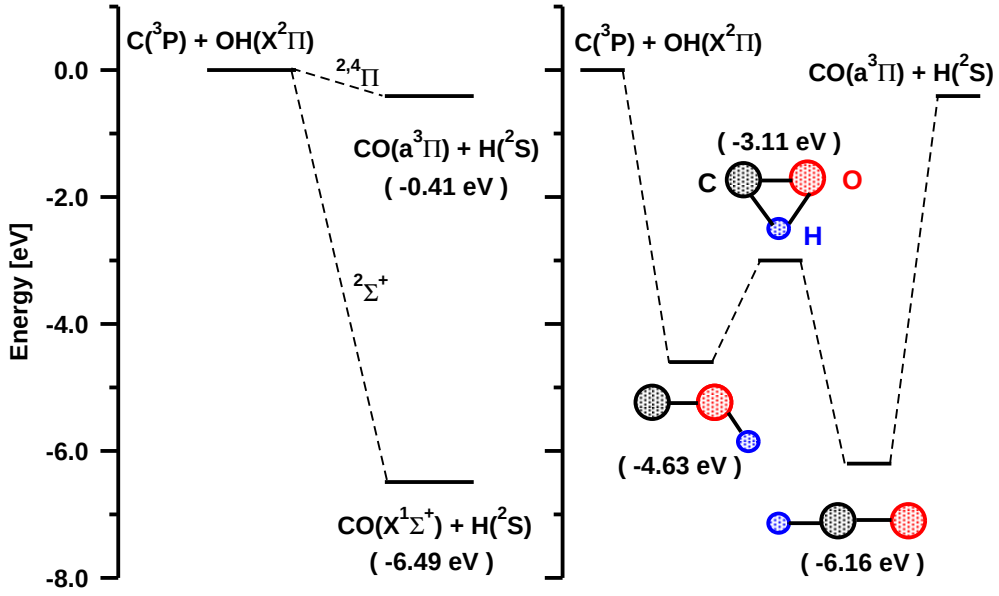

Figure 1.4: Left: Schematic plot of the energetics of the C + OH reaction. Right: Schematic plot of the stationary points located on excited $1^2A''$ PES

Davidson correction (+Q) [28] to obtain the energies at around 1500-3000 geometries. They have analytically fitted the *ab initio* points, wtih the RKHS [29, 30] and many body expansion [31] methods. For the calculations in chapter 6, the $^2A''$ excited state PES is employed.

1.1.3.1 Topography of $^2A''$ excited state PES

A schematic energy diagram of the stationary points on this surface is shown in Fig. 1.4. It is clear from the figure that, there exists two potential wells corresponding to the COH (R_{CO} = 2.49 a_0 , R_{OH}= 1.82 a_0 , $\widehat{COH}$ = 116^o) and HCO (R_{CO} = 2.25 a_0 , R_{CH}= 2.01 a_0 , $\widehat{HCO}$ = 180^o) collision complexes and a transition state (R_{CO} = 2.37 a_0 , R_{CH}= 2.34 a_0 , $\widehat{HCO}$ = 68^o) between them. These stationary points are also located on the potential energy contours

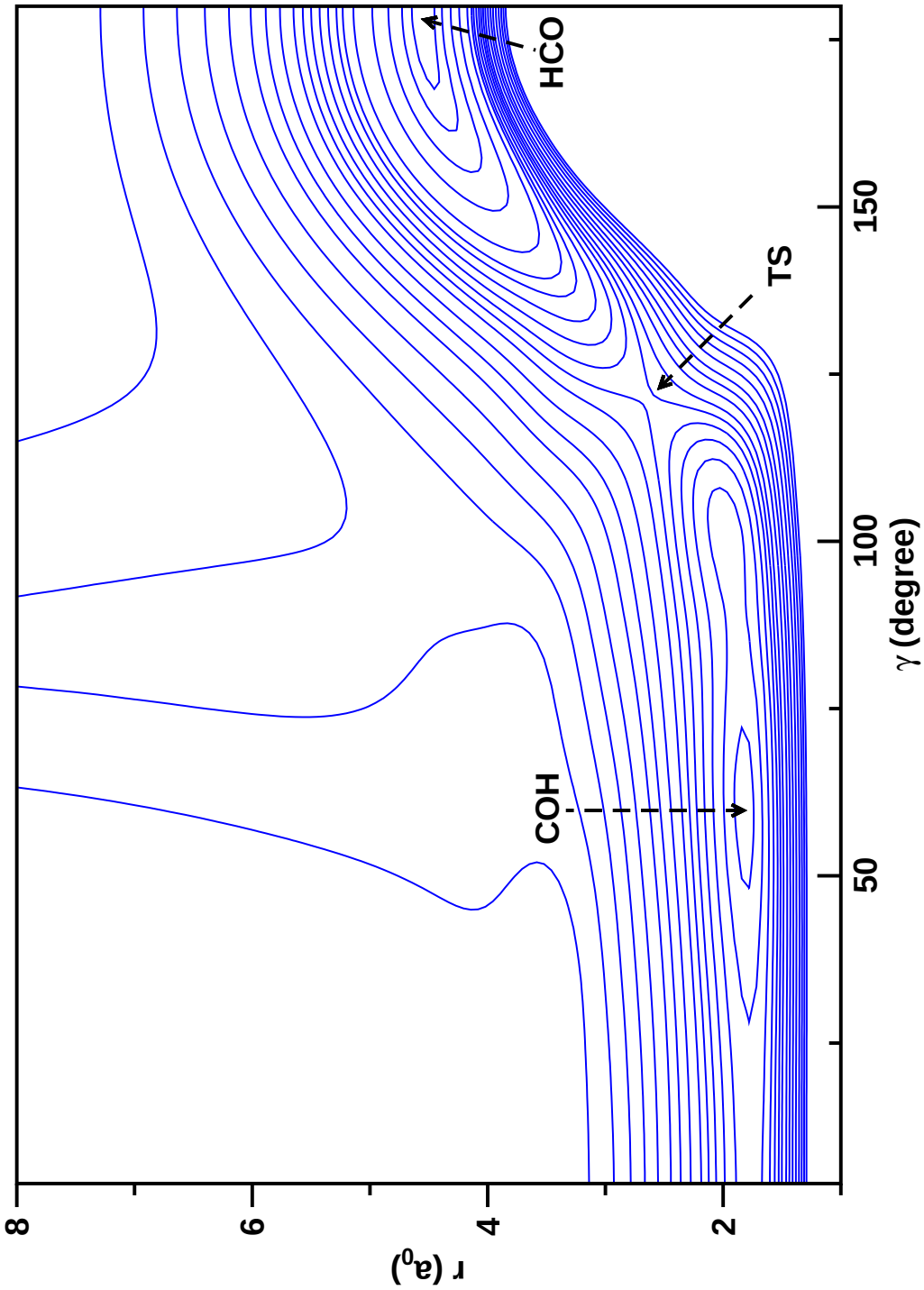

Figure 1.5: Contour plots of $1^2A''$ PES for a fixed value of R = 2.28 a_0 .

obtained for this surface as a function of Jacobi coordinates r and γ and for fixed R = 2.28 a_0 as shown in Fig. 1.5. As there is no barrier at the entrance channel, the COH minimum is easily reached. From there, the reaction may proceed via direct pathway to give the products or it may pass through the isomerisation barrier to reach the HCO minimum and then proceed to the products.

1.2 Current state of research and the aim of the present work

In this section, an overview of the theoretical and experimental advances and the aims of the various works presented in the thesis are discussed.

1.2.1 Nonadiabatic effects in hydrogen exchange reactions and optical emission spectrum of D_3

The H + H_2 exchange reaction has been a benchmark prototype for the theoretical studies, as it allows accurate quantum mechanical calculations to be performed because of its seemingly simple quantum chemistry. Its dynamical outcomes however, have been outstandingly difficult to understand [32].

The $(E \otimes e)$-JT effect [7] in the orbitally degenerate electronic ground states of H_3 leads to the occurrence of CIs of its PESs at the D_{3h} equilateral triangular geometry [5, 33]. The H + H_2 exchange reaction takes place on the repulsive lower adiabatic sheet of this JT split electronic ground state of H_3. Investigation of the role of the bound (in absence of the JT coupling) upper adiabatic JT sheet on this reaction systems has attracted much attention in the research in

contemporary chemical dynamics [34–36]. The JT coupling has been discovered to be very strong in H_3, which leads to perhaps (known ever!) fastest nonradiative relaxation of the upper adiabatic sheet of the JT split PESs within a time scale of $\sim$ 3-6 fs only [37–39]. On the other hand, the JT coupling apparently does not have such profound effects on the reactivity of the H + H_2 exchange reaction [34]. This surprising result is not clearly understood and remains to be an open issue till date.

It is well-known that the CIs of PESs are natural consequences of the JT instability of symmetric nonlinear molecular systems [5]. Electronic nonadiabatic effects prevail due to these intersections, ensuing a break-down of the adiabatic BO approximation [2]. Nuclei undergo electronic transitions during their dynamical evolution. One of the consequences of electronic nonadiabatic effects extensively exercised in the literature, is to rectify the multi-valuedness of the adiabatic electronic wavefunction when it encircles the CIs, a topological phenomenon, known as the GP effects [40]. This topological correction, understandably is a part of the explicit surface coupling effect (consisting of the singular derivative and the non-BO coupling terms) of the NAC operator. The effect of CIs on the reactive scattering dynamics of the H + H_2 and its isotopic variants are well studied in the literature in terms of the GP change of the adiabatic electronic wavefunction when encircling the CIs in a closed path in the nuclear coordinate space [41]. In order to account for the phase change and to make the total wavefunction single valued, a vector potential term is introduced into the nuclear Hamiltonian [42]. Early work on the GP effect in hydrogen exchange reaction was carried out by Mead [43, 44]. This was followed by the pioneering calculations by Kuppermann and coworkers by using multivalued basis functions to include the GP [41]. The

latter authors predicted strong GP effects in both the integral and differential reaction cross sections (DCSs). These findings stimulated further theoretical work by Kendrick [45], who performed time-independent calculations including the GP using the Mead-Truhlar vector potential formulation [42]. The GP effects were found to be small and appear in the state-to-state reaction probabilities only for the total energies higher than 1.8 eV above the H_3 potential minimum [45]. These effects which appear in the state-to-state reaction probabilities, cancel on summing over all partial wave contributions in the state-to-state integral cross sections (ICSs). Subsequently, Juanes-Marcos *et al.* confirmed Kendrick's results [45] and extended them to higher impact parameters using an entirely different theoretical approach [46]. Furthermore, these authors were able to explain these observations using a topological argument [47] by demonstrating that the nuclear wavefunction splits into two components which interfere to cancel the GP effects in the ICSs and DCSs. Kuppermann and coworkers have also investigated the GP effects on the vibrational levels of the upper adiabatic sheet and found that the GP correction shifts the energy eigenvalue and changes the symmetry properties of these levels [48]. Varandas and coworkers [49] have also carried out extensive work to analyze the properties of the transition state resonances of the lower adiabatic sheet and the bound vibrational levels of the upper adiabatic sheet including the GP correction. But all the above calculations were carried out within the realm of the BO approximation, which include the GP effects either through multivalued basis functions [41] or through the vector potential method [45, 46]. These calculations do not take an explicit account of the effects of the upper adiabatic PES on the dynamics.

All the studies mentioned above appear to consider (which will be obvious towards the end of this presentation) only a part of the explicit coupling of the two surfaces into the dynamical treatment. Mahapatra *et al.* [34, 39, 50], for the first time, studied the effects of explicit surface coupling on the spectroscopy and reactive dynamics of this system by devising a diabatic vibronic Hamiltonian based on the adiabatic electronic energies of the DMBE PES of Varandas and coworkers [12]. It was found in their studies that the surface coupling has only minor impact on the spectroscopy of the lower adiabatic sheet whereas, this coupling dramatically changes the spectrum of the upper adiabatic sheet. The reactive dynamics (the reaction probabilities for the lowest value of the total angular momentum) on the lower sheet was also found to be quite insensitive to the surface coupling [34]. Jayachander Rao *et al.* [51] extended the previous work [34] to calculate initial state-selected ICSs and thermal rate constants of H + H_2 (HD) reaction within the coupled state (CS) approximation [52, 53]. These results also revealed the minor surface coupling effects in the reaction probabilities. In a subsequent study, Jayachander Rao *et al.* reported the effects of reagent rotation and vibration [54] and Coriolis coupling (CC) terms [55] on the nonadiabatic quantum WP dynamics of H + H_2 reaction. The effects of NAC on the isotopic variants of the hydrogen exchange reaction were also performed by Ghosal *et al.* [56]. Recently, Althorpe and coworkers [35] have reported the effects of the surface coupling on the state-to-state reaction probabilities and cross sections for the H + H_2 reaction at total energies up to 4.5 eV using the diabatic theoretical model of Mahapatra *et al.* [34]. They calculated state-to-state reaction probabilities with the inclusion of (1) BH corrections, (2) GP and BH corrections to the BO adiabatic Hamiltonian and (3) by considering the complete two-states coupled Hamiltonian. Their findings revealed that state-to-state reaction proba-

bilities obtained including complete surface coupling has very minor differences with that obtained on lower adiabatic sheet with the inclusion of both GP and BH corrections. But they observed that the state-to-state reaction probabilities calculated on the lower surface without the inclusion of GP change (where BH correction is included) significantly differ from that obtained with including all of the surface coupling effects. These differences are much significant at energies greater than 3.5 eV and also exist in the state-to-state DCSs at these high energies. However, the differences cancel out in the observed ICSs. More recently, Balint-Kurti and coworkers [36] have studied effects of surface coupling on the the state-to-state probabilities, ICSs and DCSs up to a total energy of 3.0 eV for product vibrational levels v=0, 1, 2, 3. Their calculations also revealed that the nonadiabatic adiabatic effects are insignificant in the observed state-to-state ICSs and DCSs in the considered energy range.

Varandas and coworkers [57], examined the effects of NAC on the transition state resonances of the H + H_2 reaction and H + D_2 reaction dynamics [58] using two coupled diabatic surfaces. They also studied the GP effects on these resonances [49]. Both these studies revealed insignificant effects due to NAC or GP on the transition state resonances which occur at the saddle point region of the PESs occurring at the collinear configurations of the nuclei. In contrary, Lepetit *et al.* [48] and Varandas and coworkers [49] have reported considerable GP effects on the bound vibrational energy levels of the upper adiabatic sheet. Inspired by these studies, Mahapatra *et al.* [50] investigated the effects of the explicit surface coupling on the bound vibrational levels supported by the upper adiabatic sheet. Their calculations revealed that the coupling of the upper sheet with the repulsive lower sheet leads to an extremely fast non-radiative decay of

the vibrational levels of the upper sheet, occurring within 3-6 fs only [39]. The surface coupling effects in the degenerate 3pE' and 3dE' Rydberg states of H_3 have also been studied [59]. The effects were found to be far minor compared to those for the upper adiabatic sheet of the $2pE'$ ground electronic manifold of this system.

The aim of the work presented in chapter 3 is to study the effects of the NAC on the initial state-selected and energy resolved reaction probabilities, ICSs and thermal rate constants for the H + D_2 (HD) and D + H_2 (HD) reactions within the CS approximation [52, 53]. The reaction probabilities are reported up to the total energy of $\sim$ 4.7 eV both with and without the surface coupling. All partial wave contributions up to the total angular momentum $J = 50$ are considered to calculate the converged ICSs. The thermal rate constants calculated from the ICSs are compared with the available theoretical and experimental results [60–67]. In chapter 4, the nuclear dynamics of D_3 when prepared in the immediate neighborhood of the seam of CIs of its degenerate electronic ground state is critically examined. The theoretical framework is designed to mimic the optical emission experiment of the Rydberg excited D_3 [37, 38]. Keeping this reference experimental emission spectrum in mind the specific details of various terms which constitute the complete NAC of the two surfaces are obtained. To this effort, the important GP and diagonal BH corrections are examined and compared the results with those obtained from complete coupling of the two JT-split surfaces.

1.2.2 Photodetachment spectrum of ClH_2^- and ClD_2^-

As described in section 1.1.2, the approaching Cl atom forms a van der Waals (vdW) complex with H_2 at a Cl...H_2 distance of $\sim$ 5.78 $a_\circ$ where the PES supports

a well of depth of $\sim$ 0.022 eV [17]. The existence of such a well in the reagent asymptote is probed through experimental electron detachment spectroscopy of ClH_2^- [68, 69]. It emerged from the latter study that the equilibrium geometry of ClH_2^- in its electronic ground state occurs at $\sim$ 6.03 $a_\circ$ [70] and is close to the vdW minimum on the electronic states of the neutral species. Using a conventional negative ion time-of-flight photoelectron spectrometer of limited energy resolution of $\sim$ 8 to 10 meV Neumark and coworkers, for the first time, recorded the spectrum which revealed two dominant peaks separated in energy by $\sim$ 0.11 eV [68]. These two peaks are assigned to transitions of the $Cl^-...H_2$ anion complex to the ground and excited SO states of the neutral $Cl...H_2$ complex.

A few years latter, Mahapatra and co-workers [71] calculated the photodetachment spectrum of ClH_2^- using a time-dependent WP method. They reported the spectrum with and without the inclusion of the electronic and SO couplings. In this study the initial wavefunction of ClH_2^- was approximated to a Gaussian WP and also calculated by a relaxation method using the ClH_2^- PES of Ref. [72]. The CW PESs [18] was used to propagate this WP in the electronic states of neutral ClH_2 . The reduced 3 $\times$ 3 coupled states Hamiltonian developed by Alexander and coworkers [73] was used in this study. While the broad band spectral envelope obtained in this study revealed good agreement with the experimental recording of Neumark and coworkers [68], the vibronic structures obtained at finer resolution at extended energies were not observed in the experiment! Nearly at the same time, Alexander and coworkers [74] reported the photodetachment spectra of ClH_2^- and ClD_2^- using time-dependent WP method but within the BO approximation [2]. The uncoupled state calculations of Mahapatra and coworkers [71] differs with this study only in the choice of the initial WP. Alexander

and coworkers [74] employed an adiabatic bender model [72] to obtain the initial WP. Even though both were successful in reproducing the low resolution ($\sim$ 10 meV) photoelectron spectrum of Neumark and coworkers [68], the high resolution spectra ($\sim$ 1 meV) obtained by Mahapatra and coworkers [71] differ considerably with that of Alexander and coworkers [74]. The results of Ref. [71] contain numerous resolved peaks which extend even to high energies ($>$ 0.5 eV). At that time of study, high resolution experimental spectra were not available to check the correctness of these results. Later, Mahapatra and coworkers extended the work to study the electronic SO coupling effects on the resonances supported by the vdW well in the entrance valley of coupled electronic manifold of neutral ClH_2 [75] . Also the photodetachment spectrum of ClD_2^- [75], the dissociation dynamics of Cl...HD vdW complex [76] and Cl + H_2 reactive dynamics [77] were studied by them.

Subsequent to these studies highly resolved ($\sim$ 1 meV resolution) photoelectron spectra of ClH_2^- and ClD_2^- were recorded by slow electron velocity-map imaging (SEVI) technique by Neumark and coworkers [69]. Unfortunately, the high resolution photoelectron spectrum of ClH_2^- obtained in the previous work [71] differs significantly with this recent experiment especially in the high energy region. More recent coupled states theoretical calculations using time-dependent WP formalism [78–80] reveal that the experimental and theoretical results agree well even at a resolution of 1 meV. It is therefore clear that the vibronic structures obtained in the high energy region (above 0.5 eV) in the previous work presumably arising from a contribution of the dissociative Cl...H_2 continuum states. The mentioned discrepancies motivated us to revisit the previous theoretical study in order to understand their origin and to make efforts to eliminate them.

In chapter 5 aims at understanding the possible reasons for the above mentioned discrepancies by revisiting the previous theoretical study. To this effort, the adiabatic bender model of Alexander and coworkers [72] is used to prepare the initial WP pertinent to the electronic and ro-vibrational ground state of the ClH_2^- anion and its deuterated analogue. With this modification, present uncoupled state results agree well with the high resolution experimental spectra [69,78] as well as the theoretical results of Alexander and coworkers [74]. For coupled states calculations, the six-states diabatic Hamiltonian [18] is employed instead of three states Hamiltonian in Ref. [73] and introduced diabatic-to-adiabatic transformation during the propagation of the WP. With these modifications the photodetachment spectra of ClH_2^- and ClD_2^- are calculated and compared with the experimental SEVI [69,78] and available theoretical results [78,79]. The electron population dynamics is examined in addition, to assess the impact of electronic and SO coupling on the vibronic structure of the photodetachment bands.

1.2.3 Quantum reaction dynamics of C + OH reaction

The C + OH reaction belongs to a class in which both the reactants are neutral free radicals. Study of such type of reactions is quite challenging for both experimentalists and theoreticians. From an experimental point of view, preparation of free radicals and investigation of collision dynamics with them is quite difficult. As a result, till date, there is no experimental report on rate constants, cross sections or product distributions for the C + OH reaction. Theoretically, the calculation of global *ab initio* PESs and investigation of the nuclear dynamics on these surfaces is quite interesting due to the open-shell nature of both the reactants. The latter results in complex topological features involving multiple deep wells and barriers on the corresponding PESs. Consequently, accurate quantum

mechanical study of nuclear dynamics on such PESs becomes computationally expensive, in particular, for non zero total angular momentum ($J > 0$).

The C(^{3}P) + OH ($X^2\Pi$) $\rightarrow$ CO($X^1\Sigma^+$) + H (^{2}S) [say R1] and C(^{3}P) + OH ($X^2\Pi$) $\rightarrow$ CO($a^3\Pi$) + H (^{2}S) [say R2] reactions take place on the ground X^2A' state and excited $^2A''$, $^4A''$ electronic states, respectively [24, 25]. Zanchet *et al.* have obtained the global *ab initio* surfaces for all these three electronic states (X^2A', $^2A''$ and $^4A''$) [24,25] by employing a multireference internally contracted singles and doubles configuration interaction (MR-SDCI) method [27]. Their study revealed that, the reaction R1 on the ground X^2A' electronic state is barrierless and exoergic by $\sim$ 6.49 eV. This state also supports two deep wells of depth (relative to reactant asymptote) $\sim$ 5.5 eV and $\sim$ 7.3 eV, respectively, corresponding to the COH and HCO collision complexes. The dynamics of R1 on this electronic ground surface was investigated by Honvault and co-workers by quasi-classical trajectory (QCT) (QCT) [81–84] and TDQM methods [85, 86]. In the latter study, these authors have used a J-shifting approximation [87] to obtain the reaction probabilities for non zero total angular momentum ($J > 0$) to calculate state-to-state ICSs and DCSs and rate constants. The results obtained by these authors suggests that the reaction is dominated by a direct mechanism via a very short-lived intermediate complex. The total reaction probabilities are close to $\sim$ 1 in the whole range of collision energies considered and do not show any resonance structures in spite of presence of two deep wells on the PES. These findings are attributed to the high exoergicity of this reaction. The ICSs monotonically decreases from a maximum value of $\sim$ 160 Å^2 in the observed range of collision energy (0-1 eV). These authors have included the electronic degeneracy factor for calculating the initial state specific thermal rate constants. The latter

are observed to increase initially, reach a maximum value at $\sim$ 7 K, and then decrease slowly and reach almost a constant value of $\sim 1.0\times10^{-10}$ cm^3 s^{-1} molecule $^{-1}$. These authors have also found that rotational or vibrational excitation of the reagent diatom, OH, does not show much effect on the observed cross sections and rate constants. Generally, they found good agreements between the results obtained by the QCT and TDQM methods.

Subsequently, Honvault and co-workers [88, 89] reported the total and state-to-state reaction probabilities, ICSs, DCSs and state specific thermal rate constants for the reaction R2 on the $^4A''$ excited PES. To this effort , these authors have used different methods viz, QCT, time-independent quantum mechanical (TIQM), TDQM and statistical quantum mechanical. Their studies revealed that the reaction, R2, proceeds via long-lived intermediate complex supported by the two wells (COH: $\sim$ -1.85 eV relative to the reagent asymptote; HCO: $\sim$ -2.25 eV relative to the reagent asymptote) present on this surface ($^4A''$). The less exoergicity of the reaction R2 (0.41 eV) when compared with the R1 (6.5 eV) explains the reasons for the longevity of the collision intermediate in the former case. Consequently, sharp resonance structures are observed in total and state-to-state reaction probabilities [88, 89]. The cross sections and rate constants obtained for this reaction show a similar behavior as observed for the reaction R1 [88, 89]. But the authors have found that the agreement between the results obtained by different methods for R2 is not as good as observed for the R1 reaction [88, 89].

Honvault and co-workers [90] have also calculated the total and state-to-state reaction probabilities and rate constants for R2 reaction on the excited $^2A''$ PES by QCT and TIQM methods. Though the exoergicity of the reaction R2 is same on both $^4A''$ and $^2A''$ surfaces, the latter supports more deeper wells (COH: $\sim$

-4.6 eV relative to the reagent asymptote; HCO: $\sim$ -6.2 eV relative to the reagent asymptote) and thus further complicates the dynamics. The total and state-to-state reaction probabilities show sharp resonances for the same reasons as explained above. As TIQM calculations are computationally very expensive for this reaction, these authors have used a J-shifting approximation [87] to obtain the reaction probabilities for $J > 0$ and calculated the rate constants. The latter exhibit similar behavior as observed for the reaction R1 on the ground state and R2 on the $^4A''$ excited state. Here also the agreement between the results obtained using the TIQM and QCT methods is not as good as those observed for the ground state reaction [90].

The aim of the work presented in chapter 6 is to examine the initial state selected reaction probabilities, ICSs and thermal rate constants for the reaction R2 on the excited $^2A''$ electronic state employing a time-dependent WP method. The latter is computationally less expensive than the TIQM and hence reaction probabilities are also calculated for non-zero total angular momentum using the centrifugal sudden (CS) approximation [52, 53]. Within the CS approximation [52, 53], all the partial wave contributions for J = 0-95 are calculated to obtain the converged reaction cross sections and rate constants. The effect of rotational and vibrational excitations of the reagent OH on the final dynamical observables is also examined. Finally, the results obtained in this work are compared with the TIQM and QCT results of Honvault and coworkers [90].

1.3 Overview of the thesis

In chapter 2, the theoretical methods employed to study the nuclear dynamics on adiabatic PES and on coupled (nonadiabatic) electronic states of molecular sys-

tems are presented. In a coupled states situation a diabatic representation of the electronic basis is employed in the WP propagation in contrast to the adiabatic electronic basis used in the single surface propagation. A brief discussion on the adiabatic and diabatic representations is presented followed by a general scheme to solve the time-dependent Schrödinger equation (TDSE). Finally, the analysis of the time evolved wavefunction in order to extract the dynamical observables is presented.

In chapter 3, the NAC effects on the H + D_2 (HD) and D + H_2 (HD) reactions is presented and discussed. Initial state-selected total reaction cross sections and Boltzmann averaged thermal rate constants are calculated with the aid of a time-dependent WP approach employing the DMBE potential energy surfaces of the system. The theoretical results are compared with the experimental and other theoretical data whenever available.

In chapter 4, the nuclear motion of fully deuterated triatomic hydrogen, D_3 in the vicinity of CIs of the degenerate electronic ground state is presented and discussed. Vibronic energy level spectra and the eigenfunctions are examined by including, for example, (1) GP correction, (2) diagonal BH correction, (3) both GP and BH corrections to the BO adiabatic Hamiltonian and finally by considering the NAC between the two electronic surfaces explicitly. The impact of the GP and BH corrections and derivative (nonadiabatic) coupling terms on the eigenvalue spectrum and eigenvectors is examined in detail

In chapter 5, electron detachment spectroscopy of ClH_2^- and ClD_2^- is presented and discussed. Franck-Condon (FC) transition from the ground vibrational level of the electronic ground state of the anion to the coupled electronic manifold of the neutral species is investigated by a time-dependent WP approach. Rich vibronic structures due to Cl...H_2 continuum states at higher energies appeared

in the photodetachment band in the previous study [71] are eliminated by improving the representation of the anionic wavefunction and the WP propagation algorithm. The theoretical findings are compared with the available experimental and theoretical results.

In chapter 6, the reaction dynamics of the $C(^3P) + OH(X^2\Pi) \rightarrow CO(a^3\Pi) + H\ (^2S)$ reaction on the first excited PES ($1^2A''$) is presented and discussed. Initial state-selected total reaction probabilities, ICSs and thermal rate constants are obtained using time-dependent WP method. The effect of rotational and vibrational excitation on the reaction attributes is also examined. Finally the results obtained here are compared with the same obtained by Honvault and coworkers using TIQM method and QCT method.

References

[1] P.A.M. Dirac, Proc. R. Soc. London Ser. A 123 (1929) 714.

[2] M. Born, E. Oppenheimer, Ann. Phys.84 (1927) 457.

[3] M. Born and K. Huang, in The Dynamical Theory of Cryatal Lattices, Oxford University Press, 1954.

[4] V. Fock, Z. phys. 49,(1928) 323.

[5] G. Herzberg, H.C. Longuet-Higgins, Discussions Faraday Soc. 35 (1963) 77.

[6] U. von Neumann, E.P. Wigner, Physik. Z. 30 (1929) 467.

[7] H.A. Jahn, E. Teller, Proc. Roy. Soc. (London), Ser. A 161 (1937) 220.

[8] E. Renner, Z. Phys. 92 (1934) 172.

[9] W.G. Richards, H.P. Trivedi, D.L. Cooper in Spin orbit coupling in molecules, Clarendon press, Oxford, 1981.

[10] I.B. Bersuker, Chem. Rev. 101 (2001) 1067, and references therein.

[11] F. T. Smith, Phys. Rev. 179 (1969) 111.

[12] A.J.C. Varandas, F.B. Brown, C.A. Mead, D.G. Truhlar, N.C. Blais, J. Chem. Phys. 86 (1987) 6258.

[13] B. Liu, J. Chem. Phys. 58 (1973) 1925.

[14] P. Siegbahn, B. Liu, J. Chem. Phys. 68 (1978) 2457.

[15] M.R.A. Blomberg, B. Liu, J. Chem. Phys. 82 (1985) 1050.

[16] B.O. Roos, P.R. Taylor, P.E.M. Siegbahn, Chem. Phys. 48 (1980) 157.

[17] W. Bian, H.-J. werner, J. Chem. Phys. 112 (2000) 220.

[18] G. Capecchi, H.-J. Werner, Phys. Chem. Chem. Phys. 6 (2004) 4975.

[19] M.H. Alexander, G. Capecchi, H.-J. Werner, Science 296 (2002) 715.

[20] T.C. Allison, G.C. Lynch, D.G. Truhlar, M.S. Gordon, J. Phys. Chem. 100 (1996) 13575.

[21] R.A. Kendall, T.H. Dunning Jr, R.H. Harrison, J. Chem. Phys. 96 (1992) 6796.

[22] H.-J. Werner and P.J. Knowles, J. chem. Phys. 89 (1988) 5803.

[23] P.J. Knowles, H.-J. Werner, Chem. Phys. Lett. 145 (1988) 514.

[24] A. Zanchet, B. Bussery-Honvault, P. Honvault, J. Phys. Chem. A 110 (2006) 12017.

[25] A. Zanchet, B. Bussery-Honvault, M. Jorfi, P. Honvault, Phys. Chem. Chem. Phys. 11 (2009) 6182.

[26] T.H.J. Dunning, F. Chem. Phys. 73 (1980) 2304.

[27] H.-J. Werner, P.J. Knowles, J. Chem. Phys. 89 (1988) 5803.

[28] E.R. Davidson, D.W. Silver, Chem. Phys. Lett. 52 (1977) 403.

[29] T.-S. Ho, H. Rabitz, J. Chem. Phys. 104 (1996) 2584.

[30] T. Hollebeek, T.-S. Ho, H. Rabitz, J. Chem. Phys. 106 (1997) 7223.

[31] N. Murrell, S. Carter, J. Phys. Chem. 88 (1984) 4887.

[32] S.C. Althorpe, D.C Clary, Ann. Rev. Phys. Chem. 54 (2003) 493.

[33] R.N. Porter, R.M. Stevens, M. Karplus, J. Chem. Phys. 49 (1968) 5163 .

[34] S. Mahapatra, H. Köppel, L.S. Cederbaum, J. Phys. Chem. A 105 (2001) 2321.

[35] F. Bouakline, S.C. Althorpe, D.P. Ruiz, J. Chem. Phys. 128 (2008) 124322.

[36] T.-S. Chu, Ke-Li Han, M. Hankel, G.G. Balint-Kurti, A. Kuppermann, R. Abrol, J. Chem. Phys. 130 (2009) 144301.

[37] R. Bruckmeier, Ch. Wunderlich, H. Figger, Phys. Rev. Lett. 72 (1994) 2550.

[38] D. Azinovic, R. Bruckmeier, Ch. Wunderlich, H. Figger, G. Theodorakopoulos, I. D. Petsalakis, Phys. Rev. A 58 (1998) 1115.

[39] S. Mahapatra, H. Köppel, Phys. Rev. Lett. 81 (1998) 3116; S. Mahapatra, H. Köppel, J. Chem. Phys. 109 (1998) 1721.

[40] H.C. Longuet-Higgins, Proc. Roy. Soc. (London), Ser. A 344 (1975) 147.

[41] Y.M. Wu, A. Kuppermann, B. Lepetit, Chem. Phys. Lett. 186 (1991) 319; A. Kuppermann, Y.M. Wu, Chem. Phys. Lett. 349 (2001) 537.

[42] C. A. Mead, J. Chem. Phys. 72 (1980) 3839.

[43] C. A. Mead and D. G. Truhlar, J. Chem. Phys. 70 (1979) 2284.

[44] C. A. Mead, Chem. Phys. 49 (1980) 23.

[45] B.K. Kendrick, J. Chem. Phys. 112 (2000) 5679; J. Phys. Chem. A 107 (2003) 6739; J. Chem. Phys. 118 (2003) 10502.

[46] J.C. Juanes-Marcos, S.C. Althorpe, J. Chem. Phys. 122 (2005) 204324.

[47] J.C. Juanes-Marcos, S.C. Althorpe, E. Wrede, Science 309 (2005) 1227.

[48] B. Lepetit, Z. Peng, and A. Kuppermann, Chem. Phys. Lett. 166 (1990) 572.

[49] A. J. C. Varandas and H. G. Yu, J. Chem. Soc., Faraday Trans. 93 (1997) 819.

[50] S. Mahapatra and H. Köppel, J. Chem. Phys. 109 (1998) 1721.

[51] B. Jayachander Rao, R. Padmanaban, and S. Mahapatra, Chem. Phys. 333 (2007) 135.

[52] R. T. Pack, J. Chem. Phys. 60 (1974) 633.

[53] P. McGuire and D. J. Kouri, J. Chem. Phys. 60 (1974) 2488.

[54] B. Jayachander Rao and S. Mahapatra, Ind. J. Phys. 81 (2007) 1003.

[55] B. Jayachander Rao and S. Mahapatra, J. Chem. Sci. 121 (2009) 789.

[56] S. Ghosal, B. Jayachander Rao, and S. Mahapatra, J. Chem. Sci. 119 (2007) 401.

[57] A. J. C. Varandas and H. G. Yu, Chem. Phys. Lett. 259 (1996) 336.

[58] R. F. Lu, T. S. Chu, Y. Zhang, K. L. Han, A. J. C. Varandas, and J. Z. H. Zhang, J. Chem. Phys. 125 (2006) 133108.

[59] B. Jayachander Rao, S. Mahapatra, H. Köppel, and M. Jungen, J. Chem. Phys. 123 (2005) 134325.

[60] J. Vaníček, W.H. Miller, J.F. Castillo, F.J. Aoiz, J. Chem. Phys. 123 (2005) 054108.

[61] S.L. Mielke, K.A. Peterson, D.W. Schwenke, B.C. Garrett, D.G. Truhlar, J.V. Michael, M.-C. Su, J.W. Sutherland, Phys. Rev. Lett. 91 (2003) 063201.

[62] J.V. Michael, J.R. Fisher, J. Phys. Chem. 94 (1990) 3318.

[63] J.V. Michael, J. Chem. Phys. 92 (1990) 3394.

[64] T.J. Park, J.C. Light, J. Chem. Phys. 96 (1992) 8853.

[65] T.J. Park, J.C. Light, J. Chem. Phys. 94 (1991) 2946.

[66] A.A. Westenberg, N. De Haas, J. Chem. Phys. 47 (1967) 1393.

[67] A. Farkas, L. Farkas, Proc. R. Soc. London A 152 (1935) 124.

[68] M.J. Ferguson, G. Meloni, H. Gomez, D.M. Neumark, J. Chem. Phys. 117 (2002) 8181.

[69] D.M. Neumark, J. Phys. Chem. A 112 (2008) 13287.

[70] D.A. Wild, P.S. Weiser, E.J. Bieske, A. Zehnacker, J. Chem. Phys. 115 (2001) 824.

[71] S. Ghosal, S. Mahapatra, Chem. Phys. Lett. 394 (2004) 207.

[72] M.H. Alexander, J. Chem. Phys. 118 (2003) 9637.

[73] M.H. Alexander, D.E. Manolopoulos, H.-J. Werner, J. Chem. Phys. 113 (2000) 11084.

[74] D.E. Manolopoulos, M.H. Alexander, Phys. Chem. Chem. Phys. 6 (2004) 4984.

[75] S. Ghosal, S. Mahapatra, J. Phys. Chem. A 109 (2005) 1530.

[76] S. Ghosal, S. Mahapatra, J. Photochem. Photobiol. A 190 (2007) 161.

[77] S. Ghosal, S. Mahapatra, J. Chem. Phys. 121 (2004) 5740.

[78] E. Garand, J. Zhou, D.E. Manolopoulos, M.H. Alexander, D.M. Neumark, Science 319 (2008) 72.

[79] M.H. Alexander, J. Klos, D.E. Manolopoulos, J. Chem. Phys. 128 (2008) 84312.

[80] T.A. Grinev, A.A. Buchachenko, J. Chem. Phys. 128 (2008) 154317.

[81] A. Zanchet, P. Halvick, J.-C. Rayez, B. Bussery-Honvault, P. Honvault, J. Chem. Phys. 126 (2007) 184308.

[82] A. Zanchet, P. Honvault, B. Bussery-Honvault, P. Halvick, J.-C. Rayez, S.Y. Lin, H. Guo, in; J.L. Lemaire, F. Combes (Eds.) Molecules in Space and Laboratory conference proceedings, S. Diana (publisher), Paris, 2007, p. 118.

[83] A. Zanchet, P. Halvick, B. Bussery-Honvault, P. Honvault, J. Chem. Phys. 128 (2008) 204301.

[84] M. Jorfi, B. Bussery-Honvault, P. Honvault, T. Stoecklin, P. Larrégaray, P. Halvick, J. Phys. Chem. A 114 (2010) 7494.

[85] S.Y. Lin, H. Guo, P. Honvault, Chem. Phys. Lett. 453 (2008) 140.

[86] N. Bulut, A. Zanchet, P. Honvault, B. Bussery-Honvault, L. Bañares, J. Chem. Phys. 130 (2009) 194303.

[87] J.M. Bowman, J. Phys. Chem. 95 (1991) 4960.

[88] A. Zanchet, T. González-Lezana, O. Roncero, M. Jorfi, P. Honvault, M. Hankel, J. Chem. Phys. 136 (2012) 164309.

[89] M. Jorfi, P. Honvault, J. Phys. Chem. A 115 (2011) 8791.

[90] M. Jorfi, P. Honvault, J. Phys. Chem. A 114 (2010) 4742.

Chapter 2

Theoretical and computational methods

2.1 Introduction

The theoretical methods employed to study the nuclear dynamics on adiabatic PES and on coupled (nonadiabatic) electronic states of molecular systems are discussed in this chapter. To solve the dynamical equation of motion numerically, discrete grids using suitable co-ordinates (Jacobi or Hyperspherical) are constructed in the truncated Hilbert space. Depending on the nature of the problem a suitable initial wave packet (WP) is prepared on the grid, evolved in space and time and finally analysed to extract the dynamical observables. In a coupled states situation a diabatic representation of the electronic basis is employed in the WP propagation in contrast to the adiabatic electronic basis used in the single surface propagation. A brief discussion on the adiabatic and diabatic representations follows next and then a general scheme to solve the time-dependent Schrödinger equation (TDSE) is presented. Finally, the analysis of

the time evolved wavefunction in order to extract the dynamical observables is presented.

2.2 Adiabatic and diabatic electronic representations

For a coupled states situation, the nuclear Schrödinger equation in an adiabatic (in the sense that the states are coupled through the nuclear kinetic energy operator) electronic representation can be written in general form as [1]

$$\{\mathcal{H}^{BO} - E\}\chi_n(Q) = \sum_m \mathbf{\Lambda}_{nm}\chi_m(Q), \tag{2.1}$$

where, $\mathcal{H}^{BO} = T_{nuc}(Q) + V(Q)$, refers to the Born-Oppenheimer (BO) Hamiltonian (T_{nuc} and V denote the nuclear kinetic energy and electronic potential energy operator, respectively) for the isolated (uncoupled) electronic state. The quantity E is the energy eigenvalue and χ represents the nuclear wavefunction depending on the set of nuclear coordinates $\{Q\}$. The nonadiabatic coupling (NAC) between states is defined by the matrix $\mathbf{\Lambda_{nm}}$, which is given by [2, 3],

$$\mathbf{\Lambda}_{nm} = -\sum_i \frac{\hbar^2}{M_i} A^{(i)}_{nm} \frac{\partial}{\partial Q_i} - \sum_i \frac{\hbar^2}{M_i} B^{(i)}_{nm}, \tag{2.2}$$

where M_i denotes the nuclear masses and $A^{(i)}_{nm} = \langle\phi_n(q;Q)|\nabla_i|\phi_m(q;Q)\rangle$, $B^{(i)}_{nm} = \langle\phi_n(q;Q)|\nabla_i^2|\phi_m(q;Q)\rangle$. In the above the ∇_i operator refers to the nuclear coordinates and $|\phi(q;Q)\rangle$ represents the adiabatic electronic wavefunctions depending on the set of electronic coordinates $\{q\}$ and also parametrically on the

set of nuclear coordinates $\{Q\}$. The full molecular wavefunction is expanded as

$$\Psi(q;Q) = \sum_n \chi_n(Q)\Phi_n(q;Q). \tag{2.3}$$

The derivative coupling elements $A^{(i)}_{nm}$ of the NAC matrix exhibit singularity at the crossing of the electronic states n and m [2]. One therefore resorts to a complementary diabatic electronic representation [4,5] (to treat the full nonadiabatic problem) requiring removal of the singular elements of the derivative coupling matrix for all nuclear coordinates. In this new representation the states are coupled through the electronic part of the Hamiltonian and the nuclear Schrödinger equation assumes the general form [6, 7]

$$\{\mathcal{H}'^{BO} - E\}\chi_n(Q) = \sum_{(n\neq m)} \mathbf{U}_{nm}(Q)\chi_m(Q). \tag{2.4}$$

The operator $\mathcal{H}'^{BO}$ in the above retains the diagonal nuclear kinetic energy $T_N(Q)$ as in Eq.2.1 but the adiabatic potential V(Q) is replaced by the diabatic electronic potential $U_{nn}(Q)$ and $U_{mm}(Q)$. The electronic coupling elements are represented by $\mathbf{U}_{nm}(Q)$, defined by

$$\mathbf{U}_{nm}(Q) = \int dr \psi^*_n(q,Q)[T_e(q) + V(q,Q)]\psi_m(q,Q), \tag{2.5}$$

where ψ represents the diabatic electronic wavefunction, can be obtained, *via* a unitary transformation of the adiabatic ones as

$$\psi(q;Q) \;\; = \;\; \mathbf{S}\;\Phi(q;Q). \tag{2.6}$$

The quantity $T_e(q)$ in Eq.2.5 represents the electronic kinetic energy operator and $V(q;Q)$ is the adiabatic potential energy of the system.

2.3 A general scheme to solve the TDSE

In the present thesis the nuclear motion in a molecular system is investigated by numerically solving the TDSE. For a general explicitly time-independent Hamiltonian operator $\hat{H}$, the solution reads,

$$|\Psi(t)\rangle = \exp\left[\frac{-i\hat{H}t}{\hbar}\right]|\Psi(t=0)\rangle. \tag{2.7}$$

For the numerical solution of the above equation a discrete grid in a truncated coordinate space is constructed and the action of various operators (position, momentum etc.) on the wavefunction $|\Psi(t)\rangle$ is evaluated on this grid. Each node on this discrete grid is characterized by a finite value of interaction potential. The coordinate space, (x), is divided into a set of N discrete points with a spacing of Δx between two successive points. The eigenvalue of the position operator $\hat{x}$ at each grid point is given by [8]:

$$x_i = (i-1)\Delta x, i = 1, ..., N \tag{2.8}$$

The corresponding eigenvectors $|x_i\rangle$, are given by the orthogonality and completeness relations and the wavefunctions for an arbitrary physical state can be represented as $\phi(x_i) = \langle x_i|\phi\rangle$. Wavefunctions are normalized on the grid and the normalization integral becomes $\int_{-\infty}^{+\infty}\phi^\star(x)\phi(x)dx = 1$. The maximum length of the grid ($L = N\Delta x$) along the spatial coordinate x, determines the spacing

between two successive points in the momentum space (k):

$$\Delta k = \frac{2\pi}{N\Delta x}. \tag{2.9}$$

In the momentum space, the grid is centered at zero and all other points are distributed symmetrically on either side of it. If the maximum momentum is represented by p_{max} ($=\hbar k_{max}$) in the k space, then the total momentum ranges from $-p_{max}$ to $+p_{max}$.

Once the grid is set up, the nuclear motion on the electronic PESs is monitored by solving the TDSE:

$$i\hbar\frac{\partial\Psi}{\partial t} = \hat{H}\Psi \tag{2.10}$$

where, $\hat{H}$ ($=\hat{T}_{nuc}+\hat{V}$) defines the Hamiltonian operator of the system. $\hat{T}_{nuc}$ is the nuclear kinetic energy part of the Hamiltonian and $\hat{V}$ defines the potential energy part. For a general $A+BC$ atom-diatom reaction, represented in reactant Jacobi coordinates (R = distance of atom A from center of mass of reagent BC; r = BC internuclear distance; γ = angle between $\vec{R}$ and $\vec{r}$) described in a body-fixed (BF) reference frame, the nuclear kinetic energy operator is given by

$$\begin{aligned}\hat{T}_{nuc} &= -\frac{\hbar^2}{2\mu_R}\frac{\partial^2}{\partial R^2} - \frac{\hbar^2}{2\mu_r}\frac{\partial^2}{\partial r^2} - \frac{\hbar^2}{2I}\left[\frac{1}{\sin\gamma}\frac{\partial}{\partial\gamma}\sin\gamma\frac{\partial}{\partial\gamma} - \frac{j_z^2}{sin^2\gamma}\right] \\ &+ \frac{1}{2\mu_R R^2}\left[J^2 - 2J_z j_z\right] - \frac{1}{2\mu_R R^2}\left[J_+ j_- + J_- j_+\right].\end{aligned} \tag{2.11}$$

Here J and j, respectively, are the operators for the total angular momentum and rotational angular momentum of reagent diatom (BC). The raising and lowering operators, $J_\pm$ and $j_\pm$, are defined in usual way i.e. $J_\pm = J_x \pm iJ_y$ and $j_\pm = j_x \pm ij_y$. The first two terms in the right hand side of the above equation represent the radial kinetic energy operators ($\hat{T}_{rad}$) along R and r , respectively. The third and

fourth terms represent the rotational kinetic energy operator ($\hat{T}_{ang}$) for reactant diatom (AB) and the qasi molecule (ABC), respectively. In Eq. 2.11, the last term (T_{cc}) represents the Coriolis coupling (CC) between the various angular momentum states. The quantity, $\mu_R = m_A(m_B + m_C)/(m_A + m_B + m_C)$, is the $A + BC$ three-body reduced mass, $\mu_r = m_B m_C/(m_B + m_C)$, is the BC reduced mass where m_A, m_B and m_C are the masses of A, B and C nuclei, respectively. The quantity, $I = (\mu_R \mu_r R^2 r^2)/(\mu_R R^2 + \mu_r r^2)$, represents the moment of inertia of the collisional system.

In order to solve Eq. 2.7 numerically, we need to evaluate the action of the kinetic ($\hat{T}_{nuc}$) and potential ($\hat{V}$) energy operators on the Hamiltonian separately. The operators $\hat{T}_{nuc}$ and $\hat{V}$ do not commute with each other as $\hat{T}_{nuc}$ is a function of the momentum (p), where as $\hat{V}$ is a function of position (x). The operator $\hat{V}$ being local in the coordinate space, its action on Ψ is only a multiplication of its magnitude with the value of Ψ at each grid point x_i:

$$\hat{V}(x)\Psi(x_i) = V(x_i)\Psi(x_i) \tag{2.12}$$

But the kinetic energy operator ($\frac{\hat{p}^2}{2m} = \frac{\hbar^2 k^2}{2\mu}$) is non local in the coordinate space and the evaluation of the $\hat{T}_{rad}\Psi$ can not be done by a simple multiplication. This operation can be done through a suitable collocation technique [9,10] by utilizing the concept of the discrete Hilbert space.

The basic idea behind the collocation method is to use two different representations of the function: (i) A grid representation; where the function is known by its value at the grid points $\{x_i\}$, e.g. $\hat{V}$, and (ii) A basis set representation $\{g_n(x)\}$; where the continuous functions are approximated at each point by a discrete sum in terms of a finite basis set. The basis functions $\{g_n(x)\}$ at various

grid points x_i are connected through appropriate expansion coefficients (a_n) at the grid points:

$$\Psi(x_i) \equiv \overline{\Psi}(x_i) = \sum_{n=0}^{N-1} a_n g_n(x_i) \tag{2.13}$$

where N is the size of the basis set. This method is adapted for the evaluation of a non local operator, e.g. $\hat{T}_{rad}$ such that

$$\hat{T}_{rad}\Psi(x) = \frac{\hbar^2 k^2}{2\mu}\overline{\Psi}(k) = \frac{\hbar^2 k^2}{2\mu} a_k, \tag{2.14}$$

This technique is also known as a pseudospectral approximation.

A special case of the collocation technique is the Fourier method [9–12]. With the use of Fourier transform one can switch back and forth between the two reciprocal Hilbert spaces (e.g. position and momentum or the time and frequency). As a result, Fourier transform is generally used to evaluate the action of $\hat{T}_{rad}$ on Ψ.

In this method, the wavefunction $\Psi(x)$ is expanded in terms of the orthogonal plane wave basis functions:

$$\Psi(x) \approx \sum_{k=-(N/2-1)}^{N/2} a_k \exp\left[i2\pi kx/L\right], \tag{2.15}$$

where, a_k is becomes the Fourier expansion coefficient and it represents the amplitude of the wavefunction in momentum space. Using the orthogonality relation between the Fourier functions, one can obtain these coefficients by inverting the relation with a set of equidistant sampling points $\{x_i\}$

$$a_k = \frac{1}{N}\sum_{i=1}^{N} \Psi(x_i) \exp\left[-i2\pi kx_i/L\right]. \tag{2.16}$$

These are discrete Fourier transforms.

The use of fast Fourier transform (FFT) method for computing the action of the kinetic energy part of the Hamiltonian on the wavefunction was first introduced by Feit *et al.* [13] and Kosloff and Kosloff [11] In this method, the action of the kinetic energy operator on $\Psi(x)$ involves transforming the coordinate space wavefunction to momentum space by forward FFT (FT), multiplying by the kinetic energy $T(k)$, and then transforming it back to the coordinate space by an inverse FFT (FT^{-1}). In general, the continuous FFT can be represented as:

$$FT[\Psi(x)] = \overline{\Psi}(k) = \frac{1}{\sqrt{2\pi}} \int_{-\infty}^{\infty} \Psi(x) e^{-ikx} dx. \tag{2.17}$$

$$FT^{-1}[\overline{\Psi}(k)] = \Psi(x) = \frac{1}{\sqrt{2\pi}} \int_{-\infty}^{\infty} \overline{\Psi}(k) e^{ikx} dk \tag{2.18}$$

This method requires the wavefunction to satisfy periodic boundary conditions and for band-limited functions this transformation is exact [11]. Functions under these conditions remain localized in the phase space box where the amplitude of the function becomes zero at the boundary of the box. Otherwise, as time progresses the WP gradually reaches the grid edges and undergoes spurious reflections resulting interference between the outgoing and reflected components. But wavefunctions (except the semilocalized wavefunctions) can not be confined simultaneously both in coordinate and momentum spaces. This boundary conditions for the WPs can be met by multiplying the later with a damping function like,

$$f(X_i) = \sin\left[\frac{\pi}{2} \frac{(X_{mask} + \Delta X_{mask} - X_i)}{\Delta X_{mask}}\right], \qquad X_i \geq X_{mask}. \tag{2.19}$$

In this equation, X_{mask} is the point at which the damping function is initiated and

$\Delta X_{mask}(= X_{max} - X_{mask})$ is the width of X over which the function decays from 1 to 0, with X_{max} being the maximum value of X in that direction. They provide a convenient way to damp the WP components to reduce their amplitude to zero at the grid boundaries and thereby prevent the unphysical reflections. One more attractive feature of the FFT method [14] is that it scales as $O(N \log N)$ with the number of grid points N. Thus this method becomes especially suitable for large-scale problems as the computational effort increases slowly with the grid size.

But this FFT scheme is numerically inefficient to calculate the rotational part of the kinetic energy operator. This is because the rotational kinetic energy operator contains a $(1/\sin^2\gamma)$ term which leads to singularity in the discrete angle space for $\gamma = 0$ and π. One can deal with this situation by using a discrete variable representation (DVR) and finite basis representation (FBR). The DVR-FBR transformation is an example of another orthogonal collocation method which uses specific basis functions and points on the grid [15, 16]. This method uses an orthogonal transformation between the DVR and the FBR and vice versa. The DVR is a basis consists of N discrete points, whereas the FBR is a basis consisting of N square-integrable functions appropriate to the DVR coordinates. In the DVR, the continuous eigenvalues of the coordinate operator is discretized [17] by diagonalizing the relevant Hamiltonian matrix. The matrix elements are determined by orthogonal transformation relation between the points and the basis functions. Both the basis are designed to evaluate the action of the operators in their respective local representations.

It has been shown by Light and coworkers [18–20], in the framework of DVR representation, the collocation method is much more efficient when the two representations are related through some quadrature scheme. Harris *et al.* [15],

Dickinson and Certain [16] proposed the use of orthogonal polynomial basis functions (e.g. the Hermite polynomials), corresponding to the Gaussian quadrature to carry out an orthogonal transformation between the N_γ quadrature points and N_γ basis functions. For our purpose the γ_k grid points (along the Jacobi angle) have been taken as the nodes of a Gauss-Legendre quadrature (with ω_k as associated weight factor), such that the rotational kinetic energy operator is diagonal in the associated Legendre polynomial basis set $\{P_l^\Omega(\cos\gamma)\}$. If the wavefunction $\psi_J^\Omega(\gamma)$ is expanded in this basis, then operator T_{ang} (cf. third and fourth terms of Eq. 2.11) can be evaluated as [21],

$$T_{ang}\psi_J^\Omega(\gamma_k) = \sum_{l=1}^{N_\gamma} \boldsymbol{L}_{lk}\left(\frac{\hbar^2}{2I}\right)\psi_J^\Omega(\gamma_l) \text{ where} \tag{2.20}$$

$$\boldsymbol{L} = \boldsymbol{U}.\Lambda.U^t. \tag{2.21}$$

Here $\boldsymbol{\Lambda}$ is the diagonal matrix with elements $\Lambda_{l,l} = l(l+1) + J(J+1) - 2\Omega^2$ and $\boldsymbol{U}$ is the unitary transformation matrix with elements $U_{k,l}^\Omega = \sqrt{\omega_k}\tilde{P}_l^\Omega(\cos\gamma_k)$. Similar procedure can be employed for evaluating CC terms (T_{cc} in Eq. 2.11) as,

$$\begin{aligned} T_{cc}\psi_J^\Omega(\gamma_k) &= \sum_{l=1}^{N_\gamma} \boldsymbol{L}_{lk}^{\Omega-1}\left(\frac{\hbar^2}{2\mu_R R^2}\right)\psi_J^{\Omega-1}(\gamma_l) \\ &+ \sum_{l=1}^{N_\gamma} \boldsymbol{L}_{lk}^{\Omega+1}\left(\frac{\hbar^2}{2\mu_R R^2}\right)\psi_J^{\Omega+1}(\gamma_l) \text{ where} \end{aligned} \tag{2.22}$$

$$\boldsymbol{L}^{\Omega-1} = \boldsymbol{U}^\Omega\boldsymbol{\Lambda}^-\left[\boldsymbol{U}^{\Omega-1}\right]^t \text{ and} \tag{2.23}$$

$$\boldsymbol{L}^{\Omega+1} = \boldsymbol{U}^\Omega\boldsymbol{\Lambda}^+\left[\boldsymbol{U}^{\Omega+1}\right]^t. \tag{2.24}$$

Here elements of the diagonal matrices, $\mathbf{\Lambda}^-$ and $\mathbf{\Lambda}^+$ are given by

$$\Lambda^-_{l,l} = \sqrt{[J(J+1)-\Omega(\Omega-1)]\,[l(l+1)-\Omega(\Omega-1)]}, \text{ and} \quad (2.25)$$

$$\Lambda^+_{l,l} = \sqrt{[J(J+1)-\Omega(\Omega+1)]\,[l(l+1)-\Omega(\Omega+1)]}. \quad (2.26)$$

For evaluation of $T_{cc}\psi^{\Omega}_{J}(\gamma_k)$ (cf. Eq. 2.22), the value of wavefunctions corresponding to $\Omega-1$ $[\psi^{\Omega-1}_{J}(\gamma)]$ and $\Omega+1$ $[\psi^{\Omega+1}_{J}(\gamma)]$ are needed. Hence this evaluation can be done efficiently using a parallel computer code. Goldfield and co-workers [22] have advocated such an approach in which each processor does calculations corresponding to a particular set of (J,Ω) and communicates with its two immediate neighboring processors to get value of WP corresponding to $(J,\Omega-1)$ and $(J,\Omega+1)$ [23–25].

In summary, all the operations involving in the $\hat{H}\Psi$ are represented schematically in the following.
If $\Psi=\{\Psi_{ijk}=\Psi(R_i,r_j,\gamma_k)\}$ is the grid representation of the wavefunction, and χ is the corresponding momentum representation, the total Hamiltonian of Eq. 2.11 will be acted on ψ in the following way:

(i) Kinetic energy $\partial^2/\partial R^2$ term,

$$\Psi \rightarrow \underline{FFT(R)} \rightarrow \{\chi^{(R)}\} \rightarrow \underline{\times\left[-k^{(R)}\right]} \rightarrow \{\chi''^{(R)}\} \rightarrow \underline{FFT^{-1}(R)} \rightarrow \Psi^{(1)}.$$

(ii) Kinetic energy $\partial^2/\partial r^2$ term,

$$\Psi \rightarrow \underline{FFT(r)} \rightarrow \{\chi^{(r)}\} \rightarrow \underline{\times\left[-k^{(r)}\right]} \rightarrow \{\chi''^{(r)}\} \rightarrow \underline{FFT^{-1}(r)} \rightarrow \Psi^{(2)}.$$

(iii) T_{ang} term,

$$\Psi \rightarrow \underline{\boldsymbol{U}(\gamma)} \rightarrow \{\chi^{(\gamma)}\} \rightarrow \underline{\times\Lambda} \rightarrow \{\chi''^{(\gamma)}\} \rightarrow \underline{\boldsymbol{U}^t(\gamma)} \rightarrow \Psi^{(3)}.$$

(iv) Potential energy term $V(R, r, \theta)$,

$$\Psi \rightarrow \underline{\hat{V}} \rightarrow \{V(R_i, r_j, \theta_k)\psi_{ijk}\} \equiv \Psi^{(4)}.$$

Finally,

$$\hat{H}\Psi = -\frac{\hbar^2}{2\mu_R}\Psi^{(1)} - \frac{\hbar^2}{2\mu_r}\Psi^{(2)} - \hbar^2\Psi^{(3)} + \Psi^{(4)}$$

So far the propagation of the WP along space variables is discussed. The propagation of the WP in time is considered next. The exponential operator in the r.h.s. of Eq. 2.7 forms a continuous dynamical group where time t is a parameter, and is known as the time-evolution operator denoted by $\hat{U}(t, t_0)$. For $t_0 = 0$,

$$\hat{U}(t, t_0) = e^{-i\hat{H}t/\hbar}. \tag{2.27}$$

Time t is divided into smaller steps of length Δt and the time-evolution for the entire range of time is accomplished through:

$$\hat{U}(t) \quad = \quad \Pi_{n=0}^{N_t-1}\hat{U}((n+1)\Delta t, n\Delta t) \tag{2.28}$$

where, N_t is the total number of time-evolution steps and $\Delta t = t/N_t$. $\hat{U}(t, t_0)$ is a linear operator and is unitary:

$$\hat{U}\hat{U}^\dagger = \hat{U}^\dagger\hat{U} = \mathbf{1} \tag{2.29}$$

The exponential operator can be approximated in various ways. For example, by the second order differencing (SOD) scheme [26], the split operator scheme [27], the Chebyshev polynomial scheme [28] and the short iterative Lanczos (SIL) scheme [29] and more recent real WP scheme [23–25]. Among these, Chebyshev polynomial scheme, split operator scheme and real WP scheme have been used to carry out the work presented in the thesis.

2.3.1 Chebyshev polynomial Scheme

Chebyshev polynomials are found to be superior to many other polynomials and are optimal for a scalar function $F(x)$ bounded in the interval [-1,1]. So, a scalar function like e^{ax} can be expressed in terms of these polynomials in the interval -1$\leq$ x $\leq$ 1 as

$$e^{ax} = \sum_{n=0}^{\infty}(2 - \delta_{n0})J_n(\alpha)T_n(x), \tag{2.30}$$

where δ_{n0} is the Kroenecker delta and $\alpha = \Delta E\ \Delta t/2\hbar$. $J_n(\alpha)$ are the modified Bessel functions of order n. $T_n(x)$ are the Chebyshev polynomials of order n, calculated using the recursion relation [30]

$$T_{n+1}(x) = 2xT_n(x) - T_{n-1}(x) \tag{2.31}$$

with $T_0(x) = 1$ and $T_1(x) =$ x.

The evolution operator is a function of an operator. It can be shown that a function of an operator can be expressed as a function of a scalar in the complete basis of the operator. So, the function of the operator can be approximated in the Chebyshev series, provided the domain of the operator is confined to the interval [-1,1] in which the Chebyshev polynomials are optimal. In case of a Hamiltonian which is self-adjoint, the eigenvalues lie on a real axis, and they can be positioned

from -1 to 1 by renormalizing the Hamiltonian as follows:

$$\hat{H}_{norm} = 2(\hat{H} - \overline{H})/\Delta E, \tag{2.32}$$

where $\overline{H} = (E_{max} + E_{min})/2$, and, $\Delta E = E_{max} - E_{min}$. In terms of this renormalized Hamiltonian, H_{norm}, the evolution operator can be written as:

$$e^{-i\hat{H}\Delta t/\hbar} = e^{-i\overline{H}\Delta t/\hbar} e^{-i\alpha \hat{H_{norm}}}. \tag{2.33}$$

The first term in the above equation is the phase shift due to the shift of the energy scale. The second term is approximated by the chebyshev series [28, 31, 32] as

$$e^{-i\alpha H_{norm}} = \sum_{n=0}^{\infty} (2 - \delta_{n0}) J_n(\alpha) \Phi_n(-i\hat{H}_{norm}), \tag{2.34}$$

where $\Phi_n(-i\hat{H}_{norm})$ are the complex Chebyshev polynomials of order n satisfying the recursion relation:

$$\Phi_{n+1} = -2i\hat{H}_{norm}\Phi_n + \Phi_{n-1}, \tag{2.35}$$

where $\Phi_0 = 1$ and $\Phi_1 = -i\hat{H}_{norm}$. Therefore, the evolution of $\Psi(t)$ in this scheme on a discrete grid is given by:

$$\Phi(t + \Delta t) = e^{-i\hat{H}\Delta t}/\hbar \sum_{n=0}^{N} (2 - \delta_{n0}) J_n(\alpha) \Phi_n(-i\hat{H}_{norm}) \Phi(t). \tag{2.36}$$

The number of terms to be used in the above expansion is estimated from the time-energy phase space volume α. In practice the number of terms used is slightly larger than this estimate for a good convergence. Since the evolution operator

is expanded in a series of polynomials in the Chebyshev method by definition the scheme is not unitary. The deviation from the unitary corresponds to the remainder term in the expansion. This deviation is used as an accuracy check of the scheme. The errors are uniformly distributed in the bounded interval [31,33]. Since Bessel functions show exponential convergence for n > α, the error is usually very small.

2.3.2 Split operator scheme

In this method, the exponential containing the kinetic energy operator of Eq. 2.7 is symmetrically split as,

$$e^{-i\hat{H}\Delta t/\hbar} = e^{-i\hat{T}\Delta t/2\hbar}e^{-i\hat{V}\Delta t/\hbar}e^{-i\hat{T}\Delta t/2\hbar} + O(\Delta t^3). \tag{2.37}$$

Because of this symmetrical splitting, the error due to the non commutability of the kinetic ($\hat{T}$) and potential ($\hat{V}$) operators is reduced to an order of Δt^3 [27]. Now the time-evolution of the WP is done by

$$\Psi(t+\Delta t) \quad = \quad e^{-i\hat{T}\Delta t/2\hbar}e^{-i\hat{V}\Delta t/\hbar}e^{-i\hat{T}\Delta t/2\hbar}\Psi(t). \tag{2.38}$$

Each of the exponential operation in Eq. 2.38 is carried out in a local representation as explained in section 2.3. Clearly the operator in this scheme (Eq. 2.37) is linear and unitary and hence norm is strictly conserved. To obtain comparatively accurate results, an optimum time step is selected based on the maximum potential energy on the grid [13,34].

$$\Delta t < \frac{\pi}{3\Delta V_{max}}, \quad \Delta V_{max} = V_{max} - V_{min}. \tag{2.39}$$

It is noted that, similar to Eq. 2.37, the potential-energy operator can be split symmetrically with kinetic-energy operator sandwiched in between. That makes the kinetic-referenced split-operator scheme and gives the same results as that of Eq. 2.37 (called potential-referenced split-operator scheme).

2.3.3 Real wave packet scheme

In this method only the real part of the initial WP (t=0) is evolved but still all the dynamical observables for a reactive scattering process are obtained [23–25]. If, $q(t)$ and p(t), respectively, represents the real and imaginary parts of the complex WP to be propagated, then the evolution of the real part is carried out by a recursive relation

$$q(t + \Delta t) = A[-Aq(t - \Delta t) + 2H_{norm}q(t)]. \tag{2.40}$$

Here H_{norm} is the re normalized Hamiltonian as given in Eq. 2.32 and A is the absorption function (like sine damping function in Eq. 2.19) which is necessary to avoid the spurious reflections at the grid boundaries. It is clear from Eq. 2.40, that the propagation step here is independent of Δt and hence its value is considered to be one unit ($\sim$ 0.0241 fs if all equations are in atomic units). For the propagation to start, the values of real wavefunction at times t= 0 $[q(t-\Delta t)]$ and t = 1 unit $[q(t)]$ in the recursive relation Eq. 2.40 are to be evaluated first. The former is just the real part of the initial wavefunction $[q(t = 0)]$ and the latter is obtained by the relation

$$q(t) = H_{norm}q(t = 0) - \sqrt{1 - H_{norm}^2}\, p(t = 0). \tag{2.41}$$

In the Eq. 2.41, the square root of the operator, $\sqrt{1-H_{norm}^2}$ is evaluated by expanding it in terms of Chebyshev polynomials as

$$\sqrt{1-H_{norm}^2} = \sum_{n=0}^{\infty} \beta_n T_n(H_{norm}). \tag{2.42}$$

Here, $T_n(H_{norm})$ are the Chebyshev polynomials of order n (cf. Eq. 2.31) and β_n are the expansion coefficients. Using the orthonormal relation of Chebyshev polynomials, it can easily be shown that only the even terms in the expansion Eq. 2.42 survive with coefficients $\beta_{2n} = \frac{2}{\pi}\{\frac{-2}{(2n)^2-1}\}$ and $\beta_0 = \frac{2}{\pi}$.

2.3.4 Coupled sate propagation

In a coupled states propagation, a diabatic representation of the electronic basis is employed and the solution for TDSE (cf. Eq. 2.10) is now expressed as,

$$|\boldsymbol{\Psi}^{dia}(t)\rangle = \exp\left[\frac{-i\boldsymbol{H}^{dia}t}{\hbar}\right]|\boldsymbol{\Psi}^{dia}(t=0)\rangle, \text{ where} \tag{2.43}$$

$$|\boldsymbol{\Psi}^{dia}(t=0)\rangle = \begin{pmatrix} |\Psi_1^{dia}(t=0)\rangle \\ |\Psi_2^{dia}(t=0)\rangle \\ \vdots \\ |\Psi_n^{dia}(t=0)\rangle \end{pmatrix} \tag{2.44}$$

Here $|\Psi_i^{dia}(t=0)\rangle$ is the component WP corresponding to the i^{th} diabatic electronic state of the coupled electronic manifold. In Eq. 2.43 $\boldsymbol{H}^{dia}$ is the Hamilto-

nian matrix in diabatic electronic representation and is expanded as

$$\boldsymbol{H}^{dia} = T_{nuc}\boldsymbol{I}_n + \boldsymbol{U}^{dia}, \text{ where} \tag{2.45}$$

$$\boldsymbol{U}^{dia} = \begin{pmatrix} u_{1,1} & u_{1,2} & \cdots & u_{1,n} \\ u_{2,1} & u_{2,2} & \cdots & u_{2,n} \\ \vdots & \vdots & \ddots & \vdots \\ u_{n,1} & u_{n,2} & \cdots & u_{n,n} \end{pmatrix}. \tag{2.46}$$

Here T_{nuc} is the nuclear Hamiltonian (cf. Eq. 2.11) and n is the number of coupled diabatic electronic states of the system under consideration. As discussed in section 2.2, the nuclear Hamiltonian in a diabatic representation is diagonal (represented by $\boldsymbol{I}_n$ in Eq. 2.45) and the coupling between the surfaces is caused by the off-diagonal elements of the electronic part of the Hamiltonian $\boldsymbol{U}^{dia}$. As the electronic potential matrix is nondiagonal in this representation, the split operator scheme for the coupled state situation is modified as

$$\begin{aligned} \boldsymbol{\Psi}^{dia}(t+\Delta t) &= e^{\left[\frac{-i\boldsymbol{H}_{dia}\Delta t}{\hbar}\right]}\boldsymbol{\Psi}^{dia}(t) \\ &= e^{\left[\frac{-i\boldsymbol{U}_{dia}\Delta t}{2\hbar}\right]}e^{\left[\frac{-iT^{nu}\boldsymbol{I}_n\Delta t}{\hbar}\right]}e^{\left[\frac{-i\boldsymbol{U}_{dia}\Delta t}{2\hbar}\right]}\boldsymbol{\Psi}^{dia}(t) \\ &= e^{\left[\frac{-i\boldsymbol{S}V_{adia}\boldsymbol{S}^{\dagger}\Delta t}{2\hbar}\right]}e^{\left[\frac{-iT^{nu}\boldsymbol{I}_n\Delta t}{\hbar}\right]}e^{\left[\frac{-i\boldsymbol{S}V_{adia}\boldsymbol{S}^{\dagger}\Delta t}{2\hbar}\right]}\boldsymbol{\Psi}^{dia}(t) \\ &= \boldsymbol{S}e^{\left[\frac{-i\boldsymbol{V}_{adia}\Delta t}{2\hbar}\right]}\boldsymbol{S}^{\dagger}e^{\left[\frac{-iT^{nu}\boldsymbol{I}_n\Delta t}{\hbar}\right]}\boldsymbol{S}e^{\left[\frac{-i\boldsymbol{V}_{adia}\Delta t}{2\hbar}\right]}\boldsymbol{S}^{\dagger}\boldsymbol{\Psi}^{dia}(t) \end{aligned} \tag{2.47}$$

In the Eq. 2.47, $\boldsymbol{V}_{adia}$ is the diagonal adiabatic potential energy matrix and it is obtained by diagonalizing $\boldsymbol{U}^{dia}$ i.e $\boldsymbol{V}_{adia} = \boldsymbol{S}^{\dagger}\boldsymbol{U}^{dia}\boldsymbol{S}$. This $\boldsymbol{S}$ matrix is referred as diabatic to adiabatic transformation matrix and is useful in switching between adiabatic and diabatic electronic representations. It is noted that the coupled state propagation in Chebyshev scheme follows from the above discussion in a

straight forward manner and hence not discussed here.

2.4 Preparation of the initial wave packet

In a reactive scattering study the initial wavefunction is prepared in the asymptotic reagent channel (A...∞....BC) where the interaction potential almost vanishes. In this situation the initial wavefunction pertinent to the reagent asymptote is well expressed in reagent Jacobi coordinates (R, r, γ as described in section 2.3) as,

$$|\Psi^J_\Omega(R, r, \gamma, t = 0)\rangle \quad = \quad \sqrt{\omega} F(R) \phi_{vj}(r) \tilde{P}^\Omega_j(\cos\gamma). \tag{2.48}$$

The quantity Ω is the quantum number for the projection of j (and also J) on the BF z axis. In Eq. 2.48, $F(R)$ is the translational wavefunction that describes motion along R, $\phi_{vj}(r)$ is the ro-vibrational wavefunction that describes reagent diatom BC in its j^{th} rotational and v^{th} vibrational state and $\tilde{P}^\Omega_j(\cos\gamma)$ is associated Legendre polynomial. A minimum uncertainty Gaussian wave packet (GWP) is chosen for $F(R)$:

$$F(R)_{Gaussian} = \left(\frac{1}{2\pi\delta^2}\right)^{\frac{1}{4}} \exp\left[-\frac{(R - R_0)^2}{4\delta^2} - ik_0(R - R_0)\right]. \tag{2.49}$$

The quantity δ is the width parameter of the GWP, and R_0 and k_0 correspond to the location of its maximum in the coordinate and momentum space, respectively. In recent years, Balint-Kurti and coworkers [35] advocated the use of sinc WPs for $F(R)$ and used the same in their famous real WP code. The translational

wavefunction $F(R)$ in terms of sinc functions can be expressed as,

$$F(R)_{sinc} = \frac{1}{\sqrt{\alpha\pi}} \frac{sin(\alpha(R-R_0))}{R-R_0} e^{-ik_0(R-R_0)} e^{-\beta_s(R-R_0)^2}. \tag{2.50}$$

Here the parameters α and β_s, respectively, gives the range of momentum (or energy) distribution and smoothness of the wavefunction in momentum space.

The functions $\Phi_{vj}(r)$ (cf. Eq. 2.48) along with $\tilde{P}_j^{\Omega}(\cos\gamma)$ represents the ro-vibrational eigenfunction corresponding to a (v, j) state of the reagent diatom (BC). The function $\Phi_{vj}(r)$ are obtained by solving the eigenvalue equation of the free BC (reagent diatom):

$$\left[-\frac{\hbar^2}{2\mu_r}\frac{d^2}{dr^2} + V(r) + \frac{j(j+1)\hbar^2}{2\mu_r r^2}\right] \Phi_{vj}(r) = \epsilon_{vj}\Phi_{vj}(r). \tag{2.51}$$

Here μ_r is the reduced mass, ϵ_{vj} the energy eigenvalue of the reagent diatom BC. The sine-DVR approach of Colbert and Miller [36] is utilized here to solve the above eigenvalue equation. The $\mathcal{L}^2$-normalized associated Legendre polynomials (cf. Eq. 2.48) are given by

$$\tilde{P}_j^{\Omega}(\cos\gamma) = \sqrt{\frac{2j+1}{2}\frac{(j-\Omega)!}{(j+\Omega)!}} P_j^{\Omega}(\cos\gamma) \tag{2.52}$$

which are the eigenfunctions of the $\hat{j}^2$ operator.

For calculation of state-to-state probabilities or cross sections, the WP must be transformed from reagent (A + BC) to product (AB + C, or AC + B) Jacobi coordinates. In real WP method [23–25], the initial WP is prepared in the reagent Jacobi coordinates (R, r, γ described in section 2.3) and is immediately

transformed to the product Jacobi coordinates (R_p = distance between product atom C (B) to the centre of mass of the product diatom AB (AC); r_p = internuclear distance of the product diatom AB (AC); γ_p = angle between $\vec{R_p}$ and $\vec{r_p}$). This transformation is done by

$$|\Psi^J_{\Omega'}(R_p, r_p, \gamma_p, t=0)\rangle = |\Psi^J_{\Omega}(R, r, \gamma, t=0)\rangle \frac{R_p r_p}{Rr} D^J_{\Omega\Omega'}(0, \beta, 0), \tag{2.53}$$

where $D^J_{\Omega\Omega'}(0, \beta, 0)$ is a reduced Wigner rotation matrix [37] and β is the angle between $\vec{R}$ and $\vec{R_p}$.

2.5 Final analysis

The calculation of initial state-selected total reaction probabilities (i.e. summed over all open v', j' levels of the product diatom at given energy), cross sections and rate constants is done by computing the energy resolved flux of the WP across a dividing line in the product channel. This is referenced as flux operator approach initially developed by Neuhauser and coworkers [38]. This approach permits the entire calculations to be done using reagent Jacobi coordinates.

2.5.1 Flux operator

The flux operator $\hat{F}$ is most generally defined in terms of a dividing surface Θ, which is a function of a suitable coordinate (r in this case) that separates the products from the reactants [39]

$$\hat{F} = \frac{i}{\hbar} \left[H^{dia}, \Theta \right]. \tag{2.54}$$

In the present case the obvious choice for Θ is given by $\Theta = h(r - r_d)$, where h is the Heaviside step function which equals to unity for positive argument and zero otherwise. r_d is the dividing surface which is to be chosen far out in the product channel to ensure the asymptotic motion for all $r \geq r_d$. Since Θ depends only on coordinates it commutes with the electronic part of the Hamiltonian and Eq. (2.54) becomes

$$\hat{F} = \frac{i}{\hbar} \left[T_{nuc}, \Theta \right]. \tag{2.55}$$

The quantity T_{nuc} (cf. Eq. 2.11) represents the nuclear kinetic energy part of the Hamiltonian. In a coupled state situation, quantum flux operator $\hat{F}$ [cf. Eq. (2.55)] is diagonal in the diabatic electronic basis (note that nuclear Hamiltonian is diagonal in diabatic electronic basic cf. Eq. 2.45) and the non-zero diagonal elements take the form [39, 40]

$$\hat{f}_{ii} = \frac{-i\hbar}{2\mu} \left[\frac{\partial}{\partial r} \delta(r - r_d) + \delta(r - r_d) \frac{\partial}{\partial r} \right]. \tag{2.56}$$

The reaction probability is the expectation value of the above flux operator in the basis of the energy normalized time-independent reactive scattering wavefunction evaluated at $r = r_d$.

2.5.2 Calculation of reaction probability

The reaction probability is defined as the expectation value of this flux operator in the basis of energy normalized time-independent reactive scattering wavefunction at the dividing surface. The initial state i (corresponding to a specific vibrational ν and rotational j state of the reagent diatom AB) selected and energy resolved reaction probability [summed over final states $f(v', j')$ of the product (BC or AC)]

is given by

$$\begin{aligned} P_i^R(E) &= \sum_f |S_{fi}^R|^2 = \left\langle \Phi(R, r_d, \gamma, E)|\hat{F}|\Phi(R, r_d, \gamma, E)\right\rangle, \\ &= \frac{\hbar}{\mu_r}\mathrm{Im}\left[\langle\phi(R, r_d, \gamma, E)|\frac{\partial\phi(R, r_d, \gamma, E)}{\partial r}\rangle\right]|_{r=r_d}. \end{aligned} \tag{2.57}$$

where S_{fi}^R is the reactive scattering matrix from an initial state (i) of the reactant to a final state (f) of the product. The quantity in the right-hand side of Eq. 2.57 is integrated over the entire range of R and γ. The energy normalized time-independent reactive scattering wavefunction $|\phi_(R, r_d, \gamma, E)\rangle$ in Eq. 2.57 is calculated along the dividing surface at, $r = r_d$ by

$$|\phi(R, r_d, \gamma, E)\rangle = |\psi(R, r_d, \gamma, E)\rangle/\kappa_E. \tag{2.58}$$

The function $\psi(R, r_d, \gamma, E)\rangle$ is obtained by Fourier transforming the time-evolved WP $\psi(R, r_d, \gamma, t)\rangle$ along the dividing surface

$$|\psi(R, r_d, \gamma, E)\rangle = \frac{1}{\sqrt{2\pi}}\int_{-\infty}^{+\infty} e^{iEt/\hbar}|\psi(R, r, \gamma, t)\rangle dt|_{r=r_d}. \tag{2.59}$$

The quantity κ_E in Eq. 2.58 is the weight of the translational component $F(R)$ (cf. Eq. 2.49) contained in the initial WP for a given total energy E and expressed as

$$\kappa_E = (\frac{\mu_R}{2\pi\hbar k})^{1/2}\int_{-\infty}^{+\infty} F(R)e^{ikR}dR, \tag{2.60}$$

where $k = \sqrt{2\mu_R(E - \epsilon_{vj})}/\hbar$, with ϵ_{vj} being the initial ro-vibrational energy of the reagent molecule. In a coupled states situation, we resort to diabatic representation in which quantum flux operator $\hat{F}$ is diagonal. Therefore, the reaction probability here is just a summation over the same (cf. Eq. 2.57) obtained for

each component of diabatic WP (cf. Eq. 2.44), i.e.

$$P_i^R(E) = \frac{\hbar}{\mu_r}\sum_{k=1}^{n} \mathrm{Im}\left[\left\langle \phi_k^{dia}(R, r_d, \gamma, E)|\frac{\partial \phi_k^{dia}(R, r_d, \gamma, E)}{\partial r}\right\rangle\right]|_{r=r_d}. \quad (2.61)$$

2.5.3 Calculation of integral reaction cross section and thermal rate constant

The reaction probabilities depending upon J and Ω values (cf. Eq. 2.57 or 2.61) are summed up to calculate the integral reaction cross section (ICS) for a specified initial (v, j) state of reagent diatom.

$$\sigma_{vj}(E) = \frac{\pi}{k_{vj}^2}\sum_{\Omega=0}^{j}\frac{1}{(2j+1)}\sum_{J\geq\Omega}^{J_{max}}(2J+1)P_{vj}^{J\Omega}(E). \quad (2.62)$$

The initial state-selected thermal rate constant is calculated from the total ICS [41],

$$K_{vj}(T) = \sqrt{\frac{8k_BT}{\pi\mu_R}}\frac{1}{(k_BT)^2}\int_0^\infty E\sigma_{vj}(E)e^{-E/k_BT}dE, \quad (2.63)$$

where k_B is the Boltzmann constant. Finally, the rotationally averaged thermal rate constants can be obtained by averaging over a Boltzmann distribution of rotational states

$$K_v(T) = \sum_j \frac{K_{vj}(E)}{Q_{rot}}(2j+1)e^{-Bj(j+1)hc/k_BT}, \quad (2.64)$$

where B is the rotational constant of the reagent and
Q_{rot} $(= \sum_j (2j+1)e^{-Bj(j+1)hc/k_BT})$ is the rotational partition function.

2.6 Calculation of state-to-state reaction probabilities

The real WP method of Refs. [23–25] is employed here to obtain the state-to-state reaction probabilities and cross sections. In this method the initial WP pertinent to the reagent asymptote is prepared in the reagent Jacobi coordinates (R, r, γ) and immediately transformed to the product Jacobi coordinates (R_p, r_p, γ_p). Only the real part of the initial WP (cf. Eq. 2.53), let us say, $q^{J\Omega'}(R_p, r_p, \gamma_p, t)$, is evolved in space and time as described in section 2.3.3. At the end of each time step, the time-dependent expansion coefficients are obtained by [23–25],

$$C^J_{v,j,\Omega\rightarrow v',j',\Omega'}(t) = \int \varphi_{v',j'}(r_p,\gamma_p) q^{J\Omega'}(R_p = R^d_p, r_p, \gamma_p, t) dr_p sin\gamma_p d\gamma_p. \qquad (2.65)$$

Here $\varphi_{v',j'}(r_p,\gamma_p)$ is the product ro-vibrational eigenfunction and R^d_p is the analysis line which is located far in the product asymptotic region. The coefficients in Eq. 2.65 are then half Fourier transformed to give energy-dependent coefficients $A^J_{v,j,\Omega\rightarrow v',j',\Omega'}(E)$ [23–25],

$$A^J_{v,j,\Omega\rightarrow v',j',\Omega'}(E) = \frac{1}{2\pi}\int_0^\infty e^{iEt/\hbar} C^J_{v,j,\Omega\rightarrow v',j',\Omega'}(t) dt. \qquad (2.66)$$

For accurate calculation of differential cross sections (DCSs), $\boldsymbol{S}$ matrix elements should be evaluated in space-fixed (SF) reference frame [42]. To this effort, energy-dependent coefficients (cf. Eq. 2.66) are transformed from BF frame

to SF frame by,

$$\begin{aligned} \boldsymbol{A}^{SF} &= \boldsymbol{T}\boldsymbol{A}^{BF}\boldsymbol{T}_p \\ \Rightarrow A^J_{v,j,l\rightarrow v',j',l'}(E) &= \sum_{\Omega\Omega'}^{min(j',J)} T^J_{l\Omega} A^J_{v,j,\Omega\rightarrow v',j',\Omega'}(E) T^J_{l'\Omega'} \end{aligned} \tag{2.67}$$

Here $\boldsymbol{T}$ and $\boldsymbol{T}_p$ are respectively, the transformation matrix for the reactants and products. $\boldsymbol{T}_p$ is the matrix that diabatizes the tri-diagonal Coriolis coupling matrix $\boldsymbol{C}C$ (expressed in product Jacobi coordinates) whose elements are defined as,

$$\begin{aligned} cc_{\Omega',\Omega'} &= \frac{\hbar^2}{2\mu_{R_p}R_p^2}[J(J+1)+j'(j'+1)-2\Omega'^2] \text{ and} \\ cc_{\Omega',\Omega'+1} &= cc_{\Omega'+1,\Omega'} \\ &= \frac{-\hbar^2}{2\mu_{R_p}R_p^2}\sqrt{[J(J+1)-\Omega'(\Omega'+1][j'(j'+1)-\Omega'(\Omega'+1]}. \end{aligned} \tag{2.68}$$

For initial choice of $j=0$, $\boldsymbol{T}$ in Eq. 2.67 may be omitted. Now, the $\boldsymbol{S}$ matrix in the SF frame is obtained as [23–25],

$$\begin{aligned} S^J_{v,j,l\rightarrow v',j',l'}(E) &= \frac{-\hbar^2 a_s}{\sqrt{1-(a_sE+b_s)^2}}\sqrt{\frac{k_{v'j'}k_{vj}}{\mu_R\mu_{R_p}}}\left(\frac{2A^J_{v,j,l\rightarrow v',j',l'}(E)}{\bar{g}_{k_{vj}}}\right) \\ &\times \exp[-i(k_{v'j'}R_p^d+\delta\eta_{v'j'l'}+\delta\eta_{vjl})]. \end{aligned} \tag{2.69}$$

Here $a_s = 2/(E_{max}-E_{min})$ and $b=-1-a_sE_{min}$ are the parameters which scales the Hamiltonian. In Eq. 2.69, $k_{vj}(=\sqrt{2\mu_R(E-\epsilon_{vj})}/\hbar)$ and $k_{v'j'}(=\sqrt{2\mu_{R_p}(E-\epsilon_{v'j'})}/\hbar)$, respectively, are the wavevector components associated with the reactant and product channels and $g_{k_{vj}}$ is the Fourier transform of initial sinc wavefunction (cf. Eq. 2.50) in to momentum space. The phase of $\boldsymbol{S}$ matrix is adjusted to correct value by the phase corrections $\delta\eta_{vjl}$ and $\delta\eta_{v'j'l'}$ expressed

as [23–25]

$$\begin{aligned}
\delta\eta_{vjl} &= \sqrt{J(J+1)}sin^{-1}\left(-\sqrt{\frac{J(J+1)}{2\mu_R(E-\epsilon_{vj})R_0^2}}\right) \\
&- \sqrt{2\mu_R(E-\epsilon_{vj})R_0^2 - J(J+1)} + \sqrt{2\mu_R(E-\epsilon_{vj})}R_0, \qquad (2.70)\\
\delta\eta_{v'j'l'} &= \sqrt{l'(l'+1)}sin^{-1}\left(-\sqrt{\frac{l'(l'+1)}{2\mu_{R_p}(E-\epsilon_{v'j'})R_p^{d2}}}\right) \\
&- \sqrt{2\mu_{R_p}(E-\epsilon_{v'j'})R_p^{d2} - l'(l'+1)} + \sqrt{2\mu_{R_p}(E-\epsilon_{v'j'})}R_p^d \qquad (2.71)
\end{aligned}$$

where $l' = |J - j'| + 2(\Omega' - 1)$. Having calculated the $\boldsymbol{S}$ matrix in the SF basis, we now transform back to the BF basis using

$$\begin{aligned}
\boldsymbol{S}^{BF} &= \boldsymbol{T}^T\boldsymbol{S}^{SF}\boldsymbol{T}_p^T \\
\Rightarrow S^J_{v,j,\Omega\rightarrow v',j',\Omega'}(E) &= \sum_{ll'} T^J_{\Omega l}S^J_{v,j,l\rightarrow v',j',l'}(E)T^J_{\Omega' l'}. \qquad (2.72)
\end{aligned}$$

The state-to-state reaction probability is given by $|S^J_{v,j,\Omega\rightarrow v',j',\Omega'}(E)|^2$.

2.6.1 Differential and integral cross sections

After calculating the $\boldsymbol{S}$ matrix, the state-to-state DCSs are obtained by [43],

$$\begin{aligned}
\sigma(E,\theta,v,j\rightarrow v'j') &= \frac{1}{2j+1}\sum_{\Omega\Omega'}\frac{1}{4{k_{vj}}^2} \\
&\times \left|\sum_J (2J+1)S^J_{v,j,\Omega\rightarrow v',j',\Omega'}D^J_{\Omega\Omega'}(0,\theta,0)\right|^2, \qquad (2.73)
\end{aligned}$$

where $D^J_{\Omega\Omega'}(0,\theta,0)$ is a reduced Wigner rotation matrix [37] and θ is the scattering angle. The state-to-state ICSs are obtained by integrating Eq. 2.73 over all

scattering angles,

$$\sigma(E, v, j \rightarrow v'j') = \frac{\pi}{k_{vj}^2(2j+1)} \sum_{\Omega\Omega'} \sum_{J} (2J+1) \left| S^J_{v,j,\Omega \rightarrow v',j',\Omega'} \right|^2 . \quad (2.74)$$

2.7 Spectral intensity

If $\psi(t=0)$ is the WP pertinent to a molecule in its, X electronic state, and $\psi(t)$, is the WP at time, t, when evolving on a A electronic PES, then the spectral intensity for the $X \rightarrow A$ Franck-Condon (FC) transition is given by the time-dependent version of the golden rule expression [2, 44],

$$I(E) \approx \int \mid e^{iEt/\hbar} C(t) dt \mid^2 . \quad (2.75)$$

Here $c(t)$ is the time autocorrelation function of the evolving WP. For time-independent Hamiltonian operator and real initial WPs, the autocorrelation function for time $2t$ is obtained by the useful expression [45, 46],

$$C(2t) = \langle \psi^*(t) | \psi(t) \rangle . \quad (2.76)$$

The locations of the peak maximum in the spectral intensity give the energy eigenvalues and the corresponding stationary state eigenfunctions can be obtained by projecting the time evolved WP onto the desired eigenstate ψ_n of energy E_n [13] as

$$\psi_n(E) = \int_0^\infty e^{iE_n t/\hbar} \psi(t) . \quad (2.77)$$

References

[1] M. Born and K. Huang, Dynamical Theory of Crystal Lattices, Oxford University Press, New York, 1954

[2] H. Köppel, W. Domcke, L.S. Cederbaum, Adv. Chem. Phys. 57 (1984) 59 .

[3] B.H. Lengsfield, D.R. Yarkony, Adv. Chem. Phys. 82 (1992) 1.

[4] W. Lichten, Phys. Rev. 164 (1967) 131.

[5] F.T. Smith, Phys. Rev. 179 (1969) 111.

[6] W. Domcke, G. Stock, Adv. Chem. Phys. 100 (1997) 1.

[7] H. Köppel, W. Domcke, in; P.V.R. Schlyer (Eds.), Encyclopedia of computational chemistry, Wiley, New York, 1998.

[8] R. Kosloff, J. Phys. Chem. 92 (1988) 2087; Ann. Rev. Phys. Chem. 45 (1994) 145. and references therein.

[9] R. Kosloff, in; C. Cerjan (NATO ASI Ser. C 412) (Eds.), Numerical Grid methods and Their applications to Scrödinger's Equation, Kluweru Academic Publishers, Dordreht, The Netherlands, 1933, p. 175.

[10] R. Kosloff, in *Time Dependent Methods for Quantum Dynamics*, NATO ASI Ser. B**229**, Plenum Press, New York, 1992.

[11] D. Kosloff, R. Kosloff, J. Comput. Phys. 52 (1983) 35; Comput. Phys. Commum. 30 (1983) 333.

[12] J.A. Fleck, Jr., J.R. Morris, M.D. Feit, Appl. Phys. 10 (1976) 129.

[13] M.D. Feit, J.A. Fleck, Jr., A. Steiger, J. Comput. Phys. 47 (1982) 412; M.D. Feit, J.A. Fleck, Jr. J. Chem. Phys. 78 (1983) 301; J. Chem. Phys. 80 (1984) 2578.

[14] J.W. Cooley, J.W. Tuckey, Math. Computation 19 (1965) 297.

[15] D.O. Harris, G.G. Engerholm, W.D. Gwinn, J. Chem. Phys. 43 (1965) 1515.

[16] A.S. Dickinson, P.R. Certain, J. Chem. Phys. 49 (1968) 4209.

[17] G.C. Corey, J.W. Tromp, D. Lemoine, in Ref. [9], p. 187.

[18] J.V. Lill, G.A. Parker, J.C. Light, Chem. Phys. Lett. 89 (1982) 483; J.C. Light, I.P. Hamilton, J.V. Lill, J. Chem. Phys. 82 (1985) 1400; J.P. Hamilton, J.C. Light, J. Chem. Phys. 84 (1986) 306.

[19] R.M. Whitnell, J.C. Light, J. Chem. Phys. 90 (1989) 1774.

[20] Z. Bačić, J.C. Light, Ann. Rev. Phys. Chem. 40 (1989) 469.

[21] C. Leforestier, J. Chem. Phys. 94 (1991) 6388.

[22] E.M. Goldfield, S.K. Gray, Compt. Phys. Commun. 98 (1996) 1.

[23] S.K. Gray, G.G. Balint-Kurti, J. Chem. Phys. 108 (1998) 950.

[24] M. Hankel, S.C. Smith, R.J. Allan, S.K. Gray, G.G. Balint-Kurti, J. Chem. Phys. 125 (2006) 164303.

[25] M. Hankel, S.C. Smith, S.K. Gray, G.G. Balint-Kurti, Comput. Phys. commun. 179 (2008) 569.

[26] A. Askar and A.S. Cakmak, J. Chem. Phys. 68 (1978) 2794; D. Kosloff, R. Kosloff, Comput. Phys. Commun. 30 (1983) 333; J. Chem. Phys. 52 (1983) 35.

[27] M.D. Feit, J.A. Fleck Jr., A. Steiger, J. Comput. Phys. 47, (1982) 412.

[28] H. Tal-Ezer, R. Kosloff, J. Chem. Phys., 81 (1984) 3967.

[29] T.J. Park, J.C. Light, J. Chem. Phys. 85 (1986) 5870.

[30] G. Arfken, Mathematical Methods for Physicists, Academic Press Inc., Prism Books Pvt. Ltd., Bangalore, (1994).

[31] R. Kosloff, J. Phys. Chem. 92 (1988) 2087.

[32] V. Mohan, N. Sathyamurthy, Comput. Phys. Rep. 7 (1988) 213.

[33] R. Kosloff, Ann. Rev. Phys. Chem. 45 (1994) 145.

[34] D. Kosloff and R. Kosloff, Comput. Phys. Commun. 30 (1983) 333; J. Comput. Phys. 52 (1983) 35.

[35] M. Hankel, G.G. Balint-Kurti, S.K. Gray, Int. J. Quant. Chem. 92 (2003) 205.

[36] D.T. Colbert and W.H. Miller, J. Chem. Phys. 96 (1992) 1982.

[37] R.N. Zare, Angular momentum, Wiley, New York, 1988.; A.R. Edmonds, Angular momentum in quantum mechanics, Princeton university press, Princeton, 1960.

[38] D. Neuhauser, M. Baer, R.S. Judson, D.J. Kouri, Comput. Phys. Com. 63 (1991) 463.

[39] T.J. Park, J.C. Light, J. Chem. Phys. 88 (1988) 4897; W. H. Miller, J. Phys. Chem. 102 (1998) 793 and references therein.

[40] D. Neuhauser, M. Baer, J. Chem. Phys. 91 (1989) 4651; D. Neuhauser, M. Baer, R.S. Judson, D.J. Kouri, J. Chem. Phys. 93 (1990) 312.

[41] F.J. Aoiz, L. Bañares, J.F. Castillo, J. Chem. Phys. 111 (1999) 4013.

[42] S.C. Althorpe, J. Chem. Phys. 114 (2001) 1601.

[43] G.G. Balint-Kurti, Adv. Chem. Phys. 128 (2003) 249.

[44] Eric J. Heller, Acc. Chem. Res. 14 (1981) 368.

[45] V. Engel, Chem. Phys. Lett. 189 (1992) 76.

[46] U. Manthe, H.-D. Meyer, L.S. Cederbaum, J. Chem. Phys. 97 (1992) 9062.

Chapter 3

Quantum nonadiabatic dynamics of H + D_2 (HD) and D + H_2 (HD) reactions

3.1 Introduction

In this chapter the initial state-selected and energy resolved reaction probabilities, integral reaction cross sections (ICSs) and thermal rate constants obtained for the H + D_2 (HD) and D + H_2 (HD) reactions using the formalism outlined in chapter 2 are presented and discussed. To this effort, the double many body expansion (DMBE) potential energy surfaces [1] of the system is employed and the reaction probabilities up to the total energy of $\sim$ 4.7 eV both with and without the surface coupling are calculated. Within the centrifugal sudden (CS) approximation [2], all partial wave contributions up to the total angular momentum $J = 50$ are considered to calculate the converged ICSs. Analysis of the reaction probabilities, ICSs show that the nonadiabatic effects are insignificant. The

thermal rate constants calculated from the ICSs compare well with the available theoretical and experimental results [3–10].

3.2 Theoretical and computational details

The detailed theoretical framework and computational methodology to treat the reaction dynamics by the time-dependent quantum mechanical approach is outlined in chapter 2. A few essential points are described below. The interaction Hamiltonian of the ground electronic manifold of the collisional system in a diabatic electronic basis can be written as (cf. Eq. 2.45)

$$H^{dia} = T_{nuc} \begin{pmatrix} 1 & 0 \\ 0 & 1 \end{pmatrix} + \begin{pmatrix} U_{11} & U_{12} \\ U_{21} & U_{22} \end{pmatrix}, \tag{3.1}$$

where T_{nuc} (cf. Eq. 2.11) represents the nuclear kinetic energy operator, which is diagonal in this basis. The diabatic electronic matrix of Eq. 3.1 is obtained as

$$\begin{aligned} \begin{pmatrix} U_{11} & U_{12} \\ U_{21} & U_{22} \end{pmatrix} &= \mathbf{S} \begin{pmatrix} V_- & 0 \\ 0 & V_+ \end{pmatrix} \mathbf{S}^\dagger \\ &= \frac{V_- + V_+}{2} \mathbf{1} + \frac{V_+ - V_-}{2} \begin{pmatrix} -\cos\chi & \sin\chi \\ \sin\chi & \cos\chi \end{pmatrix}, \end{aligned} \tag{3.2}$$

with

$$\mathbf{S} = \begin{pmatrix} \cos\phi & \sin\phi \\ -\sin\phi & \cos\phi \end{pmatrix}. \tag{3.3}$$

In Eq. 3.2 V_- and V_+ represents the two adiabatic PESs and, $\chi = 2\phi$, represents the pseudorotation angle related to the adiabatic-to-diabatic mixing angle ϕ in a linear coupling approximation [11]. The two adiabatic sheets of the DMBE PES [1] are used for V_- and V_+. It is to be noted that this diabatization scheme is based on the idea of removing the leading (divergent) derivative coupling elements of the adiabatic basis (as discussed in Sec. 2.2). This has been successfully tested [11] and employed for a practical application [12]. In a later study this idea is extended and generalized to less symmetric systems and a consistent comparison of the diabatic model with the computed *ab initio* data has been made [13]. The explicit coupling between V_- and V_+ considered above includes all diagonal and off-diagonal coupling terms in addition to the GP change.

Having obtained the Hamiltonian in a diabatic electronic basis, the initial wave packet (WP) is first prepared in the adiabatic basis

$$\mathbf{\Psi}^{adia}(R, r, \gamma, t = 0) \;=\; \psi(R, r, \gamma, t = 0) \begin{pmatrix} 1 \\ 0 \end{pmatrix} + \psi(R, r, \gamma, t = 0) \begin{pmatrix} 0 \\ 1 \end{pmatrix}, \quad (3.4)$$

and then transformed it to diabatic basis using,

$$\mathbf{\Psi}^{dia} = \boldsymbol{S}\Psi^{adia}. \quad (3.5)$$

The first and second term in the right hand side of Eq. 3.4 represents the initiation of the reaction on the lower and upper adiabatic sheets, respectively. In Eq. 3.4, $\psi(R, r, \gamma, t = 0)$ is the initial wavefunction pertinent to the reactant asymptote is given by Eq. 2.48. The diabatic WP in Eq. 3.5 is then propagated in space and time using the Chebyshev polyn scheme described in section 2.3.1. Finally the

Table 3.1: Numerical grid parameters and properties of the initial wavefunction used in the present study

Parameter	Value	Description
$N_R/N_r/N_\gamma$	128/64/48	Number of grid points
R_{min}/R_{max} (a_0)	0.1/15.34	Extension of the grid along R
r_{min}/r_{max} (a_0)	0.5/8.06	Extension of the grid along r
$\Delta R/\Delta r$ (a_0)	0.12/0.12	Grid spacings along R and r
r_d (a_0)	4.10	Location of the dividing surface in the product channel
R_{mask}/r_{mask} (a_0)	11.74 /4.70	Starting point of the masking function
R_0 (a_0)	10.5	Initial location of the center of the GWP in the coordinate space
E_{trans} (eV)	2.0	Initial translational kinetic energy
δ (a_0)	0.16	Initial width parameter of the GWP
Δt (fs)	0.135	Length of the time step
T (fs)	413.76	Total propagation time

initial state-selected reaction probabilities (cf. Eq. 2.57), cross sections (cf. Eq. 2.62) and rate constants (cf. Eq. 2.64) are obtained by flux operator approach (see section 2.5 for details). Various grid parameters used in this work are presented in table 3.1. It is to be noted to be that the convergence of each calculation is checked with respect to the choice of these parameters.

3.3 Results and Discussion

3.3.1 Reaction Probability

The H + D_2 ($v = 0$, $j = 0$) $\rightarrow$ HD ($\sum v'$, $\sum j'$) + D reaction probability values as a function of the total energy E are plotted in Fig. 3.1 for a few selected values of the total angular momentum, $J = 0$, 10, 20, 30, 40 and 50 (indicated in the panel) and for $\Omega = 0$. It is to be noted that the pattern of variation

of reaction probabilities remains similar for $\Omega \neq 0$. The coupled and uncoupled surface results are shown by the solid and dashed lines, respectively. It can be seen from Fig. 3.1 that the threshold for the reaction shifts to the higher energy with increasing J value. The difference between the coupled and uncoupled surface results disappears below the energetic minimum ($\sim$ 2.74 eV) of CIs. But above this minimum, the difference becomes noticeable. As J increases the difference between the coupled and uncoupled surface results becomes negligible. It can be seen that above $J = 20$, the coupled and uncoupled surface results merge together. Oscillations in the probability curves reveal that at low energies the reaction proceeds via resonance formation which becomes more direct at higher energies.

The D + H_2 ($v = 0$, $j = 0$) $\rightarrow$ HD ($\sum v'$, $\sum j'$) + H reaction probability values as a function of the total energy E (D, H_2 translational + H_2 rovibrational) are plotted in Fig. 3.2 for a few selected values of the total angular momentum, J = 5, 15, 25, 35 and 45 (indicated in the panel) and for $\Omega = 0$. The coupled and uncoupled surface results are shown by the solid and dashed lines, respectively. As in the case of H + D_2 reaction, the reaction threshold shifts to the higher energy values with increasing J due to an increase in the centrifugal barrier height. The resonance structures and their energetic locations remain same in both coupled and uncoupled surface results for a given value of J. The difference between the coupled and uncoupled surface reaction probabilities for a fixed value of J is negligible at low energies. At higher energies near and above the minimum of CIs, this difference becomes noticeable which becomes insignificant for higher J values. In this case also the dynamical event is dominated by the resonance formation at low energies and smaller J values.

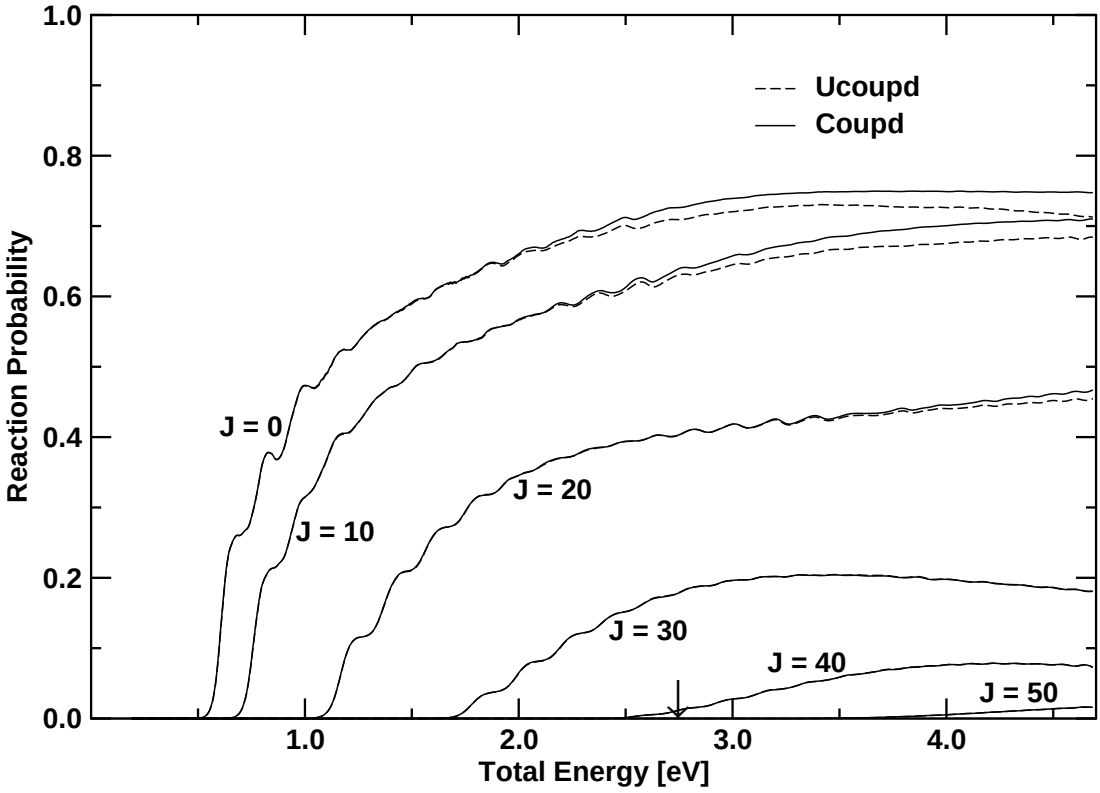

Figure 3.1: Total reaction probabilities as a function of the total energy E (H, D_2 translational + D_2 rovibrational) for the H + D_2 ($v = 0$, $j = 0$) $\rightarrow$ HD ($\sum v'$, $\sum j'$) + D exchange reaction on the DBME PES for the total angular momentum, $J = 0$, 10, 20, 30, 40 and 50 (indicated in the panel) and $\Omega = 0$. The coupled and uncoupled surface results are shown by the solid and dashed lines, respectively. The zero of the energy scale corresponds to infinitely separated reagents. The arrow in the abscissa indicates the location of the energetic minimum of the seam of CIs.

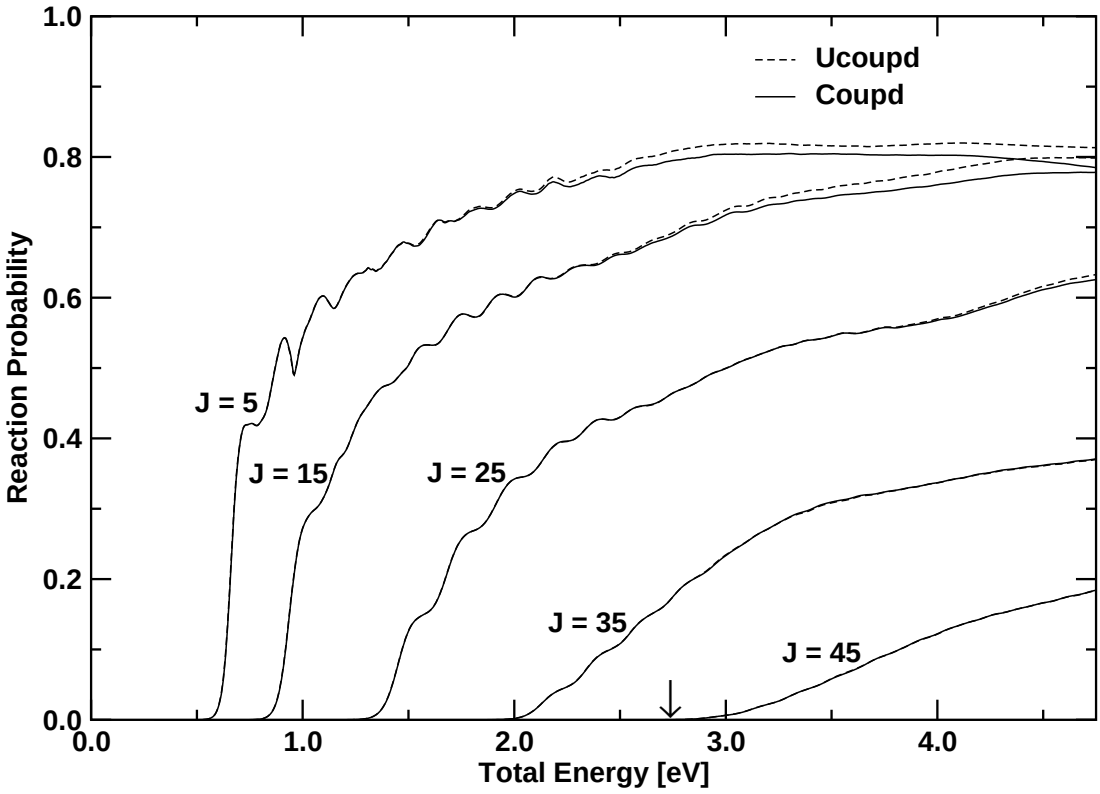

Figure 3.2: Same as in Fig. 3.1 for D + H_2 ($v = 0$, $j = 0$) → HD ($\sum v'$, $\sum j'$) + H exchange reaction for the total angular momentum, $J = 5$, 15, 25, 35 and 45 (indicated in the panel) and $\Omega = 0$.

The above dynamical quantities calculated for the isotopic H + HD and D + HD reactions are discussed here. The former gives either H_2 + D (channel R1a) or HD + H (channel R2a) products and the latter gives either DH + D (channel R1b) and D_2 + H (channel R2b) products, respectively. In the following both the channel specific as well as total reaction probabilities are presented and discussed. In our earlier work on the H + HD system [14], a technical scaling error occurred. The H and D masses were erroneously interchanged. It is corrected the in this work. The reaction probability values for the H + HD ($v = 0$, $j = 0$) reaction as a function of the total energy E are plotted in Figs. 3.3(a-c) for five selected values of the total angular momentum, $J = 0$, 10, 20, 30 and 40 and for $\Omega = 0$. The reaction probabilities obtained in the uncoupled and coupled surface situations are shown by the dashed and solid lines, respectively. The reaction probabilities for channels R1a and R2a are given in panels (a) and (b), respectively, and the overall reaction probabilities (sum total of the two channel specific probabilities) are given in the panel (c). The effect of the nonadiabatic coupling (NAC) on the channel specific reaction probabilities of panel (a) and (b) appears to be similar to the other isotopic variants. The opposite behavior observed between the uncoupled and coupled surface results for the channel specific probabilities shown in Fig. 5 of Ref. [14] is absent in Figs. 3.3(a-b). Rather, the reaction probabilities for the two channels show such behavior in the latter figures for $J < 20$.

The reaction probability values for the D + HD ($v = 0$, $j = 0$) reaction as a function of the total energy E are plotted in Figs. 3.3(d - f) for the $J = 0$, 10, 20, 30 and 40 and for $\Omega = 0$. The reaction probabilities for channels R1b and R2b are shown in panels (d) and (e), respectively. The overall reaction probabilities

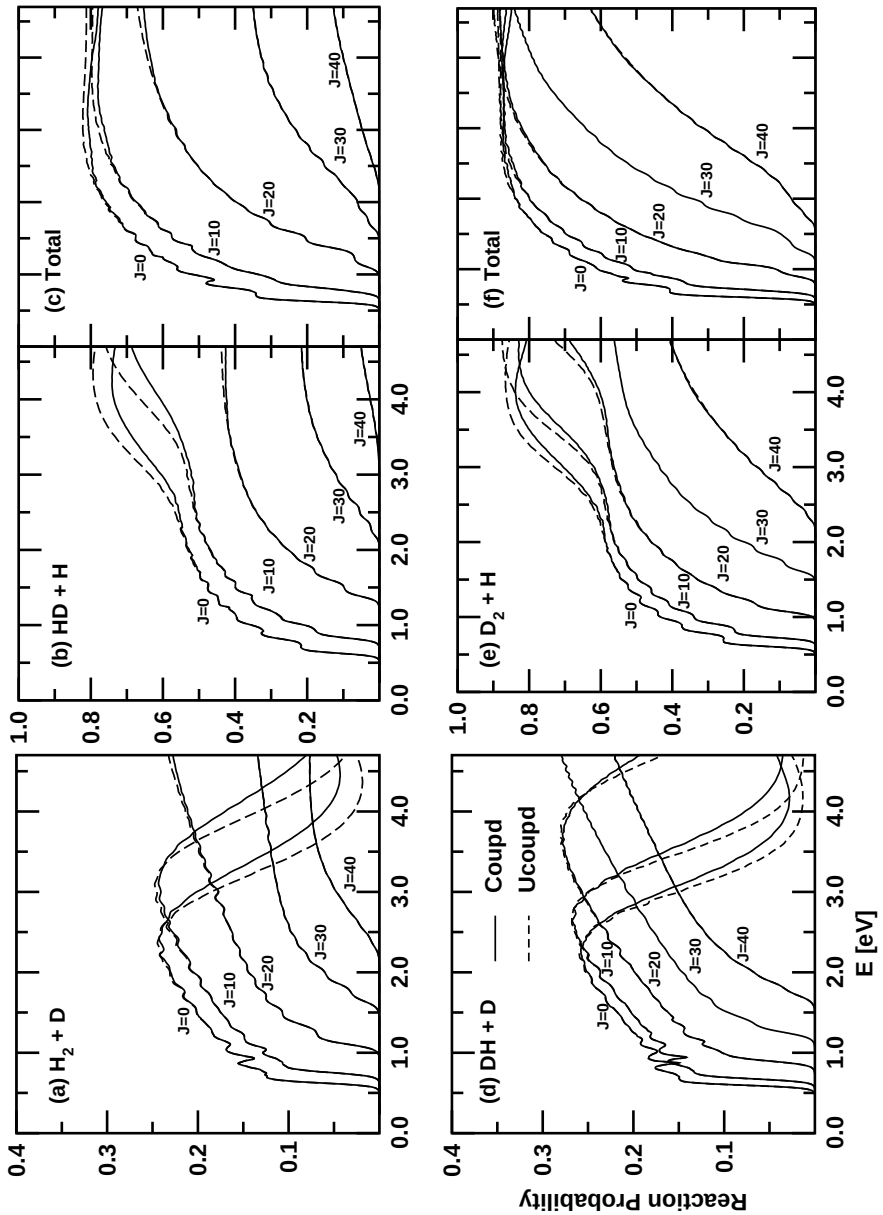

Figure 3.3: Reaction probabilities of the H + HD ($v = 0, j = 0$) reaction for the (a) H_2 + D and (b) HD + H channels as a function of total energy, E. The sum total of these probabilities are plotted in panel (c). The probabilities are shown for various values of the total angular momentum, J indicated in each panel. The coupled and uncoupled surface results are shown by the solid and dashed lines, respectively. The zero of the energy scale corresponds to infinitely separated reagents. Panel d-f: Same as panels a-c but for the isotopic D + HD ($v = 0, j = 0$) reaction.

are given in panel (f). The coupled and uncoupled surface reaction probabilities are shown by the full and dashed lines, respectively. It can be seen that both the channel specific and the total reaction probabilities in this case exhibit similar behavior as those in case of the H + HD reactions. It emerges from the above discussion that the NAC have almost similar effects in the dynamics of H + H_2 reaction and its isotopic variants.

3.3.2 Initial State-Selected Integral Reaction Cross Sections

The initial state-selected ICSs as a function of collision energies for the H + D_2 (v = 0, j) reaction are plotted in Figs. 3.4(a-b) for the reagent rotational states, j = 0 and 1, respectively. The coupled and uncoupled surface results are shown by the full and dashed lines, respectively. The cross section values for a particular j value increases reaching a maximum and then decreases. A similar trend of variation of cross sections is observed for further higher j values. The maximum cross section ($\sim$ 1.41 Å^2) for $j = 0$ occurs for the collision energy of $\sim$ 1.9 - 2.2 eV. The ICSs obtained from experimental [15] and other theoretical studies [16–19] are shown in Figs. 3.4(a-b). It can be seen from these figures that the present theoretical results are in good accord with the experiment. The difference between the cross section values calculated in the coupled and uncoupled surface situation is practically negligible. Similar conclusions have been made in a state-to-state time-dependent WP study of the H + D_2 reaction by Lu *et al.* employing a diabatic DMBE PES of H_3 [19] until a collision energy of 2 eV. It is to be noted that, the cross section values reported by the latter authors compare very well with ours (cf., Fig. 3.4(a)). Therefore, it appears that the "diabatic H_3 DMBE" is as "accurate" as our diabatic model for a reliable description of the reaction

dynamics of H + H_2 and its isotopic variants. Using a line-integral approach, Xu *et al.* [20] apparently constructed a diabatic model similar to ours and pointed out that it may yield erroneous dynamical outcomes as compared to the diabatic H_3 DMBE. This proposition is however not validated by dynamical studies and considering the present developments, it remains to be established.

The initial state-selected ICSs for the D + H_2 ($v = 0$, j) reaction are plotted in Figs. 3.4(c-d) for $j = 0$ and 1, respectively. The ICS increases to reach a maximum value ($\sim$ 2.78 Å^2) and then decreases with increasing energy. The D + H_2 reaction cross sections are larger than those of H + D_2 reaction for a given energy. This observation is consistent with the available experimental [15] and theoretical [21] data. The larger cross section of D + H_2 reaction is interpreted to be due to efficient transfer of the collision energy of the heavier D atom to the vibrational degree of freedom of the lighter H_2 molecule. The difference between the uncoupled and coupled surface results is negligible in case of the D + H_2 reaction also. Similar variation of cross sections are obtained for further higher values of j.

The initial state-selected ICSs for the H + HD ($v = 0$, j) reaction are plotted in Figs. 3.5(a-l) as a function of the collision energy. The cross section values for the R1a and R2a channels are shown in panels (a-d) and (e-h) for $j = 0$ - 3, respectively. The cross section values calculated in the coupled and uncoupled surface situation are shown by the full and dashed lines, respectively. The total cross section (sum of the two channel specific cross sections) values are shown in panels (i-l) for $j = 0$ - 3, respectively. For any given value of j, the cross section values of the R1a channel are larger than those of the R2a channel. The skew angle (the angle between mass scaled reagent Jacobi coordinate R_a and mass

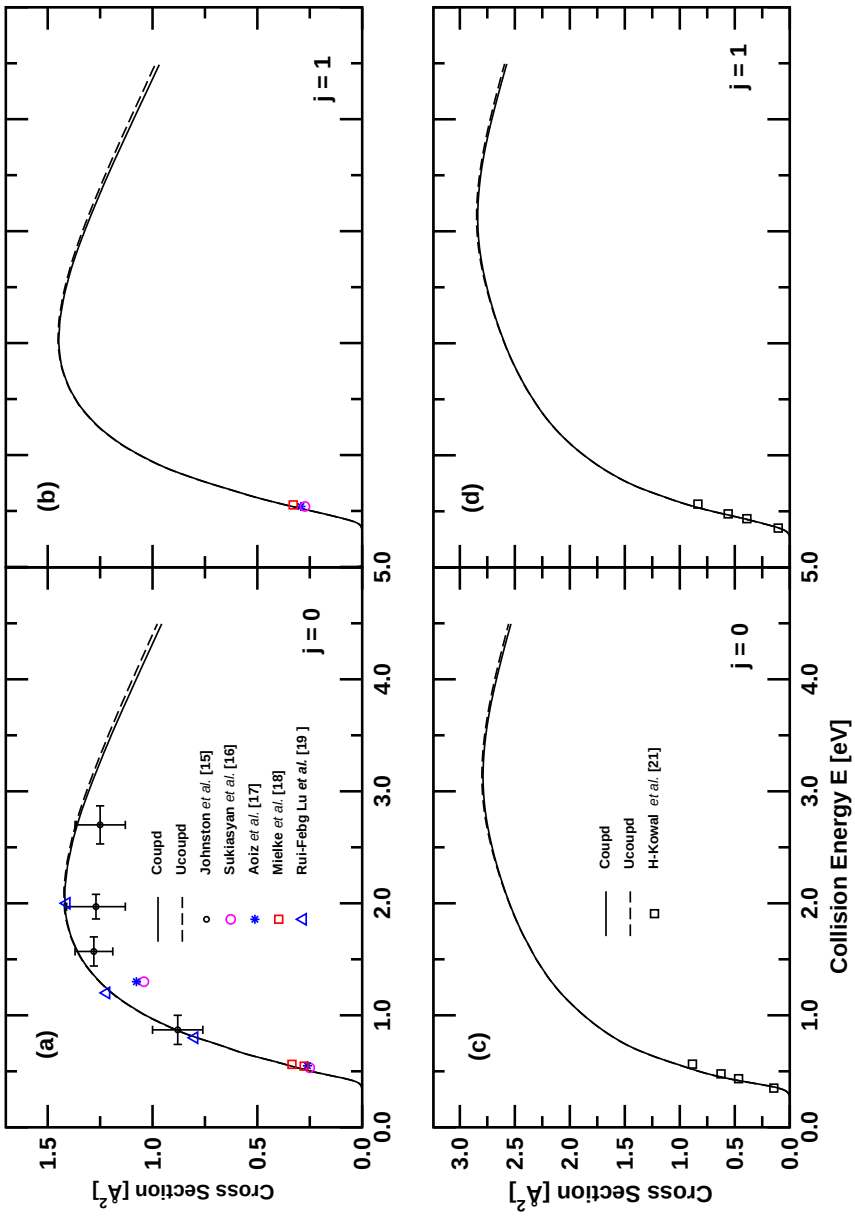

Figure 3.4: Initial state-selected ICSs of the H + D_2 ($v = 0$, j) (panels a-b) and D + H_2 ($v = 0$, j) (panels c-d) reactions, respectively, as a function of the collision energy. The reagent rotational quantum number j is indicated in each panel. The ICS values available in the literature are shown by different symbols (Refs. [15–19, 21]) as shown in the figures.

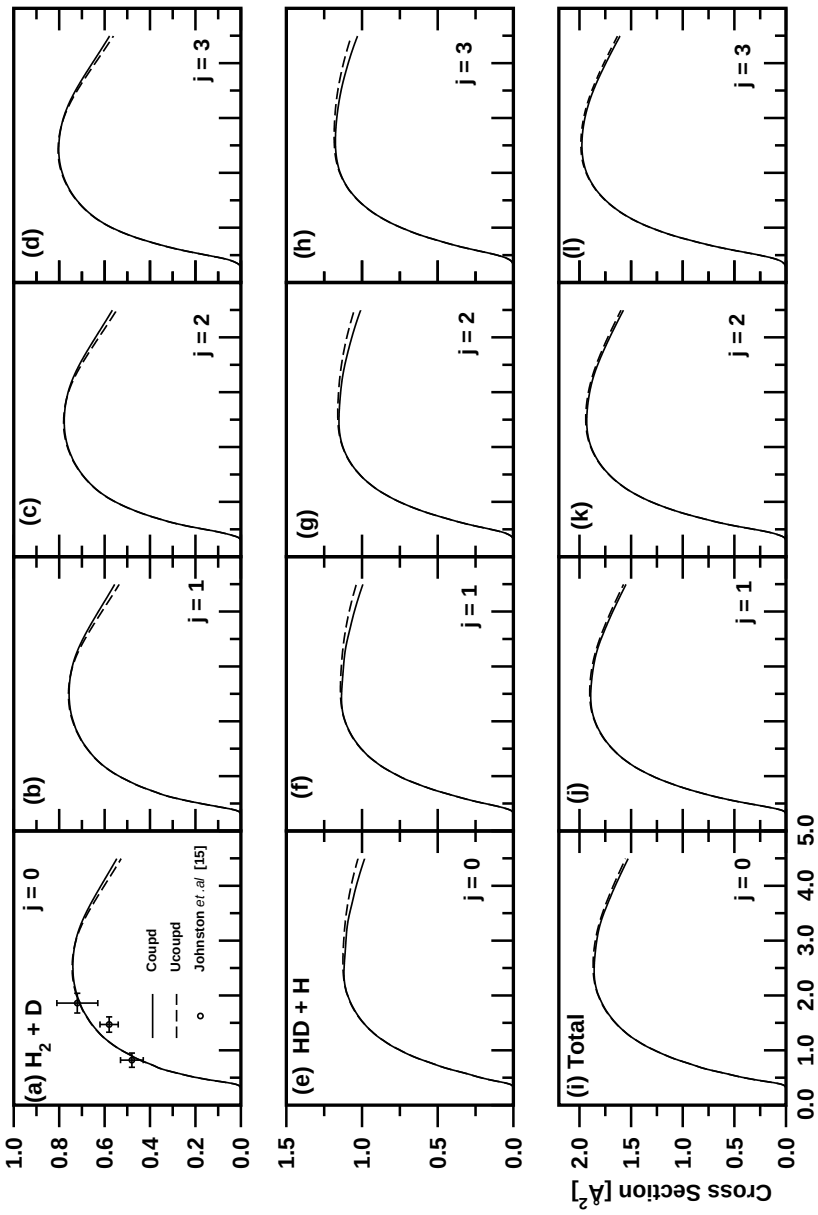

Figure 3.5: Same as in Fig. 3.4 for the $H_2 + D$ channel (panels a-d), HD + H channel (panels e-h) and the sum total of the channel specific cross sections (panels i-l) of the H + HD ($v = 0$, j) reaction. The reagent rotational quantum number j is given in each panel. The circles with error bars in panel (a) are experimental values from Ref. [15].

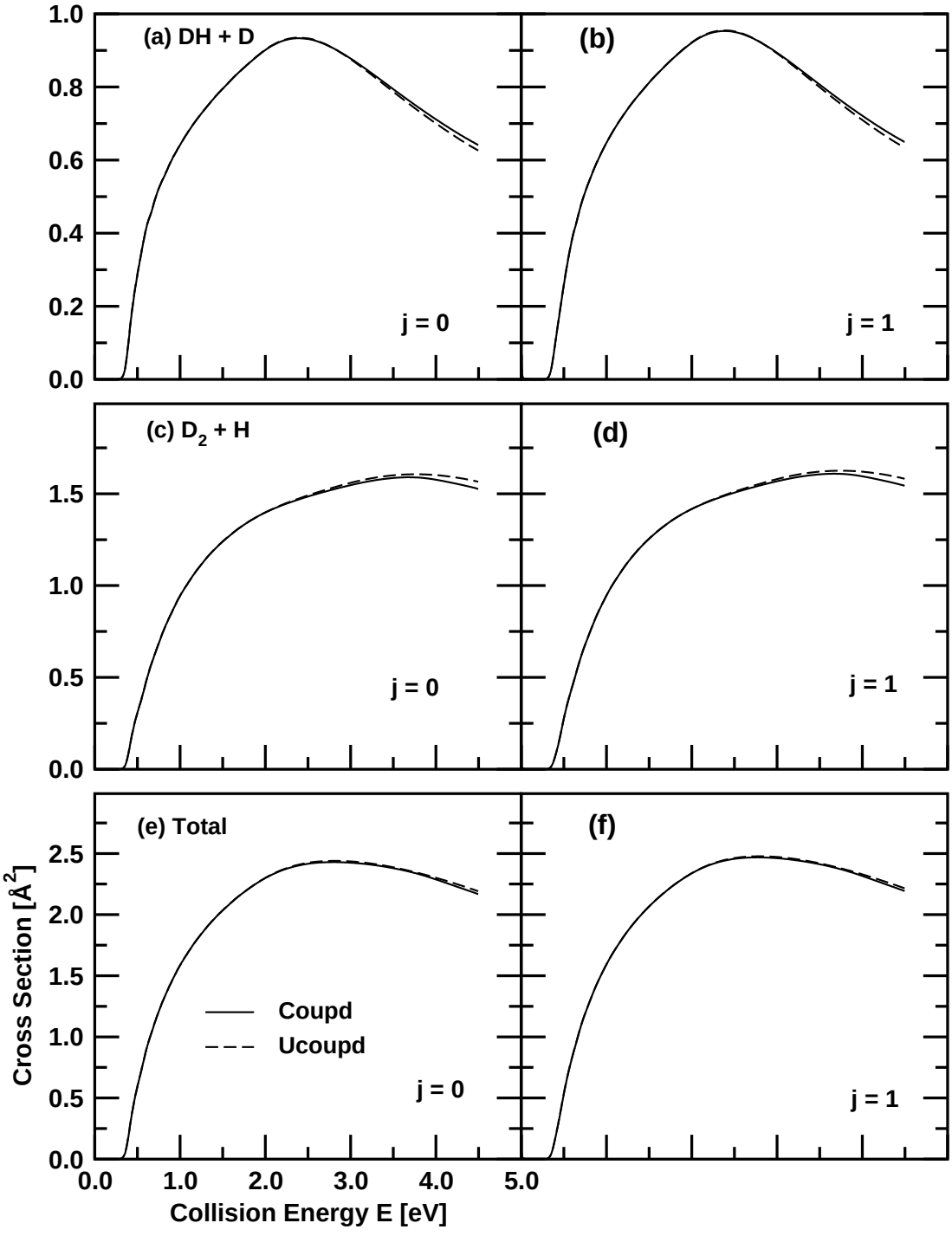

Figure 3.6: Same as in Fig. 3.5 for D + HD reaction.

scaled product Jacobi coordinate R_c) of the R2a channel is much larger than the R1a channel (70.53^0 vs 54.74^0). This qualitatively explains the greater reactivity of the R2a channel. The experimental data available [15] for the R1a channel for $j = 0$ are also given in panel a. It can be seen that the present theoretical results are fairly in good accord with the experiment. Minor difference between the cross section values calculated in the coupled and uncoupled surface situations are seen only above the minimum of the seam of CIs particularly, for the R2a channel. This difference becomes negligible in the total reaction cross sections shown in panels (i-l). It is to be noted that the above figures replace Figs. (8-10) of Ref. [14], in which a mass scaling error occurred as mentioned above. The initial state-selected ICS values for the D + HD ($v = 0$, $j = 0$ - 1) reaction are plotted in Figs. 3.6(a-f) as a function of the collision energy. The cross section values for the R1b and R2b channels are shown in panels (a-b) and (c-d), respectively. The cross section values for the overall reaction are shown in panels (e-f) for $j =$ 0 and 1, respectively. The coupled and uncoupled surface results are shown by full and dashed lines, respectively. Analogous to the H + HD reaction, the cross section values increase with energy reaching a maximum and then decrease for particular value of j. It can be seen that both the channel specific as well as the total reactivity is more in this case compared to that for the H + HD reaction. This observation is in accord with the apparent rule that the heavier D atom efficiently transfers the collision energy to the HD vibration. The reactivity of the D_2 + H channel is more than that of DH + D channel for any given energy. In this case the skew angle of the D_2 + H channel is 65.91^0 and much larger than that of the DH + D channel of 48.19^0. The effect of NAC is minimal and some minor effects are seen above the minimum of the CIs.

3.3.3 Thermal rate constants

The thermal rate constants obtained by statistically averaging over the rotational states, j = 0 - 3, of the D_2 molecule are shown in Fig. 3.7 for the H + D_2 (v = 0) reaction. The coupled and uncoupled surface results are shown by the full and dashed lines, respectively. The rate constant values available in the literature are shown by the circles (Ref. [4]), squares (Ref. [7]), triangles (Ref. [9]) and asterisks (Ref. [5]) on the diagram. The present rate constants reveal the expected Arrhenius behavior in agreement with the experimental and other theoretical data [4, 5, 7, 9]. The observed discrepancy with the literature data mainly arises from insufficient number of j values used in the Boltzmann averaging in the present case. Furthermore, other contributing factors to this discrepancy are use of CS approximation [2] (although it is a very good approximation for the hydrogen exchange reaction) and possible inaccuracies of the underlying PESs. It is to be noted that, the main purpose of this article is to examine the effect of surface coupling on the reaction dynamics of the isotopic variants of the H + H_2 reaction and therefore, the calculations are limited up to j = 3 only. Now most importantly, Fig. 3.7 reveals that the difference between the coupled and uncoupled surface results is insignificant (within the drawing accuracy) in the reported temperature range of 300 - 1200 K.

The thermal rate constants obtained for the D + H_2 (v = 0) reaction by statistically averaging over the rotational states, j = 0 - 3, are shown in Fig. 3.8. The coupled and uncoupled surface results are shown by the solid and dashed lines, respectively. The rate constant values available in the literature are shown by different symbols [4, 6, 8, 9] on the diagram. The rate constant data reveal the expected Arrhenius behavior. It can also be seen from Fig. 3.8 that the differ-

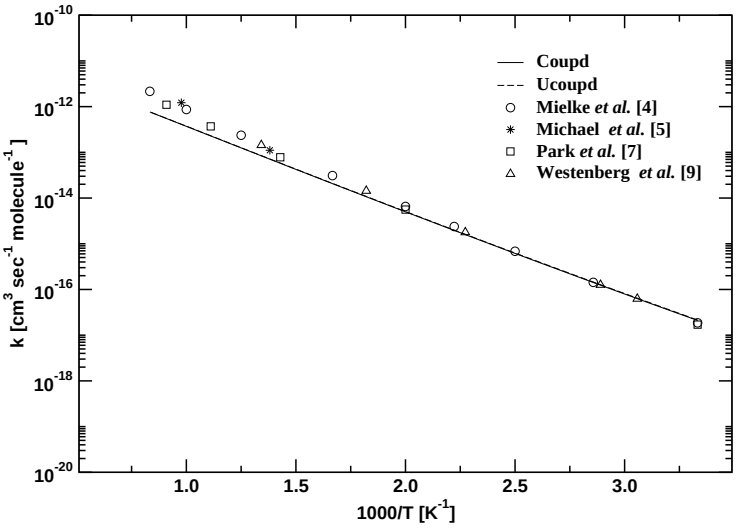

Figure 3.7: Arrhenius plot of the Boltzmann averaged (over j = 0 - 3 of the reagent diatom) thermal rate constants for the H + D_2 (v = 0) reaction. The coupled and uncoupled surface results are shown by the solid and dashed lines, respectively. The points on the diagram represents the results from the literature [4,5,7,9].

ence between the coupled and uncoupled results are insignificant in the reported temperature range of 300 - 1200 K.

In Figs. 3.9(a-b), the thermal rate constants obtained by statistically averaging over the rotational states j = 0 - 3 for the R1a and R2a channels of the H + HD reaction, respectively, are shown. The coupled and uncoupled surface results are shown by the circles and dashed lines, respectively. The rate constant values available in the literature are shown by the asterisks (Ref. [3]) and triangles (Ref. [10]) on the diagram. Also in Figs. 3.9(a-b) the thermal rate constants obtained by statistically averaging over the rotational states, j= 0 - 10, of the HD molecule for the R1a and R2a channels of the H + HD reaction in the uncoupled surface situation are shown by the dots. The latter results reveal better agreement with the literature data [3,10] when contributions from higher j values

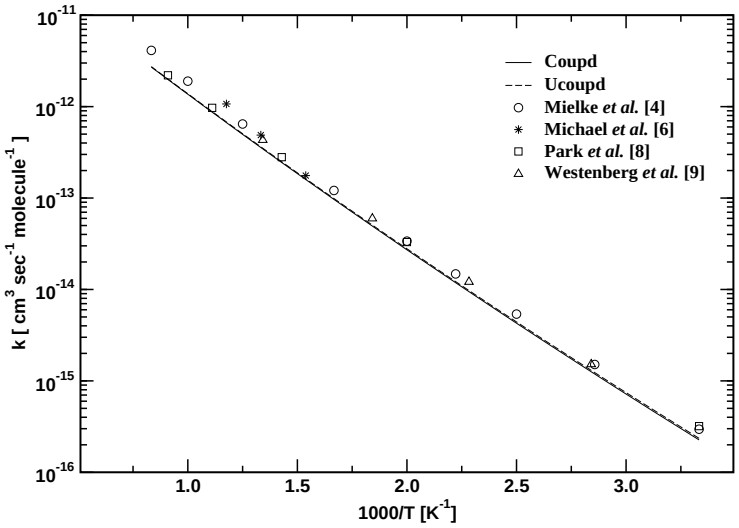

Figure 3.8: Same as in Fig. 3.7 for the D + H_2 ($v = 0$) reaction.

are included in the Boltzmann averaging. The difference between the thermal rate constants calculated in both coupled and uncoupled surface situations are again insignificant in this case. Finally we show the thermal rate constant values obtained by statistically averaging over the rotational states $j = 0$ - 3 for the R1b and R2b channels of the D + HD reaction in Figs. 3.9(c-d), respectively. The rate constant data do not reveal any effects of NAC in this case also.

3.4 Summary and outlook

A theoretical account of the electronic NAC effects on the dynamics of H + D_2 (HD) and D + H_2 (HD) reactions is presented in this article. The hydrogen exchange reaction occurs on the repulsive lower adiabatic sheet of the JT-split degenerate ground electronic manifold of H_3. Quantum dynamical calculations are carried out employing diabatic electronic states and a time-dependent WP

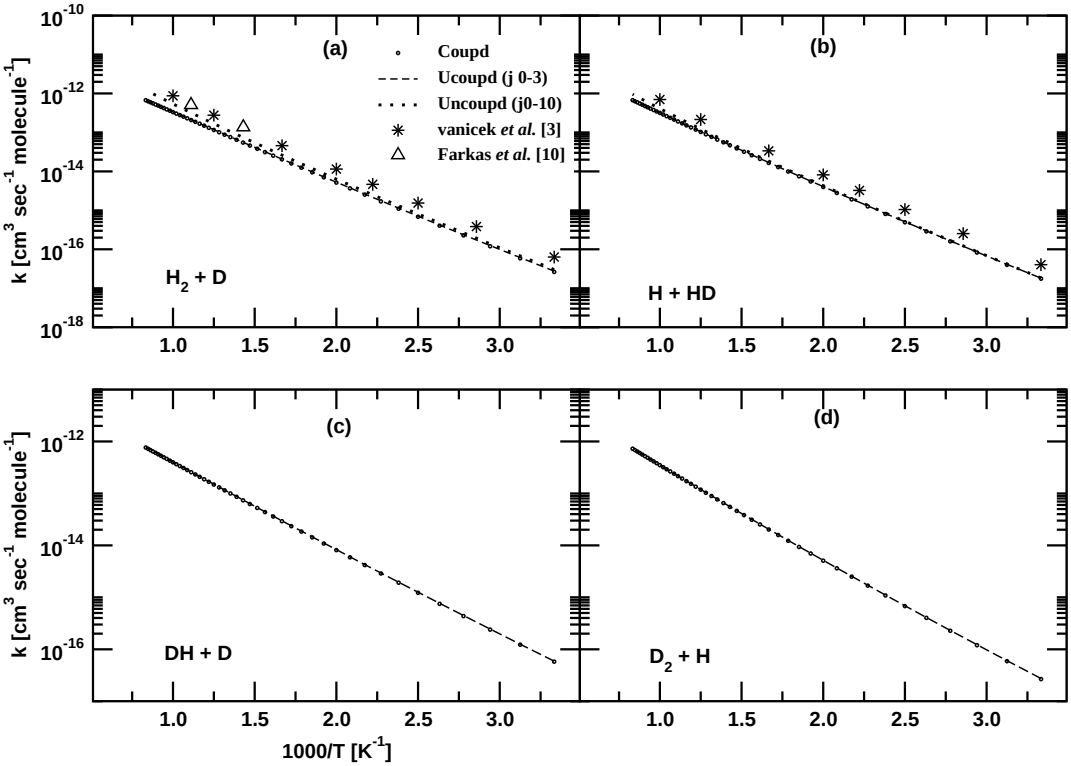

Figure 3.9: Arrhenius plot of the statistical average (over $j = 0$ - 3 (circles and dashed lines) or over $j = 0$ - 10 (dots) of the reagent diatom) for H_2 + D and H + HD channels of H + HD reaction in panels (a) and (b), respectively. The coupled and uncoupled surface results are shown by circles and dashed lines, respectively. The asterisks and triangles represent available results from the Ref [3] and Ref. [10], respectively. Same as above for D + HD reaction shown in panels (c) and (d), respectively.

method within the CS approximation and dynamical quantities *viz.,* the initial state-selected energy resolved total reaction probabilities, ICSs sections and thermal rate constants are reported. The effect of electronic NAC on these observables is explicitly examined. A study of the nonadiabatic effects on the state-to-state dynamical attributes of H + D_2 (HD) and D + H_2 (HD) reactions is currently being taken up.

Like in the case of the H + H_2 reaction, the impact of NAC on the above deuterated variants is found to be minor. Mild effect of surface coupling shows up only beyond the energetic minimum of the seam of conical intersections (CIs). ICSs are reported over a wide energy range starting from the onset of the reaction to the three-body dissociation limit. The calculated cross sections compare well with the available experimental data. The Boltzmann averaged thermal rate constants are found to be essentially same in the uncoupled and coupled surface situations for these reactions. The findings presented in this chapter are in general agreement with the recent literature data obtained by including the GP effect only. Although not clearly understood, It is reiterated that the seam of CIs in H_3 occurs at the D_{3h} configuration whereas, the minimum energy path for the reactive scattering occurs at the collinear geometry. This is perhaps one of the reasons that the surface coupling effects are minor on the dynamics of this prototypical reaction despite the minimum energy path is expected to be less relevant for the higher collision energies considered here. The exact reason, however, remains to be uncovered.

References

[1] A.J.C. Varandas, F.B. Brown, C.A. Mead, D.G. Truhlar, N.C. Blais, J. Chem. Phys. 86 (1987) 6258.

[2] R.T. Pack, J. Chem. Phys. 60 (1974) 633; P. McGuire, D.J. Kouri, J. Chem. Phys. 60 (1974) 2488.

[3] J. Vaníček, W.H. Miller, J.F. Castillo, F.J. Aoiz, J. Chem. Phys. 123 (2005) 054108.

[4] S.L. Mielke, K.A. Peterson, D.W. Schwenke, B.C. Garrett, D.G. Truhlar, J.V. Michael, M.-C. Su, J.W. Sutherland, Phys. Rev. Lett. 91 (2003) 063201.

[5] J.V. Michael, J.R. Fisher, J. Phys. Chem. 94 (1990) 3318.

[6] J.V. Michael, J. Chem. Phys. 92 (1990) 3394.

[7] T.J. Park, J.C. Light, J. Chem. Phys. 96 (1992) 8853.

[8] T.J. Park, J.C. Light, J. Chem. Phys. 94 (1991) 2946.

[9] A.A. Westenberg, N. De Haas, J. Chem. Phys. 47 (1967) 1393.

[10] A. Farkas, L. Farkas, Proc. R. Soc. London A 152 (1935) 124.

[11] A. Thiel, H. Köppel, J. Chem. Phys. 110 (1999) 9371.

[12] S. Mahapatra, H. Köppel, Phys. Rev. Lett. 81 (1998) 3116; S. Mahapatra, H. Köppel, J. Chem. Phys. 109 (1998) 1721.

[13] H. Köppel, J. Gronki, S. Mahapatra, J. Chem. Phys. 115 (2001) 2377.

[14] B. Jayachander Rao, R. Padmanaban, S. Mahapatra, Chem. Phys. 333 (2007) 135.

[15] G.W. Johnston, B. Katz, K. Tsukiyama, R. Bersohn, J. Phys. Chem. 91 (1987) 5445.

[16] S. Sukiasyan, H.-D. Meyer, J. Phys. Chem. A 105 (2001) 2604.

[17] F.J. Aoiz, L. Bañares, V.J Herrero, V.S. Rãbanos, I. Tanarro, J. Phys. Chem. A 101 (1997) 6165.

[18] S.L. Mielke, D.G. Truhlar, J. Phys. Chem. 98 (1994) 1053.

[19] Rui-Feng Lu, Tian-Shu Chu, Yan Zhang, Ke-Li Han, A.J.C Varandas, John Z.H. Zhang, J. Chem. Phys. 125 (2006) 133108.

[20] Z. Xu, M. Baer, A.J.C. Varandas, J. Chem. Phys. 112 (2000) 2746.

[21] S. Hochman-Kowal, A. Persky, Chem. phys. 222 (1997) 29.

Chapter 4

Nuclear motion on the orbitally degenerate electronic ground state of D_3

4.1 Introduction

The nuclear dynamics of D_3, when prepared in the immediate neighborhood of the seam of CIs of its degenerate electronic ground state, is presented and discussed in this chapter. The theoretical framework is designed to mimic the optical emission experiment of the Rydberg excited D_3 [1, 2] (more details are presented in section 1.2.1). The observed experimental band is reproduced in Fig. 4.1 from Ref. [1]. The two humps in this bimodal emission profile have been established to originate from the lower and upper adiabatic sheets of the Jahn-Teller (JT)-split degenerate ground electronic manifold of D_3. Keeping this reference experimental emission spectrum in mind the specific details of various terms which constitute the complete nonadiabatic coupling (NAC) of the two surfaces are examined here.

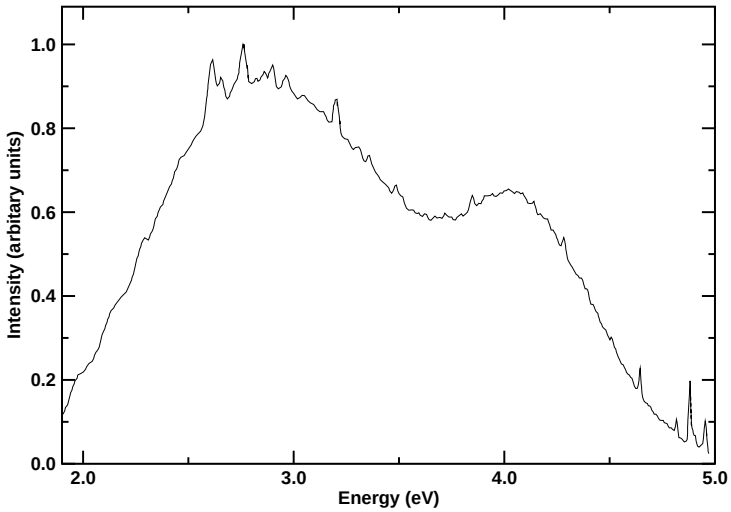

Figure 4.1: Experimentally recorded optical emission spectrum of Rydberg-excited D_3 reproduced from Fig. 1(a) of Ref. [1].

To this effort, the important GP and diagonal BH corrections are incorporated in the single surface BO Hamiltonian and the results are compared with those obtained from coupled JT-split surfaces. It is finally established in relation with the experimental findings that the broadening mechanisms of the observed bands due to the lower and upper adiabatic sheet are different. While the highly repulsive nature of the lower adiabatic sheet quickly drags the wave packet (WP) to the collinear minimum energy path that leads to dissociation, occurrence of the energetic minimum of the seam of CIs at the equilibrium minimum of the upper adiabatic sheet compels the WP to undergo extremely fast nonradiative relaxation to the lower sheet. The findings on the details of the broadening of the band due to the upper adiabatic sheet enable us to conclude that the GP and BH corrections to the adiabatic BO Hamiltonian are certainly minor when compared to the effects due to the rest of the complete NAC term. The GP and BH corrections only contribute to the shift of the maximum of the spectral

envelope in the energy axis (also the former alters the symmetry designation of energy levels), however, the detailed fine structure of the observed band can only be explained when the coupling due to the two surfaces is explicitly taken into account, which includes the GP, BH and the other off-diagonal terms of the NAC operator in a coherent fashion.

4.2 General considerations

The electronic ground state of D_3 remains degenerate along the coordinate of the symmetric stretching (breathing) vibrational mode in the D_{3h} symmetry configurations. This electronic degeneracy is split upon distortion along the coordinates of the asymmetric stretching and the bending vibrational modes. In a general coupled state situation, the representation of nuclear Schrödinger equation in an adiabatic and diabatic basis is discussed in section 2.2. Now, for the present coupled two-states problem, there are issues extensively addressed and discussed in the literature. One of the early one is concerned with the phase change of the adiabatic electronic wavefunction on encircling odd number of times around an intersection of two electronic states [the configurations where $A^{(i)}_{nm} = \langle \phi_n(q;Q)|\nabla_i|\phi_m(q;Q)\rangle$ (cf. Eq. 2.2 exhibit a singularity)]. It follows from the work of Herzberg and Longuet-Higgins [3] that the adiabatic electronic wavefunctions assume the form (in a suitable polar coordinate ϕ encircling the intersections)

$$\begin{pmatrix} \Phi_1 \\ \Phi_2 \end{pmatrix} = \begin{pmatrix} \cos(\phi/2) & \sin(\phi/2) \\ -\sin(\phi/2) & (\cos\phi/2) \end{pmatrix} \begin{pmatrix} \Phi_1^0 \\ \Phi_2^0 \end{pmatrix}, \tag{4.1}$$

where Φ_1^0 and Φ_2^0 are the basis set components of the two adiabatic electronic states.

Now, it is clear (repeatedly addressed in the literature) that both the adiabatic electronic wavefunctions would change sign and become multivalued when ϕ goes from $0 \rightarrow 2\pi$ [3–5]. To retain the single-valued property of the total wavefunction Mead and Truhlar proposed the introduction of an additional phase factor $e^{il\frac{\phi}{2}}$ (l being an odd integer number), which effectively introduces a vector potential term, $-\frac{l}{2}\nabla\phi$, into the nuclear Hamiltonian [5]. Effect of inclusion of this phase correction into the single surface (excluding the coupling between surfaces) BO Hamiltonian $\mathcal{H}^{BO}$ ($= T_{nuc}(Q) + V(Q)$; cf. Eq. 2.1) has been studied in the literature extensively [6–15]. When the diagonal terms $B^{(i)}_{mm}$ ($= \langle\phi_m(q;Q)|\nabla_i^2|\phi_m(q;Q)\rangle$; cf. Eq. 2.2) are incorporated in $\mathcal{H}^{BO}$, this is referred to as BH Hamiltonian [16]. When the full Hamiltonian of Eq. 2.1 or equivalently of Eq. 2.4 is considered, it intrinsically includes both the above corrections and the derivative NAC between the states in a consistent fashion. In the following, the nuclear dynamics is examined in five different situations *viz.*, (1) considering only $\mathcal{H}^{BO}$, (2) including the GP corrections in $\mathcal{H}^{BO}$, (3) including the BH correction in $\mathcal{H}^{BO}$, (4) including both the GP and BH corrections in $\mathcal{H}^{BO}$ and finally (5) employing the full Hamiltonian of Eq. 2.4.

4.3 Theoretical and computational details

The theoretical formalism and computational approach to describe the nuclear motion around the D_{3h} equilibrium configurations of D_3 in its degenerate $2pE'$ electronic ground state is described in this section. The theoretical scheme is formulated in accordance with the optical emission experiment of Rydberg excited D_3, which directly probed the CIs of its degenerate electronic ground state [1,2]. In particular, the time evolution of the WP is monitored in both fully adiabatic

(also including GP and BH corrections) and nonadiabatic (two coupled states) situations. The impact of the GP and BH corrections and derivative (nonadiabatic) coupling terms on the eigenvalue spectrum and eigenvectors is examined in detail. The adiabatic electronic energies of the double many body expansion (DMBE) potential energy surface (PES) of Varandas and coworkers [17] are utilized in this study.

4.3.1 The $\mathcal{H}^{BO}$ in hyperspherical coordinates

The three-dimensional (3D) adiabatic BO Hamiltonian for the D_3 system in slightly modified version of Johnson's hyperspherical coordinates [18] as adapted by Varandas *et al.* [7] is given by

$$\begin{aligned}\mathcal{H}^{BO} &= -\frac{\hbar^2}{2\mu}\frac{1}{\rho^5}\frac{\partial}{\partial\rho}\rho^5\frac{\partial}{\partial\rho} - \frac{8\hbar^2}{\mu\rho^2}\frac{1}{sin\theta}\frac{\partial}{\partial\theta}sin\theta\frac{\partial}{\partial\theta} - \frac{2\hbar^2}{\mu\rho^2}\frac{1}{sin^2(\theta/2)}\frac{\partial^2}{\partial\phi^2} \\ &+ \frac{1}{\mu\rho^2}\Big[\frac{\hat{J}^2 - \hat{J}_z^2 + sin(\theta/2)[\frac{1}{2}(\hat{J}_+^2 + \hat{J}_-^2)]}{cos^2(\theta/2)} + \frac{\hat{J}_z^2}{2sin^2(\theta/2)}\Big] \\ &+ \frac{4i\hbar\hat{J}_z cos(\theta/2)(\partial/\partial\phi}{2\mu\rho^2 sin^2(\theta/2))} + V(\rho,\theta,\phi). \end{aligned} \tag{4.2}$$

In the above, θ and ϕ are related to the Smith-Whitten's (Θ, Φ) version [19] by the relations, $\theta = \pi - 4\Theta$ and $\phi = 2\pi - 2\Phi$, rather than by the Johnson's relations, $\pi/2 - 2\Theta$ and $\pi/2 - 2\Phi$ [18]. These conventions simplify the calculations as explained by Varandas and coworkers [7] and Billing and coworkers [20]. It should be recalled that the coordinates ρ, θ, ϕ determine the size (ρ) and shape (θ, ϕ) of the molecular triangle. The Euler angles α, β, γ determine the absolute orientation of the triangle in a space-fixed (SF) system. The operators $\hat{J}_x$, $\hat{J}_y$ and $\hat{J}_z$ describe the components of total angular momentum in the body-fixed (BF) frame and $\hat{J}_\pm$ are the raising and lowering operators defined in the usual way,

i.e., $\hat{J}_x \pm i\hat{J}_y$. The quantity $V(\rho,\theta,\phi)$ is the adiabatic potential energy of a given electronic state. In the above Hamiltonian, the differential term in the variable ρ can be simplified further by defining a transformed nuclear wavefunction $\chi = \rho^{5/2}\chi\prime$ [21]. This transformation yields the time dependent Schrödinger equation (TDSE) for χ as

$$\begin{aligned} i\hbar\frac{\partial\chi}{\partial t} &= \Big[-\frac{\hbar^2}{2\mu}\frac{\partial^2}{\partial\rho^2} - \frac{8\hbar^2}{\mu\rho^2}\frac{1}{sin\theta}\frac{\partial}{\partial\theta}sin\theta\frac{\partial}{\partial\theta} - \frac{2\hbar^2}{\mu\rho^2}\frac{1}{sin^2(\theta/2)}\frac{\partial^2}{\partial\phi^2} \\ &+ \frac{1}{\mu\rho^2}\Big[\frac{\hat{J}^2 - \hat{J}_z^2 + sin(\theta/2)[\frac{1}{2}(\hat{J}_+^2 + \hat{J}_-^2)]}{cos^2(\theta/2)} + \frac{\hat{J}_z^2}{2sin^2(\theta/2)}\Big] \\ &+ \frac{4i\hbar\hat{J}_z cos(\theta/2)(\partial/\partial\phi}{2\mu\rho^2 sin^2(\theta/2))} + V(\rho,\theta,\phi) + \frac{15\hbar^2}{8\mu\rho^2}\Big]\chi. \end{aligned} \tag{4.3}$$

Following the earlier prescription, the physical wavefunction of the system can be expressed as [22, 23]

$$\chi^J_{K,M}(\rho,\theta,\phi,\alpha,\beta,\gamma) = \sum_{J,M}\sum_{K=-J}^{J}\sqrt{\frac{2J+1}{8\pi^2}}\chi^J_{K,M}(\rho,\theta,\phi)D^{J*}_{MK}(\alpha,\beta,\gamma), \tag{4.4}$$

where J, M, K represent the total angular momentum, its projection on a SF $Z-$axis and BF $Z-$axis, respectively, and D^J_{MK} is the Wigner rotation matrix [24]. By substituting the wavefunction of Eq. 4.4 in Eq. 4.3, the effective Hamiltonian

operating on the wavefunction is obtained as [7],

$$\begin{aligned}\mathcal{H}^{BO} &= \Big\{-\frac{\hbar^2}{2\mu}\frac{\partial^2}{\partial\rho^2} - \frac{8\hbar^2}{\mu\rho^2}\frac{1}{sin\theta}\frac{\partial}{\partial\theta}sin\theta\frac{\partial}{\partial\theta} - \frac{2\hbar^2}{\mu\rho^2 sin^2(\theta/2)}\frac{\partial^2}{\partial\phi^2} \\ &+ \frac{\hbar^2[J(J+1)-K^2]}{\mu\rho^2 cos^2(\theta/2)} + \frac{\hbar^2}{2\mu\rho^2 sin^2(\theta/2)}\Big[K^2 + 4Kicos(\theta/2)\frac{\partial}{\partial\phi}\Big] \\ &+ V(\rho,\theta,\phi) + \frac{15\hbar^2}{8\mu\rho^2}\Big\}\delta_{K,K'} + \Big\{\frac{\hbar^2 sin(\theta/2)}{2\mu\rho^2 cos^2(\theta/2)} \\ &\times \sqrt{(J\pm K)(J\pm K+1)(J\pm K-1)(J\pm K+2)}\Big\}\delta_{K,K'_{\pm 2}}. \qquad (4.5)\end{aligned}$$

4.3.2 Initial wavefunction and eigenvalue spectrum

The initial wavefunction (at time t=0) pertinent to the n=3 Rydberg electronic state of D_3 in the mass-weighted normal coordinates can be written as [25]

$$\chi(q_0, r, t=0) = Ne^{-\frac{\mu\omega_A q_0^2}{2\hbar}}e^{-\frac{\mu\omega_E r^2}{2\hbar}}, \qquad (4.6)$$

where N is the normalization constant, ω_A = 2301.2 cm^{-1}, and, ω_E = 1833.3 cm^{-1} are the frequencies of the symmetric stretching (breathing) and degenerate (asymmetric stretching and bending) vibrational modes, respectively [26]. Here q_0 and r $(= \sqrt{q_1^2 + q_2^2})$ represent the mass-weighted normal coordinates for the breathing and degenerate vibrational modes, respectively. These normal coordinates in terms of the three internuclear distances (r_1, r_2, r_3) are obtained by the FG-matrix method of Wilson *et al* as [27]

$$
\begin{aligned}
q_0 &= \frac{1}{3}[(r_1 - r_1^0) + (r_2 - r_2^0) + (r_3 - r_3^0)], \\
q_1 &= \frac{1}{3}[2(r_3 - r_3^0) - (r_1 - r_1^0) - (r_2 - r_2^0)], \\
q_2 &= \frac{1}{\sqrt{3}}[(r_2 - r_2^0) - (r_1 - r_1^0)], \qquad (4.7)
\end{aligned}
$$

where $r_1^0 = r_2^0 = r_3^0$ (=1.642 bohr [28]) is the distance representing the D_{3h} configuration of D_3 at the minimum of the seam of the CIs. While q_1 and q_2 represent the Cartesian components of the degenerate vibration, r defines the magnitude of this vibration in polar coordinate frame, defined as, $q_1 = rsin\varphi$ and $q_2 = rcos\varphi$. The angle φ defines the direction of the degenerate vibration. This is the pseudorotation angle that encircles the CIs at the D_{3h} symmetry configuration of D_3 and can be equated with the hyperangle introduced above, $0 \leq \phi \leq 2\pi$. The following set of equations [7, 18] establish the transformation between the internal coordinates and the hyperspherical coordinates in order to determine q_0, q_1 and q_2.

$$
\begin{aligned}
r_1^2 &= \frac{1}{2}d_2^2\rho^2[1 + sin(\theta/2)cos(\phi)], \\
r_2^2 &= \frac{1}{2}d_3^2\rho^2[1 + sin(\theta/2)cos(\phi - \delta_3)], \\
r_3^2 &= \frac{1}{2}d_1^2\rho^2[1 + sin(\theta/2)cos(\phi + \delta_2)], \qquad (4.8)
\end{aligned}
$$

where $d_k^2 = \frac{m_k}{\mu}(1 - \frac{m_k}{m_1+m_2+m_3})$, $\mu^2 = \frac{m_1m_2m_3}{m_1+m_2+m_3}$, $\delta_2 = 2tan^{-1}(\frac{m_2}{\mu})$, $\delta_3 = 2tan^{-1}(\frac{m_3}{\mu})$ and m_k is the mass of the atom k.

The above initial wavefunction (cf., Eq. 4.6) is subjected to a Franck-Condon transition to the degenerate electronic ground state of D_3. To monitor the nuclear

Table 4.1: Numerical grid parameters and properties of the initial wavefunction used in the present study.

Parameter	Value	Description
$N_\rho/N_\theta/N_\phi$	128/31/128	Number of grid points
ρ_{min}/ρ_{max} (a_0)	0.5/14.0	Extension of the grid along ρ
ϕ_{min}/ϕ_{max} (rad)	$0/2\pi$	Extension of the grid along ϕ
ρ_{mask} (a_0)	12.43	Starting point of the masking function
Δt (fs)	0.1348	Length of the time step used in the WP propagation
T (fs)	1104.0/276.0	Total propagation time for uncoupled and coupled state calculations

motion on the latter state the TDSE is numerically solved on a grid constructed in the (ρ, θ, ϕ) coordinate space. The time-dependent version of the golden rule expression is used to calculate the spectral intensity, $I(E)$. This can be equated with the Fourier transform of the time autocorrelation function, $C(t)$, of the WP evolving on the final electronic state using Eq. 2.75. For time-independent Hamiltonian operator and real initial WPs, the autocorrelation function for time $2t$, $C(2t)$ is obtained by the useful Eq. 2.76 [31, 32]. The locations of the peak maximum in the spectral intensity give the energy eigenvalues and the corresponding stationary state eigenfunctions can be obtained by projecting the time evolved WP onto the desired eigenstate of energy, E_n, using Eq. 2.77 [33].

The action of the time-evolution operator, $\exp\left[\frac{-i\hat{H}t}{\hbar}\right]$, in Eq. 2.7 is carried out by dividing the total propagation time t into N steps of length $\triangle t$. The exponential operator at each time step is then approximated by a second-order split-operator method [33]. The first derivative and second derivative terms in ρ and ϕ in Eq. 4.5 are evaluated using the fast Fourier transform (FFT) method [34] and the kinetic energy operator in θ is evaluated using a Gauss-Legendre quadrature based discrete variable representation (DVR) [35] method. To avoid

unphysical reflections of WP at the grid boundaries, it is multiplied by a damping function [36] $f(\rho_i) = \sin\left[\frac{\pi}{2}\frac{(\rho_{mask}+\Delta\rho_{mask}-\rho_i)}{\Delta\rho_{mask}}\right]$ for $\rho_i \geq \rho_{mask}$, at each time step. Here ρ_{mask} is the point at which the damping function is initiated and $\Delta\rho_{mask}(= \rho_{max} - \rho_{mask})$ is the width of ρ over which the function decays from 1 to 0. All calculations are performed within the centrifugal sudden approximation [37, 38] neglecting the Coriolis coupling (CC) term (the last term in Eq. 4.5) of the Hamiltonian. The convergence of each calculation is checked with respect to the choice of the numerical grid parameters given in table 4.1.

4.3.3 Inclusion of GP and BH corrections

Mead and Truhlar [5] proposed that the multiplication of the adiabatic electronic wavefunction by a complex phase factor $e^{i\alpha\eta}$ corrects for the GP change where $\alpha = \frac{1}{2}, \frac{3}{2}, \ldots$ and η is any parameter such that wavefunction encircles CIs when it goes from 0 to 2π. In hyperspherical coordinates η is independent of ρ but is a function of θ and ϕ. For a system of three equal masses like the one considered here η is equivalent/equal to the hyperangle ϕ (see Appendix-A). Introduction of this phase factor therefore, changes the derivative terms, $\frac{\partial}{\partial\phi} \rightarrow \frac{\partial}{\partial\phi} + i\alpha$, and, $\frac{\partial^2}{\partial\phi^2} \rightarrow \frac{\partial^2}{\partial\phi^2} + 2i\alpha\frac{\partial}{\partial\phi}$ - α^2, in the nuclear kinetic energy operator of the effective Hamiltonian of Eq. 4.5. A choice of, α=$\frac{3}{2}$, is more convenient to retain the permutation symmetry of a system involving three identical nuclei like D_3 [5]. Numerical implementation of these changes can be easily achieved by the revised FFT method outlined by Billing and Marković [22]. In this method, a simple modification in evolution of the kinetic operator in ϕ corrects the GP change. In contrast to the normal procedure, the wavefunction is first multiplied with $e^{-i\alpha\phi}$ and then Fourier transformed to obtain the wavefunction in the momentum space. The transformed wavefunction is then multiplied by $i(-k+\alpha)$ and $-(-k+\alpha)^2$,

respectively, (these momentum eigenvalues differ from that in ref. [22] as a slightly different convention in the discrete FFT equations as given in Appendix-B) is used here, to obtain the first and second derivative terms in ϕ. In the normal procedure they are, respectively, multiplied by momentum eigenvalues ik and $-k^2$. Finally the wavefunction is back transformed and multiplied with $e^{i\alpha\phi}$ to ensure the phase correction [22].

The BH diagonal correction can easily be obtained using the mass-weighted coordinate r (within a linear coupling approximation) as [39, 40]

$$\Lambda^{\circ} = \frac{\hbar^2}{8m_D r^2}, \tag{4.9}$$

where m_D is the mass of the atom D. As this term does not contain any differential operator, inclusion of BH involves just addition of this term to the adiabatic potential energy.

4.3.4 Coupled surface treatment

As stated in section 2.2, to avoid the singular behavior of the derivative coupling elements at the intersections of the electronic states The diabatic ansatz of Eq. 2.4 is used here, for the coupled states treatment of the nuclear dynamics. In this case, however, the initial WP is prepared on the realistic adiabatic representation and the diabatic ansatz is utilized for its propagation on the grid only. The final analysis can be carried out in both the representations and they yield the same results [41]. In the diabatic representation the Hamiltonian can be expressed in the form

$$H^d = T_N \begin{pmatrix} 1 & 0 \\ 0 & 1 \end{pmatrix} + \begin{pmatrix} U_{11} & U_{12} \\ U_{21} & U_{22} \end{pmatrix}, \tag{4.10}$$

where the nuclear kinetic energy operator in hyperspherical coordinates is given by the terms in the right hand side of Eq. 4.5 except the potential energy term $V(\rho, \theta, \phi)$.

The elements of the diabatic electronic matrix of Eq. 4.10 can be obtained by utilizing the $\mathbf{S}$ matrix of Eq. 2.6 as [40, 41]

$$\begin{aligned}
\begin{pmatrix} U_{11} & U_{12} \\ U_{21} & U_{22} \end{pmatrix} &= \mathbf{S} \begin{pmatrix} V_- & 0 \\ 0 & V_+ \end{pmatrix} \mathbf{S}^\dagger \\
&= \frac{V_- + V_+}{2} \mathbf{1} + \frac{V_+ - V_-}{2} \begin{pmatrix} -\cos\phi & \sin\phi \\ \sin\phi & \cos\phi \end{pmatrix}, \quad with \qquad (4.11) \\
\mathbf{S} &= \begin{pmatrix} \cos\zeta & \sin\zeta \\ -\sin\zeta & \cos\zeta \end{pmatrix}. \qquad (4.12)
\end{aligned}$$

Here $\phi = 2\zeta$ (within a linear coupling approximation [39]) is the pseudorotation angle which is also equivalent to the angle ϕ in hyperspherical coordinates (cf., Appendix-A) and V_- and V_+ represents the two adiabatic PESs. It is important to note that in contrast to the adiabatic electronic states the diabatic states are not unique. This is primarily due to the non-uniqueness of the NAC terms for different choice of electron coordinates (see Ref. [42]). It is gratifying to state that the diabatization method employed above has been well tested [39] and found to eliminate the leading singular derivative coupling terms of the NAC operator.

4.4 Results and discussion

) The dynamical outcomes of the nuclear wavefunction, pertinent to the n=3 Rydberg electronic state of D_3, upon a Franck - Condon transition to its 2pE' electronic ground state are presented and discussed here. Dynamical calculations considering both the sheets of this degenerate electronic PES explicitly are designated as coupled surface calculations whereas, calculations considering the lower adiabatic sheet of this PES are termed as uncoupled surface calculations. The latter are repeated by including (1) geometric phase (GP) correction, (2) diagonal Born-Huang (BH) correction, (3) both GP and BH corrections to the Born-Oppenheimer (BO) adiabatic Hamiltonian.

In order to clearly reveal the nuclear motion around the CIs, a movie showing the time-evolution of the WP probability density, $\frac{1}{32}\int|\chi(t)|^2 d\rho sin\theta d\theta d\phi$, is prepared. At each time step the value of ρ at the maximum of WP probability density is calculated and at this value of ρ equally spaced contours of WP probability density and potential energy are plotted in the $(X=\rho\frac{\theta}{2}sin\phi, Y=\rho\frac{\theta}{2}cos\phi)$ plane. Such a representation of the PESs proposed by Kuppermann and coworkers [43] and later revised by Varandas and coworkers [44] and also by Kuppermann and co-workers [45] provides an elegant way to portray the nuclear motion around CIs.The coordinates used above correspond to the modified Johnson's hyperspherical coordinates [18] as adapted by Varandas and coworkers [7] introduced in section 4.3.1. The entire set of these WP probability density evolution movies can be downloaded from the web (http://chemistry.uohyd.ernet.in/~sm/SMGID/animation.html). A few important snapshots are presented later in order to facilitate the discussion on the dynamical observables.

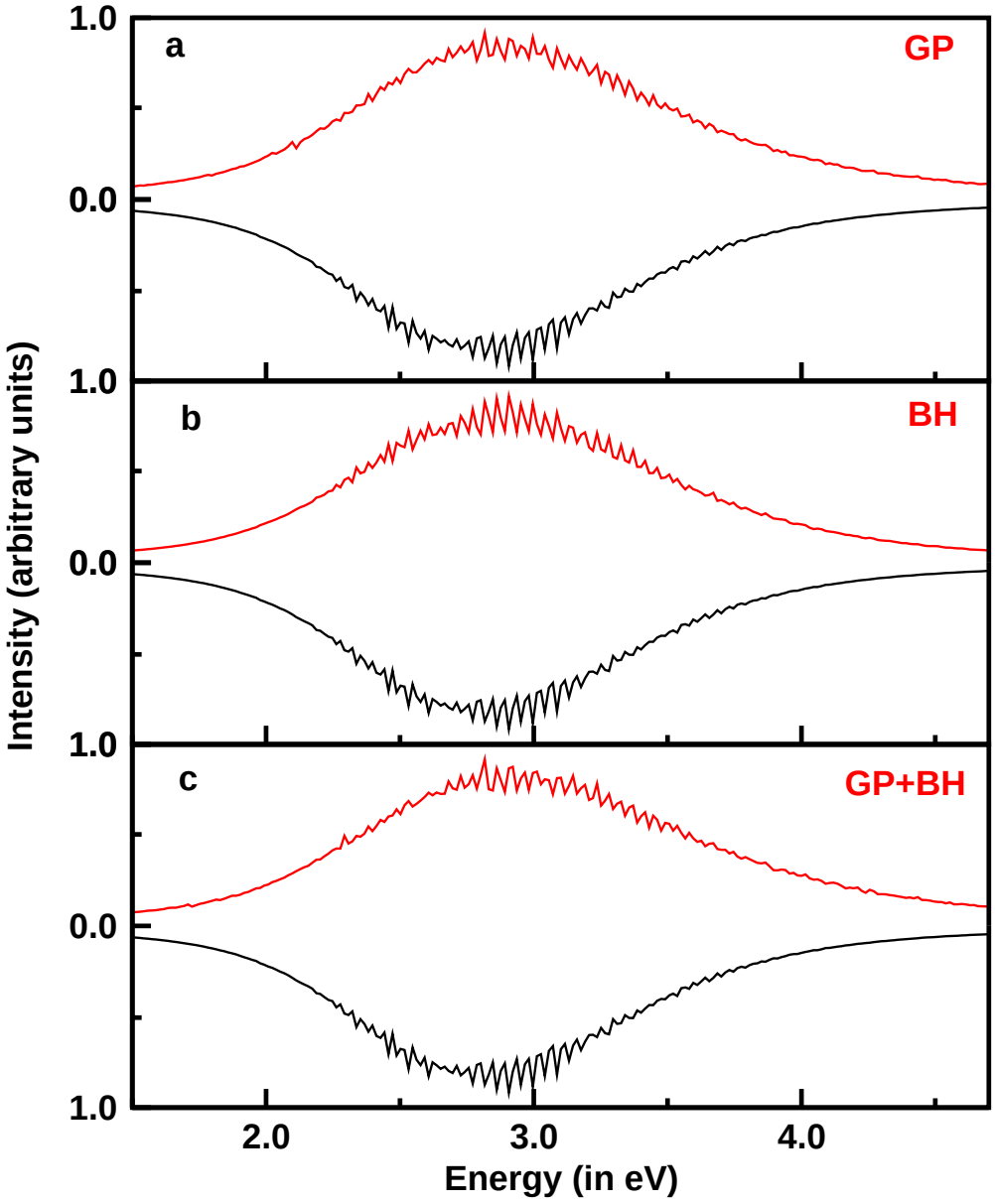

Figure 4.2: The emission profile of D_3 from the n=3 Rydberg electronic state to its lower adiabatic electronic states of the $2pE'$ ground electronic manifold. Here, emission profiles calculated without the inclusion of GP and BH corrections are plotted in the inverted Y-axis and in black color whereas, the profiles with inclusion of GP or BH or both GP and BH corrections are plotted in the normal Y-axis and shown in red color.

4.4.1 Effects of the GP and BH correction

The Rydberg (n=3) emission spectrum of D_3 for a transition to the lower adiabatic electronic sheet of its $2pE'$ ground electronic manifold obtained from the present theoretical study is plotted in Figs. 4.2 (a-c). In all the panels, emission profile calculated without the inclusion of GP and BH corrections and using the BO adiabatic Hamiltonian are plotted in the inverted Y-axis and shown in black color. The emission profiles including either GP or BH corrections or both GP plus BH corrections are plotted in the normal Y-axis and shown in red color. Throughout the paper intensity of the emission profiles are scaled to unity for a better comparison of various results and are given in arbitrary units. It can be seen from the Figs. 4.2(a-c) that the inclusion of GP or BH corrections or both GP plus BH corrections has no significant effect on the broadening of the spectral envelope and hence the lifetime of the eigenstates participating in it. The position of the maximum of the envelope, however, is shifted slightly towards the higher energy side. The spectra in Figs. 4.2(a-c) are very broad and diffuse and can be related to the highly repulsive nature of the lower adiabatic sheet which drives the WP quickly to the reactive and nonreactive channels.

Further, to shed light on the nuclear dynamics on the lower adiabatic sheet of the $2pE'$ ground electronic manifold, a few snapshots of the WP evolution movie (mentioned above) recorded at time 0.944 fs, 7.824 fs and 10.792 fs only are shown in Fig. 4.3. In this figure the panels (a-c) and (d-f), respectively, correspond to the evolution of the WP without and with the inclusion of GP correction. In these plots the center of the circle corresponds to the D_{3h} configuration of D_3 (*i.e.*, CIs geometry) where $\theta = 0°$. As one moves along the radius of the circle θ increases and D_3 approaches to the linear geometries. At the periphery $\theta =$

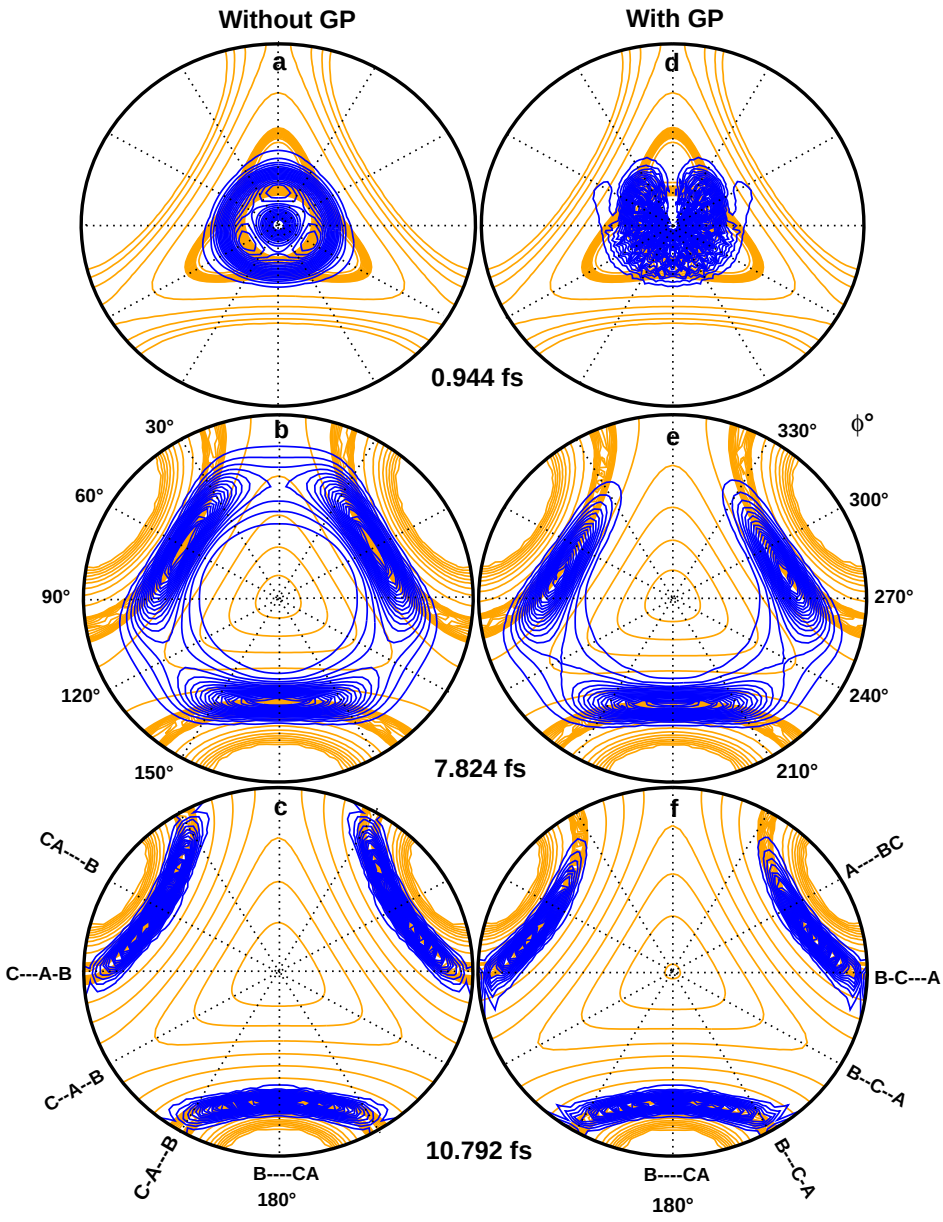

Figure 4.3: Snapshots of the WP probability density (equatorial view) during its evolution on the lower adiabatic sheet of the $2pE'$ electronic ground manifold of D_3 at times mentioned above. Contour lines in orange and blue colors, respectively, correspond to the PES and WP probability density. Panels a-c and d-f, receptively, correspond to the uncoupled state calculations without and with GP corrections.

Table 4.2: Energy values (in eV) at peak maximum of the spectrum in Figs. 4.4(a-c).

Peak No.	Without GP & BH (1)	With GP (2)	With BH (3)	With GP & BH (4)	(2)-(1)	(4)-(1)
1	3.512	3.676	3.678	3.794	0.164	0.282
2	3.663	3.821	3.822	3.935	0.158	0.272
3	3.807	3.959	3.961	4.068	0.152	0.261
4	3.942	4.088	4.090	4.191	0.146	0.249
5	4.071	4.210	4.212	4.309	0.139	0.238
6	4.193	4.324	4.326	4.416	0.131	0.223

180°, which defines the collinear geometry of D_3 and various dissociation channels (reactive and nonreactive) appear in this geometry. Note that the 'broken' line in the ABC combinations refer to the bond that ruptures while the solid line indicates the bond that forms during the unimolecular evolution of ABC on the lower adiabatic surface. It can be seen from the plots that the WP enters these fragmentation channels in about ~ 10 fs in both (with and without GP) the cases. This is because the lower adiabatic sheet is highly repulsive and quickly drives the WP to these channels as the minimum energy path occurs at the collinear arrangements of the three nuclei. As expected, the inclusion of GP correction introduces a nodal line (clearly seen in panel d) along the intersection seam, which prevents the WP to encircle the CIs and changes its phase, as a result the total (electronic *times* nuclear) wavefunction retains its single-valued property.

The emission profile of Rydberg-excited D_3 for a transition to the upper adiabatic sheet of its $2pE'$ ground electronic manifold is shown in Figs. 4.4(a-c). As in case of Fig. 4.2, the spectrum calculated without the GP and BH corrections is shown in the inverted Y- axis (in black color), whereas, the spectrum obtained with these corrections is shown in red color in the normal Y- axis. The upper

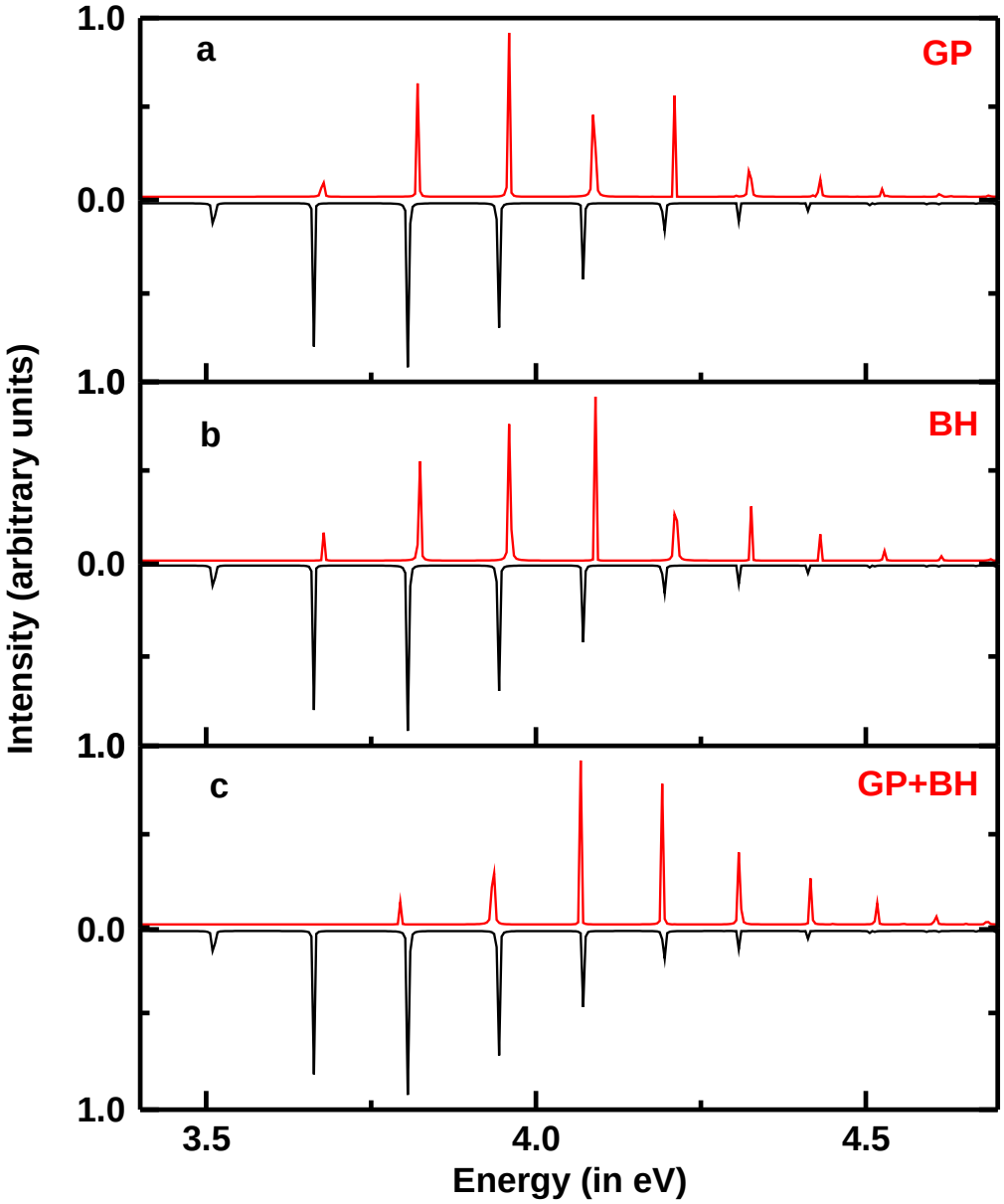

Figure 4.4: Same as in FIG. 4.2 but for a transition to the upper adiabatic sheet of the $2pE'$ electronic manifold of D_3.

adiabatic cone of D_3 is bound in nature in the absence of explicit coupling with its lower repulsive sheet. The emission spectrum in Fig. 4.4 therefore portrays the discrete vibrational level structure in this case. It can be seen from these figures that the sharp vibrational structures remain unaltered when the GP and BH corrections are included. The maximum of each peak, however, shifts significantly to the higher energy. This is in contrast to the results of Fig. 4.2, where the energy shift is not very significant. To make a better comparison, the energy eigenvalues of the first six peaks of the emission profiles of Figs. 4.4(a-c) are tabulated and shown in Table. 4.2. It can be seen from the table that inclusion of GP and BH corrections shifts the peaks towards higher energy side by almost the same magnitude ($\sim$ 0.15 eV). When both corrections are included the magnitude of the shift nearly doubles ($\sim$ 0.26 eV). Moreover, the magnitude of this shift decreases as one moves from peak 1 to peak 6 (as shown in column 6 and 7 of Table 4.2). This reveals that the lower vibrational levels supported by the upper adiabatic electronic sheet are severely affected by the GP or BH corrections when compared to the energetically higher ones. This is because the energetic minimum of the upper adiabatic sheet coincides with the minimum of the seam of CIs at $\sim$ 2.74 eV and the lower vibrational levels are closer to this minimum. As discussed in Chapter 2 that the inclusion of the GP correction introduces an additional angular momentum term in the effective Hamiltonian. Contribution of this term causes a shift of the energy eigenvalue. The BH term, on the other hand, is like any other centrifugal term causes an effective decrease of the depth of the well (see additional information at end of this chapter for more details) of the upper adiabatic sheet by $\sim$0.32 eV. This results into a shift of the vibrational energy eigenvalues.

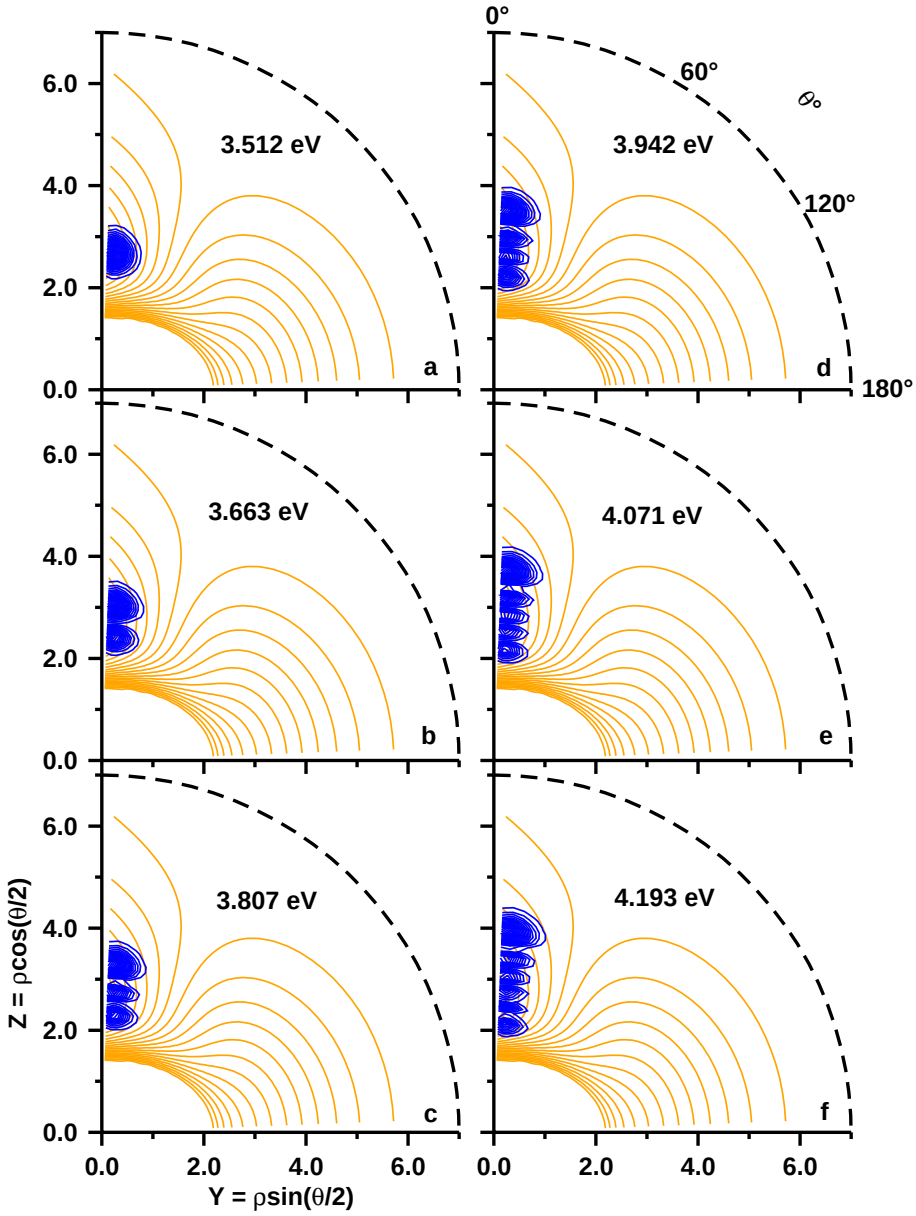

Figure 4.5: Six lowest eigenstates supported by the upper adiabatic sheet of D_3 without the inclusion of GP and BH corrections. The contours of the eigenfunctions are superimposed on the potential energy contours for $\phi = 0$ corresponding to the c_{2v} geometry of D_3. The energy eigenvalue of these functions is given in corresponding panel. Contour lines in orange and blue colors, respectively, corresponds to the PES and WP probability density.

The eigenfunctions corresponding to the first six peaks of Fig. 4.4(a-c) are shown in Figs. 4.5(a-f). Equally spaced probability density contours of the eigenfunctions superimposed on equally spaced contours of the upper adiabatic PES for the c_{2v} geometry (for $\phi = 0$) are shown in Figs. 4.5(a-f). The energy eigenvalue of each eigenfunction is indicated in the respective panel. In the above, the coordinates (Y=$\rho sin(\theta/2)$, Z=$\rho cos(\theta/2)$) are obtained by mapping hyperspherical coordinates to Cartesian coordinates for $\phi = 0$ [18, 43]. The eigenfunctions shown above are obtained without including the GP and BH corrections. Clearly, the number of nodes along ρ in the eigenfunctions increase from 0 to 5 as one moves from panel (a) to (f) as expected for the first six peaks of the emission spectrum of Fig. 4.4. The inclusion of GP or BH corrections or both has no noticeable effect on this eigenfunction pattern in the coordinate frame used above (see additional information at the end of the chapter for more details).

In Figs. 4.6(a-f), the eigenfunctions of the panel a and f, Fig. 4.5 are viewed in an equatorial plane, X=$\frac{\rho\theta}{2}\sin\phi$ and Y=$\frac{\rho\theta}{2}\cos\phi$, as defined by Kuppermann [43, 45]. In Fig. 4.6, the two panels at the top, middle and bottom represent the eigenfunctions obtained in the purely adiabatic BO situation (as in Fig. 4.5), by including the GP correction and by including the BH correction, respectively. As can be seen that the BH correction does not add any additional features to these eigenfunctions. As stated above, this correction shifts the energetic minimum of the PES uphill and therefore the eigenfunctions merely located at energetically higher potential energy contours. These eigenfunctions are single-valued and encircles the CIs in a close loop as is obvious from the plots. The total wavefunction is double-valued in this case owing to the double-valued nature of the adiabatic electronic wavefunction. The inclusion of the GP correction

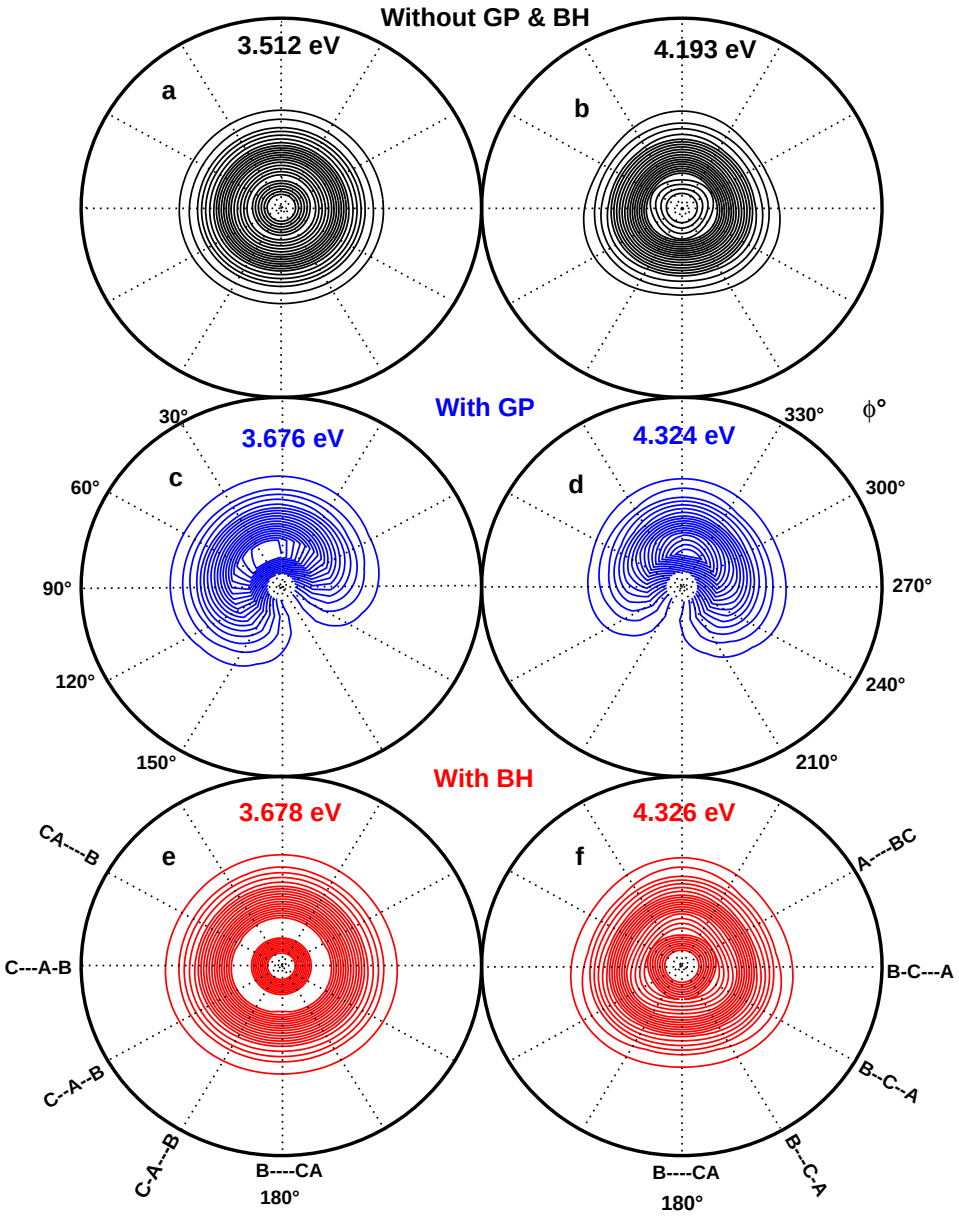

Figure 4.6: Equatorial view of the eigenfunctions of panels a and f of FIG. 4.5. Contours in black, blue and red color, respectively, correspond to the results obtained in the purely adiabatic BO situation, by including the GP correction and by including the BH correction. The energy eigenvalue of the eigenstate is given in each panel..

however, reveals dramatic changes in the overall features of these eigenfunctions as can be seen from plots given in the middle panels of Fig. 4.6. In this case the plane-wave components arising from vector potential term in the ∇^2 operator introduce interesting interference effects. The wavefunction components to the left and right of CIs experience opposite interference effects resulting into an overall destructive interference. This introduces the observed node along ϕ in the eigenfunction. Such effects on a bound JT system [46] as well as on a scattering problem [47] in two-dimensions have been discussed in the literature. Appearance of this additional node in the eigenfunction (which confirms the restoration of the single-valued nature of the total wavefunction) shifts its energy eigenvalue when compared to the purely BO case.

4.4.2 Effects of explicit surface(s) coupling

After analyzing the effects due to the "important" correction terms (*viz.*, the GP and BH) to H^{BO}, it is worthwhile to examine how the results presented above are modified when the two electronic surfaces are coupled explicitly! This exercise considers the complete Hamiltonian of Eq. 2.1 or equivalently Eq. 2.4. For the numerical computation, the adiabatic initial Rydberg WP (cf., Eq. 4.6) is subjected to a Franck-Condon transition to the adiabatic electronic sheets of the degenerate ground electronic manifold and then transformed to the diabatic electronic basis (as stated in chapter 2) and propagated thereafter in both space and time. Finally, the evolved WP is transformed back to the adiabatic electronic basis to analyze the final outcome. This follows naturally from the fact that an adiabatic basis is a realistic representation of the electronic state(s), while a diabatic electronic basis provides an interim solution to propagate the WP by avoiding the singularity of the interstate derivative coupling terms (cf., Eq. 2.2)

of the adiabatic electronic basis.

In Figs. 4.7(a-c) it is shown how the spectral features changes upon inclusion of the surface coupling, when the WP is launched on the lower adiabatic sheet of the ground electronic manifold of D_3. The results shown in previous figures including the GP and BH corrections are also presented again for clarity. In these figures the results obtained by including GP, BH and GP plus BH corrections are plotted in normal Y-axis, respectively, whereas, the result of coupled (CP) surface calculation is plotted in the inverted Y-axis. It can be seen that, there is no significant visible effects of the surface coupling (when compared with the results obtained with the GP and BH corrections) on the WP evolving on the lower adiabatic sheet of the ground electronic manifold of D_3. As mentioned above, this sheet is highly repulsive and quickly (within $\sim$ 10 fs) drags the WP into the dissociative channels. This time scale seems to be far shorter than that required for a single pseudo-rotation of the evolving WP around the conical intersections (CIs) at the D_{3h} symmetry configuration on the lower adiabatic sheet. Furthermore, the minimum energy path on this sheet for the D + D_2 reaction occurs at the collinear configurations of D_3. This outcome is on par with the earlier extensive research on the H + H_2 reactive dynamics [8–10,40,41,48–51]. It appears that the highly repulsive nature of the lower adiabatic sheet does not allow the WP for a pseudo-rotation around the CIs to have any observable consequence on its dynamical evolution on this sheet.

Contrary to the above, dramatic effects of the surface coupling can be seen when the WP is initially launched on the upper adiabatic sheet as depicted in Figs. 4.8(a-c). In these figures the broad envelope represents the vibronic energy level structure of the upper adiabatic sheet when its coupling to the lower sheet

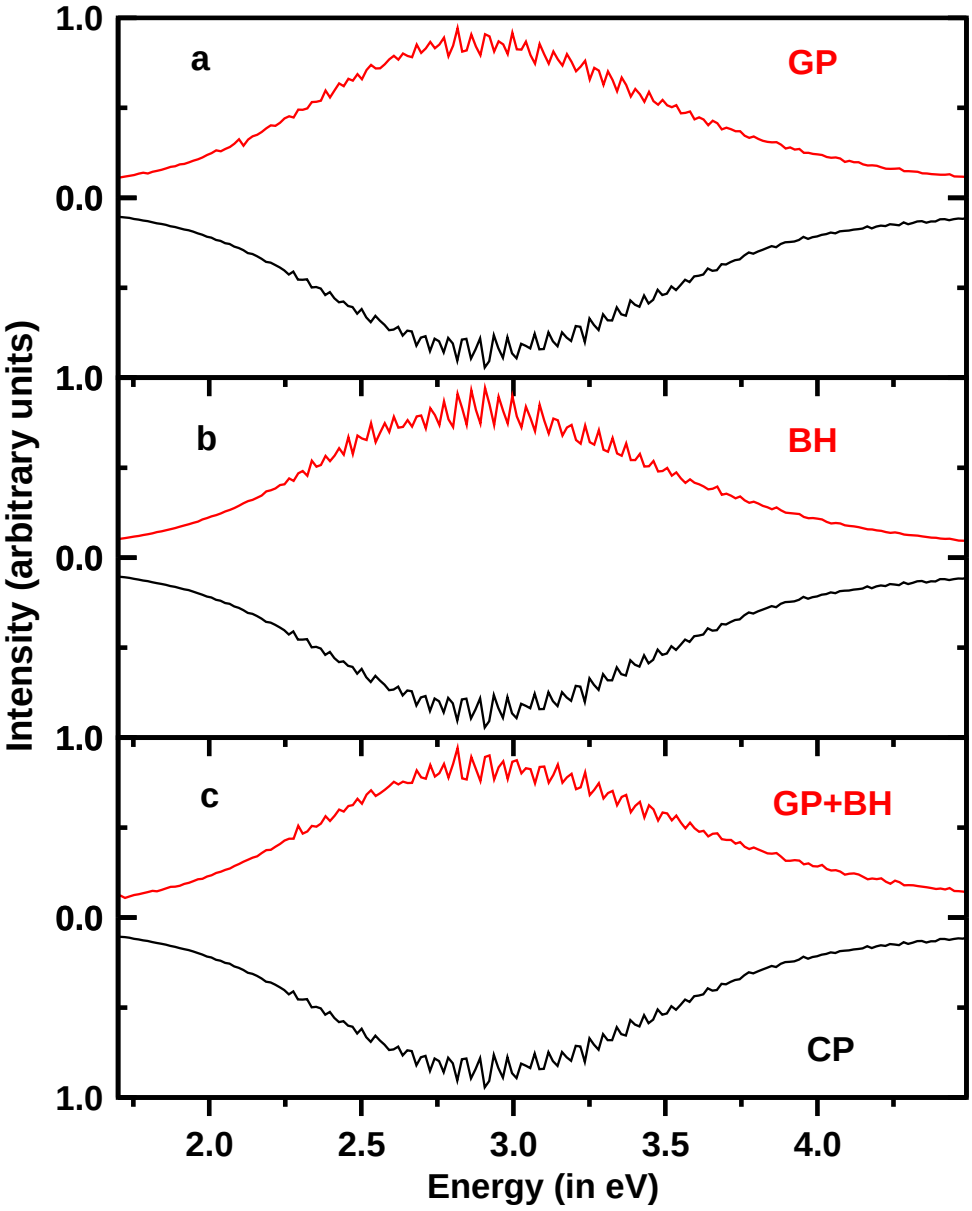

Figure 4.7: Same as in FIG. 4.2 and including also the complete surface coupling in the dynamics.

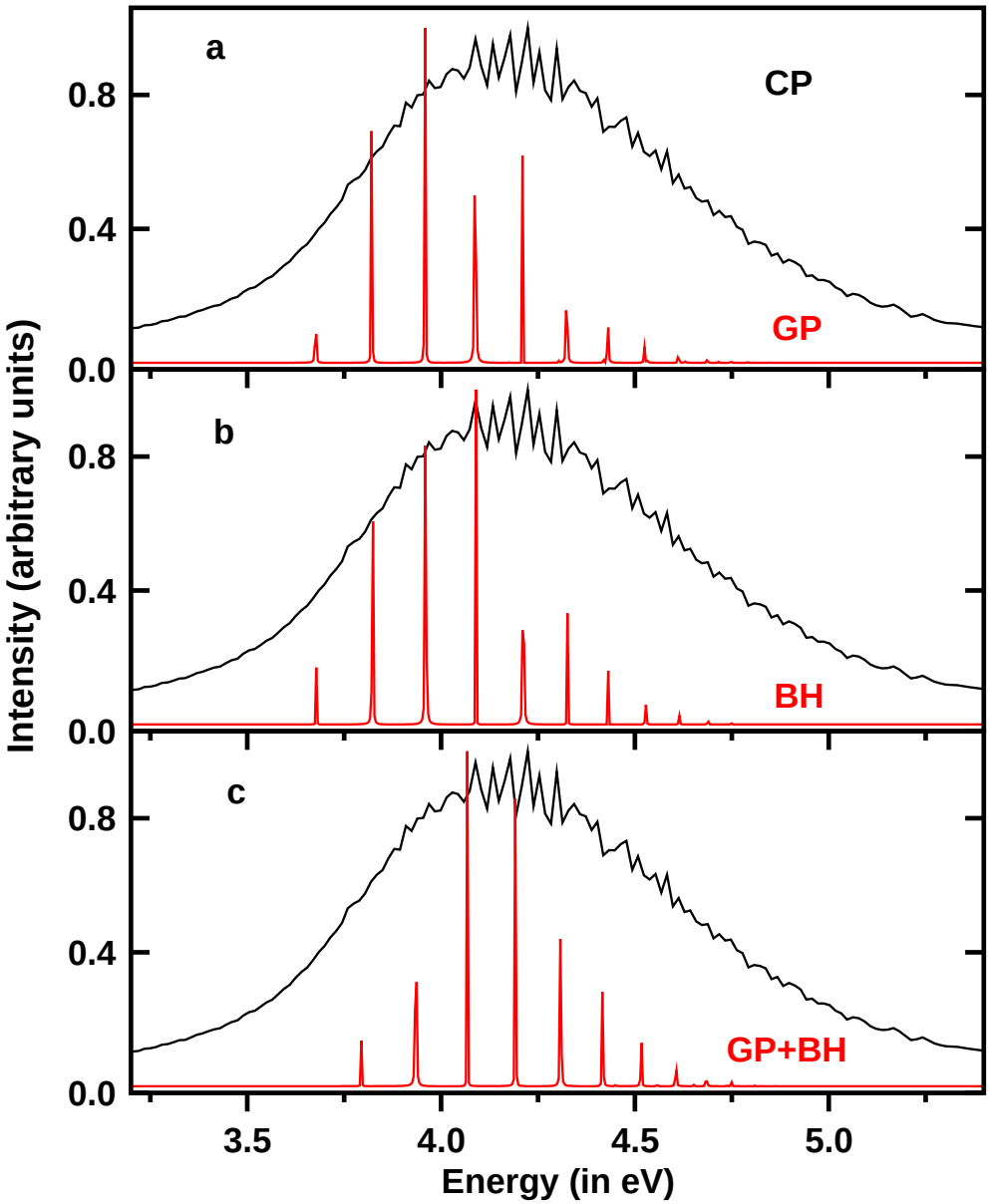

Figure 4.8: Same as in FIG. 4.4 and including also the complete surface coupling in the dynamics.

is explicitly included in the dynamics (cf., Eq. 2.4). The sharp line structures on the other hand represent uncoupled surface results including the GP and BH corrections as given in Figs. 4.4(a-c). It can be immediately seen that neither the GP nor the BH correction contributes to the huge broadening of the spectrum of this adiabatic sheet! Therefore, it is clear that this broadening solely originates from the off-diagonal derivative coupling terms of the nonadiabatic coupling operator of Eq. 2.2. Furthermore, it is important to note that neither the GP nor the BH correction alone could place the maximum (center-of-gravity) of the exact spectral envelope at the right energy eigenvalue. It can be seen from panel c that a combined contribution from the GP plus BH correction is required to obtain this maximum at the right place. This concludes that, with inclusion of both the GP and BH corrections, the shape of the spectral peaks remains unaffected however, their energy eigenvalue is altered. Additionally, the symmetry properties of the eigenstates also change upon inclusion of GP corrections as already discussed in the literature [6,52,53]. It is worthwhile to add that, Alijah and Varandas [53] have extended Watson's formalism [54] to describe the symmetry properties and designation of the rovibrational levels of the upper adiabatic cone by taking the GP effects into account. It is shown that the levels are described by a half-integer quantum number when the GP effects are considered.

The effect of complete surface coupling and the GP on the dynamics of the upper adiabatic sheet is demonstrated in Fig. 4.9. Wherein, the time evolution of the nuclei is presented in terms of the probability density plot of the WP in the equatorial plane as defined above. The panels in the left (a-c) and right (d-f) column of the figure represent the evolution of the WP including the surface coupling and the GP correction, respectively. It can be seen that in both the cases

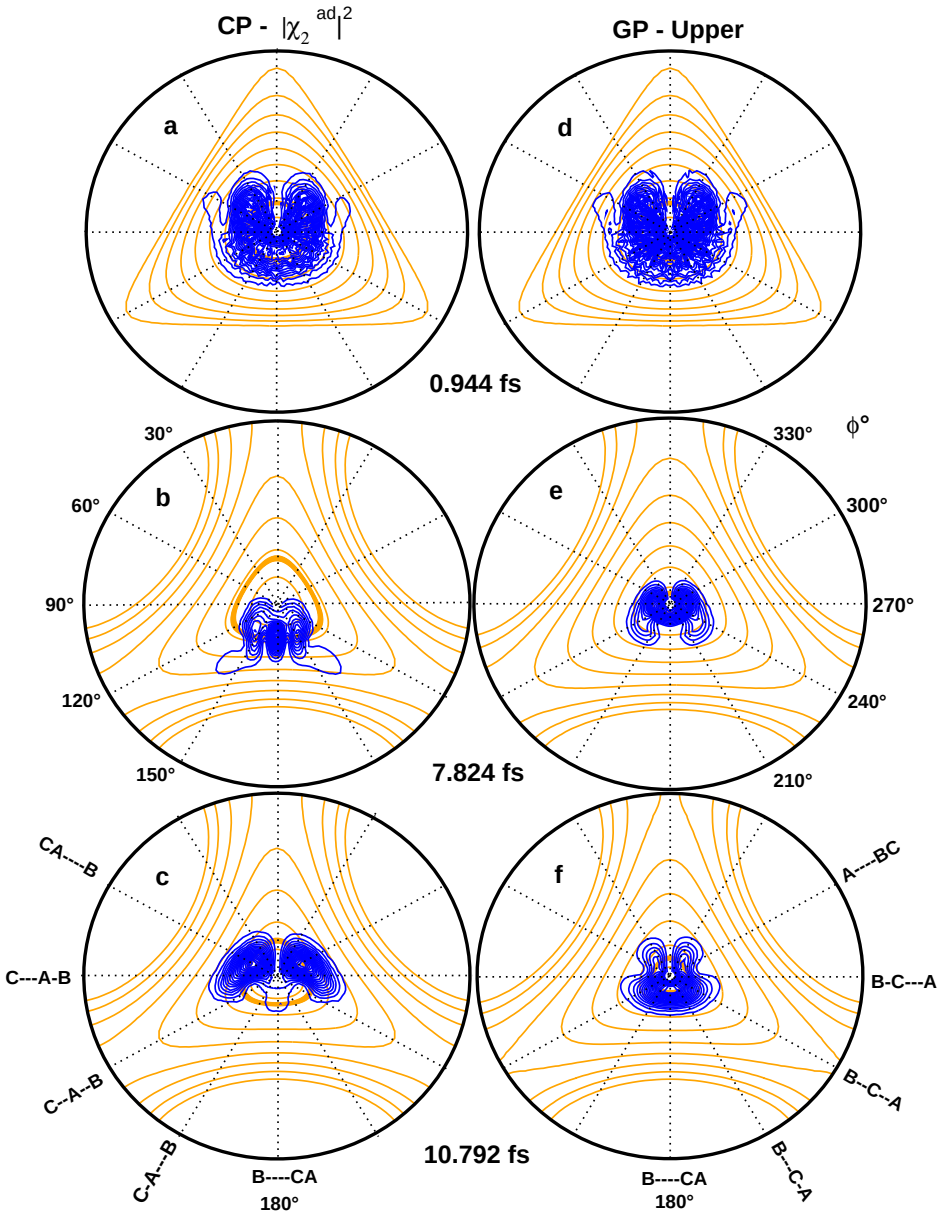

Figure 4.9: Probability density contours of the WP (shown in blue color) evolving on the upper adiabatic sheet (shown in orange color) of D_3 in the equatorial view. The evolution of the WP at various times (indicated in the figure) in the coupled (panels a-c) and uncoupled (panels d-f, including the GP correction) situations are shown.

the nodal line along ϕ is restored confirming the expected single-valued nature of the total wavefunction. Additionally, in the coupled surface situation the WP can be seen to access CIs (see panel b) to relax (nonradiatively) to the repulsive lower adiabatic sheet of the ground electronic state where it finally dissociates. It is therefore confirmed from the above demonstration (both mathematically and also visually) that the consideration of the complete two-states Hamiltonian (cf., Eq. 2.4) includes the GP and BH corrections and most importantly the interstate coupling effects that triggers an internal conversion of the nuclear WP. This internal conversion process allows a mixing of levels of both the adiabatic sheets of the degenerate state and causes a huge increase of the vibronic line density. The latter in turn causes the broad and diffuse nature of the spectral envelope as seen in Fig. 4.8, which is in very good accord with the upper hump of the bimodal experimental emission profile [1, 2] shown in Fig. 4.1.

To this end, the experimental optical emission spectrum [1, 2] of D_3 shown in Fig. 4.1 is referred again. Both the humps in this bimodal emission profile are extremely broad and diffuse. According to the theoretical results presented and discussed above, it should be recognized that the broadening mechanism of the band corresponding to the lower and upper adiabatic sheet is different. While in the former case it originates from a fast dissociation of the nuclear WP, in the later case, it is due its fast relaxation through the CIs. The energetic minimum of the upper adiabatic sheet coincides with the minimum of the seam of CIs and therefore strong nonadiabatic surface coupling effect is immediately encountered by the WP evolving on this sheet. In an earlier study it was estimated that the WP evolving on this sheet relaxes to the lower adiabatic sheet within $\sim$3 - 6 fs only [55]. It therefore emerges from the above discussion that the nonadiabatic

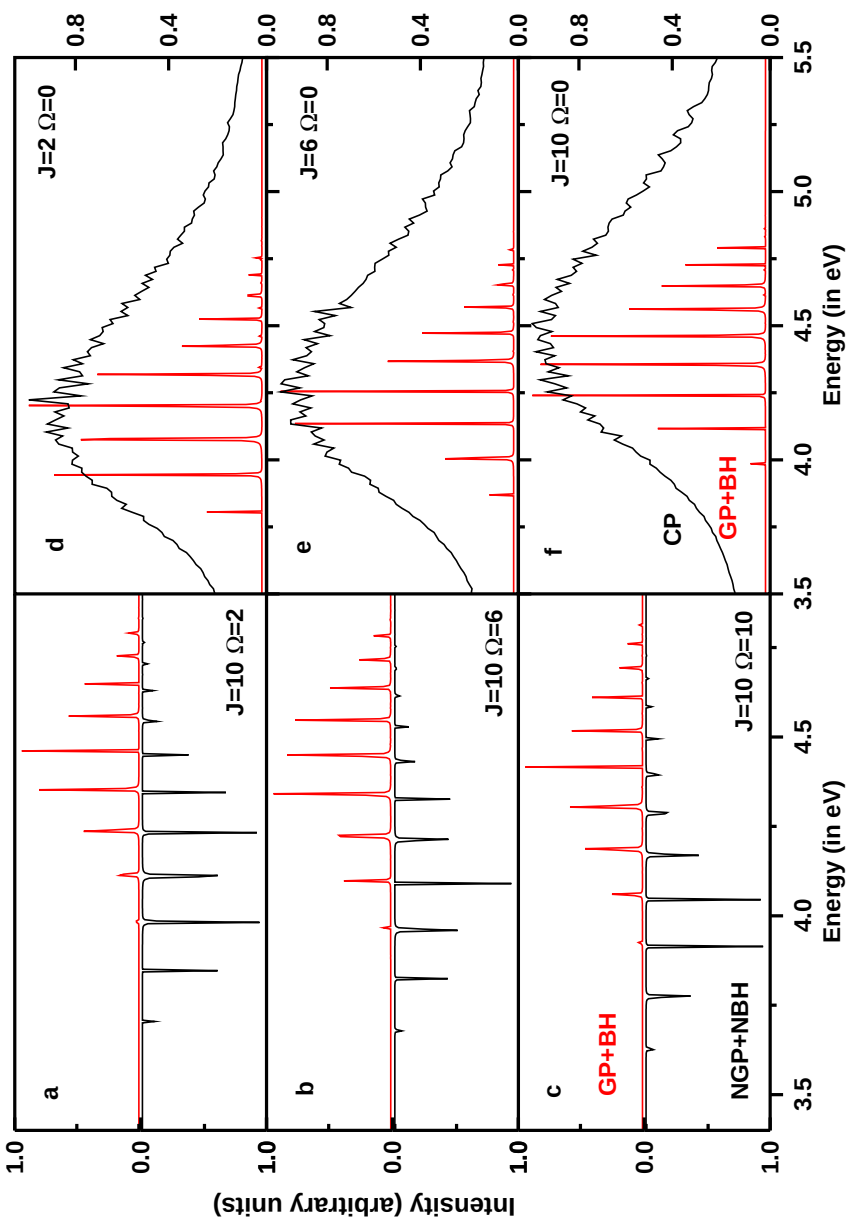

Figure 4.10: Effects of the total angular momentum J and its projection on the BF Z-axis (Ω) on the uncoupled and coupled state dynamics of the upper adiabatic sheet of the $2pE'$ ground electronic manifold of D_3.

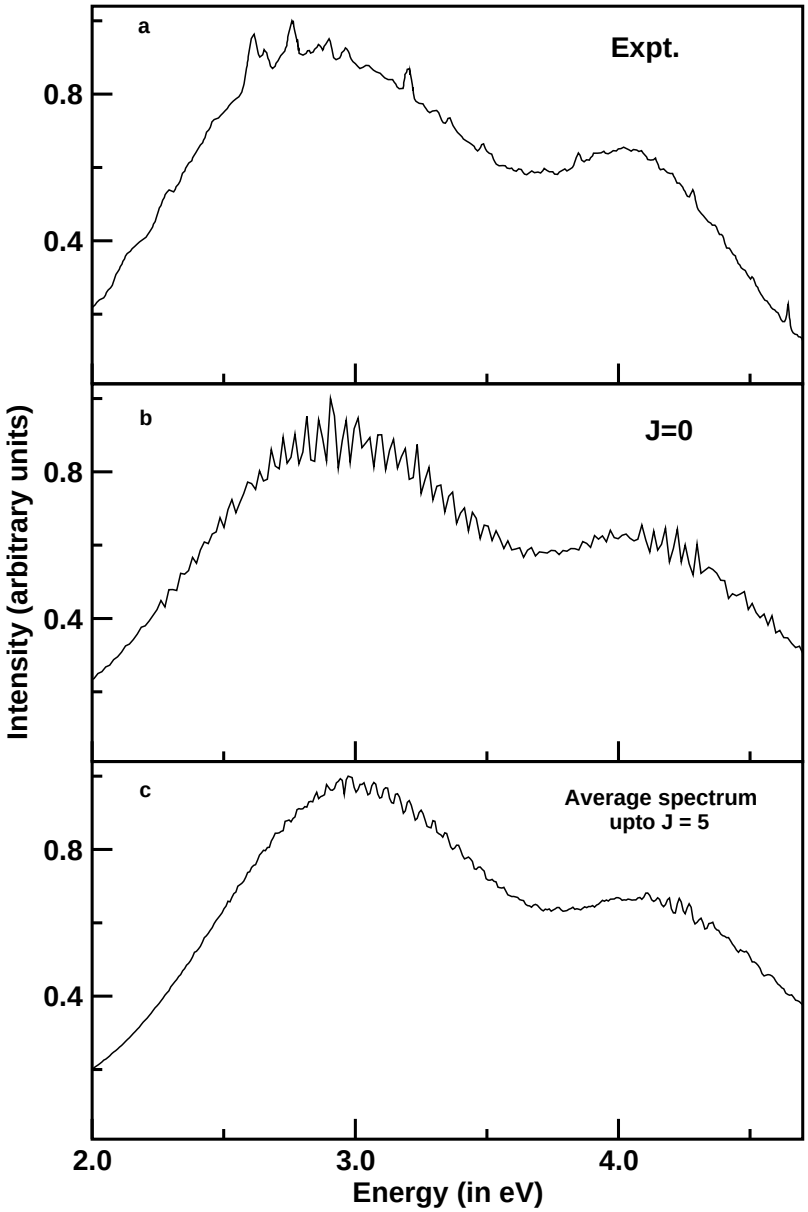

Figure 4.11: Optical emission spectrum of Rydberg-excited D_3, (a) experimental results reproduced from Fig. 1(a) of Ref. [1], (b) coupled states theoretical results for J=0, and (c) coupled states results for $J \neq 0$. Intensities are scaled to unity for a better presentation.

surface coupling does not play any significant role in the nuclear dynamics on the repulsive lower adiabatic sheet. Therefore, no noticeable differences can be derived from the GP plus BH corrections and complete surface(s) coupling results. The GP and BH corrections on the other hand constitute a minor part of the complete surface coupling effects on the dynamics of the upper adiabatic sheet. The overall spectral feature in this case is mostly governed by the off-diagonal derivative coupling elements of the nonadiabatic matrix.

Finally, the effect of total angular momentum J on the emission profiles of Rydberg-excited D_3 from its n=3 electronic state to the upper adiabatic electronic state of the $2pE'$ ground electronic manifold is examined and shown in Fig. 4.10(a-f). The value of the total angular momentum J and its projection on the BF axis Ω for which the emission profiles are obtained are shown in each panel. Here, for a better comparison, the emission profile obtained in the uncoupled state calculation without the inclusion of GP and BH corrections is plotted in the inverted Y-axis and in black color (panels a-c) whereas, the emission profiles obtained with the inclusion of these corrections are plotted in red color (panels a-f) in the positive Y-axis. Also the emission profile obtained in the coupled state calculation is plotted in panels d-f (black color). It is observed that for a fixed value of Ω the energy eigenvalue of the peaks increases with increase in value of J (panels d-f) whereas, the reverse effect is observed *i.e.*, the eigenvalue of the peaks decreases with increase in the value of Ω and for a fixed value of J (panels a-c). These shifts are due to either decrease or increase of the centrifugal contributions to the overall adiabatic potential energy. In coupled state calculations along with the shift of the entire diffuse broad band towards higher energy, more structure at the right wing is observed with increasing J. The emission profiles to the lower

adiabatic electronic state also showed similar effects due to the change in total angular momentum *i.e.*, shifts in the maximum of the envelope of the spectra in accord with the magnitude of the centrifugal term.

A direct comparison of experimental and theoretical spectra was made in an earlier publication [55,56]. Such a comparison is presented here also including the $J \neq 0$ results. The spectral intensities for various J and K values are averaged as

$$I_{avg}(E) = \sum_{J=0}^{5}(2J+1)\sum_{K=0}^{J} g_K I^{JK}(E), \tag{4.13}$$

where the quantity g_K is the degeneracy factor; $g_K = 1$ for $K = 0$, and g_K =2 for $K \neq 0$. The results are shown in Figs. 4.11(a-c). The experimental spectrum in Fig. 4.11(a) is reproduced from Ref. [1]. The emission spectrum obtained for $J =$ 0 is shown in Fig. 4.11(b). The spectrum derived from $J \neq 0$ ($J =$ 0-5) results with the aid of Eq. 4.13 is shown in Fig. 4.11(c). It can be seen that the $J \neq$ 0 results are much closer to the experiment interms of the detail fine structure. The sharp structures seen in the $J = 0$ results average out with contributions from different partial waves. The structures in the experimental spectrum are due to Cs background [1].

4.5 Summary and outlook

The effects of GP, BH corrections to the adiabatic BO Hamiltonian and of explicit surface coupling on the nuclear dynamics in the degenerate electronic ground state of D_3 are theoretically investigated. The theoretical tools are designed in accordance with the optical emission experiment of Rydberg excited D_3 which directly probed the CIs of its electronic ground state. The time-dependent Schrödinger

equation is numerically solved in hyperspherical coordinates and the nuclear dynamics in both the adiabatic sheets is critically examined. The emission profile for a transition to the uncoupled lower adiabatic sheet is a very broad and diffuse band. This is due to a highly repulsive nature of this surface which quickly (within $\sim$ 10 fs) drags the WP to various reactive and nonreactive channels. On the other hand, emission to the uncoupled upper adiabatic sheet yields discrete peaks of the vibrational states supported by this sheet. Inclusion of GP and BH corrections to the BO Hamiltonian causes a shift of the energy eigenvalues of these emission profiles. The extent of this shift is far greater for the discrete peaks of the upper sheet when compared to the same for the broad and diffuse envelope of the lower sheet. Furthermore, it is found that energy shift of nearly same magnitude is caused by either GP or BH correction to the eigenvalues of the discrete peaks of the upper sheet. The magnitude of this shift decreases with an increase in the peak energy. The vector and centrifugal potential terms that appear in the Hamiltonian on inclusion of GP and BH corrections, respectively, cause such shifts in the energy eigenvalue.

Apart from this energy shift, the overall spectral features remain unaltered with GP and BH corrections. The BH correction merely modifies the adiabatic potentials and WP encircles the CIs in this case also like in the uncoupled state situation and therefore the total wavefunction remains multi-valued. Inclusion of GP on the other hand introduces an overall destructive interference, which results into a phase change of the nuclear wavefunction and a nodal line at the CIs. The WP therefore does not encircle the CIs in this case and total wavefunction retains its single-valued property.

The effect of explicit surface coupling on the dynamics of the lower adiabatic sheet has been found to be minor. Despite the overall energy shift (which is obtained already as a combined GP and BH effects) the fine structure of the spectral envelope remains unaltered. It is reiterated, that the observed broad and diffuse structure of this band primarily arises from an extremely fast dissociation of the nuclear WP to the reactive / nonreactive channels. On the other hand, extremely strong effect of surface coupling has been found on the dynamics of the upper adiabatic sheet. In this case the off-diagonal derivative coupling terms of the nonadiabatic operator play major role in the evolution of the WP. In this case the WP does not encircle the CIs (like the effect of GP correction) and in addition it undergoes internal conversion to the lower adiabatic sheet. This nonradiative relaxation process mediated by the off-diagonal derivative coupling terms causes a complete blurring of the discrete vibrational structure of the upper sheet. When compared with the effects due to GP and BH corrections (also keeping the experimental findings of Fig. 4.11(a) in mind), it can be unambiguously concluded that these corrections constitute a minor part of the entire surface coupling in a situation where the seam of CIs is readily accessible to the evolving WP. The huge broadening of the spectral envelope of the upper adiabatic sheet (also observed in the experiment) is therefore an effect arising from the off-diagonal derivative coupling terms of the nonadiabatic operator. The latter when considered explicitly can be seen to include the GP and BH corrections also in an consistent fashion into the overall dynamics of the system. A similar study of the nuclear motion on the orbitally degenerate electronic ground state of H_3^+ and D_3^+ is currently being taken up.

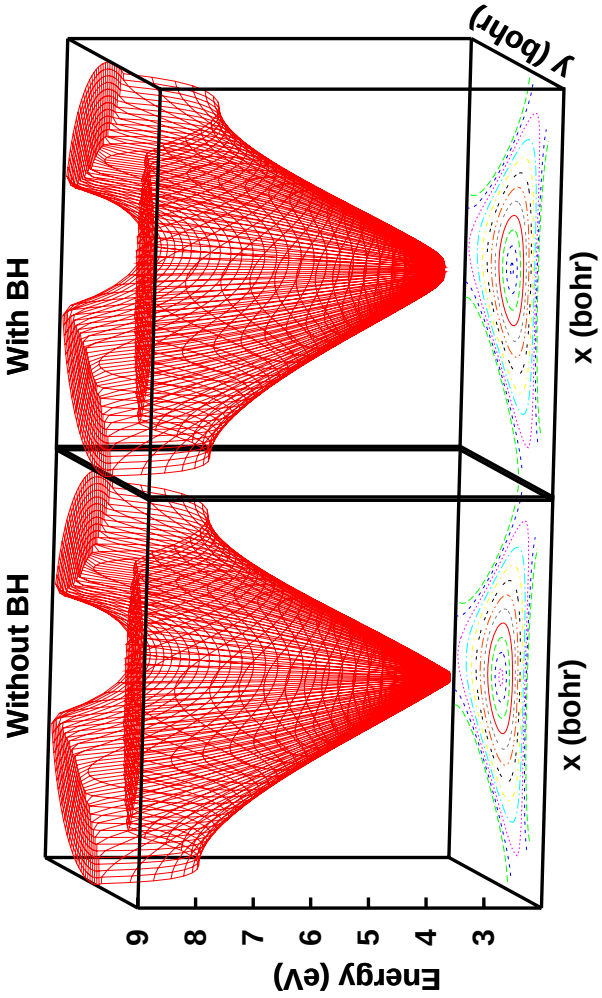

Figure 4.12: Equatorial view (for $\rho = 2.58$ bohr) of the upper adiabatic electronic state of $2pE'$ ground electronic manifold of D_3. Left: without BH correction; Right: with BH correction.

4.6 Additional information

For brevity, some of the obvious results are omitted in the discussion above. Some of those findings are presented here for completeness.

As discussed in section 4.4.1 the BH term is like any other centrifugal term and causes an effective decrease of the depth of the well of the upper adiabatic sheet. This is pictorially shown here in Fig. 4.12. These represent the equatorial view of upper adiabatic sheet at $\rho = 2.58$ bohr with and with out the BH corrections, respectively, shown in right and left panels. It is clear from Fig. 4.12 that the well depth decreases with the inclusion of BH correction and thus shifting the eigenvalue spectrum to the right.

In section 4.4.1, the probability density contours of the first six eigenstates states supported by the upper adiabatic sheet of D_3 and with out the inclusion of GP or BH corrections are presented. Here the similar plots but with the inclusion of GP corrections, BH corrections and both GP and BH corrections are, respectively, shown in Fig. 4.13, Fig. 4.14 and Fig. 4.15. These represent the contours of the eigenfunctions superimposed on the potential energy contours for ϕ= 0 corresponding to the c_{2v} geometry of D_3. The energy eigenvalue of these functions is given in corresponding panel. Contour lines in orange and blue colors, respectively, corresponds to the PES and WP probability density. It is seen from these figures (and also discussed in section 4.4.1) that the inclusion of GP or BH corrections or both has no noticeable effect on this eigenfunction pattern in the coordinate frame used, only the value of the contours are shifted to higher energies.

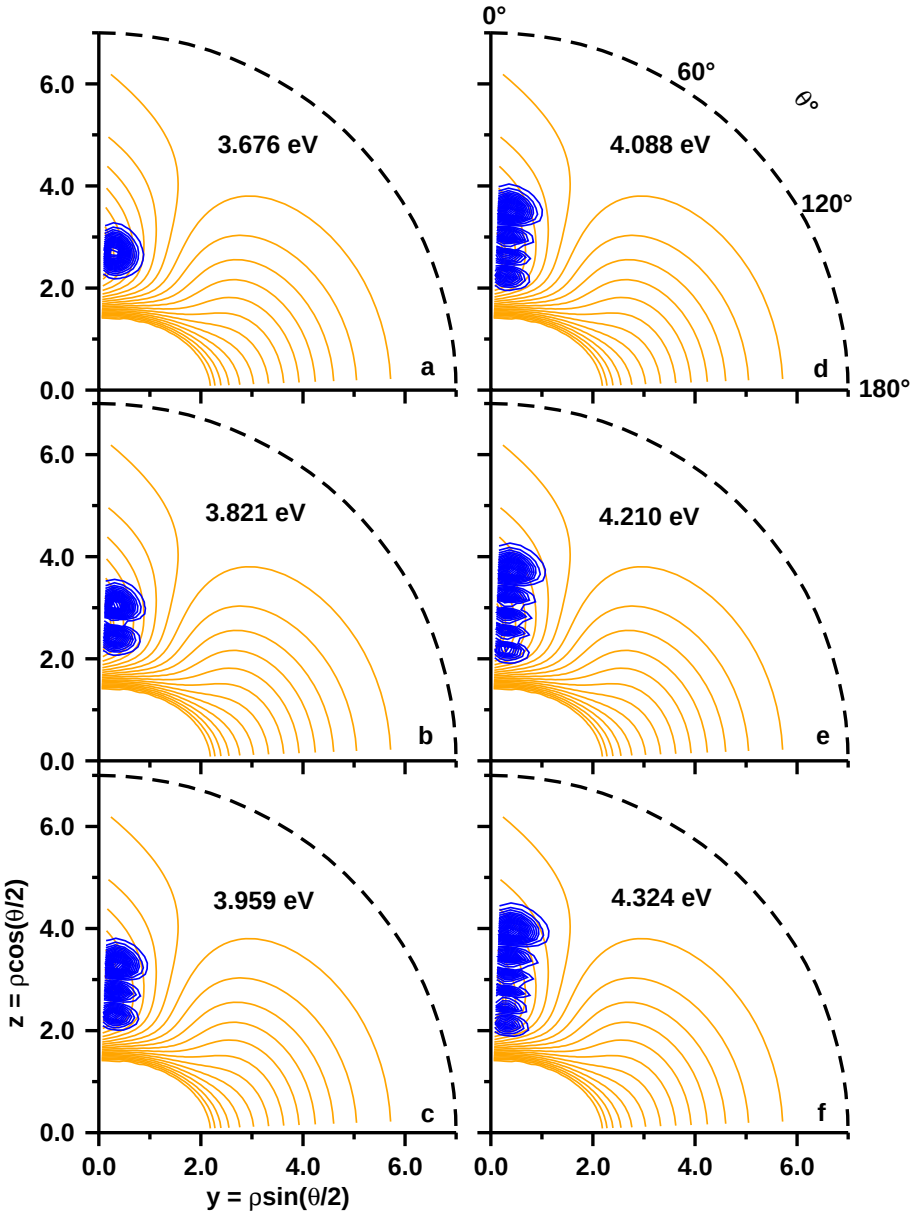

Figure 4.13: Same as in Fig. 4.5 but with inclusion of GP corrections.

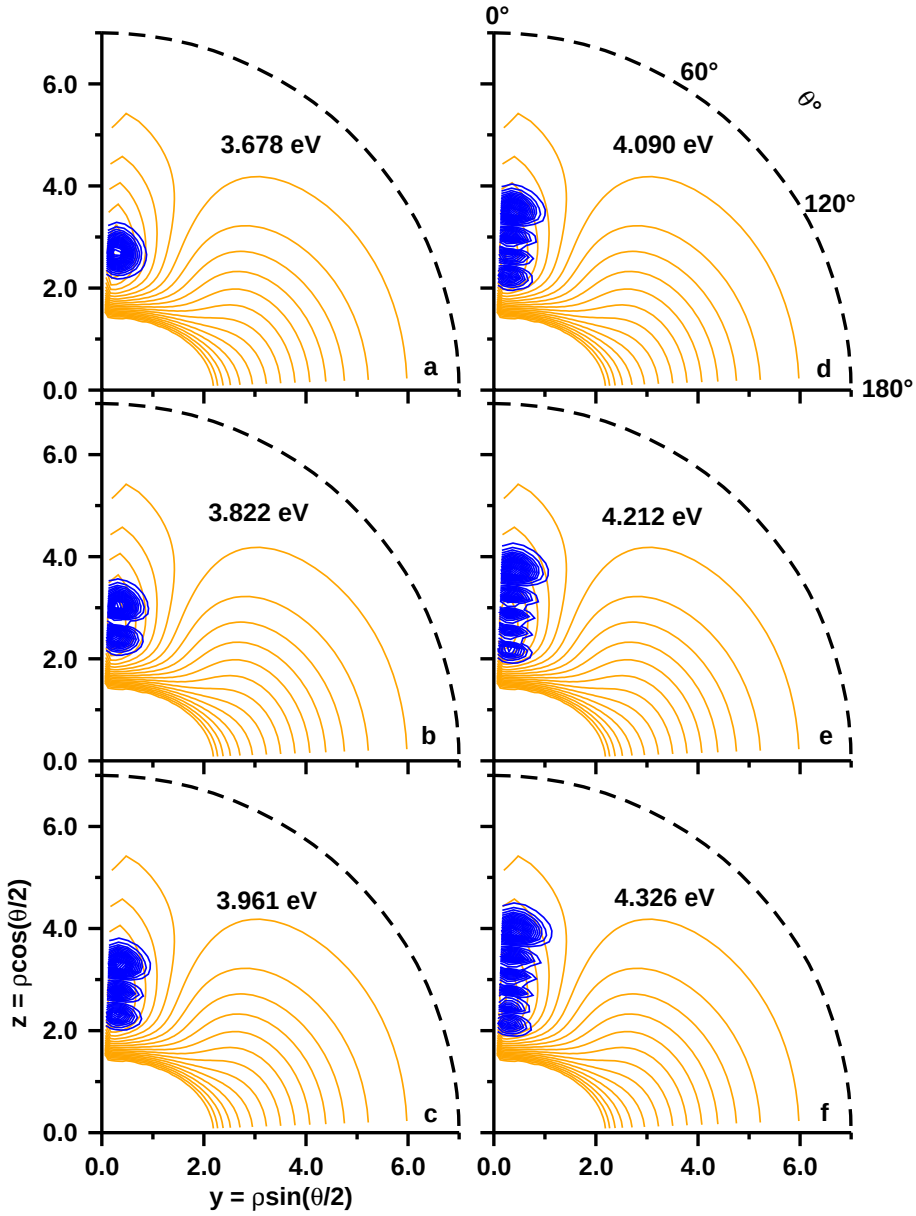

Figure 4.14: Same as in Fig. 4.5 but with inclusion of BH corrections.

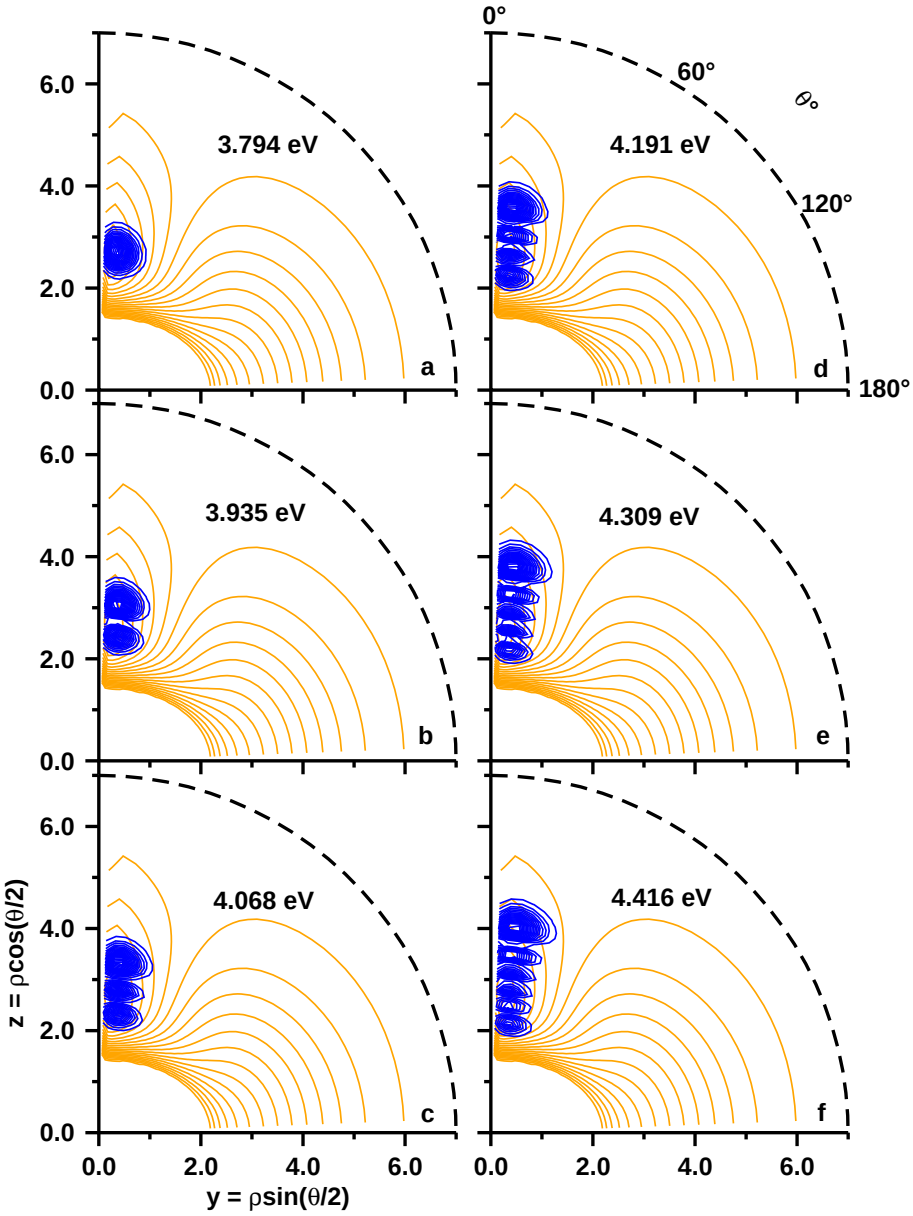

Figure 4.15: Same as in Fig. 4.5 but with inclusion of both GP and BH corrections.

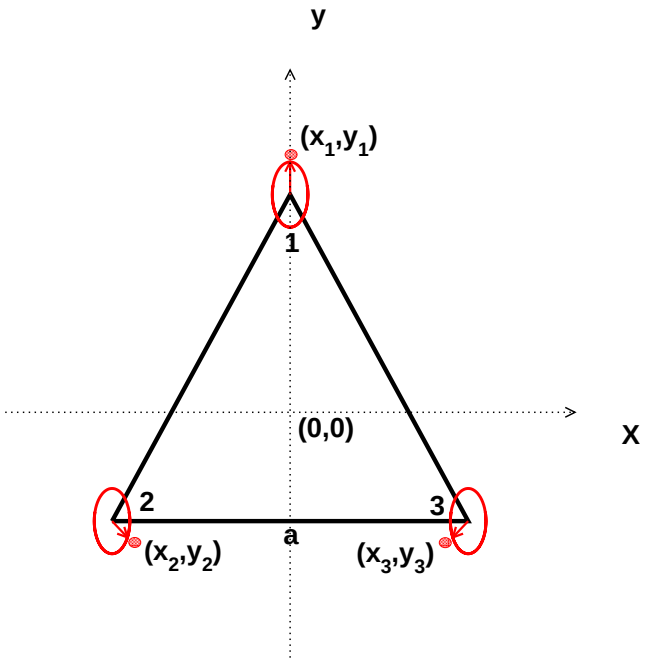

Figure 4.16: Schematic diagram illustrating the pseudorotation of nuclei in D_3.

4.7 APPENDIX A

For the case of equal masses of three nuclei, it is obtained from Eq. 4.8,

$$r_1^2 + r_2^2 + r_3^2 = \sqrt{3}\rho^2, \tag{4.14}$$

$$r_2^2 - r_3^2 = \rho^2 sin(\theta/2) sin(\phi), \tag{4.15}$$

$$\sqrt{3}r_1^2 - \rho^2 = \rho^2 sin(\theta/2) cos(\phi), \tag{4.16}$$

and therefore,

$$tan(\phi) = \frac{r_2^2 - r_3^2}{\sqrt{3}r_1^2 - \rho^2}. \tag{4.17}$$

Now let the molecule is placed in the $z = 0$ plane and the origin is taken as the

centroid of the equilateral triangular configuration of D_3 with length of each side is taken as a as shown in Fig. 4.16. The coordinates of the nuclei labeled 1, 2 and 3, respectively, in their equilibrium geometry are obtained in the Cartesian (x,y) frame as $(0, \frac{a}{\sqrt{3}}), (\frac{-a}{2}, \frac{-a}{2\sqrt{3}})$, and $(\frac{a}{2}, \frac{-a}{2\sqrt{3}})$. When the nuclei make a pseudorotation around these equilibrium geometry then the coordinates of the nuclei change to

$$\begin{aligned}
(x_1, y_1) &= (rcos\varphi, \frac{a}{\sqrt{3}} + rsin\varphi) \\
(x_2, y_2) &= (\frac{-a}{2} + rcos(\varphi + \frac{4\pi}{3}), \frac{-a}{2\sqrt{3}} + rsin(\varphi + \frac{4\pi}{3})) \\
(x_3, y_3) &= (\frac{a}{2} + rcos(\varphi + \frac{2\pi}{3}), \frac{-a}{2\sqrt{3}} + rsin(\varphi + \frac{2\pi}{3})).
\end{aligned} \tag{4.18}$$

Here r and φ represent the polar coordinates as introduced in section 4.3.2. Considering these transformations the internuclear distances of D_3 can be expressed as

$$r_1^2 = a^2 + 3r^2 - 2\sqrt{3}arsin\varphi, \tag{4.19}$$

$$r_2^2 = a^2 + 3r^2 - 3arcos\varphi + \sqrt{3}arsin\varphi, \tag{4.20}$$

$$r_3^2 = a^2 + 3r^2 + 3arcos\varphi + \sqrt{3}arsin\varphi. \tag{4.21}$$

From Eqs. 4.20 to 4.21 we obtain

$$r_1^2 + r_2^2 + r_3^2 = 3(a^2 + 3r^2), \tag{4.22}$$

$$r_2^2 - r_3^2 = -6arcos\varphi. \tag{4.23}$$

Now, considering Eqs. 4.15, 4.20 and 4.23 we obtain

$$\sqrt{3}r_1^2 - \rho^2 = -6arsin\varphi. \tag{4.24}$$

This leads to

$$cot\varphi = \frac{r_2^2 - r_3^2}{\sqrt{3}r_1^2 - \rho^2}. \tag{4.25}$$

A comparison of Eqs. 4.17 and 4.25 yields, $\phi = \varphi - \frac{\pi}{2}$. This confirms the equivalence of $\phi \leftrightarrow \varphi$.

When considering an angle equivalent to φ as defined as θ in Eqs. 12-15 of Ref. [57] which is also adapted later by Varandas and coworkers [17], we get

$$\begin{aligned} tan\varphi &= \frac{\sqrt{3}(r_2^2 - r_3^2)}{2r_1^2 - (r_2^2 + r_3^2)} \\ &= \frac{\sqrt{3}(r_2^2 - r_3^2)}{2r_1^2 - (\sqrt{3}\rho^2 - r_1^2)} \quad \text{from Eq. 4.15)} \\ &= \frac{r_2^2 - r_3^2}{\sqrt{3}r_1^2 - \rho^2}, \end{aligned} \tag{4.26}$$

which yields $\phi = \varphi$.

4.8 APPENDIX B

Discrete fast Fourier transformation algorithm as in *Numerical Recipes* [58] is used here, hence the Eq. 51 of the ref. [22] takes the form

$$e^{-i\alpha\phi} f(\phi) = \sum_k g_k e^{-ik\phi}, \tag{4.27}$$

where the coefficients g_k are obtained by Fourier transformation of $e^{-i\alpha\phi} f(\phi)$. The derivatives of $f(\phi)$ are obtained as,

$$\begin{aligned}
\frac{\partial f}{\partial \phi} &= \frac{\partial}{\partial \phi} e^{i\alpha\phi} \sum_k g_k e^{-ik\phi} \\
&= \sum_k g_k \frac{\partial}{\partial \phi} e^{i\phi(\alpha-k)} \\
&= \sum_k i(\alpha-k) g_k e^{i\phi(\alpha-k)} \\
&= e^{i\alpha\phi} \sum_k i(\alpha-k) g_k e^{-ik\phi}. \qquad (4.28)
\end{aligned}$$

Similarly, we get

$$\frac{\partial^2 f}{\partial \phi^2} = e^{i\alpha\phi} \sum_k -(\alpha-k)^2 g_k e^{-ik\phi} \qquad (4.29)$$

References

[1] R. Bruckmeier, Ch. Wunderlich, H. Figger, Phys. Rev. Lett. 72 (1994) 2550.

[2] D. Azinovic, R. Bruckmeier, Ch. Wunderlich, H. Figger, G. Theodorakopoulos, I.D. Petsalakis, Phys. Rev. A 58 (1998) 1115.

[3] G. Herzberg, H.C. Longuet-Higgins, Discuss. Faraday Soc. 35, (1963) 77.

[4] H.C. Longuet-Higgins, Proc. Roy. Soc. (London), Ser. A 344 (1975) 147.

[5] C.A. Mead, D.G. Truhlar, J. Chem. Phys. 70 (1979) 2284.

[6] B. Lepetit, Z. Peng, A. Kuppermann, Chem. Phys. Lett. 166 (1990) 572.

[7] A.J.C. Varandas, H.G. Yu, J. Chem. Soc., Faraday Trans. 93 (1997) 819.

[8] B.K. Kendrick, J. Chem. Phys. 112 (2000) 5679.

[9] B.K. Kendrick, J. Phys. Chem. A 107 (2003) 6739.

[10] B.K. Kendrick, J. Chem. Phys. 118 (2003) 10502.

[11] B. Lepetit, A. Kuppermann, Chem. Phys. Lett. 166 (1990) 581.

[12] Y.M. Wu, A. Kuppermann, B. Lepetit, Chem. Phys. Lett. 186 (1991) 319.

[13] A. Kuppermann, Y.M. Wu, Chem. Phys. Lett. 205 (1993) 577.

[14] A. Kuppermann, Y.M. Wu, Chem. Phys. Lett. 241 (1995) 229.

[15] A. Kuppermann, Y.M. Wu, Chem. Phys. Lett. 349 (2001) 537.

[16] M. Born, K. Huang, *Dynamical Theory of Crystal Lattices* (Oxford University Press, New York, 1954)

[17] A.J.C. Varandas, F.B. Brown, C.A. Mead, D.G. Truhlar, N.C. Blais, J. Chem. Phys. 86 (1987) 6258.

[18] B.R. Johnson, J. Chem. Phys. 73 (1980) 5051.

[19] R.C. Whitten, F.T. Smith, J. Math. Phys. 9 (1968) 1103.

[20] J.T. Muckerman R.D. Gilbert, G.D. Billing, J. Chem. Phys. 88 (1988) 4779.

[21] B.R. Johnson, J. Chem. Phys. 79 (1083) 1916.

[22] G.D. Billing, Nikola Marković, J. Chem. Phys. 99 (1993) 2674.

[23] Nikola Marković, G.D. Billing, J. Chem. Phys. 100 (1994) 1085.

[24] A. R. Edmonds, *Angular Momentum in Quantum Mechanics*, (Princeton University press, Princeton, 1960).

[25] S. Mahapatra, H. Köppel, Chem. Phys. Lett. 306 (1999) 387.

[26] W. Meyer, P. Botschwina, P. Burton, J. Chem. Phys. 84 (1986) 891.

[27] E.B. Wilson Jr., J.C. Decius, P.C. Cross, *Molecular Vibrations*, (McGrawHill, New York, 1955).

[28] H.F. King, K. Morokuma, J. Chem. Phys. 71 (1979) 3213.

[29] H. Köppel, W. Domcke, L.S. Cederbaum, Adv. Chem. Phys. 57 (1984) 59.

[30] Eric J. Heller, Acc. Chem. Res. 14 (1981) 368.

[31] V. Engel, Chem. Phys. Lett. 189 (1992) 76.

[32] U. Manthe, H.-D. Meyer, L.S. Cederbaum, J. Chem. Phys. 97 (1992) 9062.

[33] M.D. Feit, J.A. Fleck Jr., A. Steiger, J. Comput. Phys. 47 (1982) 412.

[34] D. Kosloff, R. Kosloff, J. Comput. Phys. 52 (1983) 35.

[35] G.C. Corey, D. Lemoine, J. Chem. Phys. 97 (1992) 4115.

[36] S. Mahapatra, N. Sathyamurthy, J. Chem. Soc. Faraday Trans. 93 (1997) 773.

[37] R.T. Pack, J. Chem. Phys. 60 (1974) 633.

[38] P. McGuire, D.J. Kouri, J. Chem. Phys. 60 (1974) 2488.

[39] A. Thiel, H. Köppel, J. Chem. Phys. 110 (1999) 9371.

[40] S. Mahapatra, H. Köppel, L.S. Cederbaum, J. Phys. Chem. A 105 (2001) 2321.

[41] S. Mahapatra, H. Köppel, J. Chem. Phys. 109 (1998) 1721.

[42] A.J.C. Varandas, J. Chem. Phys. 131 (2009) 124128 and references therein.

[43] A. Kuppermann, Chem. Phys. Lett. 32 (1975) 374.

[44] A.J.C. Varandas, Chem. Phys. Lett. 138 (1987) 455.

[45] S. Rogers, D. Wang, S. Walch, A. Kuppermann, J. Phys. Chem. A 104 (2000) 2308.

[46] J. Schön, H. Köppel, J. Chem. Phys. 103 (1995) 9292.

[47] D. Stelitano, Phys. Rev. D 51 (1995) 5876.

[48] J.C. Juanes-Marcos, S.C. Althorpe, J. Chem. Phys. 122 (2005) 204324.

[49] J.C. Juanes-Marcos, S.C. Althorpe, E. Wrede, Science 309 (2005) 1227.

[50] F. Bouakline, S.C. Althorpe, D.P. Ruiz, J. Chem. Phys. 128 (2008) 124322.

[51] R.F. Lu, T.S. Chu, Y. Zhang, K.L. Han, A.J.C. Varandas, J.Z.H. Zhang, J. Chem. Phys. 125 (2006) 133108.

[52] A.J.C. Varandas, Z.R. Xu, Chem. Phys. Lett. 316 (2000) 248.

[53] A. Alijah, A.J.C. Varandas, Phys. Rev. Lett. 93 (2004) 243003.

[54] J.K.G. Watson, J. Mol. Spectrosc. 103 (1984) 350.

[55] S. Mahapatra, H. Köppel, Phys. Rev. Lett. 81 (1998) 3116.

[56] S. Mahapatra, H. Köppel, Faraday Discuss. 110 (1998) 248.

[57] C.A. Mead, Chem. Phys. 49 (1980) 23.

[58] W.H. Press, S.A. Teukolsky, W.T. Vetterling, B.P. Flannery, *Numerical Recipes in Fortran*, (Cambridge university press, Cambridge, 1992).

Chapter 5

Theoretical study of electron detachment spectroscopy of ClH_2^- and its isotopomer ClD_2^-

5.1 Introduction

The electron detachment spectroscopy of ClH_2^- and ClD_2^- is examined and the results are presented, compared with recent high-resolution measurements and discussed in this chapter. Franck-Condon (FC) transition from the electronic and vibrational ground state of the anion (ClH_2^- or ClD_2^-) to the coupled electronic manifold of the neutral species (ClH_2 or ClD_2) is investigated by a time-dependent wave packet (WP) propagation method as described in chapter 2. Rich vibronic structures extending to higher energies appeared due to Cl...H_2 continuum states in the photodetachment band in the previous study [1] are not observed in the recent experiment [2] (see section 1.2.2 for more details). This discrepancy motivated us to revisit the previous theoretical study in order to understand the origin

of the discrepancies and to make efforts to eliminate them. For this purpose, the following modifications are introduced in the present study as compared to the earlier theoretical [1].

1. The initial anionic wavefunction is prepared using the adiabatic bender model of Alexander and co-workers [3] including an ortho / para selection. This is in contrast to the anionic WP prepared in Ref. [1] where it is approximated by a Gaussian WP and also generated using the anionic potential energy surface (PES) of Alexander *et al.* [3].

2. The 6 × 6 coupled states Hamiltonian of the spin states ClH_2 / ClD_2 introduced by Alexander and co-workers [4] is employed in contrast to a 3 × 3 spin-orbit (SO) Hamiltonian employed in Ref. [1].

3. An adiabatic-to-diabatic transformation of the electronic basis is carried out in the present study in contrast to a diabatic electronic basis used throughout the entire calculations in Ref. [1].

The results obtained with the above modification of the theoretical treatment are in good accord with the recent experimental and theoretical studies [2, 5, 6].

5.2 Theoretical and computational details

The Σ and Π states of ClH_2 (ClD_2) are coupled through electronic nonadiabatic interactions. In addition, SO coupling causes a splitting of these states into $^2\Sigma_{\frac{1}{2}}$, $^2\Pi_{\frac{3}{2}}$, and $^2\Pi_{\frac{1}{2}}$ (in linear configurations). Therefore, the Hamiltonian for these energetically lowest SO states of neutral ClH_2 and its deuterated isotopomer in

Table 5.1: Angular momentum terms used in the Hamiltonian [cf. Eqs. 5.3].

Description	Symbol	Quantum No.	z-component
Electronic orbitalangular momentum of Cl	$\boldsymbol{l}$	$l = 1$	λ = -1, 0, +1
Electronic spin angular momentum of Cl	$\boldsymbol{s}$	$s = \frac{1}{2}$	$\sigma = \frac{1}{2}$, -$\frac{1}{2}$
Nuclear orbital angular momentum of H_2	$\boldsymbol{j}$	j = 0, 1, 2,...	k= -j to j
Nuclear orbital angular momentum of Cl relative to H_2	$\boldsymbol{L}$	L = 0, 1, 2,...	
Total electronic and nuclear angular momentum	$\boldsymbol{J=L+l+s+j}$	J = 1/2, 3/2,...	K = -J to J

a diabatic electronic basis can be symbolically expressed as (cf. 2.45)

$$\boldsymbol{H}^{dia} = T_{nuc}\boldsymbol{I}_6 + \boldsymbol{H}^{el+so}. \tag{5.1}$$

In the above equation T_{nuc} is the Hamiltonian matrix corresponding to the nuclear kinetic energy operator. In a diabatic electronic basis this is a 6 × 6 diagonal matrix (including the spin degeneracy) indicated by the symbol $\boldsymbol{I}_6$ for a 6 × 6 unit matrix. The quantity $\boldsymbol{H}^{el+so} = (\boldsymbol{H}^{el} + \boldsymbol{H}^{so})$ represents the diabatic potential matrix including the electronic and SO coupling. The nuclear Hamiltonian T_{nuc}, in reagent Jacobi coordinates is given by

$$T_{nuc} = -\frac{\hbar^2}{2\mu_R}\frac{\partial^2}{\partial R^2} - \frac{\hbar^2}{2\mu_r}\frac{\partial^2}{\partial r^2} - \frac{\hbar^2}{2I}\frac{1}{\sin\gamma}\frac{\partial}{\partial\gamma}\left(\sin\gamma\frac{\partial}{\partial\gamma}\right) + \frac{(\boldsymbol{J}-\boldsymbol{l}-\boldsymbol{s}-\boldsymbol{j})^2}{2\mu R^2}, \tag{5.2}$$

where $I = (\mu_R \mu_r R^2 r^2)/(\mu_R R^2 + \mu_r r^2)$. Following the work of Rebentrost *et al.* [7] and Schatz and co-workers [8], the angular momentum operators (cf. last term of Eq. 5.2) and their projection on the body-fixed (BF) z-axis are defined and listed in Table 5.1 for completeness. The elements of the angular momentum operator $(\boldsymbol{J} - \boldsymbol{l} - \boldsymbol{s} - \boldsymbol{j})^2$ (neglecting Coriolis coupling) can be expressed as [4],

$$\begin{aligned}(\boldsymbol{J} - \boldsymbol{l} - \boldsymbol{s} - \boldsymbol{j})^2 |Kk\lambda\sigma\rangle &= [J(J+1) + j(j+1) + 2.75 - \\ &\quad 2K^2 + 2k\lambda + 2k\sigma + 2\sigma\lambda] |Kk\lambda\sigma\rangle. \end{aligned} \tag{5.3}$$

The electronic (including SO interactions) Hamiltonian in a diabatic signed-$\lambda\sigma$ basis [4] is given by

$$\boldsymbol{H}^{el+so} =$$

$$\begin{array}{c} \lambda \quad \sigma \\ \langle \ 0+\frac{1}{2}| \\ \langle \ 0-\frac{1}{2}| \\ \langle +1+\frac{1}{2}| \\ \langle +1-\frac{1}{2}| \\ \langle -1+\frac{1}{2}| \\ \langle -1-\frac{1}{2}| \end{array} \begin{array}{c} \begin{array}{cccccc} | \ 0+\frac{1}{2}\rangle & | \ 0-\frac{1}{2}\rangle & |+1+\frac{1}{2}\rangle & |+1-\frac{1}{2}\rangle & |-1+\frac{1}{2}\rangle & |-1-\frac{1}{2}\rangle \end{array} \\ \begin{pmatrix} V_\Sigma & 0 & -V_1 & -\sqrt{2}B & V_1 & 0 \\ 0 & V_\Sigma & 0 & -V_1 & -\sqrt{2}B & V_1 \\ -V_1 & 0 & V_\Pi - A & 0 & V_2 & 0 \\ -\sqrt{2}B & -V_1 & 0 & V_\Pi + A & 0 & V_2 \\ V_1 & -\sqrt{2}B & V_2 & 0 & V_\Pi + A & 0 \\ 0 & V_1 & 0 & V_2 & 0 & V_\Pi - A \end{pmatrix} \end{array}. \tag{5.4}$$

In Eq. (5.4) the matrix elements V_Σ, V_Π, V_1, V_2, A, and B are defined as $\langle\Sigma|H^{el}|\Sigma\rangle$, $1/2\ \{\langle\Pi_x|H^{el}|\Pi_x\rangle + \langle\Pi_y|H^{el}|\Pi_y\rangle\}$, $1/\sqrt{2}\langle\Sigma|H^{el}|\Pi_x\rangle$, $1/2\ \{\langle\Pi_x|H^{el}|\Pi_x\rangle - \langle\Pi_y|H^{el}|\Pi_y\rangle\}$, $\mathrm{i}\{\langle\Pi_y|H^{so}|\Pi_x\rangle$ and $\{\langle\Pi_x|H^{so}|\Sigma\rangle$, respectively, where, Σ, Π_x, Π_y states correlate to the asymptotic P_z, P_x, P_y orbitals of Cl-atom, respectively. These matrix elements are obtained using Capecchi and Werner (CW) [9] PES and the matrix is numerically diagonalized to obtain the adiabatic potentials of

the $^2\Sigma_{\frac{1}{2}}$, $^2\Pi_{\frac{1}{2}}$, and $^2\Pi_{\frac{3}{2}}$ SO states and the adiabatic-to-diabatic transformation matrix **S**. It is to be noted that the $|0+\frac{1}{2}\rangle$, $|0-\frac{1}{2}\rangle$ form the doubly degenerate spin components of the V_{Σ} ($^2\Sigma_{\frac{1}{2}}$) diabatic state. Similarly, $|+1+\frac{1}{2}\rangle$ and $|-1-\frac{1}{2}\rangle$ and $|+1-\frac{1}{2}\rangle$, $|-1+\frac{1}{2}\rangle$ form the doubly degenerate spin components of the $V_{\Pi-A}$ ($^2\Pi_{\frac{3}{2}}$) and $V_{\Pi+A}$ ($^2\Pi_{\frac{1}{2}}$) SO states, respectively.

Having obtained the diabatic electronic Hamiltonian, the initial wavefunction pertinent to the electronic and ro-vibrational ground state of the ClH_2^- (ClD_2^-) is expanded using the adiabatic bender model of Alexander *et al.* [10] as

$$\Psi(R,r,\gamma,t=0) = \psi(R)\phi(r)\sum_j T_j(R)\tilde{P}_j(cos\gamma). \tag{5.5}$$

In Eq. (5.5), $\psi(R)$ is approximated with the ground Morse vibrational wavefunction for the Cl^- ... H_2 (D_2) anion complex. Similarly, $\phi(r)$ is also taken as the ground Morse vibrational wavefunction of the diatom H_2 (D_2). The quantity $T_j(R)$ represents the eigenvector matrix corresponding to the lowest adiabatic bender state of ClH_2^- (ClD_2^-) which is expanded as [3]

$$T_j(R) = exp(-c_{0j} - \frac{c_{1j}}{R} - \frac{c_{2j}}{R^2} - \frac{c_{3j}}{R^3} - \frac{c_{4j}}{R^4}). \tag{5.6}$$

The parameters required for obtaining the ground Morse vibrational wavefunctions in Eq. (5.5) and $T_j(R)$ in Eq. (5.6) are available in the Appendix of Ref. [3]. It is to be noted that, the sum in Eq. (5.5) is restricted to the lowest three rotational levels, viz., j=0, 2, 4 for para, $p-H_2$ (ortho, $o-D_2$) and j=1, 3, 5 for $o-H_2$ ($p-D_2$) isomeric configurations.

The anionic wavefunction prepared above is subjected to a FC transition to the three spin states of the neutral species separately. Condon approximation of constant transition dipole moment applicable in a diabatic electronic basis is utilized. The initial WP prepared on the final electronic states of the neutral species for these three transitions can be expressed in a matrix vector notation as

$|\mathbf{\Psi}^{dia}(R,r,\gamma,t=0)\rangle =$

$$\begin{pmatrix} \Psi(R,r,\gamma)|0+\frac{1}{2}\rangle \\ \Psi(R,r,\gamma)|0-\frac{1}{2}\rangle \end{pmatrix} \begin{pmatrix} \frac{1}{\sqrt{2}} \\ \frac{1}{\sqrt{2}} \\ 0 \\ 0 \\ 0 \\ 0 \end{pmatrix} + \begin{pmatrix} \Psi(R,r,\gamma)|+1+\frac{1}{2}\rangle \\ \Psi(R,r,\gamma)|+1-\frac{1}{2}\rangle \end{pmatrix} \begin{pmatrix} 0 \\ 0 \\ \frac{1}{\sqrt{2}} \\ 0 \\ 0 \\ \frac{1}{\sqrt{2}} \end{pmatrix}$$

$$+ \begin{pmatrix} \Psi(R,r,\gamma)|-1+\frac{1}{2}\rangle \\ \Psi(R,r,\gamma)|-1-\frac{1}{2}\rangle \end{pmatrix} \begin{pmatrix} 0 \\ 0 \\ 0 \\ \frac{1}{\sqrt{2}} \\ \frac{1}{\sqrt{2}} \\ 0 \end{pmatrix} \tag{5.7}$$

where $\begin{pmatrix} \frac{1}{\sqrt{2}} \\ \frac{1}{\sqrt{2}} \\ 0 \\ 0 \\ 0 \\ 0 \end{pmatrix}$, $\begin{pmatrix} 0 \\ 0 \\ \frac{1}{\sqrt{2}} \\ 0 \\ 0 \\ \frac{1}{\sqrt{2}} \end{pmatrix}$ and $\begin{pmatrix} 0 \\ 0 \\ 0 \\ \frac{1}{\sqrt{2}} \\ \frac{1}{\sqrt{2}} \\ 0 \end{pmatrix}$ denote the two components of the V_{Σ}, $V_{\Pi-A}$ and $V_{\Pi+A}$ spin states of Eq. (5.4), respectively. It is clear from Eq. (5.7) that both the degenerate spin components ($\pm\frac{1}{2}$) of a given state are simultaneously populated at t=0. The spatial part of the initial wavefunction in the above equation, $\Psi(R, r, \gamma)$, is taken as the function given in Eq. (5.5). The transformation from the diabatic to the adiabatic representation is carried out by, $|\boldsymbol{\Psi}^{adia}\rangle = \boldsymbol{S}^{\dagger}|\boldsymbol{\Psi}^{dia}\rangle$. As stated above the transformation matrix, $\boldsymbol{S}$, represents the eigenvector matrix obtained by numerically diagonalizing the diabatic Hamiltonian given in Eq. (5.4). The initial WP [of Eq. (5.7)] is propagated in time by dividing the total time T into N steps. The time-evolution operator of Eq. (2.7) at each step of length, Δt, is approximated by a second-order split-operator method [11] (see sections 2.3.2 and 2.3.4 for full details). At each time step the autocorrelation function of the time evolved WP is calculated by (cf. Eq. 2.76)

$$C(2t) \quad = \sum_{i \in V_{\Sigma}, V_{\Pi-A}, V_{\Pi+A}} \langle \Psi^{i}(\Delta t)^{*} | \Psi^{i}(\Delta t) \rangle. \tag{5.8}$$

This autocorrelation function is finally Fourier transformed [cf. Eq. (2.75)] to calculate the photodetachment spectrum. The numerical grid parameters used in the present calculations are given in table 5.2. It is to be noted that the spectra reported here are for the two lowest values of total angular momentum, $J = 1/2$ and $3/2$.

Table 5.2: Numerical grid parameters used to propagate WPs in the present study

Parameter	Value	Description
$N_R/N_r/N_\gamma$	128/64/49	Number of grid points
R_{min}/R_{max} (a_0)	0.1/14.0	Extension of the grid along R
r_{min}/r_{max} (a_0)	0.1/8.0	Extension of the grid along r
$\Delta R/\Delta r$ (a_0)	0.109/0.125	Grid spacings along R and r
R_{mask}/r_{mask} (a_0)	11.81/5.49	Starting point of the masking function
T (fs)	2208.0	Total propagation time

5.3 Results and Discussion

5.3.1 Photodetachment spectrum

Photodetachment spectra of ClH_2^- and ClD_2^- for a transition to the coupled electronic states of the corresponding neutral species are presented and discussed in this section. To reveal the impact of the electronic and SO coupling on the vibronic structure of the photodetachment bands, comparison calculations are also carried out considering the uncoupled adiabatic SO states.

5.3.1.1 ClH_2^-

The photodetachment spectra of $Cl^-...o{-}H_2$ and $Cl^-...p{-}H_2$ are shown in panels a-c and d-f of Fig. 5.1, respectively. While the coupled states results are plotted along the normal ordinate, the corresponding uncoupled state results are plotted along the inverted ordinate for comparison. These represent partial spectra corresponding to transition to the spin states (V_Σ , $V_{\Pi-A}$ and $V_{\Pi+A}$ as indicated in each panel) of neutral ClH_2. In each case both the spin states of a given $\mid \Omega(= \lambda + \sigma) \mid$ are initially populated and then the WP is propagated in the uncoupled or coupled electronic state(s) with the aid of Eq. (2.7). The WP is propagated up to $\sim$ 2.2 ps in order to generate each spectrum presented in Fig.

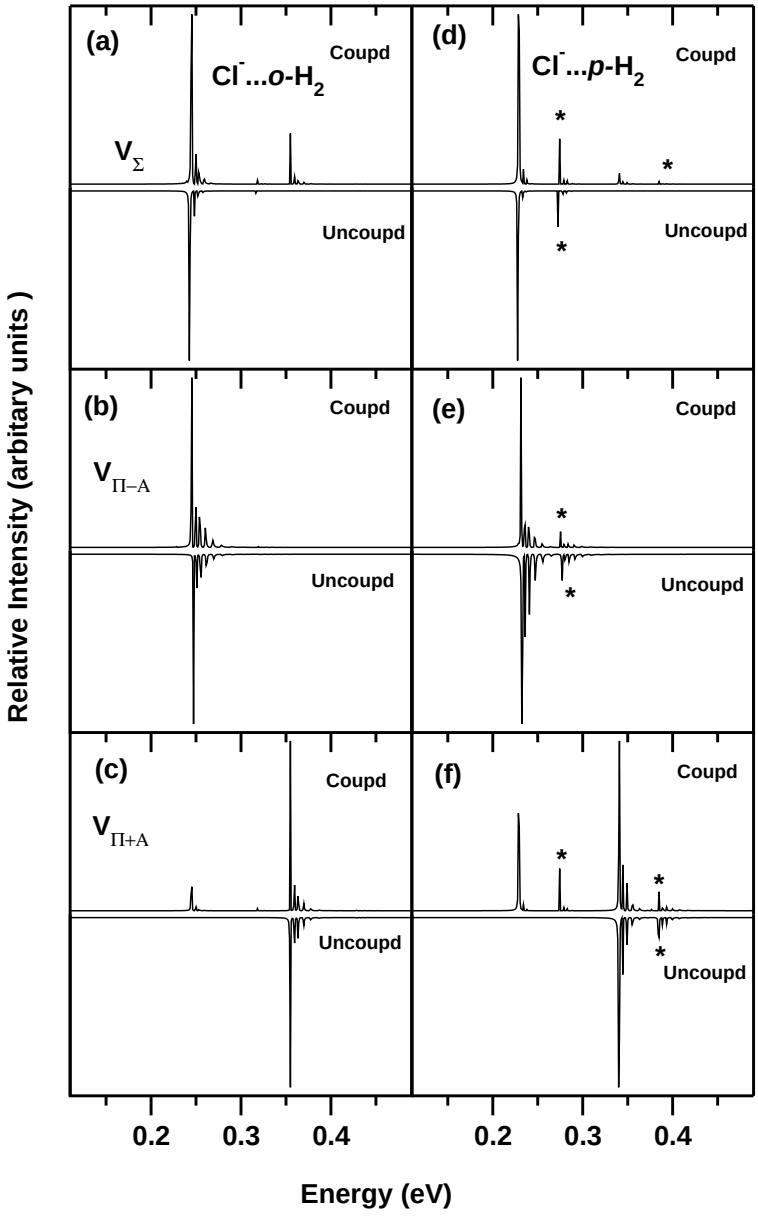

Figure 5.1: Photodetachment spectra of $Cl^-...o{-}H_2$ (panel a-c) and $Cl^-...p{-}H_2$ (panel d-f) for a transition to the V_Σ ($^2\Sigma_{\frac{1}{2}}$), $V_{\Pi-A}$ ($^2\Pi_{\frac{3}{2}}$) and $V_{\Pi+A}$ ($^2\Pi_{\frac{1}{2}}$) SO states of neutral ClH_2. The uncoupled state and coupled states spectra are shown along the normal and inverted ordinate, respectively. Relative intensity in arbitrary unit is plotted as a function of the energy of the final vibronic states. The zero of energy corresponds to the asymptotically separated Cl and H_2 on the V_Σ SO sate.

5.1. The zero of the energy scale in the figure corresponds to the asymptotically separated Cl + H_2 fragments on the V_Σ spin state of ClH_2. A careful comparison of the uncoupled and coupled states results of each panel immediately reveals the impact of coupling among the electronic states on the individual vibronic bands of Fig. 5.1. This impact is relatively stronger on the vibronic structure of the V_Σ and $V_{\Pi+A}$ SO states in contrast to that on the $V_{\Pi-A}$ SO state both for the $o-$ and $p-$ isomers. It can be seen that the coupling among the states only mildly increases the density of vibronic lines in the spectrum. The two dominant peaks in the coupled state spectrum of V_Σ state in panel a of Fig. 5.1 are $\sim$ 0.11 eV spaced. This spacing corresponds to the asymptotic SO splitting of V_Σ and $V_{\Pi+A}$ electronic states. The second set of peaks in the coupled state spectrum of V_Σ state arises from its coupling with the $V_{\Pi+A}$ diabatic state (which is also evident from the observed time-dependence of diabatic electronic populations discussed below). The origin peak of $V_{\Pi+A}$ state occurs $\sim$ 0.11 eV above that of $V_{\Pi-A}$ state (cf. the inverted spectra of these states in panels b and c) which corresponds to the asymptotic SO splitting of the $V_{\Pi-A}$ and $V_{\Pi+A}$ SO states of ClH_2.

It can be seen that the uncoupled and coupled states spectra of $V_{\Pi-A}$ state are mostly identical (cf. panel b or e). This implies very minor role of electronic coupling on this state. The $V_{\Pi-A}$ state is quasidegenerate with the V_Σ state along the approach coordinate of Cl to H_2 and relatively more repulsive. The latter accounts for relatively more broadening of this spectrum when compared to the same of the V_Σ state. In contrast to the coupled state spectrum of V_Σ and $V_{\Pi+A}$ SO states, no signature of coupling can be discerned from that of $V_{\Pi-A}$ SO state (cf. panel b or e) . The weak peak structure on the left of the main peak of the coupled states spectrum of $V_{\Pi+A}$ SO state (cf. panel c) bears the signature of

the V_Σ state (cf. panel a) . In addition to the signature of V_Σ and $V_{\Pi+A}$ coupling in the coupled state spectrum of the $p-$ isomer shown in panels d-f some additional structures (absent in the $o-$ isomer) marked with asterisk are found in this case. These structures arise from an excitation of Cl + H_2 (j=2) on the corresponding state. It is to be noted that the spectra presented above are calculated without multiplying the time autocorrelation function with any damping function. It can be seen that the present theoretical results are in excellent agreement with those published in Ref. [10]. It is worthwhile to add that, unlike the similar spectra presented in Ref. [1], the present ones do not extend to higher energies. As regard to the uncoupled state results the only change made in the present contribution is the representation of the initial wavefunction. It is therefore clear that the initial wavefunction used in Ref. [1] was contaminated by many continuum states of Cl...H_2.

In order to assess the electronic and SO coupling effects on the vibronic spectrum of the individual states, the time-dependence of diabatic electronic populations is shown in Fig. 5.2. While the electronic population dynamics of the $o-$ isotopomer is shown in Fig. 5.2, a similar trend of time variation of populations is found for the $p-$ isotopomer (see additional information at end of the chapter). Now the curves presented in panel a, b and c of Fig. 5.2 corresponds, respectively, to an excitation to the V_Σ ($^2\Sigma_{\frac{1}{2}}$), $V_{\Pi-A}$ ($^2\Pi_{\frac{3}{2}}$) and $V_{\Pi+A}$ ($^2\Pi_{\frac{1}{2}}$) electronic states of ClH_2. The electronic populations are extracted from the calculations with the 6 $\times$ 6 diabatic Hamiltonian [4] and the sum total of the population of the degenerate spin components of each state is presented in Fig. 5.2. It can be seen from the latter that the electronic population oscillates back and forth between the V_Σ ($^2\Sigma_{\frac{1}{2}}$) and $V_{\Pi+A}$ ($^2\Pi_{\frac{1}{2}}$) electronic states (panels a and c) and the $V_{\Pi-A}$

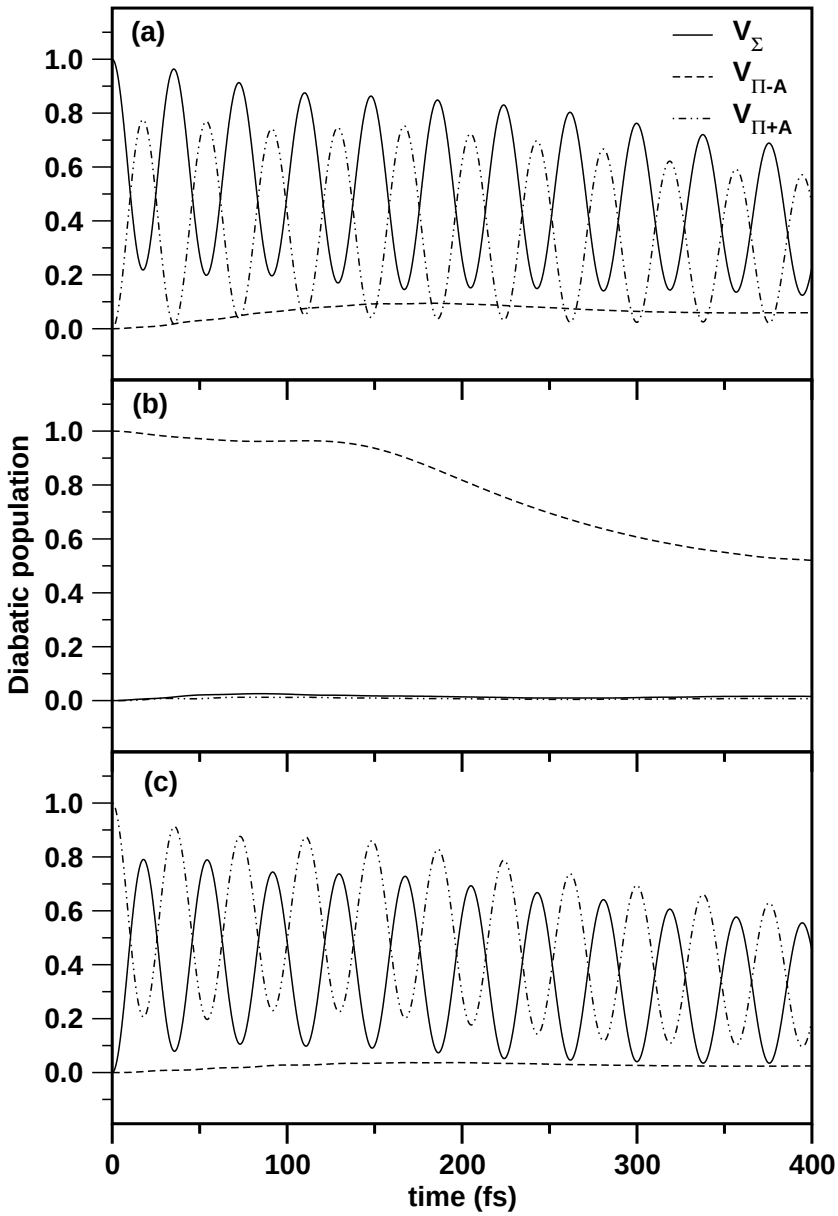

Figure 5.2: The sum total of the population of the degenerate spin components of V_Σ (solid line), $V_{\Pi-A}$ (dashed line) and $V_{\Pi+A}$ (dot-dashed line) as a function of time in the coupled states dynamics of $Cl^-...o-H_2$. Panels a, b and c, respectively, show the populations for the initial excitation of WP on the V_Σ , $V_{\Pi-A}$ and $V_{\Pi+A}$ SO states of ClH_2.

($^2\Pi_{\frac{3}{2}}$) electronic state has insignificant participation in the overall dynamics. Quantitatively, a maximum of $\sim$ 79 % population flows to the $V_{\Pi+A}$ state for an initial excitation to the V_Σ electronic state. A similar population flow to the V_Σ state can be observed when the $V_{\Pi+A}$ state is initially populated (cf. panel c). At longer times, population of both these states fluctuates around a mean value of $\sim$ 40 % . It can be seen from Fig. 5.2(b) that when the WP is initially excited to the $V_{\Pi-A}$ electronic state, hardly any population flows to the remaining two states. Rather the population of this state is quickly (after $\sim$ 150 fs; cf. panel b) reaches to the absorbing boundary. This reveals more repulsive nature of this state and supports the observed broadening of its vibronic spectrum. It is therefore clear that the $V_{\Pi-A}$ ($^2\Pi_{\frac{3}{2}}$) state is very weakly coupled to the remaining two states and since it is asymptotically quasidegenerate with the V_Σ ($^2\Sigma_{\frac{1}{2}}$) SO state the minimal contribution of it to the overall vibronic spectrum ought to be buried within the energy range of the V_Σ SO state.

The findings presented in Fig. 5.2 above are utilized to combine the partial photodetachment spectra of $Cl^-...o{-}H_2$ and $Cl^-...p{-}H_2$ shown in Fig. 5.1 to obtain the full composite spectrum. As discussed above the contribution of the $V_{\Pi-A}$ state is $\sim$ 50 times less compared to that of V_Σ and $V_{\Pi+A}$ SO states. This is considered in the combination in addition to a 3:1 contribution of the ortho : para isomers. The resulting composite spectrum is plotted in the upper part of Fig. 5.3 (panel a) showing the results in the energy range of V_Σ and $V_{\Pi+A}$ separately. The results obtained from the uncoupled and coupled states spectra of Fig. 5.1 are shown by dotted lines and as shaded area in Fig. 5.3(a), respectively. In order to compare, the experimental and theoretical results of Ref. [5] are reproduced in the lower part of Figs. 3 (panel b). It is to be noted

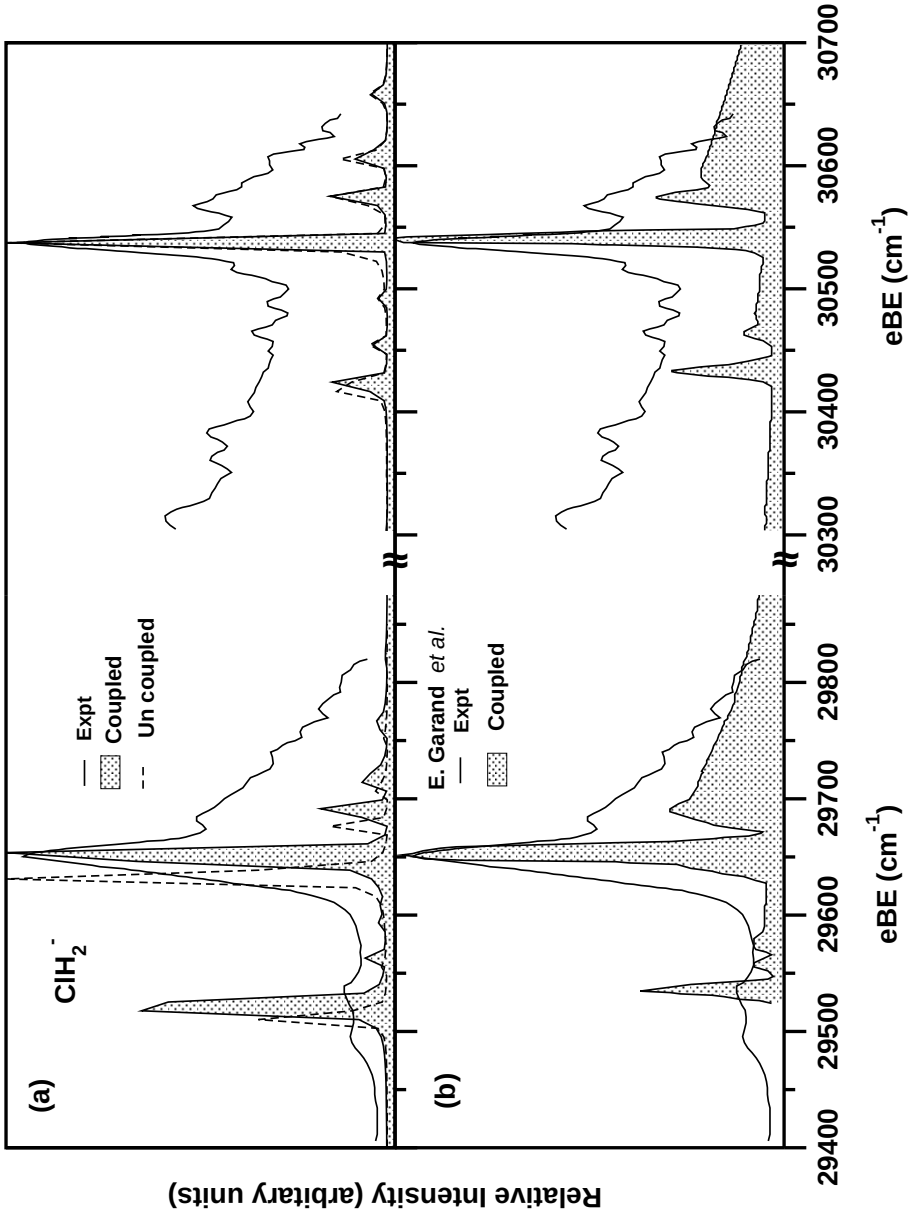

Figure 5.3: Composite theoretical photodetachment spectrum of ClH_2^- in the energy range of V_Σ and $V_{\Pi+A}$ SO states of ClH_2 (see text for details). The present theoretical and experimental results are shown in panel a and the results of Ref. [5] are shown in panel b. Relative intensity in arbitrary units is plotted as a function of the electron binding energy in cm^{-1}.

that the present theoretical spectra of panel a are shifted slightly to correct for the zero point energy contribution in order to obtain the experimental adiabatic ionization energy at $\sim$ 29521 cm^{-1}. It can be seen that the present theoretical results are in excellent agreement with the experimental and theoretical results of Ref. [5]. The peaks in the spectrum are assigned to the bend-stretch states of the Cl...H_2 van der Waals (vdW) complex. The separation between the two intense peaks of panel a is $\sim$ 885 cm^{-1}, compares well with its experimental value of 887 cm^{-1} [5]. This separation corresponds to the SO splitting of the V_Σ and $V_{\Pi+A}$ states of ClH_2. This separation is slightly larger (by $\sim$ 20 cm^{-1}) in the uncoupled state results of Fig. 5.3. The nonadiabatic coupling (NAC) of the electronic states causes a reduction of this value.

5.3.1.2 ClD_2^-

The uncoupled and coupled state photodetachment spectra of Cl^-...o−D_2 and Cl^-...p−D_2 are also calculated and examined in detail. These spectra are analogous to those presented in Fig. 5.1 for ClH_2^-, except a change in the o−, p− definition in case of ClD_2^-. In contrast to ClH_2^- many more lines are observed in the ClD_2^- spectra (see additional information at end of the chapter for more details). Understandably the additional lines in the latter arise from the heavier mass of D_2 and as a result its vibrational levels are closely spaced in energy. Apart from these the spectra of Cl^-...o−H_2 (Cl^-...p−D_2) and Cl^-...p−H_2 (Cl^-...o−D_2) closely resemble each other. The excitation to the higher j level as found in Cl^-...p−H_2 is found in the Cl^-...o−D_2 isotopomer. It is also noted that the electron population dynamics of ClD_2^- is also analogous to that of ClH_2^- shown in Fig. 5.2. In this case $\sim$ 2 % contribution of the $V_{\Pi-A}$ SO state has been found in the vibronic dynamics (see additional information at end of the chapter).

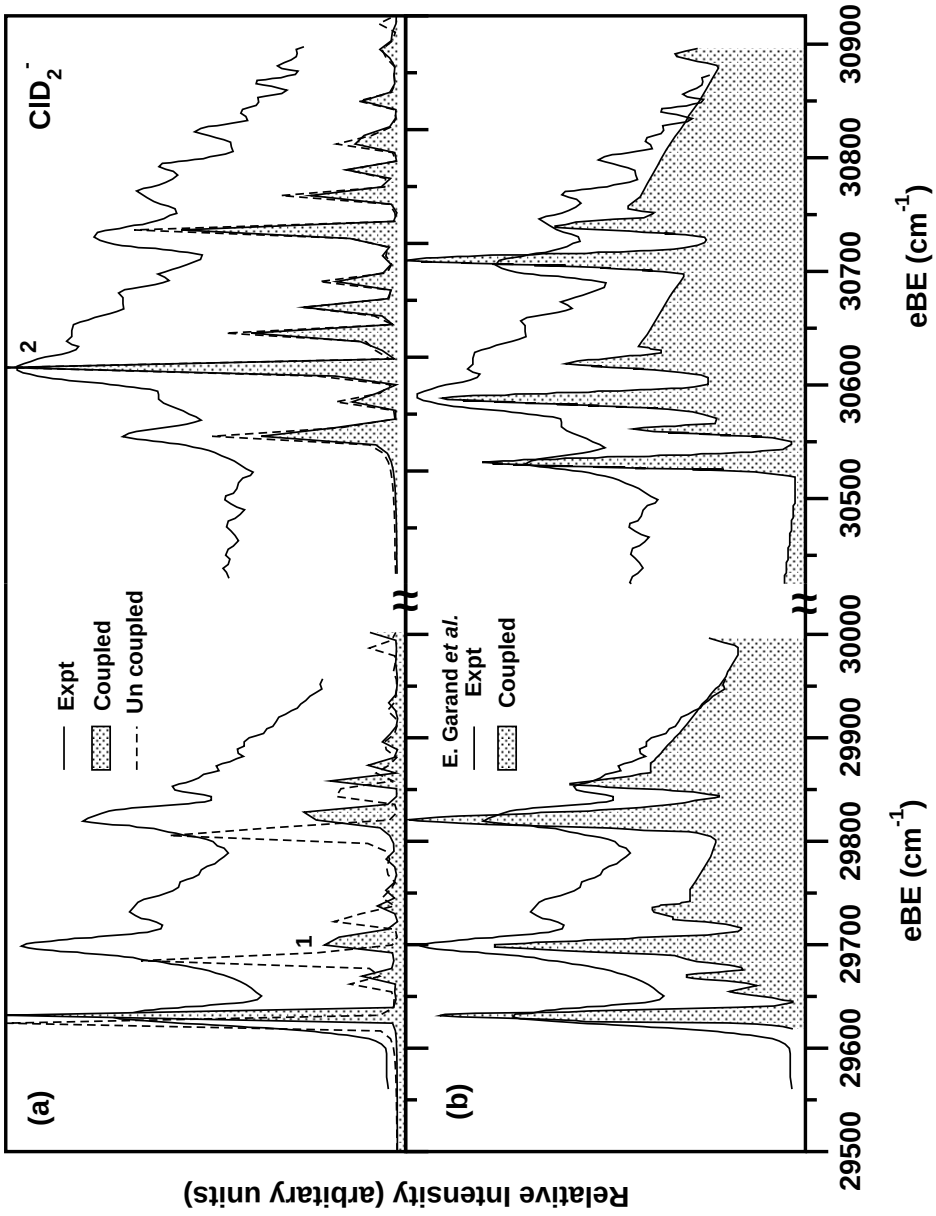

Figure 5.4: Same as in Fig. 5.3 for the photodetachment of ClD_2^-.

Analogous to that in Fig. 5.3, the partial spectra of ClD_2^- are combined in the $o-$, $p-$ ratio of 2:1 also considering the relative contribution of each SO state to the overall composite spectrum. The latter are presented in Fig. 5.4 in the energy range of the V_Σ and $V_{\Pi+A}$ (panel a) SO states. The experimental and theoretical results available in the literature are reproduced from Ref. [5] and plotted in panel b of Fig. 5.4. The origin peak of the present theoretical spectrum is placed at its experimental value of 29631 cm^{-1}. It can be seen from Fig. 5.4 that the present theoretical results are in very good accord with the experimental and theoretical results of Ref. [5]. The two main peaks marked 1 and 2 in panel a are $\sim$ 887 cm^{-1} spaced in the coupled states results (shaded area). This spacing is again, as found in Fig. 5.3, $\sim$ 20 cm^{-1} less in the uncoupled state results (dashed lines). In contrast to Fig. 5.3 for ClH_2^- the ClD_2^- spectrum of Fig. 5.4 reveals more structures. As stated above, these are arising from the closely spaced vibronic levels of the deuterated isotopomer.

To this end the effect of three body rotation ($J > \frac{1}{2}$) on the composite photodetachment spectrum of ClH_2^- and ClD_2^- is briefly discussed here. In Fig. 5.5 the spectra for $J = \frac{1}{2}$, $K = \frac{1}{2}$; $J = \frac{3}{2}$, $K = \frac{1}{2}$; $J = \frac{3}{2}$, $K = \frac{3}{2}$ are plotted in panels a-c and d-f, respectively, for ClH_2^- and ClD_2^-. It can be seen from these plots that there is no dramatic effect arising from higher J and K values. The origin peak shifts to the higher energy for higher J and K. Understandably, this shift arises from the appearance of centrifugal barrier on the PESs with the increasing J and K values. The intensity of the peaks (which is in arbitrary units in the present work) also alters however, the overall vibronic structures of the composite bands remain almost similar for all J and K values considered in this chapter.

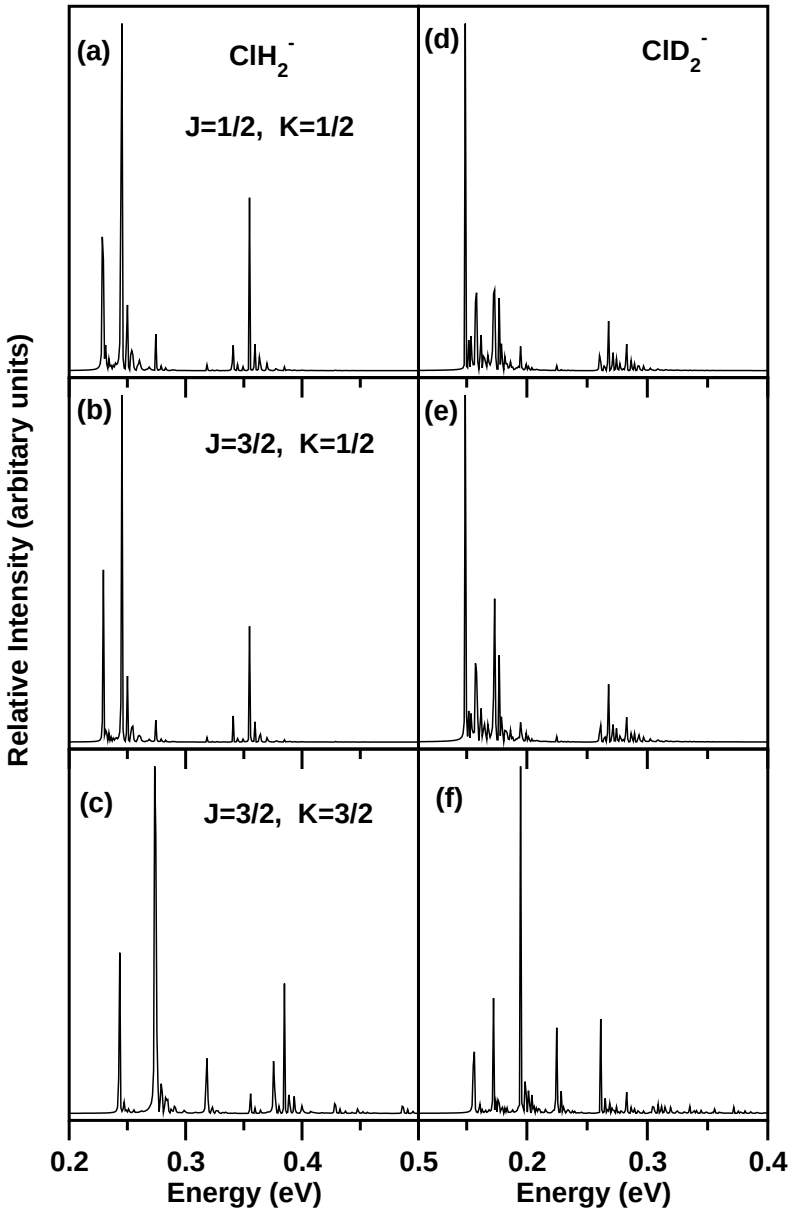

Figure 5.5: Composite theoretical photodetachment spectrum of ClH_2^- (panel a-c) and ClD_2^- (panel d-f) for different values of J and K as indicated in each panel.

5.4 Summary and outlook

A theoretical study of the electron detachment spectroscopy of ClH_2^- and ClD_2^- is presented in this chapter employing a time-dependent WP propagation approach. The present results are found to be in very good accord with the highly resolved experimental [2, 5] as well as recent theoretical results [5, 6, 12]. In contrast to the earlier work on this subject [1], it is found that that an improvement on the representation of the initial anionic wavefunction, transformation of electronic basis (diabatic-to-adiabatic) and the use of a complete Hamiltonian eliminates the contribution of continuum states of Cl...H_2 (D_2) vdW complexes and simplifies the vibronic structures of the photodetachment bands in agreement with the recent experimental and theoretical results. A study of the effects of electronic and SO coupling on the state-to-state reaction dynamics of Cl + H_2 (D_2) reaction is currently being taken up.

5.5 Additional information

For brevity, some of the obvious results are omitted in the discussion above. Those findings are presented here in brief.

As discussed in section 5.3.1.2 the uncoupled and coupled state photodetachment spectra of Cl^-...$o-D_2$ and Cl^-...$p-D_2$ are analogous to those presented in Fig. 5.1 for ClH_2^- and are shown here in Fig. 5.6. These represent the photodetachment spectra of Cl^-...$o-D_2$ (panel a-c) and Cl^-...$p-D_2$ (panel d-f) for a transition to the V_Σ ($^2\Sigma_{\frac{1}{2}}$), $V_{\Pi-A}$ ($^2\Pi_{\frac{3}{2}}$) and $V_{\Pi+A}$ ($^2\Pi_{\frac{1}{2}}$) SO states of neutral ClD_2. The uncoupled state and coupled states spectra are shown along the normal and inverted ordinate, respectively. Relative intensity in arbitrary unit

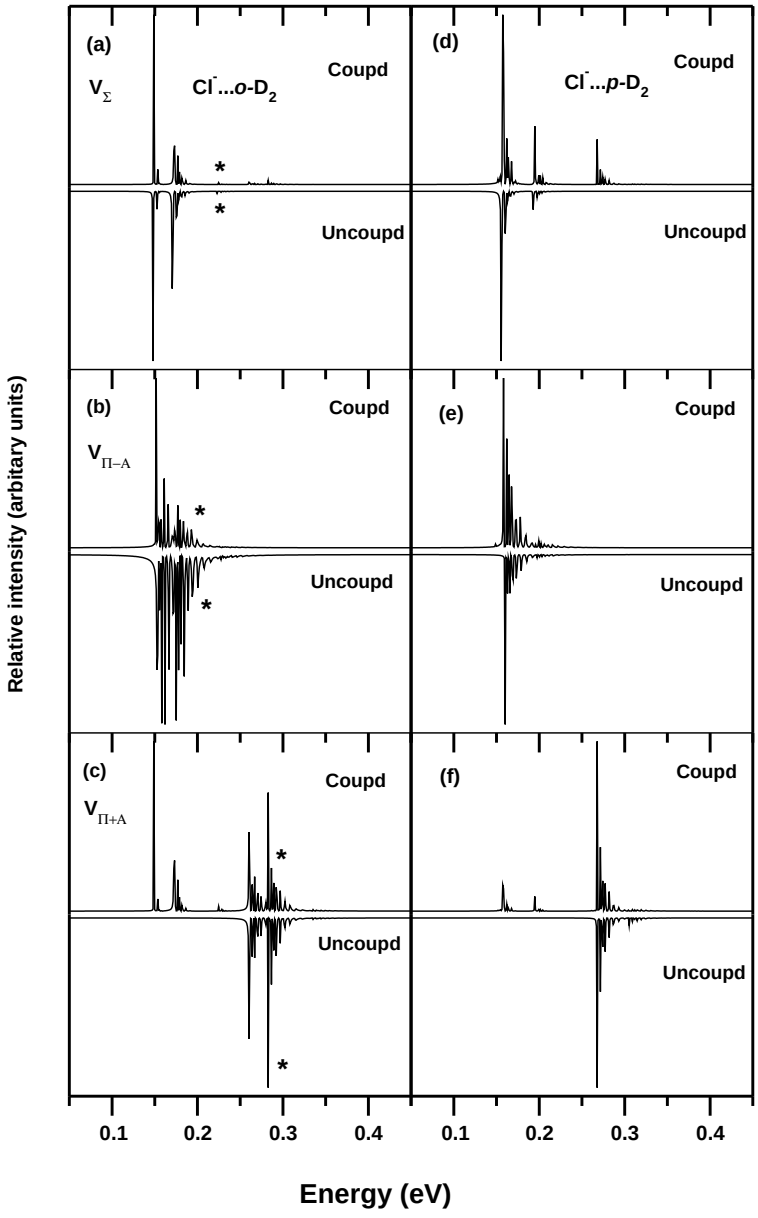

Figure 5.6: Same as in Fig. 5.1 but for ClD_2^-.

is plotted as a function of the energy of the final vibronic states. It can be seen from these figures that, more lines are observed in the ClD_2^- spectra when compared with the same obtained for ClH_2^-. Understandably the additional lines in the former arise from the heavier mass of D_2 and as a result its vibrational levels are closely spaced in energy. Apart from these the spectra of $Cl^-...o{-}H_2$ ($Cl^-...p{-}D_2$) and $Cl^-...p{-}H_2$ ($Cl^-...o{-}D_2$) closely resemble each other. The excitation to the higher j level as found in $Cl^-...p{-}H_2$ is found in the $Cl^-...o{-}D_2$ isotopomer and are marked with asterisk in panels a-c.

In section 5.3.1.1 the time-dependence of diabatic electronic populations during the excitation of $Cl^-...o{-}H_2$ to the V_Σ ($^2\Sigma_{\frac{1}{2}}$), $V_{\Pi-A}$ ($^2\Pi_{\frac{3}{2}}$) and $V_{\Pi+A}$ ($^2\Pi_{\frac{1}{2}}$) electronic states of ClH_2 is shown in Fig. 5.2. Similar plots for the excitations of $Cl^-...p{-}H_2$, $Cl^-...o{-}D_2$ and $Cl^-...p{-}D_2$ are, respectively, shown in Fig. 5.7, Fig. 5.8 and Fig. 5.9. It is clear from these figures that the behavior of the electronic populations is similar in all the cases, i.e., the latter oscillates back and forth between the V_Σ ($^2\Sigma_{\frac{1}{2}}$) and $V_{\Pi+A}$ ($^2\Pi_{\frac{1}{2}}$) electronic states (panels a and c) and the $V_{\Pi-A}$ ($^2\Pi_{\frac{3}{2}}$) electronic state has insignificant participation in the overall dynamics. It is therefore clear that the $V_{\Pi-A}$ ($^2\Pi_{\frac{3}{2}}$) state is very weakly coupled to the remaining two states and since it is asymptotically quasidegenerate with the V_Σ ($^2\Sigma_{\frac{1}{2}}$) SO state the minimal contribution of it to the overall vibronic spectrum ought to be buried within the energy range of the V_Σ SO state.

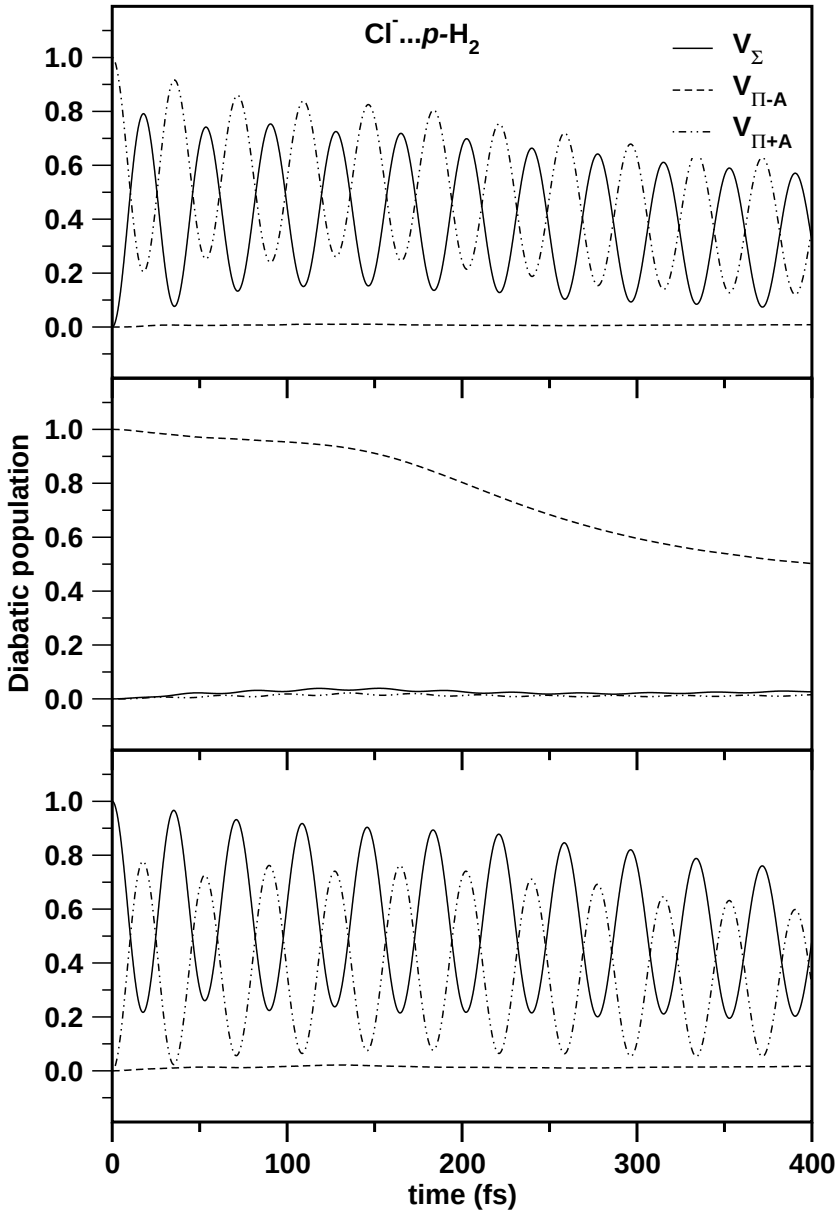

Figure 5.7: Same as in Fig. 5.2 but for $Cl^{-}...p{-}H_2$.

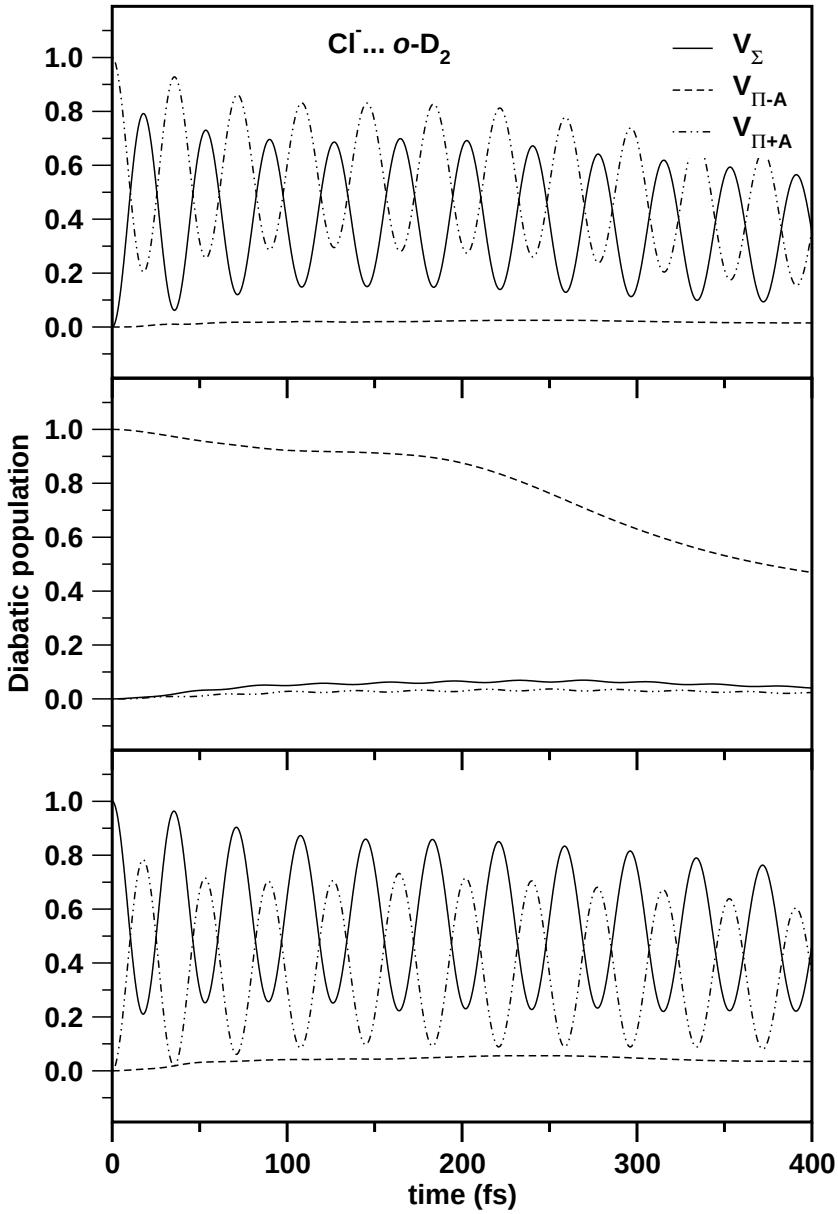

Figure 5.8: Same as in Fig. 5.2 but for Cl^{-}...o−D_2.

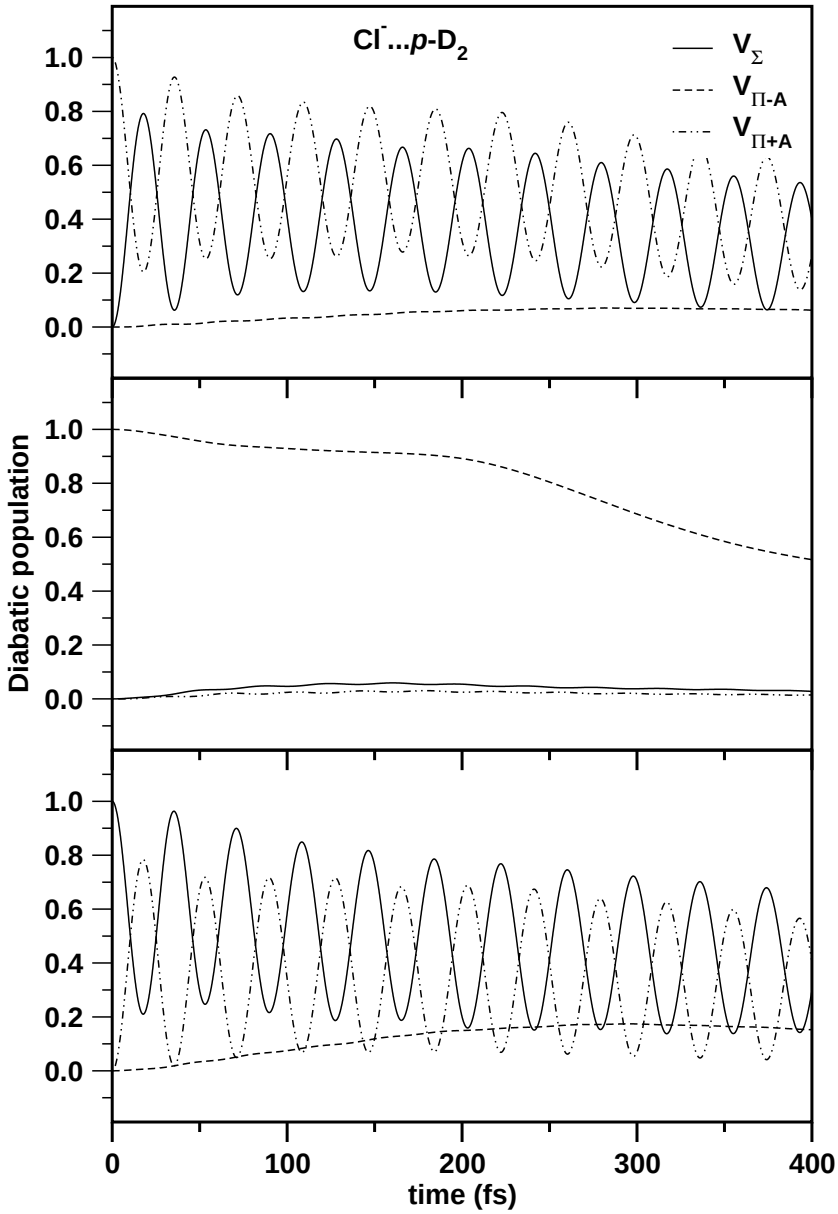

Figure 5.9: Same as in Fig. 5.2 but for $Cl^{-}...p{-}D_2$.

References

[1] S. Ghosal, S. Mahapatra, Chem. Phys. Lett. 394 (2004) 207.

[2] D.M. Neumark, J. Phys. Chem. A 112 (2008) 13287.

[3] M.H. Alexander, J. Chem. Phys. 118 (2003) 9637.

[4] M.H. Alexander, D.E. Manolopoulos, H.-J. Werner, J. Chem. Phys. 113 (2000) 11084.

[5] E. Garand, J. Zhou, D.E. Manolopoulos, M.H. Alexander, D.M. Neumark, Science 319 (2008) 72.

[6] M.H. Alexander, J. Klos, D.E. Manolopoulos, J. Chem. Phys. 128 (2008) 84312.

[7] F. Rebentrost, W.A. Lester, Jr., J. Chem. Phys. 63 (1975) 3737.

[8] G.C. Schatz, P. McCabe, J.N.L. Connor, Faraday Disc. 110 (1998) 139.

[9] G. Capecchi, H.-J. Werner, Phys. Chem. Chem. Phys. 6 (2004) 4975.

[10] D.E. Manolopoulos, M.H. Alexander, Phys. Chem. Chem. Phys. 6 (2004) 4984.

[11] M.D. Feit, J.A. Fleck, A. Steiger, J. Comput. Phys. 47 (1982) 412.

[12] T.A. Grinev, A.A. Buchachenko, J. Chem. Phys. 128 (2008) 154317.

Chapter 6

Time-dependent quantum wave packet dynamics of C + OH reaction on the first excited potential energy surface

6.1 Introduction

Initial state-selected dynamical attributes of the C(^{3}P) + OH ($X^2\Pi$) → CO($a^3\Pi$) + H (^{2}S) reaction on the first excited electronic potential energy surface (PES) ($1^2A''$) are calculated by the time-dependent wave packet (WP) method described in chapter 2. The findings on the reaction probability, integral reaction cross section (ICS) and thermal rate constant are presented and discussed here. Reaction probabilities are calculated as a function of collision energies up to 1 eV and for different values of the total angular momentum J. Within the centrifugal sudden (CS) approximation [1], all the partial wave contributions for J =0-95 are

included to obtain the converged cross sections and rate constants. The effect of reagent rotational and vibrational excitation on these dynamical attributes is also discussed here. It is to be noted that the other product channel, O (^3P) + CH ($X^2\Pi$) for this reaction is endothermic by about 1 eV and hence, is asymptotically closed in the present conditions of investigation. In addition, the state-to-state reaction probabilities of the reaction obtained for total angular momentum, J =0 are also presented and discussed in this chapter.

6.2 Theoretical and computational details

The theoretical formalism and computational methods employed to calculate the initial state-selected and energy resolved reaction probabilities, ICSs and thermal rate constants for the C + OH reaction are outlined in chapter 2. A few essential points are described below. The initial wavefunction,$|\Psi(t = 0)\rangle$ (cf. Eq. 2.48), pertinent to the reagent asymptote is prepared and propagated on the first excited electronic $^2A''$ PES with the aid of the time-dependent Schrödinger equation (TDSE). In order to calculate the wavefunction at time t, $|\Psi^J_\Omega(R, r, \gamma, t)\rangle$, the time axis is divided into N segments of length Δt and the exponential time evolution operator of Eq. 2.7 is approximated by a split-operator method [2] at each time step Δt. The fast Fourier transformation method (FFT) [3] is used to evaluate the action of the radial kinetic energy operators on the wavefunction, whereas, the action of the angular kinetic energy operator is evaluated by a discrete variable representation (DVR) [4] method. For the latter purpose a γ grid is constructed by diagonalizing the $\cos(\gamma)$ operator in the basis of the associated Legendre polynomials. Finally, the unphysical reflections at the grid boundaries are controlled by multiplying with a damping function [5] (cf. Eq.

Table 6.1: Numerical definition of the coordinate grid, initial wavefunction and the damping function used to obtain converged dynamical results of the C + OH collisional system.

Parameter	Value	Description
$N_R/N_r/N_\gamma$	1024/128/31	Number of grid points
R_{min}/R_{max} (a_0)	0.1/36.0	Extension of the grid along R
r_{min}/r_{max} (a_0)	0.1/9.0	Extension of the grid along r
$\Delta R/\Delta r$ (a_0)	0.035/0.07	Grid spacings along R and r
r_d (a_0)	5.92	Location of the dividing surface in the product channel
R_{mask}/r_{mask} (a_0)	25.51 /7.04	Starting point of the damping function
R_0 (a_0)	14.0	Initial location of the center of the GWP in the coordinate space
E_{trans} (eV)	0.5	Initial translational kinetic energy
δ (a_0)	0.08	Initial width parameter of the GWP
Δt (fs)	0.135	Length of the time step used in the WP propagation
T (fs)	4049.0	Total propagation time

2.19) to the WP at each time step. The properties of the initial WP and the grid parameters used for the numerical calculations are listed in Table 6.1.

The reaction probability is obtained from the expectation value of the quantum flux operator, $\hat{F}$, in the basis of energy normalized time-independent reactive scattering wavefunction recorded at a dividing surface located along the product channel (see section 2.5 for more details). The initial state i (corresponding to a specific vibrational v and rotational j state of the reagent diatom OH) selected and energy resolved total reaction probability [summed over final states $f(v', j')$ of the product CO] is given by Eq. 2.57. The reaction probabilities depending upon J and Ω values (cf. Eq. 2.57) for a given collision energy are summed up to calculate the ICS for a specified initial (v, j) state of reagent diatom (cf. Eq. 2.62). The initial state-selected thermal rate constant is calculated from the total

ICS [6] (cf. Eq. 2.63). Finally, the thermal rate constants obtained using Eq. 2.63 are multiplied with the electronic partition function, $f_e(T)$, given by [7,8]

$$\begin{aligned} f_e(T) &= 2exp\left(\frac{-\Delta E_1}{T}\right)\frac{1}{[g_0^C + g_1^C exp\,(-\Delta E_1/T) + g_2^C exp\,(-\Delta E_2/T)]} \\ &\times \frac{1}{\left[g_{1/2}^{OH} + g_{3/2}^{OH} exp\,(-\Delta E_{13}/T)\right]}. \end{aligned} \tag{6.1}$$

Here g_0^C (=1), g_1^C (=3) and g_2^C (=5) are, respectively, the electronic degeneracies of $^3P_0$, $^3P_1$ and $^3P_2$ fine structure sublevels of carbon atom in its ground electronic state (^3P). In Eq. 6.1, ΔE_1 (=$^3P_1 - ^3P_0$ = 23.6 K) and ΔE_2 (=$^3P_2 - ^3P_1$ = 62.6 K) are the energy separations of these fine structure sublevels of carbon atom expressed in Kelvin units. Similarly, ΔE_{13} (=205 K) is the energy splitting of doubly degenerate $^2\Pi_{1/2}$ and $^2\Pi_{3/2}$ electronic states of OH molecule. As $^2\Pi_{1/2}$ and $^2\Pi_{3/2}$ states are doubly degenerate, $g_{1/2}^{OH} = g_{3/2}^{OH} = 2$.

To obtain the state-to-state reaction attributes, the initial wave packet (WP) pertinent to the reagent asymptote is prepared in the reagent Jacobi coordinates (R, r, γ) and immediately transformed to the product Jacobi coordinates (R_p, r_p, γ_p). Only the real part of the initial WP (cf. Eq. 2.53) is evolved in space and time as described in section 2.3.3. At the end of each time step, the time-dependent expansion coefficients are obtained using Eq. 2.65. These coefficients are then half Fourier transformed to give energy-dependent coefficients, $A^J_{v,j,\Omega\rightarrow v',j',\Omega'}(E)$ using Eq. 2.66. The latter are then transformed from body-fixed (BF) frame to space-fixed (SF) frame (cf. Eq. 2.67) and the $\boldsymbol{S}$ matrix in the SF frame is obtained using Eq. 2.69. Finally, the state-to-state reaction probability is given by $|S^J_{v,j,\Omega\rightarrow v',j',\Omega'}(E)|^2$. The state-to-state differential cross sections (DCSs) and ICSs are then obtained from the $\boldsymbol{S}$ matrix, respectively, using Eq.

Table 6.2: Numerical definition of the coordinate grid, initial wavefunction used to obtain state-to-state reaction attributes for the C + OH collisional system.

Parameter	Value	Description
$N_{R_p}/N_{r_p}/N_{\gamma_p}$	199/299/100	Number of grid points in product Jacobi coordinates
min/max of R_p (a_0)	0.1/17.0	Extension of the grid along R_p
min/max of r_p (a_0)	0.1/18.0	Extension of the grid along r_p
R_p^d (a_0)	12.0	Location of the dividing surface in the product channel
R_0 (a_0)	10.0	Initial location of the center of the sinc WP in the reagent Jacobi coordinates
E_{trans} (eV)	0.1	Initial translational kinetic energy
α/β_s	10/0.5	Width and smoothness of the initial sinc WP
v', j'	0-4, 0-50	Product rotational and vibrational levels considered for the final analysis
N_{time}	80000	Number of time steps

2.73 and Eq. 2.74. The properties of the initial WP and the grid parameters used for obtaining the state-to-state reaction probabilities are listed in Table 6.2. It is to be noted that the initial parameters presented in this table are not perfectly optimized. As a result, the state-resolved reaction probabilities presented in this chapter should be considered as the preliminary results. Finding of the optimized parameters and the state-to-state reaction attributes are still going on at the time of writing this thesis.

6.3 Results and discussion

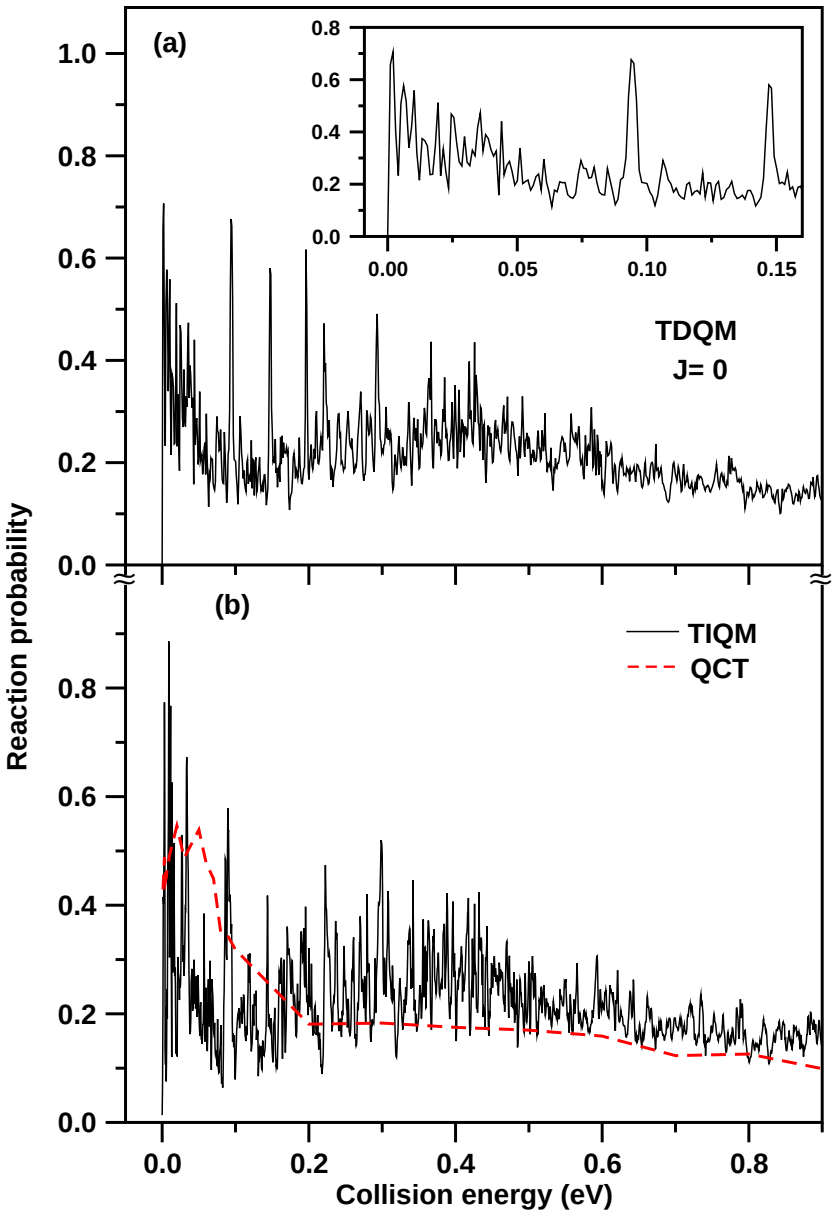

Figure 6.1: Total reaction probabilities as a function of the collision energy for the $C(^3P)$ + OH ($X^2\Pi$, v=0, j=0) → $CO(a^3\Pi)$ + H (^2S) reaction on its first excited electronic PES ($1^2A''$) and for $J = 0$. Panels a and b, respectively, show the results obtained in the present work using a TDQM method and the results obtained by Jorfi and Honvault [9] using both TIQM and QCT methods.

6.3.1 Initial state-selected reaction probabilities

Initial state-selected probabilities for the reaction C(^{3}P) + OH ($X^2\Pi$, v=0, j=0) $\rightarrow$ CO($a^3\Pi$, $\sum v'$, $\sum j'$) + H (^{2}S) on the first excited PES ($1^2A''$) are plotted as a function of collision energy in Fig. 6.1. These represent the energy resolved (ΔE $\sim$ 0.001 eV) total reaction probabilities (summed over all open v' and j' levels of the product CO at the given energy) and for the total angular momentum $J = 0$. It can be seen from the probability curve of Fig. 6.1 that the reaction does not have a threshold as expected for a barrierless reaction. The maximum probability is found at low collision energy (maximum value of $\sim$0.7 is at $\sim$ 0.002 eV). The reaction probability starting from a maximum value generally decreases with increasing collision energies. This behavior, as expected, is typical of an exothermic reaction. In the present case, as can be seen from Fig. 6.1(a), the probability curve supports numerous sharp oscillations. It is therefore clear that the underlying PES supports many long-lived quasibound (resonance) states and the reaction proceeds via quasibound complex formation. Starting from the onset, it can be seen that the probability reduces till the collision energy reach a value $\sim$ 0.088 eV (see the inset in panel a). Immediately after this drop in probabilities, a sharp and intense resonance peak is observed at around $\sim$ 0.09 eV collision energy (this is more clearly visualized in the inset of Fig. 6.1(a) by magnifying a part of the probability curve). From there onward a slow and steady increase in the probabilities is observed with the increase in collision energy till $\sim$ 0.45 eV, with regular appearance of sharp and intense resonance peaks. Above 0.5 eV collision energy, probabilities are found to decrease again and reach a constant value of $\sim$ 0.13 at energies greater than $\sim$ 0.8 eV. It is observed that at these high collision energies ($>$ 0.5 eV) the resonance peaks are not sharp and intense.

The total reaction probabilities of this reaction on the first excited PES were also obtained by Honvault and co-workers using time-independent quantum mechanical (TIQM) as well as quasi-classical trajectory (QCT) methods [9]. In order to compare, these results are reproduced in panel b of Fig. 6.1. It can be seen from panels a and b that the present reaction probabilities are in good accord with the TIQM and the QCT results of Ref. [9], despite the obvious fact that the signature of the resonance structures does not appear in the QCT results.

Honvault and co-workers also studied this reaction on the adiabatic ground electronic PES (X^2A') [10–16] and its second excited electronic state ($1^4A''$) [7,17,18]. The total reaction probabilities obtained by them on the first ($1^2A''$) and second ($1^4A''$) excited PESs show similar behavior i.e., sharp and intense resonance peaks at low collision energies (< 0.45 eV) and low (~ 0.1) and almost constant probabilities at high collision energies (> 0.7 eV). The sharp resonance peaks originate from the two deep wells of depth (relative to the reagent asymptote) ~ 4.6 eV (corresponding to the COH configuration) and ~ 6.2 eV (corresponding to the HCO configuration) supported by the first excited electronic ($1^2A''$) PES [7]. Similar well depths of ~ 1.85 eV and ~ 2.25 eV are supported by the second excited electronic ($1^4A''$) PES in that order [7]. The low probabilities (~ 0.1) observed at high collision energies (> 0.7 eV) for the reaction on first and second excited states are due to the dominant back dissociation at these energies [19]. In contrast to these results, the reaction probabilities obtained on the ground PES (X^2A') do not show any resonances and are close to ~ 1 in the whole range of collision energies considered (see Fig. 1 of Ref. [15]). Here the absence of the resonance peaks is explained on the basis of high exoergicity (6.5 eV) of the reaction on the ground (X^2A') PES. Though the latter is characterized by two deep wells of

depth (relative to the reactant asymptote) 5.5 eV (corresponds to COH configuration) and 7.3 eV (corresponds to HCO configuration) [10], the high exoergicity makes the product channel accessible more readily and hence results in the faster decay of the resonances. In contrast, the reaction on the first ($1^2A''$) and second ($1^4A''$) excited PESs have relatively low exoergicity ($\sim$ 0.41 eV) [7] and hence the resonances seem to have longer lifetimes and therefore show up in the total reaction probabilities.

The initial state-selected reaction probability values of the C + OH reaction on the first excited ($1^2A''$) PES are also obtained for the total angular momentum values $J > 0$. These are plotted in Fig. 6.2 for selected values of J and $\Omega = 0$ as indicated in each panel. It can be seen form Fig. 6.2 that with an increase in the value of J, there is a clear increase in the threshold ($\sim$ 0.0 eV for $J = 5$; $\sim$ 0.013 eV for $J = 45$; $\sim$ 0.082 eV for $J = 75$; $\sim$ 0.125 eV for J =85) and a clear decrease in the magnitude of total reaction probability. This energy shift of the onset of the reaction is far less than the similar reactions involving lighter atoms [20–22]. This is expected as the height of the centrifugal barrier slowly increases with increasing J for this reaction involving relatively heavy atoms. It can also be seen from panels e-h that the reaction probabilities at higher J (> 65) behave differently form that obtained at lower J (cf. panels a-d). In the former case, the total probabilities are relatively larger at an intermediate collision energies and remain almost constant thereafter (cf. panels e-h). In contrast, the probabilities obtained for $J < 65$ (cf. panels a-d), show relatively higher magnitudes at low collision energies (< 0.45 eV) with sharp and intense resonance structures. It is to be noted that the probabilities obtained for $J > 65$ show much dense resonance (less intense) oscillations at higher collisional energies (> 0.7 eV) when compared

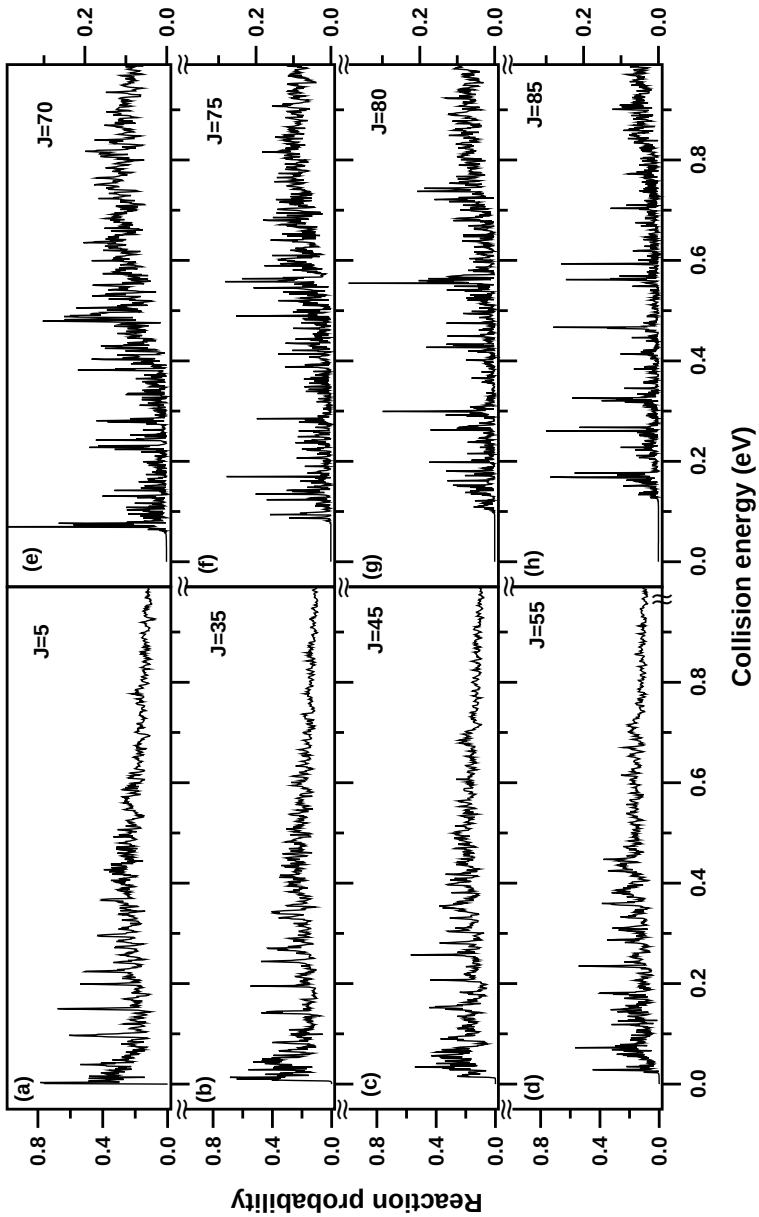

Figure 6.2: Same as in Fig. 6.1, but for different values of total angular momentum (J) as indicated in each panel and for $\Omega = 0$.

with that obtained for $J < 65$.

6.3.1.1 Rotational excitation of the reagent [OH (v=0, j=1)]

The effect of rotational excitation of reagent [OH (v=0, j=1)] on the C + OH reaction probability on the first excited $1^2A''$ PES is shown in Fig. 6.3. Panels a-f show the probabilities obtained for different values of J and for Ω (BF z-component of J) as indicated in the figure. It can be seen from Figs. 6.2 and 6.3 in comparison, that the overall behavior of the probability curves (with varying J) is similar in both the situations where the initial reagent is either in the ground rotational state [OH (v=0, j=0)] or first excited rotational state [OH (v=0, j=1)]. But in the latter case and for $\Omega = 0$, it is observed that the probabilities are relatively larger (by 5-10%) in magnitude (cf. panels a-d of Fig. 6.3 and panels a,c,e,g of Fig. 6.2). In contrast, the probabilities obtained for $\Omega = 1$ (panels e-h of Fig. 6.3) are $\sim$ 10 times smaller when compared with the same obtained for $\Omega = 0$ (cf. panels a-d of Fig. 6.3). It therefore concludes that the reagent rotational excitation has only slightly increased the reaction probabilities for $\Omega = 0$ but it drastically reduces the probabilities for $\Omega = 1$.

6.3.1.2 Vibrational excitation of the reagent [OH ($X^2\Pi$, v=1-2, j=0)]

The effect of vibrationally hot reagent [OH ($X^2\Pi$, v=1-2, j=0)] on the reaction probability is shown in Fig. 6.4. In panels a-c, the initial state-selected reaction probabilities for the reagent in its first excited vibrational state [OH ($X^2\Pi$, v=1, j=0)] and for selected values of J and $\Omega = 0$ are plotted as a function of collision energy. The same for the reagent OH ($X^2\Pi$, v=2, j=0) are plotted in panels d-f. These figures reveal that the probability curves (cf. Fig. 6.4) obtained with vibrationally excited reagent and for $J < 65$ look similar both in shape

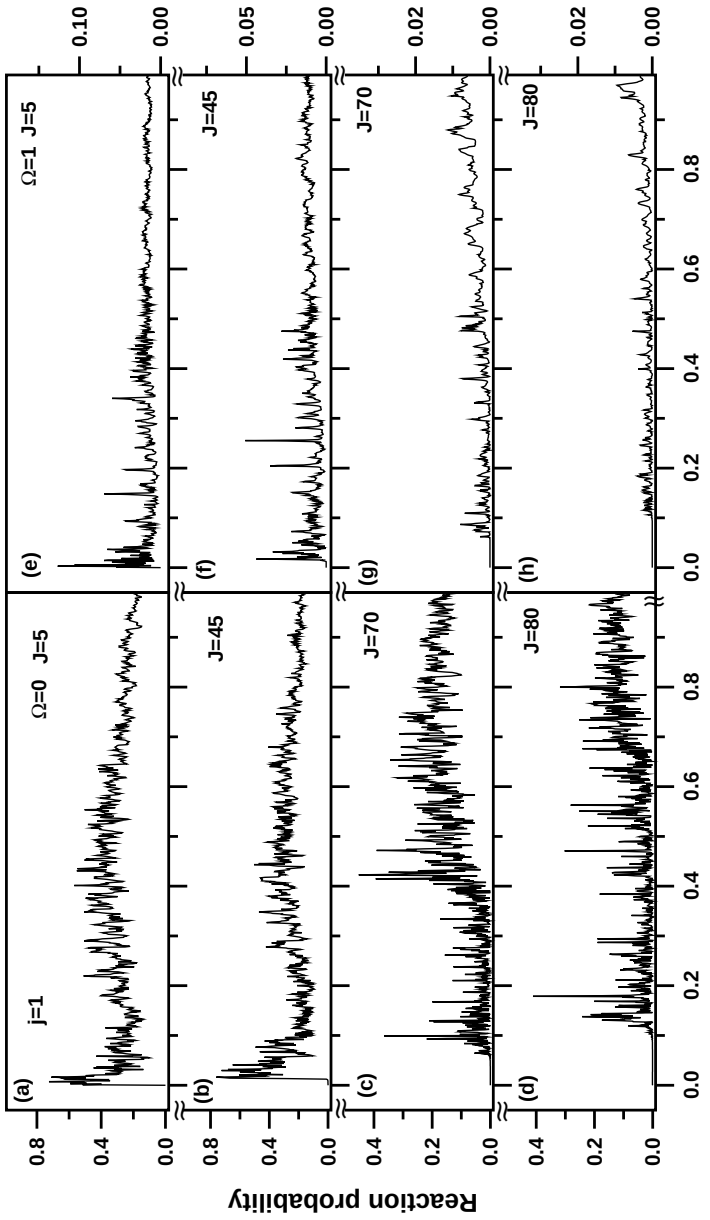

Figure 6.3: Same as in Fig. 6.2, but with rotationally excited [OH (v=0, j=1)]. Panels a-d and e-h, respectively, show the reaction probabilities for $\Omega = 0$ (BF z-component of J) and 1 and for selected values of J as indicated in each panel.

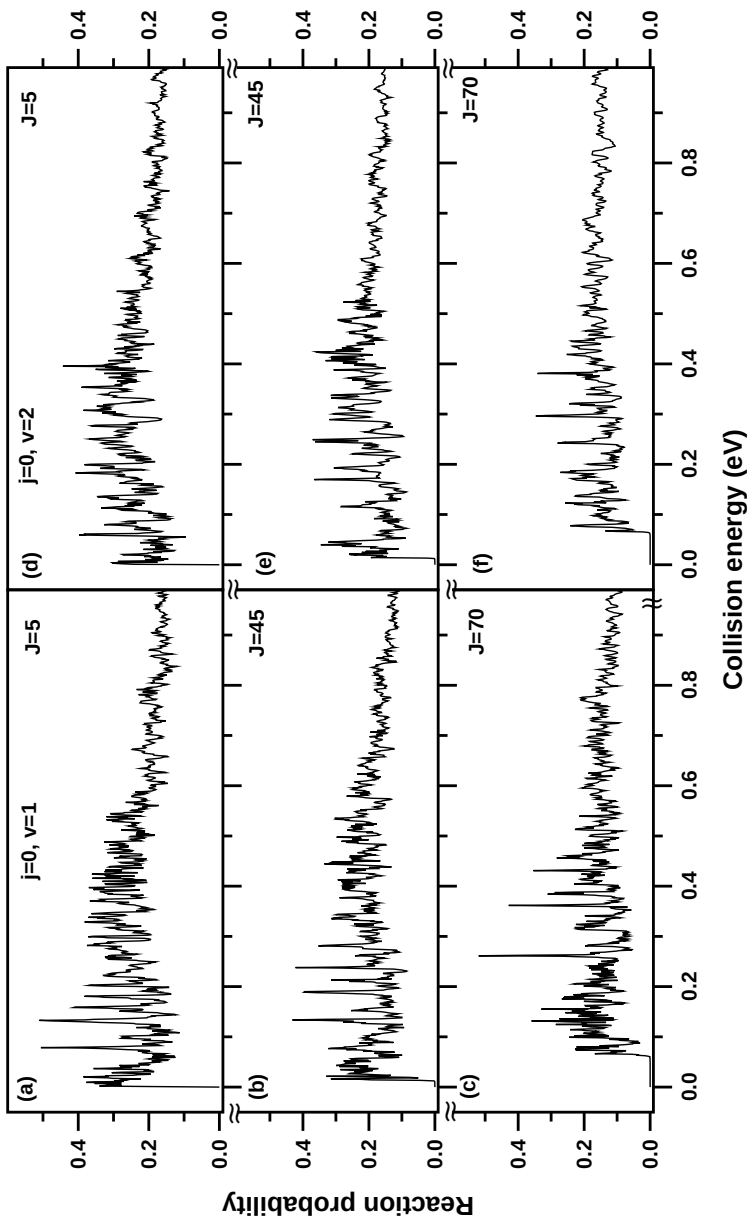

Figure 6.4: Same as in Fig. 6.2, but with reagent OH molecule in its first (panels a-c) and second (panels d-f) excited vibrational levels [OH (v=1,2, j=0)]. Panels a-f show the reaction probabilities for $\Omega = 0$ and for selected values of J as indicated in each panel.

and magnitude when compared with the same obtained for reagent in its ground vibrational level (cf. panels a and c of Fig. 6.2). But for higher values of J (cf. panels c and f of Fig. 6.4) the probabilities obtained for OH (v=1-2, j=0), are relatively larger at low collision energies which then slightly decrease but remain almost constant thereafter. This behavior is in contrast to that obtained for OH (v=0, j=0) at higher J (cf. panel e of Fig. 6.2). In the latter case, relatively smaller probability values are observed at low collision energies and relatively larger and almost constant probabilities at high collision energies. It therefore appears that the reagent vibrational excitation has minor effects on the overall shape and magnitude of the probabilities obtained for $J < 60$. But for higher J values, significant differences, viz., relatively larger probabilities at low collision energies and a slightly lower but almost constant probabilities at high collision energies are observed.

6.3.2 Vibrational and rotational state-resolved reaction probabilities

The vibrational state-resolved reaction probabilities obtained for the ground (v' = 0), first (v' = 1) and third excited (v' = 3) vibrational states of the product CO ($a^3\Pi$) are shown, respectively, in panels a, b and c of Fig. 6.5. These are the sum total of the probabilities obtained for all open product rotational states and for total angular momentum $J = 0$. The overall behavior of the vibrational state-resolved probabilities resembles very close to the total reaction probabilities presented in Fig. 6.1 except for the $v' = 3$ vibrational state of the product CO ($a^3\Pi$). For the latter product vibrational state, the reaction probabilities show a threshold of $\sim$ 0.08 eV. This is due to the inaccessibility of the CO ($a^3\Pi$, $v' = 3$) + H (^{2}S) product channel at energies below this threshold. Panels d, e and f of

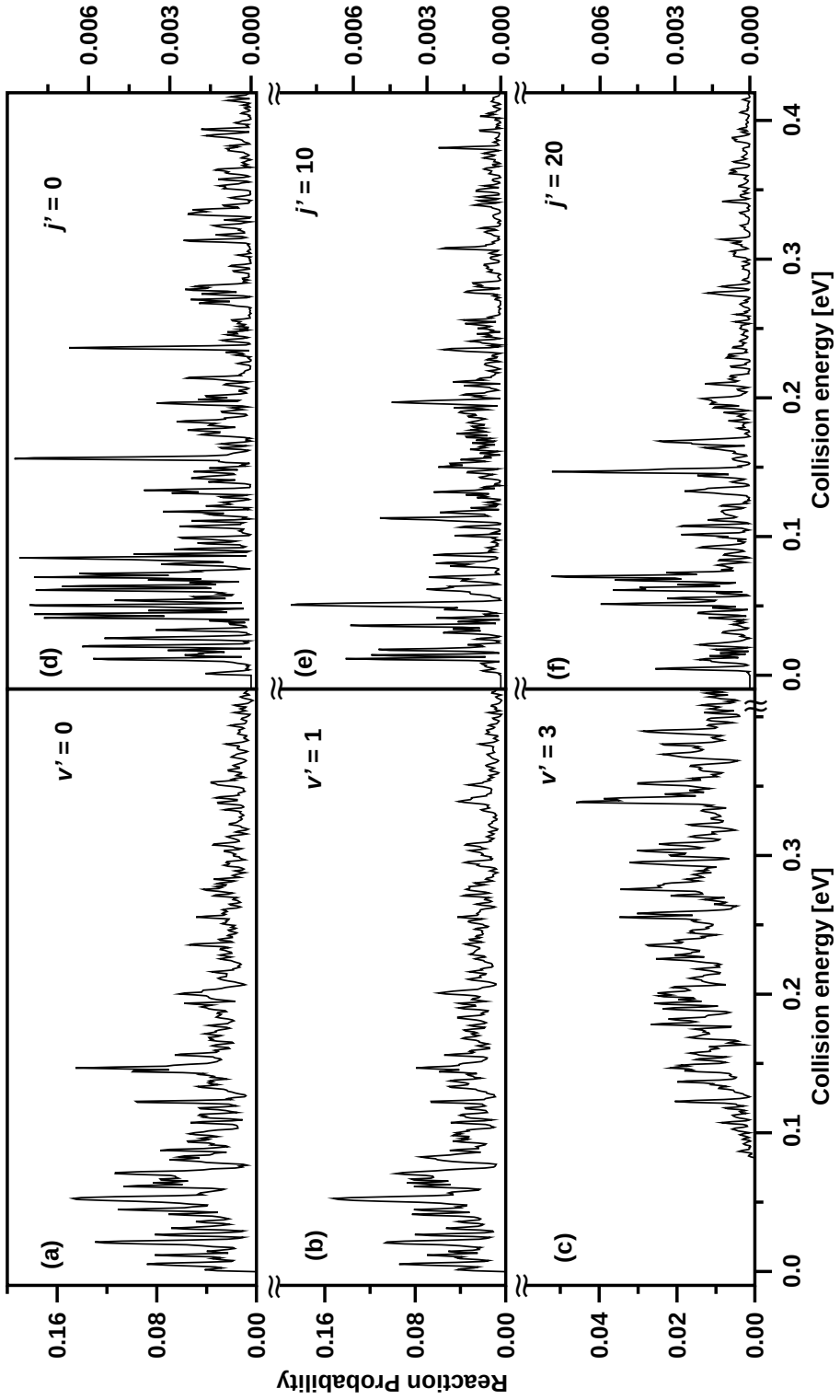

Figure 6.5: The vibrational (panels a-c) and rotational (panels d-f) state-resolved reaction probabilities for $C(^3P)$ + OH ($X^2\Pi$, v=0, j=0) $\rightarrow$ CO($a^3\Pi$, v' = 0-4, j' = 0-50) + H (^2S) reaction on its first excited electronic PES ($1^2A''$).

Fig. 6.5, respectively, show the rotational state-resolved reaction probabilities for the product CO ($a^3\Pi$, $v' = 0$) in $j' = 0$, 10 and 20 rotational states and for total angular momentum $J = 0$. It can be seen from panels d-f, that the rotational state-resolved reaction probabilities show sharp and dense resonance structures similar to the total reaction probabilities obtained at low collision energies and for total angular momentum $J > 65$ (cf. panels e-h of Fig. 6.2). In addition, it is clear from panels d-f, that the rotational state-resolved reaction probabilities do not depend strongly on the final rotational state j' of the product CO. Jorfi and Honvault obtained the vibrational and rotational state-resolved reaction probabilities for this reaction using TIQM method (cf. Figs. 2 and 3 of Ref. [9]. Qualitatively, the results presented here are matching well with that obtained by Jorfi and Honvault [9]. But at low collision energies, the reaction probabilities obtained by the latter authors showed relatively larger magnitude. As stated above, the present state-to-state results are not well optimized especially at low collision energies. Efforts are being made to remove these discrepancies.

6.3.3 Product vibrational and rotational distributions

The product vibrational distributions, i.e, the vibrational state-resolved reaction probabilities as a function of the product vibrational quantum number v', for the C(^{3}P) + OH ($X^2\Pi$, v=0, j=0) $\rightarrow$ CO($a^3\Pi$, $\Sigma j'$) + H (^{2}S) reaction on its first excited electronic PES ($1^2A''$) are shown in Fig. 6.6. These vibrational distributions obtained at some selected values of collision energies 0.01, 0.05 0.1 and 0.3 eV are, respectively, shown by circles, squares, diamonds and triangles in Fig. 6.6. It can be seen form the figure, that the product vibrational distributions behave differently at different collision energies. At low collision energies (0.01 and 0.05 eV), the vibrational distributions are almost statistical, i.e, decreasing

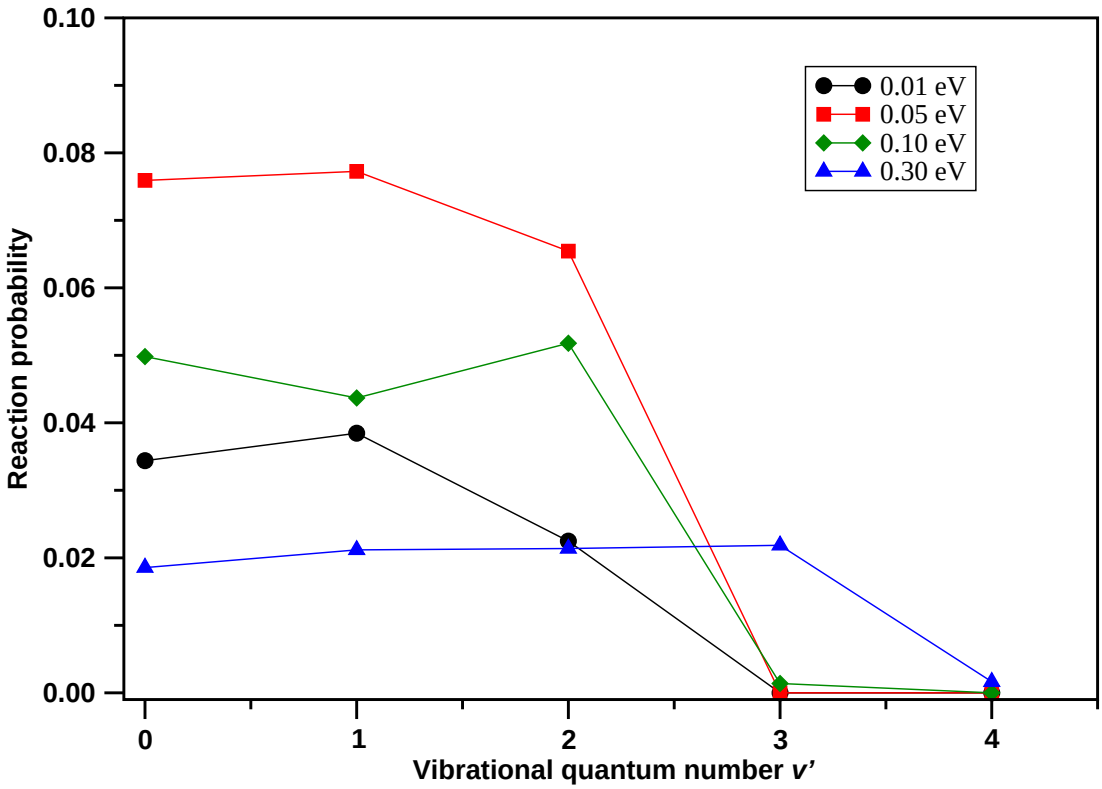

Figure 6.6: The product vibrational distributions for the C(^{3}P) + OH (X$^2\Pi$, v=0, j=0) → CO(a$^3\Pi$, $\Sigma v'$) + H (^{2}S) reaction on its first excited electronic PES ($1^2A''$) obtained at selected values of collision energies 0.01 eV (circles), 0.05 eV (squares), 0.1 eV (diamonds) and 0.3 eV (triangles).

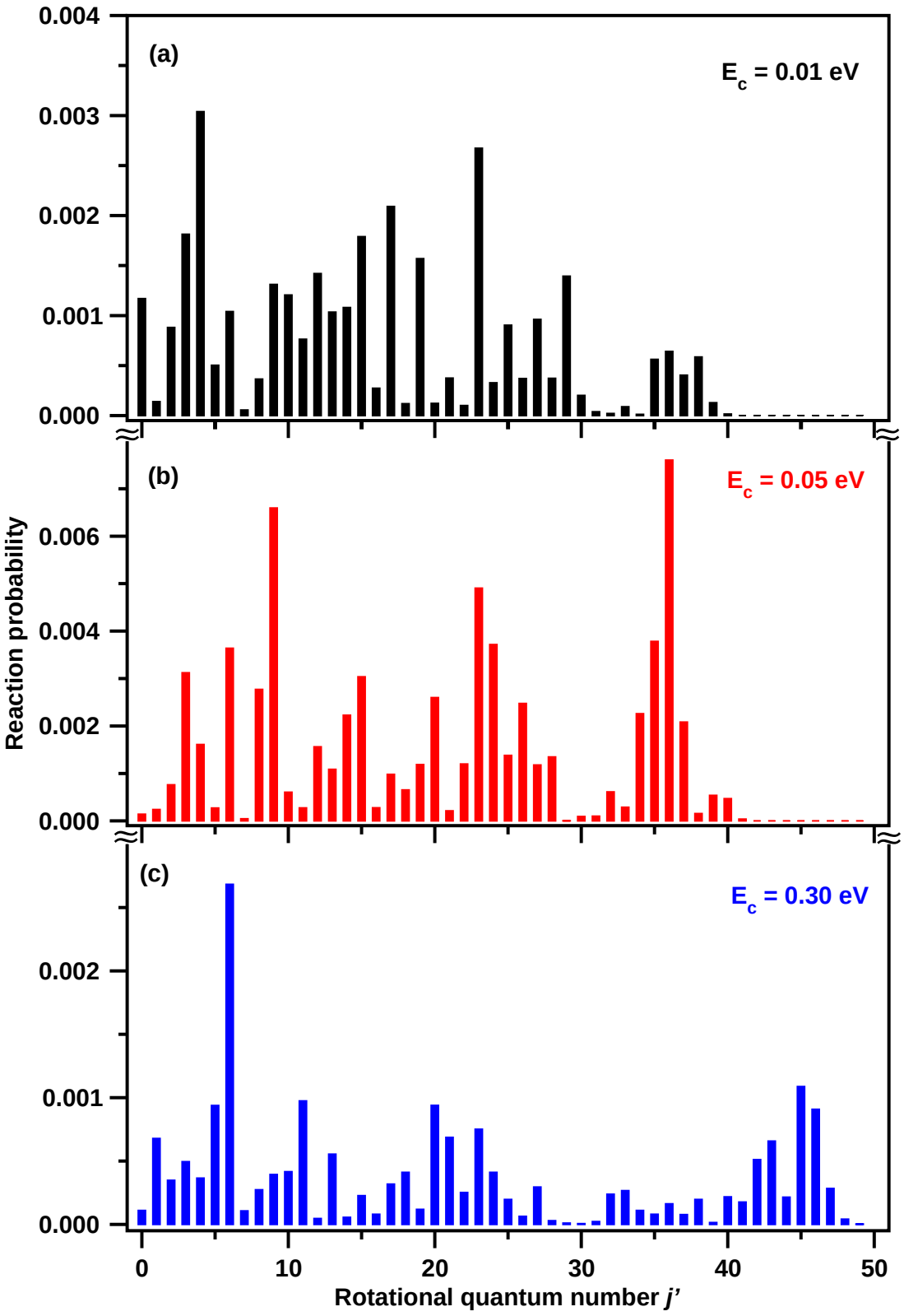

Figure 6.7: The product rotational distributions for the C(^{3}P) + OH (X$^2\Pi$, v=0, j=0) → CO(a$^3\Pi$, v' = 0) + H (^{2}S) reaction on its first excited electronic PES ($1^2A''$) obtained at selected values of collision energies as indicated in each panel.

with increasing v' except for $v' = 1$, at which the reaction probability is slightly larger when compare with that at $v' = 0$. In contrast, at 0.3 eV, the product vibrational distributions are almost constant for v' = 0-3 and then decreases. These observations infer that the reaction involves both direct (COH complex) and indirect (HCO) complex mechanisms.

The product rotational distributions for the C(^{3}P) + OH (X$^2\Pi$, v=0, j=0) $\rightarrow$ CO(a$^3\Pi$, $v' = 0$) + H (^{2}S) reaction on its first excited electronic PES (1^{2}A$''$) are obtained at some selected collision energies. These are shown in panels a-c of Fig. 6.7 and the collision energy at which the distributions are obtained is indicated in each panel. It can be seen from the figure, that the product rotational distributions are oscillatory in the entire span of product rotational states ($j\prime$ =0-50) considered here. This oscillatory behavior is observed at all collision energies. In addition, at some values of j', the probabilities are observed to be zero. As stated above, the results obtained here are qualitatively in good accord with those obtained by Jorfi and Honvault (cf. Figs. 4-5 of Ref. [9]) using TIQM method. Once the initial parameters for these calculations are optimized, a good quantitative agreement can also be attained. Hence the efforts are being made in that direction.

6.3.4 Initial state-selected integral reaction cross sections

The initial state-selected and energy resolved ICSs for the C(^{3}P) + OH (X$^2\Pi$, v=0-2, j=0-1) $\rightarrow$ CO(a$^3\Pi$) + H (^{2}S) reaction on its first excited PES (1^{2}A$''$) are plotted in Fig. 6.8. The cross sections obtained for rotationally ground OH (v=0, j=0) and excited reagent OH (v=0, j=1) are shown in black and red colors, respectively, in panel a. Similarly, the cross sections obtained for

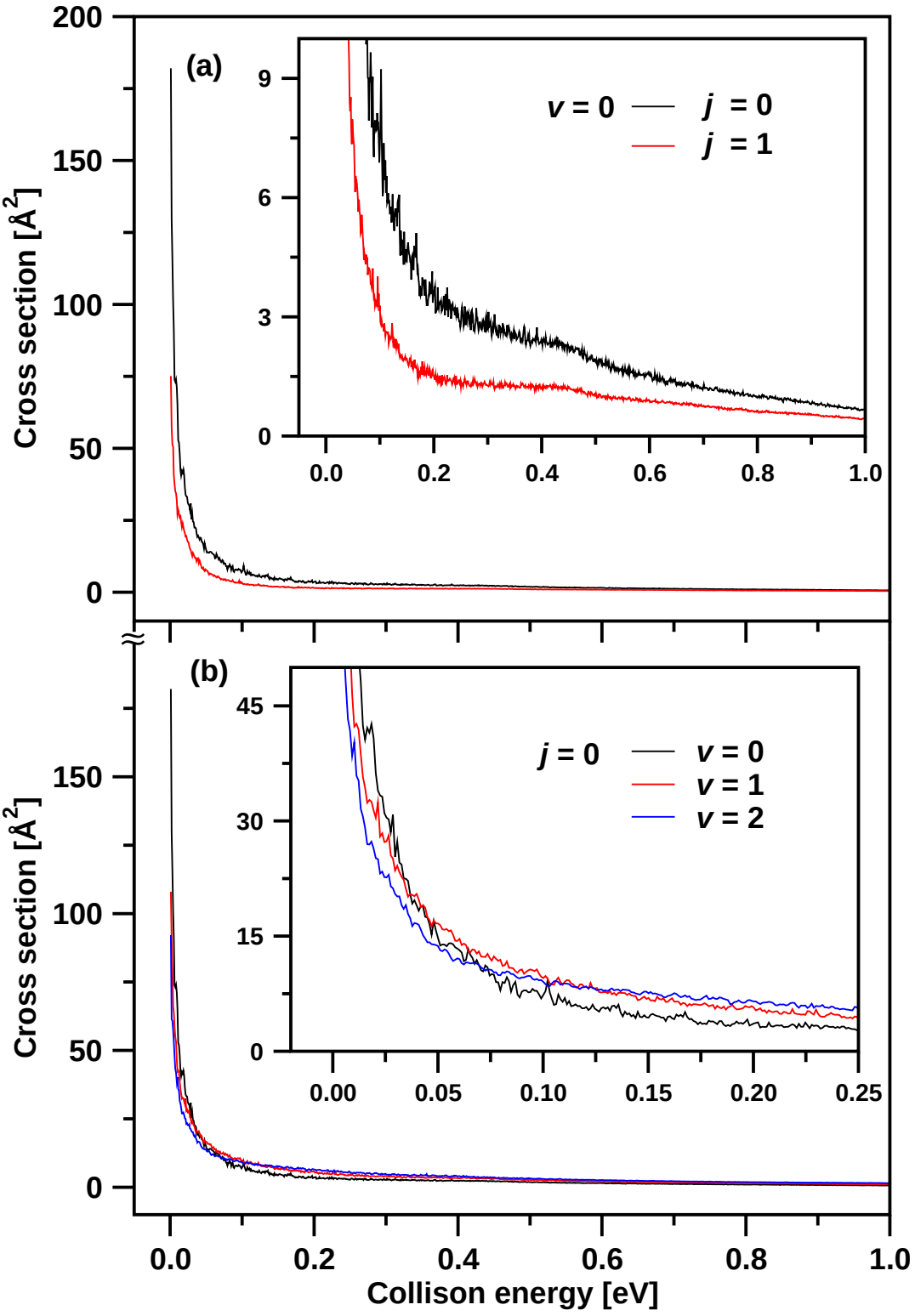

Figure 6.8: Initial state-selected ICSs as a function of the collision energy for the C(^{3}P) + OH ($X^2\Pi$, v=0-2, j=0-1) → CO($a^3\Pi$) + H (^{2}S) reaction on its first excited electronic PES ($1^2A''$). Panel a shows cross sections for the reagent in its ground (black) and first excited (red) rotational state. Similarly, panel b shows cross sections for the reagent in ground (black), first (red) and second (blue) excited vibrational state.

vibrationally ground OH (v=0, j=0) and excited OH (v=1-2, j=0) are shown in black (v=1), red (v=2) and blue (v=3) colors, respectively, in panel b. Within the CS approximation, all partial wave contributions of the total angular momentum up to $J = 95$ [and 120 for OH (v=1, j=0) and OH (v=2, j=0) reagent] are included to obtain the converged cross sections up to 1.0 eV collision energy. In case of rotationally excited reagents [OH ($j > 0$)], partial wave contributions, $0 \leq \Omega \leq \min(j, J)$, are also included in the calculations. It can be seen from panel a of Fig. 6.8 that, for a given value of j, the magnitude of reaction cross section is maximum at the onset ($\sim$ 181 Å^2 for j=0; $\sim$ 75 Å^2 for $j = 1$) and then decreases steeply at low collision energies (< 0.2 eV) reaches a value around $\sim$ 4 Å^2 ($\sim$ 1.5 Å^2 for j =1). Thereafter, the cross section decreases slowly with increasing collision energy. This trend of variation of cross section is typical of a barrierless reaction proceeding on a steep downhill reaction path. In regard to the effect of rotational excitation, it can be seen from panel a that reaction cross sections obtained for rotationally hot reagent [OH (v=0, j=1)] are relatively lower in magnitude when compared with the same obtained for OH (v=0, j=0). It is to be noted that the signature of the resonances due to the two deep wells present in the (1^2A$''$) PES are observed in the reaction cross sections. This is shown clearly in the inset of panel a. Vibrational excitation of the reagent also shows similar effects on the observed reaction cross sections. But in this case, two different trends are observed. At low collision energies (< 0.05 eV), the reaction cross sections decrease with the increasing vibrational quantum number of the reagent (see inset of panel b). In contrast, at collision energies greater than $\sim$ 0.1 eV, the reaction cross sections increase with increasing vibrational excitation of the reagent OH. But in either case, the rise or fall in the magnitude of the cross sections with the vibrational excitations is not as prominent as observed during

rotational excitation (cf. panel a and panel b).

Honvault and co-workers also obtained the ICSs for this reaction on the adiabatic ground electronic state (X^2A') [11–13,15] and second excited electronic state ($1^4A''$) [18]. Their calculations reveal that the overall behavior of the reaction cross sections obtained on the ground X^2A' PES and second excited $1^4A''$ PES is very similar to the same obtained in present calculations on the first excited $1^2A''$ PES (cf. Fig. 6 of Ref. [15], Fig. 7 of Ref. [18] and Fig. 6.8 of present study). But in terms of magnitude, the reaction cross sections obtained on the electronic ground PES are relatively larger. This is expected because the exoergicity of the reaction on the ground PES is relatively higher ($\sim$ 6.5 eV) compared to the same ($\sim$ 0.41 eV) on the first and second excited electronic states. It is to be noted that the clear signature of the resonances is observed in the ICSs obtained here on the first excited $1^2A''$ PES (cf. inset of Fig. 6.8)). But such signatures are not observed in the reaction cross sections calculated on the ground and second excited electronic states.

6.3.5 Initial state-selected rate constants

The initial state-selected and temperature dependent rate constants for the C(^{3}P) + OH ($X^2\Pi$, v=0-2, j=0-1) $\rightarrow$ CO($a^3\Pi$) + H (^{2}S) reaction on the first excited PES ($1^2A''$) are plotted in Fig. 6.9(a). The rate constants obtained for the reagent in its ground [OH ($j = 0$, $v = 0$)] and first excited [OH ($j = 1$, $v = 0$)] rotational state are shown by the solid and dashed lines, respectively. It can be seen from Fig. 6.9(a) that for a given value of j, the magnitude of rate constant increases sharply at the onset and reaches a maximum value ($\sim 4.65 \times 10^{-11}$ cm^3 sec^{-1} molecule^{-1} at $\sim$ 34 K for $j = 0$; $\sim 2.14 \times 10^{-11}$ cm^3 sec^{-1} molecule^{-1} at $\sim$ 38

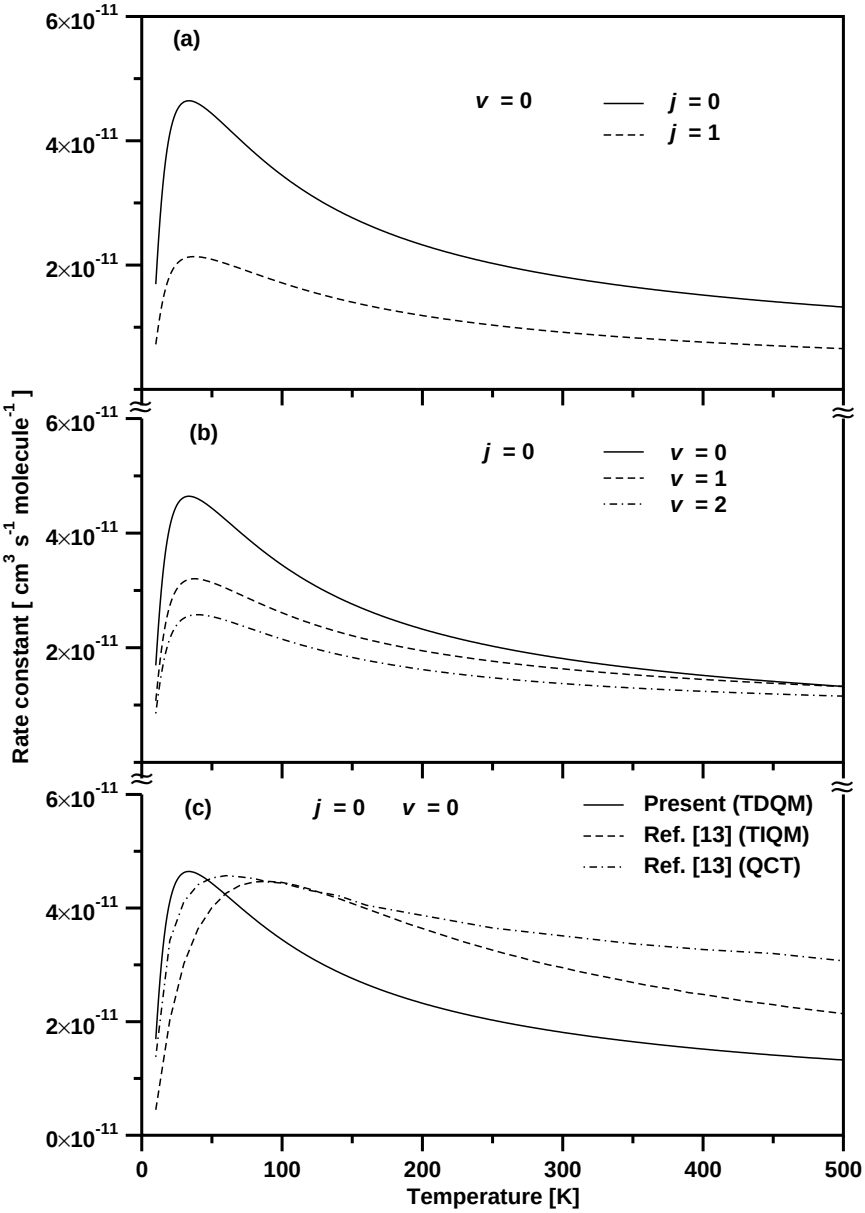

Figure 6.9: Initial state-selected rate constants as a function of temperature for the $C(^3P) + OH\ (X^2\Pi, v{=}0, j{=}0\text{-}1) \rightarrow CO(a^3\Pi) + H\ (^2S)$ reaction on its first excited PES ($1^2A''$). Panel a shows rate constants obtained in the present TDQM calculations and for the reagent $j = 0$ (solid line) and $j = 1$ (dashed line) rotational states. Similarly panel b shows rate constants obtained for vibrationally ground (solid line), first (dashed line) and second (dot-dashed line) excited levels of the reagent OH. Panel c compares the rate constants obtained in the present work (solid line) with those obtained by Jorfi and Honvault [9] by a TIQM method (dashed line) and the QCT method (dot-dashed line).

K for $j = 1$) and then slowly decreases with increasing temperature. Analogous to the cross section results of Fig. 6.8(a), the reaction rates also decrease (by about a factor of two) with rotational excitation of the reagent OH molecule. The effects of vibrational excitation of the reagent on reaction rates are shown in panel b. Here the rate constants obtained for the reagent in its ground, first and second excited vibrational states are, respectively, shown by the solid, dashed and dot-dashed lines. It can be seen from panel b that reaction rates decrease with increasing vibrational excitation of the reagent OH. However, the extent of decrease is far lower than the same found with the rotationally hot reagent (cf. panel a and b). As stated above the cross sections also showed similar behavior at collision energies less than ~ 0.05 eV (where the magnitude of the cross sections is dominant). Now it is clear from panels a and b that both rotational and vibrational excitations in general demotes the reaction and the effect is stronger in the former case. As many factors govern the reactivity of the system, it is hard to find the precise cause for this demotion. One possible factor could be the degree of alignment and orientation of the reagent species. This reaction which proceeds via complex formation mechanisms, the orientation and alignment is expected to play a vital role. In general, the rotationally excited reagent has less degree of alignment or orientation which could interrupt the formation of the intermediate complex (COH or HCO). As a result, a lower reactivity is observed for the reagent in rotationally excited state. On the other hand, vibrational excitation does not lower the degree of orientation as much as observed for the rotational excitation. Hence in this case the decrement in the rates is less prominent.

In order to compare, the results obtained by Jorfi and Honvault [9] using the TIQM method (dashed line) and QCT method (dot-dashed line) are reproduced

in panel c of Fig. 6.9 along with the same obtained in the present study (solid line). It can be seen from panel c that the rates obtained here using the time-dependent quantum mechanical (TDQM) method are of the same order of magnitude when compared with the rates obtained using TIQM and QCT methods [9]. The rates obtained by latter methods are overestimated in the broad temperature range 60-500 K but in the low temperature range (0-60 K) they are underestimated. It is to be noted that Jorfi and Honvault used a J-shifting approximation [23] in their TIQM study [9] to calculate the reaction probabilities for non-zero total angular momentum J. As discussed earlier that the exact probabilities for $J > 0$ are significantly different from those for $J = 0$, the J-shifting approximation obviously is not a good approximation here and thus leading to the observed discrepancies. It is to be noted that, Honvault and co-workers also obtained the rate constants for this reaction on the electronic ground X^2A' PES [11–13, 15, 16] and second excited $1^4A''$ PES [17]. As expected the rates for the reaction on the ground X^2A' PES are higher because of its high exoergicity.

6.4 Summary and outlook

A theoretical account of the C(^{3}P) + OH ($X^2\Pi$, v=0, j=0-1) → CO($a^3\Pi$) + H (^{2}S) reaction on the first electronic excited state ($1^2A''$), employing a time-dependent WP method is presented in this chapter. The initial state-selected dynamical attributes, viz, reaction probabilities, ICSs and rate constants are reported. The dense resonance structures are observed in the reaction probabilities and finally in the ICSs. These resonance structures stem from the two deep wells present on the surface and also because of the low exoergicity of the reaction on this surface. In addition, the effect of rotational and vibrational excitation on the

reaction attributes are examined. Reagent rotational and vibrational excitation demotes the reactivity and the effect is more prominent in the former case. The results presented here are in good accord with those obtained by Honvault and co-workers using TIQM and QCT methods. A study of the C + OH reaction dynamics by considering the nonadiabatic coupling (NAC) between the excited PESs are currently being taken up.

References

[1] R.T. Pack, J. Chem. Phys. 60 (1974) 633; P. McGuire, D.J. Kouri, J. Chem. Phys. 60 (1974) 2488.

[2] M. D. Feit, J .A. Fleck Jr., and A. Steiger, J. Comput. Phys. **47**, 412 (1982).

[3] D. Kosloff, and R. Kosloff, J. Comput. Phys. **52**, 35 (1983).

[4] J. C. Light, I. P. Hamilton, and J. V. Lill, J. Chem. Phys. **82**, 1400 (1985).

[5] S. Mahapatra, and N. Sathyamurthy, J. Chem. Soc. Faraday Trans. **93**, 773 (1997).

[6] F. J. Aoiz, L. Bañares, and J. F. Castillo, J. Chem. Phys. **111**, 4013 (1999).

[7] A. Zanchet, B. Bussery-Honvault, M. Jorfi, P. Honvault, Phys. Chem. Chem. Phys. 11 (2009) 6182.

[8] M.M. Graff, A.F. Wagner, J. Chem. Phys. 92 (1990) 2423.

[9] M. Jorfi, P. Honvault, J. Phys. Chem. A 114 (2010) 4742.

[10] A. Zanchet, B. Bussery-Honvault, P. Honvault, J. Phys. Chem. A 110 (2006) 12017.

[11] A. Zanchet, P. Halvick, J.-C. Rayez, B. Bussery-Honvault, P. Honvault, J. Chem. Phys. 126 (2007) 184308.

[12] A. Zanchet, P. Honvault, B. Bussery-Honvault, P. Halvick, J.-C. Rayez, S.Y. Lin, H. Guo, in; J.L. Lemaire, F. Combes (Eds.) Molecules in Space and Laboratory conference proceedings, S. Diana (publisher), Paris, 2007, p. 118.

[13] S.Y. Lin, H. Guo, P. Honvault, Chem. Phys. Lett. 453 (2008) 140.

[14] A. Zanchet, P. Halvick, B. Bussery-Honvault, P. Honvault, J. Chem. Phys. 128 (2008) 204301.

[15] N. Bulut, A. Zanchet, P. Honvault, B. Bussery-Honvault, L. Bañares, J. Chem. Phys. 130 (2009) 194303.

[16] M. Jorfi, B. Bussery-Honvault, P. Honvault, T. Stoecklin, P. Larrégaray, P. Halvick, J. Phys. Chem. A 114 (2010) 7494.

[17] M. Jorfi, P. Honvault, J. Phys. Chem. A 115 (2011) 8791.

[18] A. Zanchet, T. González-Lezana, O. Roncero, M. Jorfi, P. Honvault, M. Hankel, J. Chem. Phys. 136 (2012) 164309.

[19] M. Jorfi, P. Honvault, P. Bargueno, T. González-Lezana, P. Larrégaray, L. Bonnet, P. Halvick, J. Chem. Phys. 130 (2009) 184301.

[20] Tanmoy Roy, T. Rajagopala Rao, S. Mahapatra, Chem. Phys. Lett. 501 (2011) 252 .

[21] Tanmoy Roy, S. Mahapatra, J. Chem. Phys. 136 (2012) 174313.

[22] R. Padmanaban, S. Mahapatra, J. Chem. Phys. 121 (2004) 7681.

[23] J.M. Bowman, J. Phys. Chem. 95 (1991) 4960.

List of Publications:

1) **T. Rajagopala Rao**, B. Jayachander Rao and S. Mahapatra, “Quantum nonadiabatic dynamics of hydrogen exchange reactions", Chem. Phys., 365, 129-137, (2009).”

2) Tanmoy Roy, **T. Rajagopala Rao** and S. Mahapatra,"Quantum dynamics of H + LiH^+ reaction on its electronic ground state ". Chem. Phys. Lett. ,501, 252-256 (2010).

3) **T. Rajagopala Rao** and S. Mahapatra, “ Nuclear motion on the orbitally degenerate electronic ground state of fully deuterated triatomic hydrogen.” J. Chem. Phys., 134, 204307 (2011).

4) **T. Rajagopala Rao** and S. Mahapatra, “Theoretical study of ClH_2^- electron detachment spectroscopy revisited.” (submitted)

5) **T. Rajagopala Rao**, Sugata goswami, S. Mahapatra, B. Bussery-Honvault, P. Honvault, “Time-dependent quantum wave packet dynamics of the C + OH reaction on the excited electronic state.” (submitted)

6) Sugata goswami, **T. Rajagopala Rao**, S. Mahapatra, B. Bussery-Honvault, P. Honvault, “Time-dependent quantum wave packet dynamics of the S + OH reaction.” (manuscript under preparation)

Presentations in Conferences:

1) **Poster** presented in “Theoretical Chemistry Symposium (TCS 2009)”, January 18-22, 2009, Indian Institute of Science and Jawaharlal Nehru Centre for Advanced Scientific Research, Bangalore.

2) **Poster** presented in “Theoretical Chemistry Symposium (TCS 2010)”, December 8-12, 2010, Indian Institute Technology, Kanpur.

3) **Posters** presented in “Chemfest 2008, 2009, 2010”, School of Chemistry, University of Hyderabad, Hyderabad.

4) **Oral presentation** in “Chemfest 2011”, February 25-26, 2011, School of Chemistry, University of Hyderabad, Hyderabad.

5) **Oral presentation** in “International meeting on atomic and molecular physics and chemistry”, July 5-8, 2011, Rennes, France.

6) **Poster** presented in “International conference on applied theory on molecular systems”, November 2-5, 2011, Indian Institute of Chemical Technology, Hyderabad, India.

Acknowledgments

Understanding the maths behind the quantum mechanics....., coding the equations..., shouting with joy when it really works...., serious debugging when it fails...., making snapshots of the evolving wave packets and showing it to every one in the lab..., motivating discussions with my advisory and colleagues...., grappling with paper writing (still a tough job to me)....., making posters and power point presentations (with utmost use of animation effects)...., presenting them at conferences...., staying up until the birds start singing and people start jogging....., and most importantly struggling to staying focused..., Wow.... it is a wonderful and overwhelming experience with working on the Ph. D. Many people made this journey enjoyable and unforgettable and I am very much indebted to all of them.

Firstly, I express my profound respect and deep sense of gratitude to my adviser Prof. Susanta Mahapatra. Dear Sir! To work with you has been a wonderful experience to me, with loads of fun and excitement. I still remember my initial days of the Ph.D where we both had lot of technical discussions mostly in the corridor (old chemistry building i.e, science complex) or at drinking water place. Whenever you see me, you used to ask me the question, “How far do you go?” and I used to tell you some technical problem with the codes and as a reply, you used to give me a ready reference to it. I really admired you at that time for your memory to remember all those references. That is Indeed a most exciting way of learning the subject and those memories always make me nostalgic. Apart from those learning days, you have been a steady influence throughout my Ph.D. career; you have always shown lot of confidence in me, supported me with promptness and care, and have always been patient and encouraging in times of new ideas and difficulties; you have listened to my ideas and discussions with you frequently led to key insights. Your ability to select and to approach compelling research problems, your high scientific standards, and your hard work and your paper writing and editing skills set an example. I admire your ability to balance research interests and personal pursuits. Above all, you supported me when I am going through the most difficult phase of my life. I am very much indebted to you for the moral support you gave me at that time and also through out my Ph. D career. I thank you very very.... much for giving me this wonderful Ph. D experience.

When I said in CHEMFEST-20011 that “Prof. M. Durga Prasad has introduced me to this exciting field of quantum chemistry”, most of the people felt that I am trying to flatter Prof. M. Durga Prasad to avoid questions from him after my oral presentation. Dear sir! I really meant it when I said those words

as it came spontaneously, deeply, from my heart. Indeed I very much admired your lectures during my M.Sc days and am still longing for them. The physical significances you link to the mathematical equations are the most exciting features of your lectures. It changed my perception towards quantum mechanics and made it as my favorite subject. It compelled me to go through more books on the subject and discuss more with my fellow classmates. I really thank you deeply from my heart for making quantum chemistry as my favorite subject and thus introducing me to this field.

I thank Prof. Pascal Honvoult and B. Bussery-Honvault for the scientific collaboration and also for their hospitality during my visit to the Dijon. The work presented in the last chapter of this thesis is the result of our scientific collaboration.

I thank Prof. Stuart Althorpe, Prof. Millard H. Alexander, Prof. M. Hankel, Prof. Jacek Klos, Prof. Nikola Markovic for their immediate and prompt replies to many of my technical queries. In addition, I thank Prof. Stephen K. Gray, Prof. Gabriel G. Balint-Kurti and Prof. Marlies Hankel for providing the DIFFREAL wave code.

I thank the former and present Deans, School of Chemistry and all other faculty members, non-teaching staff (especially Durgesh) of the school for their cooperation and assistance on various occasions. I also thank all the faculty members of school of chemistry for their support in various occasions.

I thank the Council of Scientific and Industrial Research (CSIR, New Delhi) and Indo-French Centre for the Promotion of Advanced Research (IFCPAR, New Delhi) for their financial support. I also thank Center for Modeling Simulation and Design (CMSD, University of Hyderabad) for providing a high-class computational facilities.

I thank my labmates Subash bhayya, Jayachander bhayya, Venkatesh bhayya, Tanmoy Mondal bhayya , Sivaranjan bhayya, Rajagopala Reddy, Tanmoy Roy, Naga Prasad, Sugatho, Rudro, Krishna, Subhramanyam and Arpita for motivated discussions in the lab and helping me in solving various problems. Special thanks to Subash bhayya and Jayachander bhayya for helping me in understanding various FORTRAN codes used in our lab. Also a special thanks to Nagaprasad for supporting me in my hard times.

I thank Mrs. Gitashree Mahapatra (madam) for providing me a homely feeling in several occasions. I really enjoyed the time spent with the kids Anusha (she taught me some dance steps) and Anish. May be because of my looks he calls me “best vilan”.

I use this opportunity to thank all of my teachers, especially Devadas sir, Shaym babu sir and Sri Vidhya madam. My journey towards this Ph. D would not have been possible with out their support.

I thank all my M.Sc friends (Naveen, Gupta, Hari, Manoj, Santosh, Satish, Venu, Raghavaiah, Ravinder etc.), Ph. D friends, (P. Kishore, R. Kishore, Anand, Bharat, Karunakar, Durga prasad (TEM), Yasin, Sasi (my coach), Ramam, Nagarjuna (VB lab), Geetha, Shuvra, Subrata, Saritha, Dinesh (MDP lab), Sridhar, Sudalai, Ashok, Chandu, Santosh (AS lab), Rajesh bhayya (TPR lab), Abijit bhayya, Ramesh anna (TPR lab), Balaswamy, Kesav, Lasya, anji anna, Satpal bhayya, Malli, Rama raju, Vijji, DK anna, Santhanam, Raju, Malakappa, Sudhangshu, Balu (SP lab), Tulika di, Vikrat, Obhayya, Murali, Bharani, Srinivas (DBR lab), Naidu etc.), B. Sc friends (Aditya, Naresh, Chalam, Venki etc.) With out their company my journey would have been very boring.

I thank my friends at home town Srikakulam, Kiran, Nani, Sailaja and her cute daughter Babbi. I also thank my uncle M. Venkateswara Rao babai and aunt Kamala pinni and their children Buzzi and Ravi for their support at various ocassions.

Finally and most importantly, I thank all the members of my family for their unconditional support and encouragement. I dedicate this thesis to my parents, though they are not here to share this moment with me. But I am sure they are showering their blessing from the heaven.